

# **Additives for Faster Separation in Melt Layer Crystallization**

Dissertation  
zur Erlangung des  
Doktorgrades der Ingenieurwissenschaften (Dr.-Ing.)

der

Naturwissenschaftlichen Fakultät I – Biowissenschaften –

der Martin-Luther-Universität  
Halle-Wittenberg

vorgelegt

von Herrn Dipl.-Ing. Felix Johannes Seidel

geb. Eisenbart am 18.04.1989 in Clausthal-Zellerfeld

Gutachter:

Prof. Dr.-Ing. Dr. h.c. Joachim Ulrich

Prof. Dr.-Ing. Gerhard Schembecker

Prof. Dr.-Ing. René Androsch

Tag der öffentlichen Verteidigung:

Mittwoch, 31.05.2017

## Acknowledgement

The present thesis is the result of my work at Martin-Luther-Universität Halle-Wittenberg. It would not have been possible without Prof. Dr.-Ing. Dr. h.c. Joachim Ulrich, who set the task of the research endeavour, commented on the experimental methodology as well as manuscript, and secured the funds, especially a scholarship from Martin-Luther-Universität Halle-Wittenberg itself. He also acted as reviewer alongside Prof. Dr.-Ing. Gerhard Schembecker of TU Dortmund and Prof. Dr.-Ing. René Androsch of Martin-Luther-Universität. Profs. Ulrich and Androsch also were part of the exam committee which was chaired by Prof. Dr. rer. nat. Thomas Groth. Prof. Dr. Jörg Kreßler and Prof. Dr. Hans-Joachim Radusch acted as further members of the committee. I thank all of them for their participation.

I thank Nadine Angermeier for contributing to the work in form of a diploma-thesis, as well as Baharak Sayapour, Drucilla Mumba and Christina Höser for contributing laboratory work. Furthermore, I have to thank the technicians of the workshop of Zentrum für Ingenieurwissenschaften, especially its chief, Bertram Kleinert, as well as those of the workshop of the Physicists department and lampworker Torsten Schurig, all of Martin-Luther-Universität Halle-Wittenberg.

For providing valuable information as well as material for experimentation, I thank Sulzer Chemtech AG, Winterthur, Switzerland, and thereof especially Claudia Pudack, Manfred Stepanski and Mathias Pfeil, EDL Anlagenbau Gesellschaft mbH, Leipzig, Germany, Institut für Nichtklassische Chemie e.V., *ibid.*, Air Liquide Global E&C Solutions Germany GmbH, Frankfurt am Main and thereof especially Ulrike Streiber, as well as Hallesche Ölverarbeitungswerke GmbH, Halle (Saale), and thereof especially Wolfgang Tappe.

I thank my colleagues at the department of thermal process engineering at Martin-Luther-Universität, Sandra Peterson, Patrick Froberg, Ahmed Abouzeid, Muhammad Ahmad, Hamid Altahar, Mariam Fardmostafavi, Anne Hartwig, Julia Herfurth, Jiting Huang, Miaomiao Jin, Franziska Kreißig, Yi Liu, Ronny Oswald, Stefanie Selbmann, Yuzhu Sun, Haihao Tang, Martha Wellner, Xiaoxi Yu, and especially Julia Seidel for support.

I very much thank Sohie Rüttinger for helpful comments on the manuscript.

I further acknowledge that some parts and results of this study have been published previously under my primary authorship [Eis14a,b,15a-c,16a-d].

Für die moralische Unterstützung während der Promotion danke ich meiner Familie; meiner Frau, meinen Eltern und Schwestern, und zum Schluss, aber sicher nicht zuletzt, Sophie.

## List of Contents

Acknowledgement .....	1
1 Introduction .....	1
2 State of the Art and Theory .....	3
2.1 Industrial context .....	3
2.1.1 Industrial crystallization terminology .....	3
2.1.2 Melt layer crystallization as industrial separation technology .....	6
2.1.3 Separation techniques for glycerol purification and paraffin wax deoiling .....	9
2.2 Theory of melt layer crystallization .....	11
2.2.1 Nucleation .....	11
2.2.2 Growth .....	14
2.2.3 Separation on a microscopic scale: lattices and lattice defects.....	18
2.2.4 Separation on a macroscopic scale: phase diagrams, porosity and concentration polarization.....	21
2.3 Research techniques in melt layer crystallization .....	24
2.3.1 Crystallization equipment, experimental setups and measuring techniques ....	24
2.3.2 Scale up, correlation and prediction .....	27
3 Motivation.....	30
4 Materials and Methods .....	31
4.1 Materials .....	31
4.1.1 General .....	31
4.1.2 Paraffin.....	31
4.1.3 Glycerol - water system (gw) .....	31
4.1.4 Raw glycerol system (rg).....	32
4.2 Setups and procedures .....	32
4.2.1 General .....	32
4.2.2 Glycerol seed production.....	33
4.2.3 Seed crystal growth.....	33
4.2.4 Magnetic stirrer cold finger setup (MCF).....	34

## List of Contents

4.2.5	Glass setup (GL) .....	35
4.2.6	Bottle tests .....	35
4.2.7	Experiments on layer stability .....	36
4.2.8	Static cold finger setup (SCF).....	37
4.2.9	Translating beaker cold finger setup (TBCF) .....	39
4.2.10	Experiments on raw glycerol .....	40
4.2.11	Sweating of paraffin slack wax .....	41
4.3	Analytics and data evaluation .....	42
4.3.1	Analytics.....	42
4.3.2	Growth rate evaluation .....	42
4.3.3	Processing of DSC curves for the analysis of paraffin .....	46
5	Results .....	50
5.1	Paraffin.....	50
5.1.1	Influence of the crystallization kinetics on the melting behaviour .....	50
5.1.2	Thermodynamic limits to the deoiling of mmo slack wax in layer crystallization 51	
5.1.3	Photometric evidence of separation of paraffin from non-paraffinic impurity ....	53
5.2	System glycerol-water .....	54
5.2.1	Glycerol seed production.....	54
5.2.2	Seed crystal growth rate and viscosity .....	55
5.2.3	Growth in the MCF setup without solvent-aiding.....	56
5.2.4	Influence of BuOH as assisting agent in the MCF process .....	58
5.2.5	Growth geometry in the SCF setup .....	59
5.2.6	Separation performance of growth step in SCF and GL setups .....	60
5.2.7	Layer stability .....	61
5.2.8	Post treatment.....	62
5.2.9	Influence of other solvents, of surfactants and of strong agitation.....	64
5.3	Raw glycerol.....	65
5.3.1	Sodium chloride determination via electrical conductivity .....	65
5.3.2	Separation success of the crystallization .....	66

## List of Contents

6	Discussion.....	69
6.1	Macroscopic crystal layer roughness.....	69
6.2	Uniform representation and fitting of $k(G)$ relations from experiments on the system glycerol-water-BuOH.....	71
6.2.1	A suitable fitting function .....	71
6.2.2	Comparability between setups .....	74
6.3	Stronger natural convection as results of the additional liquid .....	76
6.3.1	Gradients of density, viscosity and diffusivity near the crystal front.....	76
6.3.2	The overall mass transfer coefficient $\beta$ at the crystal front .....	83
6.4	Combined kinetic and thermodynamic effect of the additive .....	90
6.4.1	Quantitative comparison of different simplified simulation results to experimental values .....	90
6.4.2	Classification of additives according to their effect on the separation .....	93
6.5	New approaches to use and manipulation of layer growth kinetics in industrial separation technology.....	95
6.5.1	Agitation by additives .....	95
6.5.2	Choice of the cooling profile for paraffin deoiling .....	96
6.6	Conclusion .....	98
7	Summary.....	100
8	Zusammenfassung.....	101
	Literature.....	102
	List of Symbols.....	120
	Latin letters .....	120
	Greek letters .....	122
	Hebrew letters.....	123
	Subscripts.....	123
	Superscripts.....	123
	Abbreviations .....	123
	List of Figures.....	125
	List of Tables.....	135

## List of Contents

Appendix .....	135
A.1 Correlations for the properties of ternary glycerol-water-BuOH mixtures. ....	135
A.1.1 Viscosity .....	135
A.1.2 Density .....	136
A.1.3 Thermal conductivity .....	137
A.1.4 Heat capacity .....	138
A.1.5 Diffusivity .....	139
A.1.6 Solid-liquid equilibrium temperature .....	139
A.2 Properties of the crystal layer .....	140
A.2.1 Porosity .....	140
A.2.2 Density .....	140
A.2.3 Thermal conductivity .....	140
A.2.4 Heat capacity .....	140
A.3 Mass transfer coefficient in a falling film .....	141
A.4 Refractive index of ternary mixtures of glycerol, water and sodium chloride .....	141
Authorship Statement .....	143
Curriculum Vitae .....	144
Personal data .....	144
Education and professional experience .....	144
List of Publications and Conference Contributions .....	145
Papers in scientific journals .....	145
Contributions to conferences .....	145
Patents .....	146

## 1 Introduction

The separation of mixtures has always been among the most important tasks of process engineering. A lot of thought and energy has been put into processes that allow the attainment of the desired product from the mixtures it naturally occurs in or from the product mixtures of chemical reactions. Some applications of separation techniques predate the industrial era. Among these are the distillation of alcoholic beverages and the crystallization of salt from seawater or brine. The blacksmith's forging of the steel is also in part a separation process as it removes residues of slag. With the modern-era development of petrochemistry, where hundreds of chemicals are produced from only one feedstock, industrial separation processes reached larger scales, became more complex and much more elaborate. Other branches of the chemical industry, like biochemistry or inorganics, have applied similarly powerful separation processes, allowing e.g. the isolation of vitamins from their natural sources and the purification of rare elements for use in the electronic industry. More recently, the matter has become increasingly important in the context of the recycling or safe disposal of liquid waste streams, mostly wastewater but also organic solvent waste. The more and more pressing need for higher energy efficiency and the generally increasing desire for higher purities, not only for electronics but also for functional polymers, pharmaceuticals and foods, have left a lot to do when it comes to parting the product and impurity.

The most common industrial separation technique is distillation both under ambient or reduced pressure. The major advantages of distillation are that it is relatively easy to control and that kinetic hindrances are low because of the high temperature level, resulting in low investment costs. Theoretically, distillation is one of the separation techniques with the highest energy expenditure because of the high enthalpy of evaporation of most substances. However, the long history of its use and optimization has brought forward effective means of energy recovery. Therefore, other separation techniques, like liquid-liquid-(LL)-extraction, membrane processes or crystallization, can generally only compete with distillation if the distillation temperatures become very high, the pressures very low, as in molecular distillation, or the vapour-liquid-equilibrium (VLE) makes little or no difference between the compositions of the 2 phases. The latter case is encountered at or close to azeotropic points and with close boiling mixtures, like e.g. racemates. It is also a problem when the feed already contains the product in a high purity and the purification to an even higher purity is desired. Such tasks of ultra-purification are generally rather challenging for distillation and LL-extraction. Membrane processes and melt crystallization, on the other hand, usually work

## Introduction

better if the overall level of impurity is lower. In comparison to membrane processes, melt crystallization is often favourable because the equipment is cheaper and easier to maintain. Melt crystallization is an established technique for the ultra-purification of acids for the electronic industry, of monomers and other chemicals. Sometimes the overall process combines distillation for pre-purification and melt crystallization for the final purification steps. In some cases, melt crystallization is used instead of distillation. An example is the concentration of fruit juices, where the older process requires the extraction of volatile flavours prior to evaporating the water. A new crystallization process has been established, which removes the water as ice, so the lower temperature and higher pressure level keep the volatiles in the concentrate. Melt crystallization is also used when complex mixtures are not to be completely separated into chemically uniform parts but rather into fractions of different melting points. This process, called dry fractionation [Ham95], is established e.g. for the production of hard candle wax and softer lubricant oil from paraffin mixtures and for the processing of edible fats into harder and softer fractions. These 3 applications (ultra-purification, freeze concentration and fractional crystallization) can all be performed with the crystals growing suspended in the melt (suspension melt crystallization) or fixed to a cooled surface (melt layer crystallization). In the industrial application, dry fractionation is mostly performed in layer crystallization while freeze concentration is performed in suspension. Ultra-purification processes have been realized in both suspension and layer. However, layer crystallization often has the advantage of higher possible growth rates and smaller solid-liquid (SL)-interface.

The present study deals with the most important problem of melt layer crystallization: kinetic hindrance of the separation. The temperature of the melt close to the crystal layer is necessarily close to the crystallization temperature. Such a low temperature level slows down both diffusive and convective transport of impurities, but these mass transport rates put upper limits to the speed with which the separation can succeed. So far, in literature and industry, the only method to speed up the process and, thus, allow smaller crystallizers for processing a given feed stream, is agitation of the melt, either by introducing moving parts of machinery in contact with the melt (stirring, pulsation, pumping around) or by bubbling gas through it. The possibility of using liquid additives has been mentioned before, but is investigated in detail for the first time in this study. Experiments are presented on 3 different systems: A paraffin slack wax for dry fractionation, glycerol pitch for freeze concentration and a synthetic binary glycerol-water mixture as model system for ultra-purification. After proposing solutions to some common methodology problems, a detailed and quantitative discussion will reveal how a suitably chosen additive can speed up the process by influencing the fluid mechanics but also the SL-interface.



## 2 State of the Art and Theory

### 2.1 Industrial context

#### 2.1.1 Industrial crystallization terminology

Crystallization, in the broadest sense of the word, refers to any phase transition in which the long-range order increases substantially. The resulting phase is a solid. Liquids exhibiting a certain degree of long-range order are sometimes called 'liquid crystals', but this terminology is commonly rejected in crystallization science [Mul01]. Crystal formation from a vapour or glass are also called desublimation and devitrification, respectively. They may, therefore, be excluded from 'crystallization' in the narrower sense, which is then only the formation of a long-range ordered solid from a liquid. Some authors, e.g. [Lew15], exclude only one but include the other. Industrially, crystallization is mainly applied for 3 purposes: Shaping, control of material properties, and separation. Tab. 2.1 gives further details and examples.

**Table 2.1. Classification of industrial application tasks of crystallization with examples. Abbreviation API is active pharmaceutical ingredient.**

Goal	Examples	Example literature
Shaping	Outer appearance	Candied sugar, table salt [Rig12], [Hus14]
	Porosity or surface area	Freeze-dried instant coffee, freeze-cast biomaterials [Dev10], [Mus11]
	Inclusion or coating	Candies, pastillation, microcontainers [Wen15], [Sei15], [Her16]
Material	Mechanical properties	Metal alloys, polymers, ceramics, diamond [Wac96], [Ask10]
	Electrical properties	Semiconductor doping [Jac08]
	Thermokinetic properties	Polymorphs of APIs, chocolate [Kar06], [Afo07]
Separation	Of close boiling mixtures	Enantiomers of APIs, fatty acids, monomers, electrochemicals [Lor07], [Fuk13], [Ark95], [Tan16]
	At low temperature or high pressures	Proteins, juice concentration, fats and waxes [Jud95], [Ham95], [Kus10], [Rav12]

The industrial separation technique of crystallization is also called fractional crystallization [OED17]. Some authors, e.g. [Ulr03a], restrict this term to processes including multiple steps of crystallization. It is, furthermore, common to use 'fractional crystallization' and 'dry

fractionation' (cf. above, Ch. 1) synonymously [Lew15]. Because of this confusion, the term shall not be used hereafter but the 3 abovementioned process types shall be called separative crystallization (or simply crystallization), multi-step crystallization, and dry fractionation, respectively. The separative crystallization technique is divided into 2 branches: solution crystallization and melt crystallization.

Attempts to give exact definitions of the 2 process classes based on physical phenomena can be found in the literature [Mul92, Ulr03a, Lew15] but shall not be of concern here. Common usage of the terms distinguishes 2 branches of process design that encounter different sets of challenges and developed different types of strategies. Especially, the types of crystallization equipment differ between solution and melt crystallization. Apart from a few intermediary processes, the distinction between the 2 process types can be described as follows: In solution crystallization, the product crystallizes from a liquid mixture in which it is a minor component. The major component is a liquid that is often, but not necessarily, fed into the process on purpose. It is called the solvent. The temperature level in the crystallizer is generally much higher than the freezing point of the solvent. In melt crystallization, the temperature level in the crystallizer is close to or below the freezing temperature of the liquid's main component. The desired product is very often a major but may be a minor component in the liquid. In the solution crystallization, crystals almost always grow as particles, suspended in the mother liquor. Melt crystallization can be carried out similarly, and then is explicitly called suspension melt crystallization, or the crystals can grow as a solid layer on a cooled surface. Tab. 2.2 compiles further systematics and examples.

**Table 2.2. Common classification of separative crystallization processes and the typical equipment of the different classes.**

Goal	Separative crystallization			
Common class	Solution crystallization	Melt crystallization		
Crystals	Suspension		Layer	
Agitation	Dynamic			Static
Typical industrial equipment	Forced circulation crystallizer; Draft tube baffled crystallizer; Fluidized bed crystallizer [Nýv82], [Jon02] [GEA12a]	Scraped crystallizer with wash column    [GEA12b], [Lew15], [Sul16a]	Falling film crystallizer    [Ulr03b], [Sul16b]	Plate or tube crystallizer    [Özo91], [Ark95]

Like the distinction between solution and melt crystallization, the further classification of melt crystallization is based on the equipment that is usually applied. It might, therefore, seem somewhat arbitrary from a scientific point of view. For instance, in the most common suspension melt crystallization processes, a solid layer of crystals first grows on the surface of the crystallizer and is then scraped off [GEA12b, Lew15, Sul16a]. In some industrial types of layer crystallization, the layer is allowed to break from the wall before being molten, or even before a substantial part of the residual melt is removed, forming essentially a suspension [Ste06]. A process called solvent freeze-out uses simultaneous layer crystallization of the solvent and suspension crystallization of the product [Día12, Ryu12, Yu14].

A simple distinction between layer and suspension processes can be made, when only applying it to the established large-scale processes: In layer crystallization, crystal matter and residual melt are separated within the crystallizer and, thus, waste and product are removed through the same outlet of the crystallizer at different times. In suspension crystallization, crystals and melt are removed simultaneously from the crystallizer and separated over a filter in a different vessel, the wash column.

Static crystallization does not mean that the melt is completely static. In most static melt layer crystallizations natural convection is strong enough to cause ideal mixing at least in a part of the bulk of the melt [Bei13]. The distinction is sometimes made between dynamic mode, in which the melt is pumped around, and static mode, in which it is not [Kus90, Ulr03b]. This definition excludes from the dynamic mode equipment that imposes forced convection by stirring, rising bubbles or pulsation. These are then either called static [Ulr03b] or quasidynamic crystallization [Ulr06]. They have not become an established technique in the industry. Forced convection is, in recent large-scale industrial applications, almost exclusively applied by the falling film technique, which pumps the melt around. However, laboratory setups simulating this dynamic operation may employ a variety of different methods of agitation, mostly not including a pumping circuit (cf. Tab. 2.3) Therefore, the present study will call dynamic any process that sets any moving interface (to solid, liquid or vapour) in contact with the melt in order to agitate it.

Within the present study, the liquid from which the crystal grows is called the melt or the mother liquor. The substance that forms defectless lattice parts is called the nutrient (index a). All other substances in the melt are called solutes (index b or no index). In the literature, solutes are often named according to the way they entered the melt: Additives or solvents if added on purpose, impurities if not. Sometimes, the state they were in before entering the melt is mentioned (dissolved solids, solvents, dissolved gases). Such classification will not be used here, because an ion, molecule or atom in solution usually bears no memory of its previous state. Within the present study, the most important substance entering the melt from

the vapour will be water. Sensibly, the solutes are, therefore, classified according to their influence on the liquid and interface, which not only eases understanding but also analysis. This is not new. For instance, a WHO guideline [WHO96] on water analytics explicitly defines  $\text{HCO}_3^-$ ,  $\text{CO}_3^{2-}$  and  $\text{Cl}^-$  as total dissolved solids even though they may have entered the liquid via  $\text{CO}_2$  or  $\text{HCl}$  vapour.

Much research on crystallization has been carried out on salts or metals and the findings have been translated to crystallization of molecules. In the present study only molecules are crystallized and for brevity, theories will only be explained on molecules, instead of always mentioning molecules, ions and atoms.

### 2.1.2 Melt layer crystallization as industrial separation technology

Melt layer crystallization is a thermal separation technique using the phase transition from liquid to crystal upon cooling of walls that touch the feed. Fig. 2.1 sketches typical process steps, giving the temperature of the cooling medium in comparison to the melting temperature of the pure desired product.

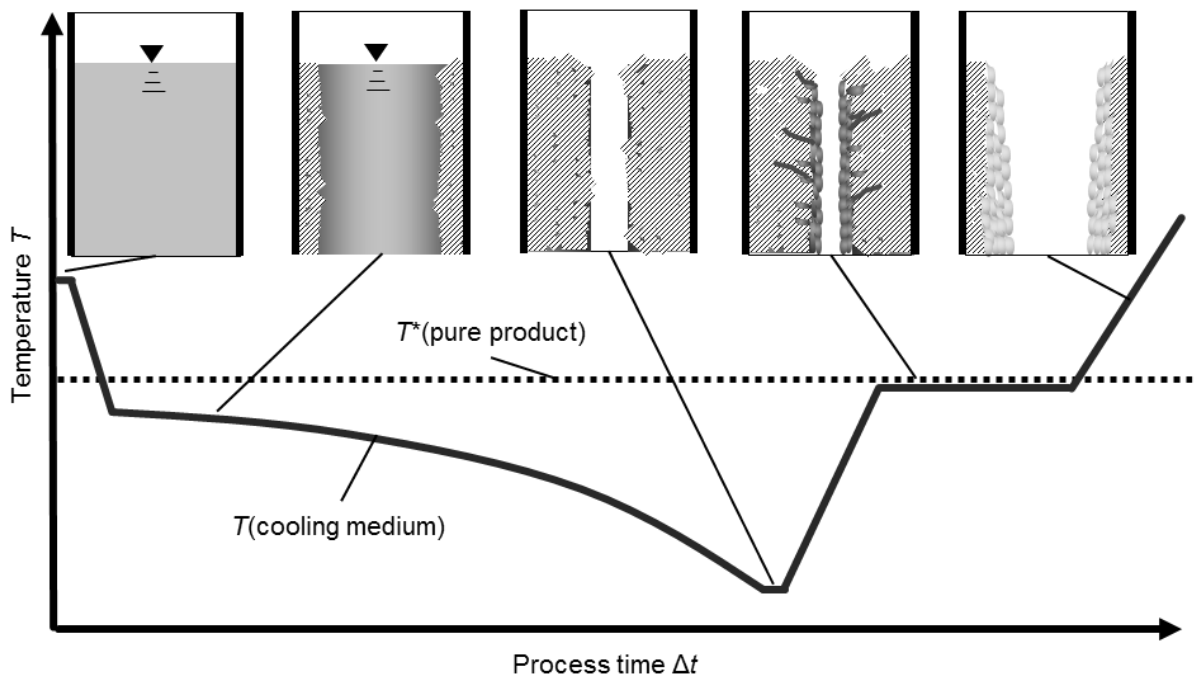


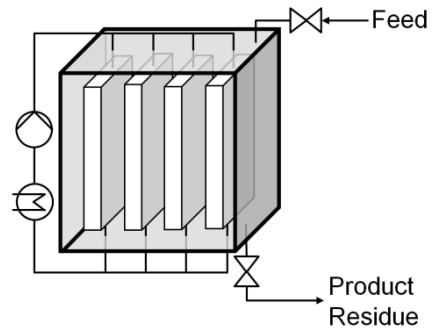
Figure 2.1. Typical process of layer crystallization in the industry with sweating step. The temperature of the cooling medium is drawn vs. the process time, together with the melting temperature of the pure product and sketches of the crystal layer and melt.

Initially, the volume between cooled walls is filled with the feed. The walls are then cooled to crystallization temperature. Seed crystals may be kept at the wall or added, but often, the temperature is chosen such that crystallization starts spontaneously. Then, a layer grows on the cold walls and the cooling temperature is decreased in order to compensate for the insulating effect of the layer and keep the growth rate constant. When the layer has reached the desired thickness, the residual melt is drained and subsequently the temperature is

raised in order to melt the crystal layer. The product is removed in liquid form. If the crystal layer grows compact and all the residual melt is drained the process may achieve very high selectivity (cf. above, Chs. 2.2.3-4).

However, in most cases the melt will not be drained completely but some will stay included in pores in the crystal layer or adhere to its surface. Part of it can be removed by a post treatment like sweating or washing. In sweating, also shown in Fig. 2.1, the cooling liquid is slowly heated or held at a temperature just below the melting point of the pure liquid [Jan87]. Those parts of the crystal layer in contact with impure liquid will melt and give way for the melt to flow out. The molten product will also rinse the remaining layer from adhering melt when it flows out. Such a rinsing effect can also be achieved by washing, i.e. letting clean liquid product flow over the crystal layer. Washing may also remove impurity from inside the crystal channels because it imposes a concentration gradient that causes diffusion. This is called diffusion washing [Wan94b, Neu96]. The literature provides some systematic research, both theoretic and experimental, on washing, e.g. [Pos93, Wan94a, b], and sweating, e.g. [Erd75, Mya88, Jia13], but this research is not of immediate interest to the present study.

Industrial equipment for layer crystallization resembles common heat exchangers [Bar63, Sax68, Win76]. Fig. 2.2 gives a simplified sketch of the most common commercially available apparatus for static layer crystallization, which consists of many cooling plates in a container that is filled with the melt. For a detailed drawing see [Ark95]. Tubes may be used instead of plates. The dynamic process was originally realized by pumping the melt through a cooled pipe (Fig. 2.3.a) but is nowadays mostly done by letting the melt flow down the pipe as a falling film (Fig. 2.3.b). Proposed alternatives are pulsation, i.e. pumping back and forth [Kus90], or introduction of rising gas bubbles into the melt [Sto82]. An overview over different types of equipment will be given below, together with the discussion of experimental strategies.



**Figure 2.2. Sketch of an industrial static layer crystallizer, showing four cooling plates instead of the large number that is used in a real apparatus.**

The 2 most important parameters to assess the performance of a layer crystallization process are the overall distribution coefficient  $k$

$$k = \frac{w_{\text{imp}}^{\text{Product}}}{w_{\text{imp}}^{\text{Residue}}} \quad (2.1)$$

with impurity mass fractions  $w_{\text{imp}}$  in product and residue, and the growth rate

$$G = \frac{ds}{dt} \quad (2.2)$$

with layer thickness  $s$  and time  $t$ . Averaging of the growth rate in laboratory setups is a problem that is investigated in the present study (cf. Ch. 4.3.2). In many industrial applications the average growth rate can simply be put as  $G = s/\Delta t$ . The residence time  $\tau_r$  for one crystallization step including post-treatment in a crystallizer of the type depicted in Fig. 2.2 with a large number of large plates is

$$\tau_r \approx \frac{1}{Y_{PT}} \left( \frac{L}{2G} + t_{PT} \right) \quad (2.3)$$

where  $L$  is the distance between plates,  $t_{PT}$  is the time needed for post treatment or draining and  $Y_{PT}$  is the post treatment yield. This approximate linearity with  $G^{-1}$  is preserved for other geometries. In the usual case, where feed and product purity are determined by the market, the overall desired distribution coefficient,  $k^l$ , is, thus, fixed. If the distribution coefficient of one step,  $k_i$ , is too high, more steps have to be added until

$$\prod_i k_i \leq k^l \quad (2.4)$$

The overall residence time  $\tau_r^{tot}$  can be estimated as

$$\tau_r^{tot} > \sum_i \tau_{r,i} \quad (2.5)$$

From Eqs. 2.4-5 follows that  $\tau_r^{tot}$  increases with increasing  $k$  and decreases with increasing  $G$ . Therefore  $(dk/dG)^{-1}$  can be used to describe the time-efficiency of the process.

Most melt crystallization processes are performed on systems with a very favourable equilibrium distribution coefficient (cf. Chs. 2.2.3-4). The time efficiency is, therefore limited by the kinetics of solute redistribution, which is slower when the viscosity of the melt is high, cf. e.g. [Ulr90c] and below (Chs. 2.2.4 & 6.2-3). Therefore, melt layer crystallization has only been performed on melts of rather low viscosity before the present study.

Fig. 2.4 shows the most important applications of melt layer crystallization according to STEPANSKI & SCHÄFER [Ste03], with their viscosities at the melting temperature drawn versus the melting temperature. Falling film technique is applied for substances with low viscosities and moderate melting temperatures. The latter limitation is caused by the higher necessary temperature differences between melt and cooling medium in falling film technique.

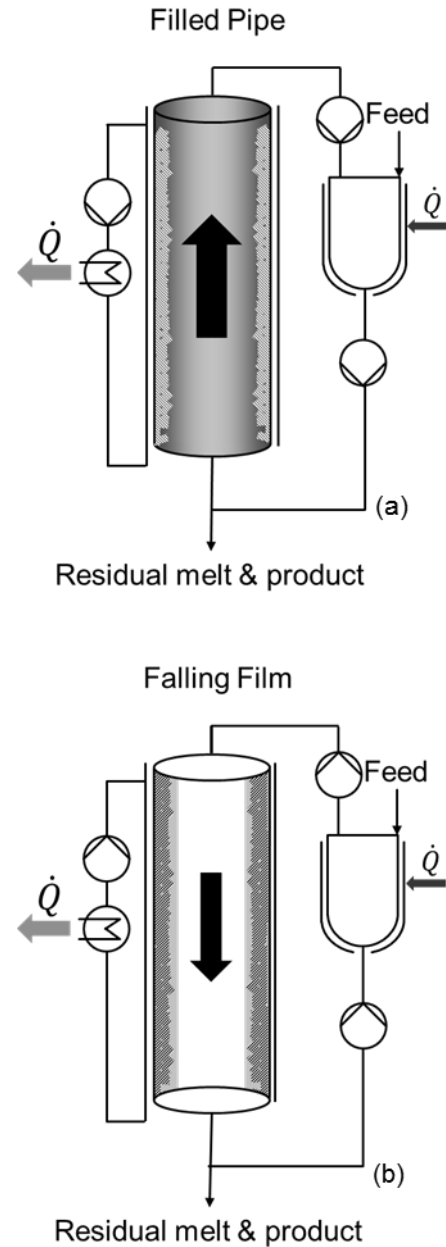
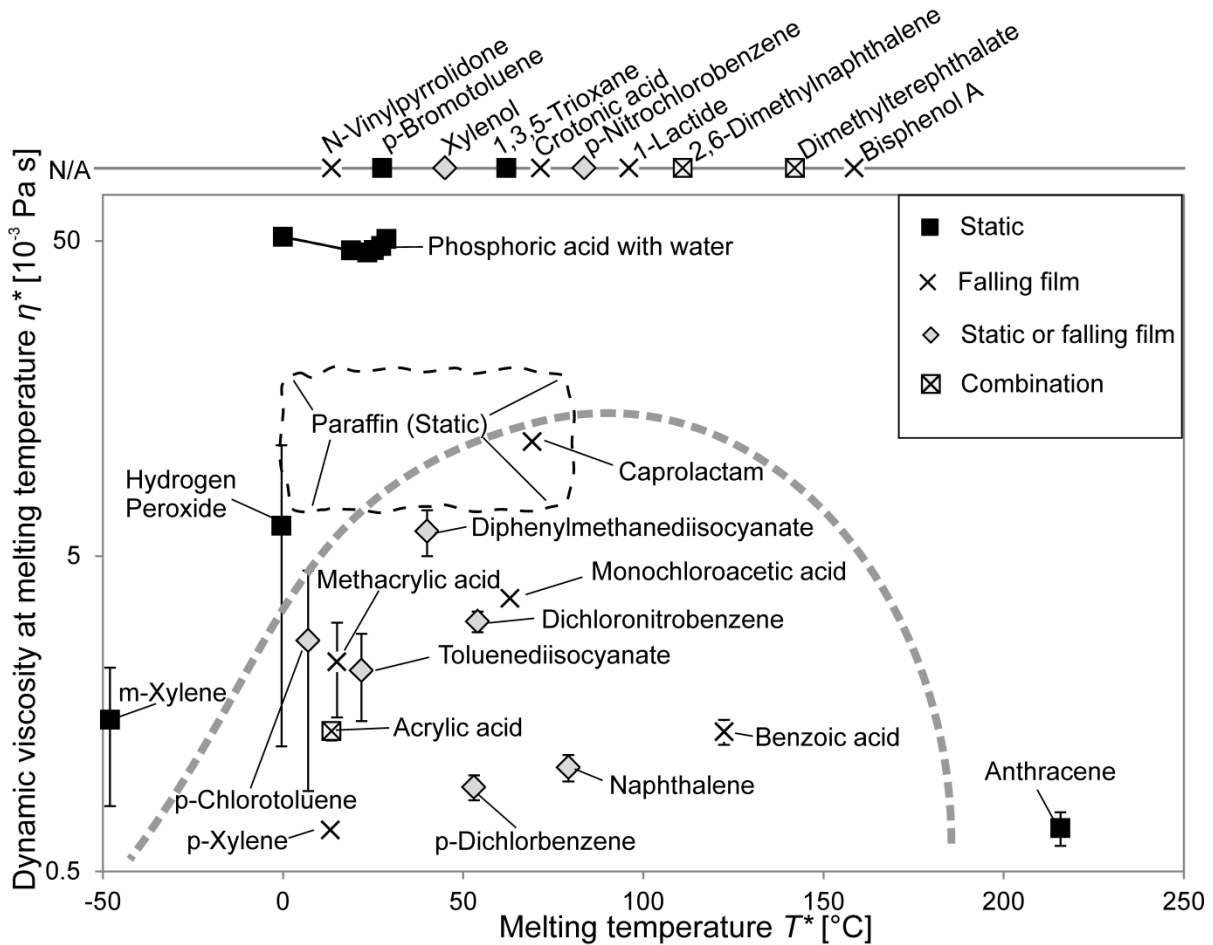


Figure 2.3. Examples of industrial equipment for dynamic layer crystallization.

The highest reported viscosity that is encountered in industrial dynamic layer crystallization is the  $\eta^* \approx 12$  mPa·s of caprolactam. On a lab scale, aqueous phosphoric acid ( $\eta^* \approx 50$  mPa·s) [Jia11,12a,b,13,14a] and the ionic liquid EMIM-Cl ( $\eta = 47$  mPa·s) [Kön08] were processed in falling films. Phosphoric acid is crystallized to be purified from metal ions, in a process in which the melt as well as the crystal phase contain water. In Fig. 2.4 points for different water contents in the interesting range are given. Though the agitation of the melt would all the more be desirable when viscosities are high, the static layer crystallization is the common approach to melts with higher viscosities, but melts with viscosities above 100 mPa·s are considered not processible [Ulr06]. The present study will be the first to perform a layer crystallization on a melt of glycerol that exceeds this limit by far, with  $\eta^* \approx 1600$  mPa·s.



**Figure 2.4. Most important industrially established applications of melt layer crystallization [Ste03].** The dynamic viscosity at melting temperature, obtained from extrapolating an exponential fit of data from various sources to the melting temperature, is drawn vs. the melting temperature of the pure product. Products for which the viscosities are not reported in the literature are represented with their melting temperature on the N/A-line. For paraffin, en lieu of a cloud of points, the area in which most of the paraffin waxes in question are found, is denoted. Error bars are chosen symmetrically such that the lower end of the error bar is the closest literature value. The lines are only added as guides to the eye.

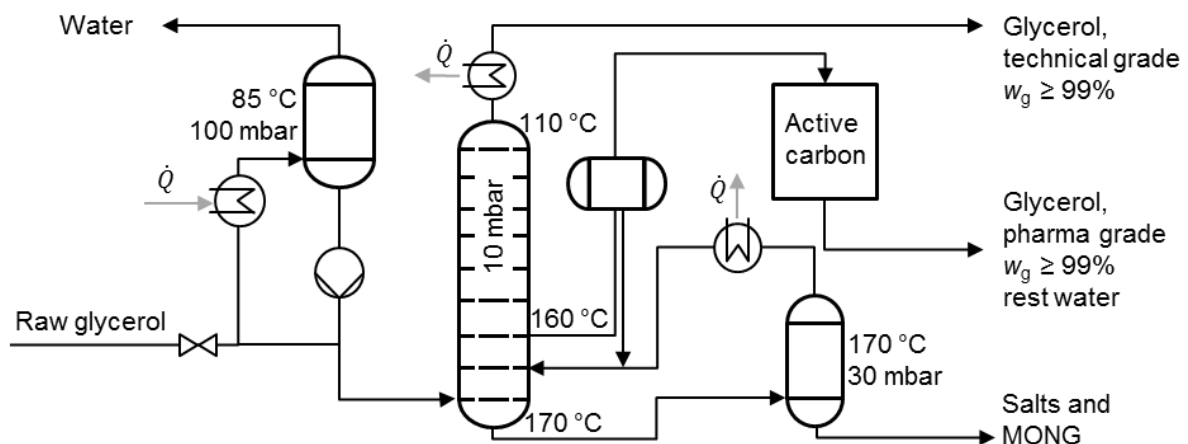
### 2.1.3 Separation techniques for glycerol purification and paraffin wax deoiling

The present study contains experimental results on 3 different systems. A binary mixture of glycerol (g) and water (w) will act as model system for the ultra-purification. The 2 real systems are both waste streams of fuel industry. A medium-heavy paraffin slack wax from

the long residue of petroleum distillation and raw glycerol, also called glycerol pitch, from the biodiesel production. As of now, none of the 3 are separated by layer crystallization on an industrial scale.

In the biodiesel production, vegetable and animal fats and oils react with methanol (MeOH) to fatty acid methyl esters (FAMES) and glycerol, and the polar, dense glycerol phase separates from a light, non-polar biodiesel phase [Ma99, Ger05, Meh06, Leu10]. The reaction is most often catalysed by a base but other methods are reported, e.g. [Lot05, Fje09]. Excess MeOH and catalyser as well as side products, like salts, soaps and water from the esterification of free fatty acids, mostly remain in the glycerol phase. Its glycerol content is often lower than 50%. Without purification, crude glycerol can be used as additive to cattle feedstock [Cle13] or in cement production [Ros08]. For all of its many other uses [Pag07] it has to be purified [Cir14, Wie14].

Often, a first distillation step is carried out at the biodiesel plant, evaporating the MeOH and most of the water in order to recycle the MeOH. The remaining liquid phase typically contains  $60\% < w_g < 90\%$  glycerol and is marketed as raw glycerol. An established process for its further separation is sketched in Fig. 2.5.



**Figure 2.5. Simplified flow chart of an established process for the purification of glycerol, comprising 3 distillation units and one adsorption over active carbon. Abbreviation MONG is matter organic non glycerol.**

Glycerol of technical grade and especially glycerol of pharma grade are valuable products [Pag07, Rah10, Ayo12]. The purification process has, therefore, drawn some attention and literature is available. Some of it is concerned with recovery of glycerol directly out of the biodiesel phase [Yor06, Abb07, Dub07]. Others remove special impurities by adsorption [Wie14], ion exchange [Str51, Zag51, Ash56, Lan08, Car09a,b] or by a combination of chemical and physical treatment [Bra38, Haz03, Chi05, Aik06, Háj10, Kon10, Pot10]. An early study [Has41] on suspension melt crystallization is also available but does not provide any quantitative data.



The refining of petroleum shall only briefly be mentioned here. It comprises, among other separation steps like the removal of sulphur and aromatic compounds, 2 distillation columns. The first yields light fractions for fuels at the head and middle. Its bottom product, the long residue, is either cracked into shorter molecules or it is fed into a second distillation column, which operates under high vacuum. This high vacuum distillation is coupled with the LL-extractive deasphalting unit. The gathered fractions are the aromatic asphalt and aliphatic slack waxes with different melting points. From light (low melting) to heavy (high melting), slack waxes are called, spindle oil (spo), light machine oil (lmo), middle machine oil (mmo) and de-asphalted oil (dao). They are either used as cheap lubricants or further refined into higher-value lubricants and candle wax by separating the shorter alkanes (oil) from the longer ones (wax).

For this separation step, performed on a lighter feed (spo or lmo), a melt layer crystallization process is established. Its separation is mainly achieved in the sweating step. For mmo and dao slack waxes, the established technique is suspension crystallization using large amounts of a mixture of different solvents and temperatures well below 0°C, along with a filtration of the soft crystals [Moh04, Moh08, Zak10]. Extending the applicability of the layer crystallization technique towards mmo is of great economic interest, but first attempts have shown limitations [Kus10].

The crystallization of paraffinic mixtures is interesting not only for the separation but also in context of petroleum pipeline blocking. Therefore, a large body of literature on the thermodynamics of this process can be found. It includes experimental data [Sch55,56, Ped91, Dir98, Mus98, Met99, Che00b, Mey09], measuring strategies [Fal71, Gia73, Ger91, Bou05, Cot08, Cot10, Esp13] and modelling attempts [Han88, Cou95,97,05,06, Pau01, Che07, Gha12, Mor13, Yan16]. Reviews are given by SRIVASTAVA et al. [Sri93] and DIRAND et al. [Dir02]. The SLE of paraffin waxes in solvents is also described [Hau87, Sri97, Che00a, Pau04] as is the fact that the wax can gelatinize the solvent [Abd00].

## **2.2 Theory of melt layer crystallization**

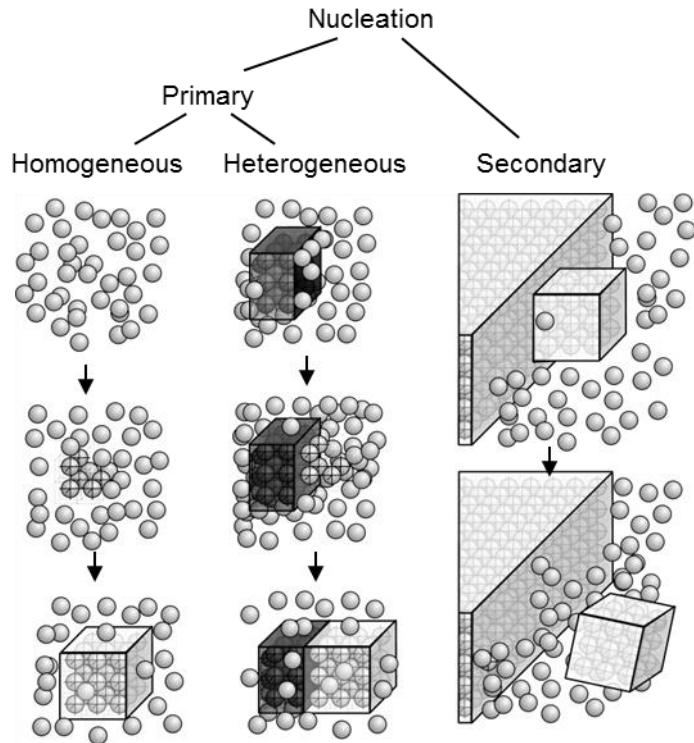
### **2.2.1 Nucleation**

Nucleation is the process in which minute crystal particles, called embryos, nuclei or seeds [Mul91], form. An extensive literature on the subject is available, e.g [Bec35, Hoa76, Kre91, Kas03], review of which would go beyond the scope of the present study. Only a few points that are especially important to the subject at hand are to be cited and 2 shortcomings of the widespread literature are to be explained: first, the discrepancy between the classic nucleation theory, which is still prominent in the handbooks, and more modern and realistic theories, and secondly, the discrepancy between the theoretical description of the problem and the practical approaches to its measurement or control.

Since MULLIN [Mul01], nucleation is commonly classified into primary homogeneous, primary heterogeneous and secondary nucleation, like shown in Fig. 2.6. In primary nucleation, nuclei form by growth of ordered clusters beyond the critical size of stable crystalline bodies. In secondary nucleation, they form by partition (abrasion, attrition) of larger crystals.

The driving force for primary nucleation is the undercooling  $\Delta T = T^* - T$ , where  $T^*$  is the liquidus temperature and  $T$  the actual temperature. At  $\Delta T > 0$ , the crystal lattice's orientation and distance between nutrient molecules is energetically most favourable.

In terms of the chemical potential  $\mu$ , the process of molecules organizing into the lattice possesses  $\Delta\mu_{L \rightarrow S} < 0$ . However, the formation of a crystal particle has to pass an energy barrier, which in classical nucleation theory is attributed to the building of a SL-interface with an interfacial Gibbs



**Figure 2.6. Classification of nucleation with sketch of mechanisms.**

free energy  $\gamma > 0$ , hereafter called surface tension. In the terminology of KASHCHIEV [Kas95], the organizing molecules form a cluster of thickness  $s$  that first grows as subnucleus against the energy barrier ( $d\mu/ds > 0$ ) to become a nucleus at critical size  $s^*$  with  $(d\mu/ds)_{s=s^*} = 0$ , and then grows further as a supernucleus at  $d\mu/ds < 0$  to eventually form a crystal. This process may take place in the melt (homogeneous) or at an existing interface (heterogeneous) with only a part of the cluster being in contact with the melt. Like a chemical reaction passing an energy barrier, the rate of primary nucleation, the number of particles formed per unit time  $\dot{n}$ , depends on the driving force  $\Delta\mu(T^*(w) - T) = \Delta\mu(T, w)$  and on the extend of energetic fluctuations, because these are necessary to pass the energy barrier. When the system is isobaric, the temperature is the measure for the fluctuation, thus  $\dot{n}(T, w)$ .

Because a subnucleus is unstable and consists only of a few molecules, the postulation of an interface between subnucleus and its melt is rather far-fetched. Classical nucleation theory has, therefore, been challenged. An example is the research on nucleation of  $\text{CaCO}_3$  polymorphs calcite, aragonite and vaterite from aqueous solutions [Geb08,10,11, Rai10, Dem11, Wol11]. It has been shown that ordered clusters exist in overheated solutions and

the chemical potential change upon nucleation varies from the one predicted by classical theory (Fig. 2.7).

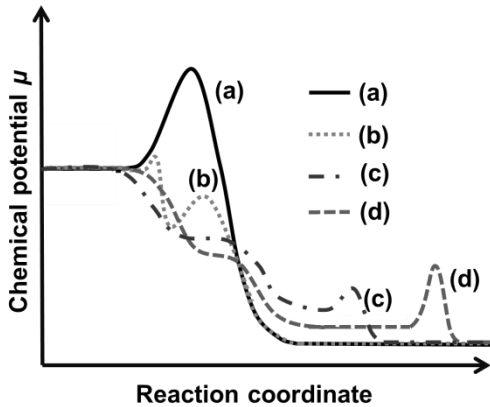


Figure 2.7. Qualitative plot of chemical potential vs. reaction coordinate for the nucleation of  $\text{CaCO}_3$  from aqueous solution, according to classical nucleation theory (a), experimental values (b) [Geb08], and dynamic simulation results assuming dry (c) or wet (d) clusters [Rai10]. Reproduced from [Eis12].

Furthermore, the formation of nuclei in the above sense should use up energy because  $\Delta\mu_{s=s^*} > 0$ , i.e. an adiabatic system should cool upon nucleation, but it is commonly stated that heat is released upon nucleation and the quasi-adiabatic temperature increase is even used to measure nucleation. The real process called nucleation that is encountered in experiments and industrial processes is mostly a combination of growth and attrition (secondary nucleation) of crystal particles. However, when a stagnant and viscous melt forms crystal particles that do not interact with each other and are not broken, the number of particles formed per unit time  $\dot{n}$  is equal to the rate of primary nucleation.

Nevertheless, in the case of organic melts, classical nucleation theory commonly fails to predict  $\dot{n}(\Delta T)$ . Many real organic melts show behaviour similar to the one of glycerol, depicted in Fig. 2.8.

For use in process design, it is practical to combine information on nucleation behaviour with the phase diagram. The theoretical justification of this is somewhat controversial and shall briefly be discussed here.

The nucleation rate  $\dot{n}$  can be interpreted as the probability that a small liquid volume turns into a crystal in a unit time, divided by the ratio of unit volume to particle volume. This is a quantity dependent only on the thermodynamic state of the melt. Therefore it could rigorously be combined with the phase diagram in a plot like Fig. 2.9. The path

dependence caused by finite cooling rates, time intervals and volumes with interaction between crystal particles in measurements of  $\dot{n}(T, w)$  would not necessarily be higher than in common dynamical methods for determination of  $T^*(w)$ . However, measuring the data for a diagram like Fig. 2.9 would be tedious and it has never been done. Usually, a curve representing the  $\dot{n}(T)$ -curves for each  $w$  by only one point is drawn into a phase diagram.

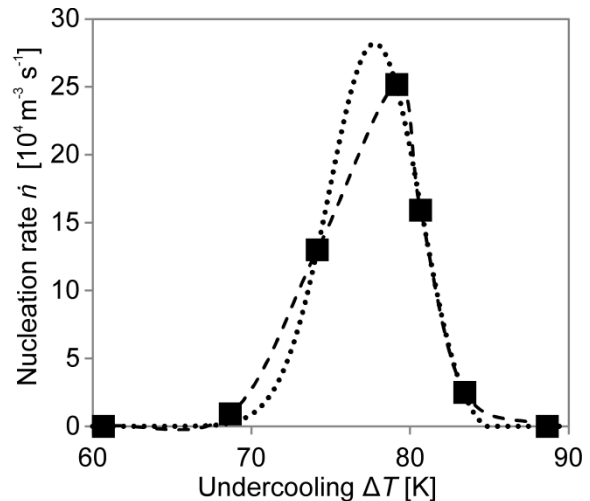


Figure 2.8. Nucleation rate vs. undercooling for glycerol, according to experimental data from Tamman [Tam22, Mat69]. Lines are drawn as guide to the eye.

Such a curve is commonly called supersaturation curve or supersaturation limit. Together with the liquidus line, it encloses the metastable zone [Ost97]. The definition of the supersaturation curve varies. TING & MCCABE [Tin34] defined 2 types: The first is the line at which first nuclei are detectable.

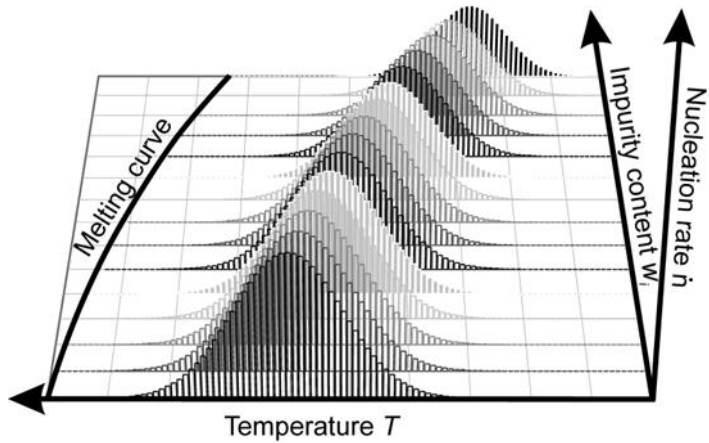


Figure 2.9. Hypothetical  $\dot{n}(T, w)$ -diagram, combining phase diagram and nucleation behaviour independent of the cooling profile.

The second one is passed when the dissipation of heat of fusion becomes substantial. A third possibility is to define the supersaturation curve as the curve that cannot be passed by cooling of a liquid. The growing mass fraction of solid phase in the system changes the composition of the remaining liquid in such a way that certain points  $(T, w_L)$  can never be reached. These 3 different definitions are sometimes assumed to basically represent the same curve, although this is only the case when  $\dot{n}(\Delta T)$  can be approximated by an offset Dirac delta function or an infinitely high step function.

For all 3 of the abovementioned definitions, the position of the supersaturation curve depends on the number of formed nuclei

$$n(t) = \int \dot{n}(t) dt. \quad (2.6)$$

In order to combine this time-function  $n(t)$  with a phase diagram, it has to be transformed into  $n(w)$ , for which not only the liquidus line,  $w^*(T)$ , but also the cooling profile,  $T(t)$ , has to be given. The relation between  $n(w)$  and the actual heat-or-composition-change-related position of the supersaturation curve further depends on the cooling profile. Therefore, the supersaturation curve, added to a phase diagram, cannot be used with the same universality as the melting curves. For example, one would conclude from Fig. 2.8 that the metastable zone of glycerol has a width of no less than 60 K. However, KRAUT [Kra71] reports primary nucleation of glycerol at  $10 K < \Delta T < 18 K$ , when holding such temperature for a week or more. This illustrates how, in accordance with theory, the nucleation rate in the metastable zone is low, but it is not zero and the occurrence of crystals is time-and-path-dependent.

### 2.2.2 Growth

Crystal growth is the process in which growth units are incorporated into an existing stable crystal. These growth units may be ions, molecules or atoms in the amorphous phase, but they may also be nuclei or grown crystals that merge with the growing one. In the latter case, the definitions of growth and agglomeration overlap. The growth rate depends on the nutrient, the presence of impurities, the gradients of temperature and impurity on both sides

of the SL-interface, and the orientation of the interface with respect to the crystal lattice. Even more so than in the case of nucleation, a huge body of information on crystal growth phenomena is available in the literature. The monographs of TILLER [Til91a, Til91b] shall serve as an example, giving very detailed insight into different growth phenomena.

Only those 4 aspects which are most important for the present study shall briefly be mentioned here: The concept of constitutional undercooling, the influence of surface tension, of lattice orientation and of impurities.

The influence of lattice orientation and small amounts of impurities can best be shown in a particle mechanic approach. Fig. 2.10 illustrates some important aspects for the example of a cubic primitive lattice. According to the classic model, the growth units are first adsorbed to the crystal surface and then integrated. Integration of a growth unit into the lattice has to pass an energy barrier, which is the lower the more neighbours of the adsorbed unit are already in the crystal lattice. A unit adsorbed into a kink position has 3 neighbours, one in a ledge position has 2 and one on a terrace has only one. Positions with 4 or 5 neighbours are also possible. A (111)-face consists mainly of kinks, a (110)-face phase of ledges and a (100)-face of terraces. Therefore  $G_{(100)} < G_{(110)} < G_{(111)}$ . Integration of a unit at a terrace is sometimes called surface nucleation because it is close to primary nucleation, which would be integration at a position without crystalline neighbours. Units that are adsorbed but not yet integrated may still move and will diffuse to positions with more neighbours. Solute molecules with affinity to the nutrient will also be adsorbed on the SL-interface. If they form strong bonds, e.g. hydrogen bridges, with the lattice molecules, they may show little mobility on the interface and thus block the surface diffusion. Furthermore, they block the growth of the position they occupy, which may slow down the overall growth but also lead to distortions in the growth shape. Some solutes adsorb selectively onto certain surfaces and can, thus, promote these surfaces to remain without growing [Mee02].

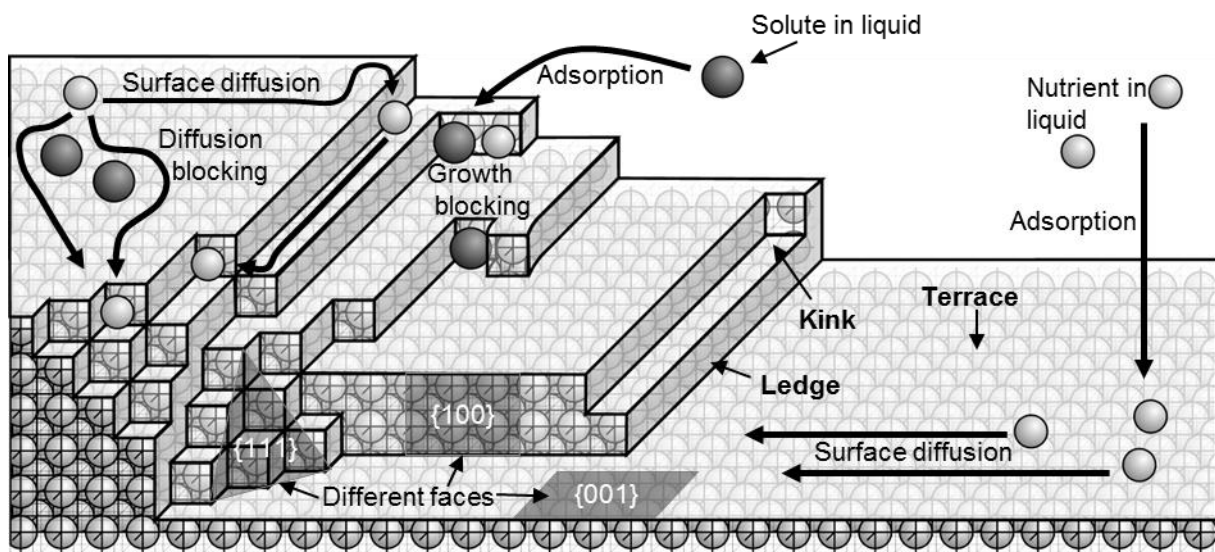


Figure 2.10. Illustration of important phenomena on the growing crystal surface on a microscopic scale.

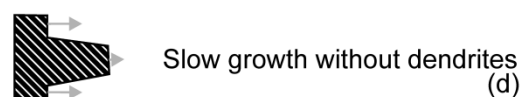
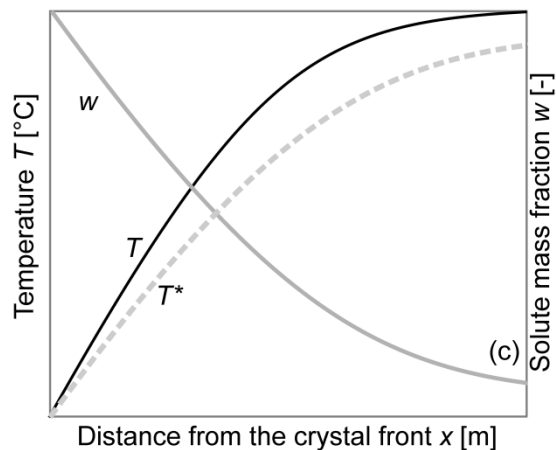
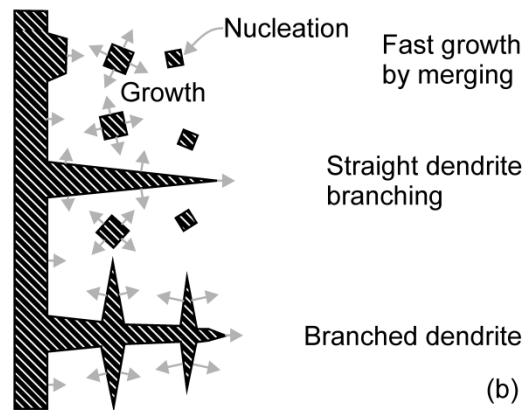
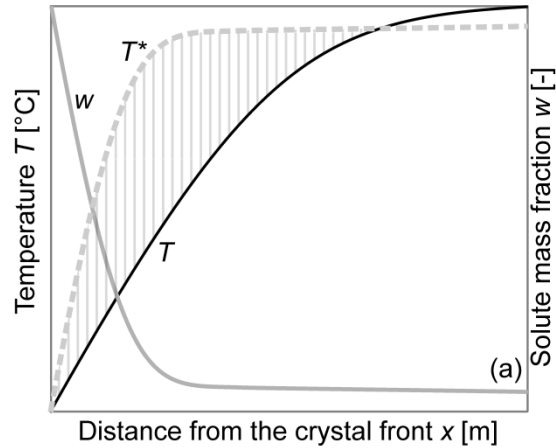
When describing a growing crystal layer, the origin of the coordinates is commonly moved along with the crystal front. Within this coordinate system, the melt moves towards the SL-interface. At a low distribution coefficient, the nutrient molecules enter the crystal lattice, one might say, they pass the SL-interface, while the solute molecules are mostly rejected at the interface. The solute will then partly diffuse back into the bulk of the melt and partly accumulate at the crystal front, forming a concentration profile like the one depicted in Fig. 2.11.a,c. An analogy can be drawn to membrane filtration, where this accumulation is called concentration polarization.

Concentration polarization in layer crystallization may cause constitutional undercooling. The concept of constitutional undercooling (also called constitutional supercooling) was first introduced by RUTTER & CHALMERS [Rut53] and has found a more quantitative description by TILLER et al. [Til53]. Its statement is that a crystal layer will maintain a smooth surface when

$$\left(\frac{dT^*}{dx}\right)_0 = \left(\frac{dT^*}{dw}\right)_{w_0} \cdot \left(\frac{dw}{dx}\right)_0 < \left(\frac{dT}{dx}\right)_0 \quad (2.7)$$

where the index 0 indicates quantities at the SL-interface and  $dT^*/dw$  is the slope of the liquidus line. The basic idea is that, if Eq. 2.7 is not met, the liquid next to the layer is undercooled (Fig. 2.11.a), allowing the surface nucleation to form a protrusion, whose growth will be favoured by the undercooled environment. While the protrusion grows faster than the rest of the layer, it rejects more solute and, thus, a concentration profile parallel to the crystal front forms that eventually leads to the formation of a periodical layer thickness perturbation [Rut53].

If, in turn, Eq. 2.7 is met, the liquid next to the



**Figure 2.11. Constitutional undercooling (a) and one possible mechanism of fast dendritic growth caused by it (b), as opposed to no constitutional undercooling (c) and a growth mechanism that flattens out the crystal layer (d).**

crystal layer is overheated (Fig. 2.11.c) and any protrusion in the crystal layer will recess in this overheated environment (Fig. 2.11.d).

As  $dw/dx$  is a function of the growth rate,  $G$  has to be chosen sufficiently low to meet Fig. 2.7. Industrial melt layer crystallizations without constitutional undercooling typically yield  $G \approx 10^{-7}$  m/s, while  $10^{-6}$  m/s  $< G < 10^{-5}$  m/s is typical for layer crystallizations with constitutional undercooling [Lew15]. The dependence between growth rate and constitutional undercooling is reciprocal: High growth rates cause constitutional undercooling but constitutional undercooling also increases the growth rate. Fig. 2.11.b gives an example where a strongly undercooled regime in front of the crystal layer causes nucleation in the melt. A thick suspension forms, whose particles eventually merge with this solid layer to form dendrites. Such a mechanism can explain much faster growth than the integration of single molecules into the crystal layer.

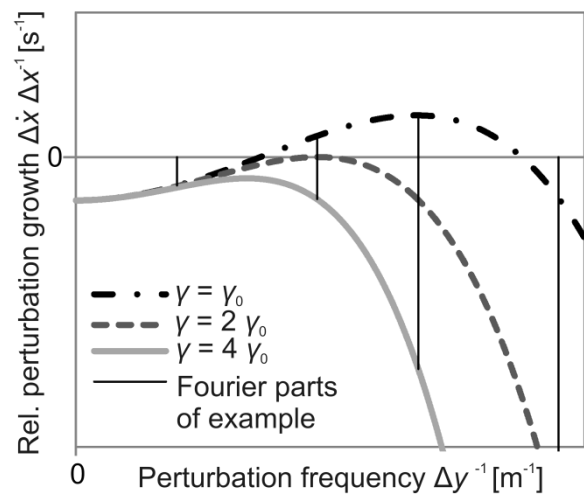
A smooth crystal layer has the smallest SL-interface in comparison to its volume.

Any roughening increases the relative interfacial area and, thus, the Gibbs free energy. The surface tension is, therefore, another factor in the tendency of a crystal surface to roughen,

which is neglected in the original concept of constitutional undercooling. MULLINS & SEKERKA [Mul63] combined the influence of surface tension and normal gradients and derived an algebraic expression for the relative growth rate  $\Delta\dot{x}/\Delta x = (G_{\max} - G_{\text{mean}})/\Delta x$  of a sinusoidal crystal layer  $x = x_{\text{mean}} + \Delta x \sin(y/\Delta y)$ , moving with an average growth rate  $G_{\text{mean}}$  in a stationary state. Like TILLER et al. [Til53], they neglected convection. Within their set of simplifications, superposition of multiple sinusoidal perturbations is possible without interference. Therefore, the change of shape of any periodical crystal front  $x^{\text{tot}}$  can be calculated by using Fourier transformation

$$x^{\text{tot}} = x_{\text{mean}} + \sum_i \Delta x_i \sin\left(\frac{y}{\Delta y_i}\right). \quad (2.8)$$

To show the influence of the surface tension, values calculated with their formula are plotted in Fig. 2.12 and the so predicted change of the shape of an arbitrarily chosen perturbation is drawn in Fig. 2.13.



**Figure 2.12.** Example for the influence of the surface tension on the tendency of a periodical perturbation to change the amplitude of its Fourier parts. The lines are calculated by the formula in [Mul63]. The four marked frequencies are the Fourier parts of the perturbation in Fig. 2.13. Except for the surface tension, the exact same quantities are used for all three curves.

In this example, a ratio of 4 in the surface tension makes the difference between flattening out of the surface and formation of a thick layer that contains almost as much melt as crystal, a so called mushy layer [Fel06]. The simplifications of [Mul63] cause this layer to be predicted as lamellar but in reality branching is likely and liquid inclusions of any shape may form. The given examples shall suffice for the purpose of the present study but this is not to deny that a lot more research on surface roughening and mushy layers can be found in the literature, including, among others, the introduction of the roughening factor [Jac04], non-steady state simulation [Gre99], allowance of geometrical confinement [Gué88] and a detailed description of what happens in the mushy layer [Fel99, Ale06, Ase06, Sri11].

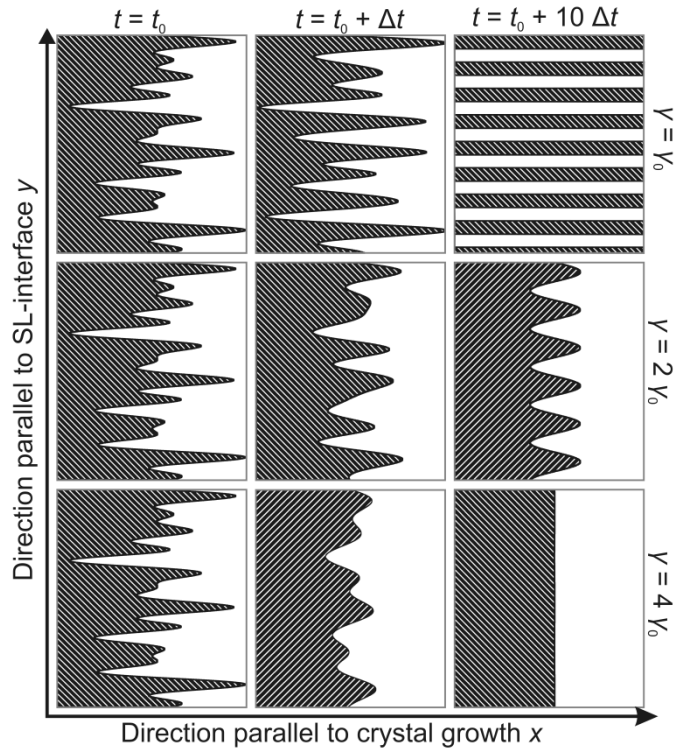


Figure 2.13. Perturbation in the crystal layer growing or retreating, depending on the surface tension. The plot is constructed from the data shown in Fig. 2.12.

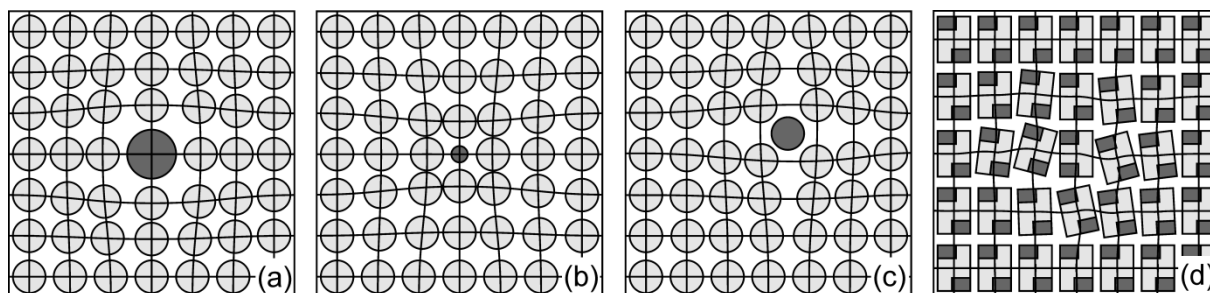
### 2.2.3 Separation on a microscopic scale: lattices and lattice defects

Crystallization is a powerful tool for separation because the long-range-ordered structure of a perfect crystal imposes much stronger restrictions on its composition than can be found in glasses, liquids or vapours. The fact that not all crystallization processes achieve the same separation success is due to lattice imperfections in the grown crystalline matter. For information on the concept of crystal imperfections, the reader is referred to the standard literature on crystallography, e.g. [Til06, Ver91, Vai00].

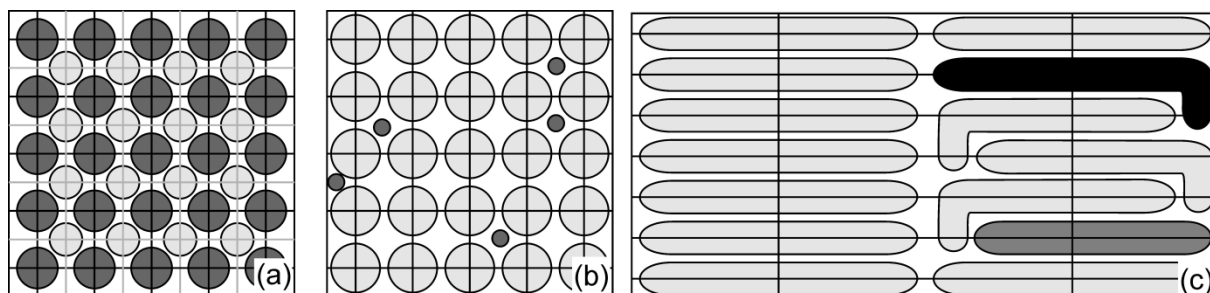
In the context of industrial crystallization, distinctions are often made between equilibrium and non-equilibrium separation, and between the partition upon the crystallization itself and the subsequent separation of crystals and residual melt. These distinctions are sensible in an integral approach to the engineering solutions and they will be used later on in this study. For a basic understanding, especially with respect to layer crystallization, they are not necessary. This is because, first, all processes of impurities entering the crystal can be described under the assumption of local equilibrium and, secondly, because the crystal-melt interface is, like any crystal surface, a 2-dimensional lattice defect. For clarity, this chapter will depict the impurity incorporation purely in the frame of lattice defects.



Molecules of 2 different species vary in size, or strength or orientation of possible intermolecular interaction. The same is true for atoms and ions. If the strength of possible intermolecular interaction, i.e. the polarity, is substantially different, the miscibility in the crystalline state is limited by the same argument that is well known for the liquid state. Differences in size or orientation generally cause the miscibility in the crystalline state to be lower than in the liquid state. This is because incorporation of an impurity particle, like a molecule, causes distortion of the lattice. If the overall orientation of the lattice is preserved, incorporated impurities form point defects (Fig. 2.14). The influence of orientation is especially important because it allows the separation of racemic mixtures. The restriction to miscibility is not without exception (Fig. 2.15). In cocrystals, salts and solvates, one potentially undisturbed lattice is formed containing 2 or more species in fixed molar ratios. Extensive miscibility with variable molar ratio may occur when the impurity particles are sufficiently small to fit into interstitial places without strongly distorting the lattice. An example is the storage of hydrogen in metal alloys [Sch01]. Flexibility in the shape of a molecule may relax the restriction to size differences for substitutional molecules. The crystalline mixtures of long-chained n-alkanes are an example [Dir98].



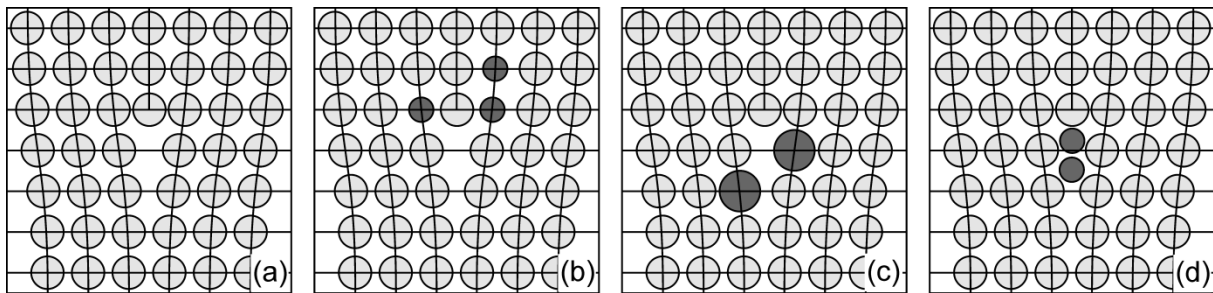
**Figure 2.14. Point defects and the lattice distortion caused by it: substitutional molecule of larger (a) or smaller size (b), interstitial molecule (c) and molecule of same size but different structure (d).**



**Figure 2.15. Mixed crystals: cocrystal (a), small interstitial molecules (b) and flexible molecules (c).**

The presence of 1-dimensional and 2-dimensional defects can ease the incorporation of impurities. The distorted lattice in the vicinity of the defect may fit the impurity atom better than the regular lattice, causing less distortion by the additional point defect. Fig. 2.16 shows the example of an edge dislocation (1-dimensional). The idea is the same for grain

boundaries (2-dimensional). In metallic crystals, it is widely known that impurities like oxides tend to diffuse to the grain boundaries.



**Figure 2.16. Edge dislocation (a) and its influence on solute uptake: small substitutional molecules in compressed volume above the edge (b), large substitutional molecules in stretched volume below the edge (c) and interstitial molecules in stretched volume below the edge (d).**

At the S-L-interface the geometrical restriction to positioning of impurity particles are much weaker. Different faces of the crystal may display different attraction to certain species in the liquid. The 2 determining factors are, first, the relative numbers of kinks and ledges, the face has on a molecular level and, secondly, the side or, in a cocrystal, the type of molecule that is next to the liquid side. When a particle from the liquid adsorbs to the interface, the number of neighbours in the crystal it has is highest in the kink position, lower in the ledge position and lowest on a terrace. The strength of attractive or repulsive forces to these neighbours is dependent on the second aspect. Impurities may be selectively adsorbed into certain positions on the crystal surface. When they are, they block growth on these positions. Furthermore, the impurities that are adsorbed onto the flat surfaces may hinder the surface diffusion of the main component. These 2 effects can lead to an immense influence of small amounts of impurity on shape or growth rate of the crystal. The tendency of a species to be adsorbed onto the crystal surface is related to its influence on the surface tension  $\gamma$ . A species that reduces  $\gamma$ , because its polarity is closer to the polarity of the crystal surface than the average polarity of the liquid, is preferentially adsorbed. In the case of a polar crystal, such an impurity would also be less mobile on the surface because it forms stronger bonds with the crystal. An impurity that is much less polar than the crystallizing matter would exhibit weaker adsorption and more mobility on the crystal surface. Therefore, it would not only be less likely incorporated into the crystal, but it would slow down the crystal growth to a lesser extent.

The influence of a certain impurity on the growth rate is related to the likelihood of it being included into the crystal layer in 3-dimensional defects, i.e. in channels or closed pores. Within the present study 'closed pores' shall refer to cavities that are completely surrounded by the crystal layer and 'channels' to cavities that are not. 'Liquid inclusions' refers to both of the above in so far as they are filled with melt. Like all defects, a liquid inclusion is energetically disadvantageous when the crystal lattice is the equilibrium state. The resulting

driving force to not form liquid inclusions can be quantified by means of the surface tension (cf. above, Ch. 2.2.2). Driving forces for the formation of liquid inclusions are also to be found above.

#### 2.2.4 Separation on a macroscopic scale: phase diagrams, porosity and concentration polarization

As shown above (Chs. 2.2.2-3), different mechanisms can lead to the uptake of solutes into the crystal phase. Some of these, like the liquid inclusions, depend on the distortion of the interface as a result of fast crystal growth. They cause, thus, non-equilibrium solute uptake. Others, like the uptake of substitutional or interstitial molecules, may also appear in equilibrium, but are favoured by fast growth. Whether or not the growth is fast has to be determined by comparing it to the mobility of solute in the liquid phase. As described above (Ch. 2.2.2), the rejection of solute at the SL-interface causes concentration polarization: the solute mass fraction in the melt at the crystal front  $w_{b,0}$  is higher than in the bulk of the melt  $w_{b,\infty}$ , i.e.

$$\kappa = \frac{w_{b,0}}{w_{b,\infty}} \geq 1. \quad (2.9)$$

The solute mass fraction in the crystal phase at the crystal front  $w_{b,c0}$  is connected to  $w_{b,0}$  by the equilibrium distribution coefficient  $k^*$ , making the assumption of local equilibrium at the growing SL-interface:

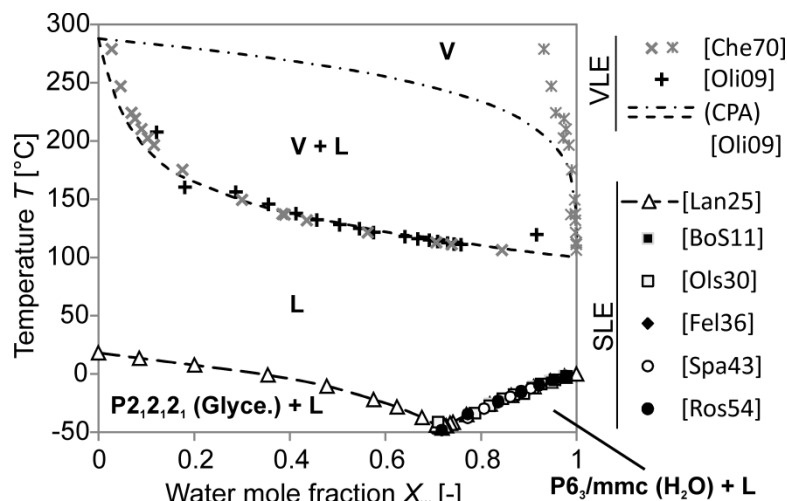
$$k^* = \frac{w_{b,c0}}{w_{b,0}} \leq 1. \quad (2.10)$$

The inequalities are given within the framework of the present study, but they can be abandoned [Til91b]. If the crystal layer forms liquid inclusions, the included melt has solute mass fraction  $w_{b,0}$ . Therefore, the momentary overall distribution coefficient is

$$k_0 = \frac{w_{b,0}^{Layer}}{w_{b,\infty}} = \kappa \frac{\Phi \rho_0 + k^* (1 - \Phi) \rho_{c0}}{\Phi \rho_0 + (1 - \Phi) \rho_{c0}} \quad (2.11)$$

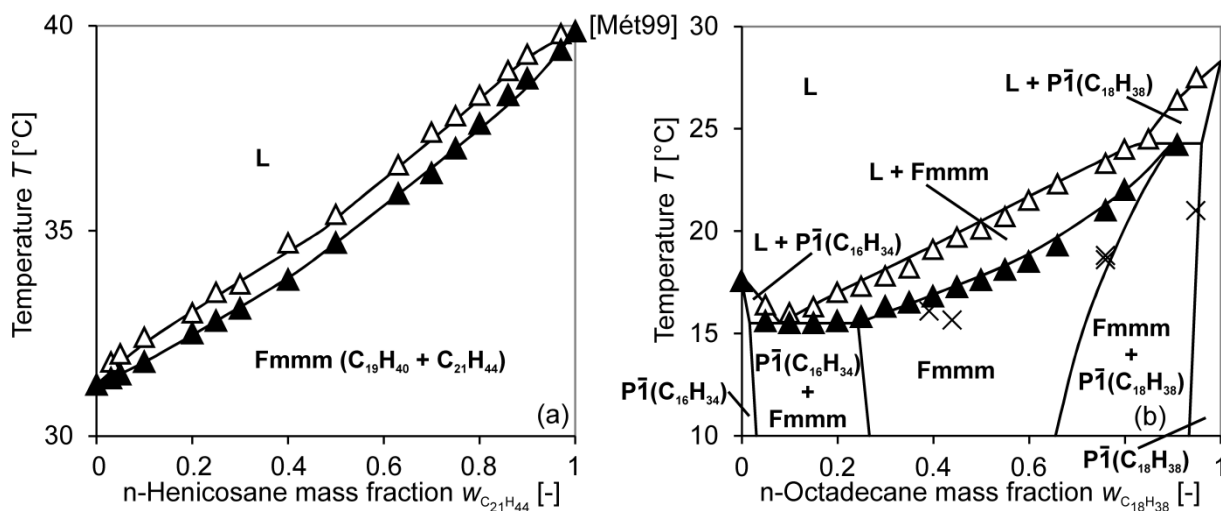
with the liquid inclusion volume fraction, i.e. porosity,  $\Phi$ , and the liquid and solid densities at the crystal front,  $\rho_0$  and  $\rho_{c0}$ , respectively. The equilibrium distribution coefficient  $k^*$  is a thermodynamic variable like the liquidus temperature  $T^*$ . Both can be read from the phase diagram. Fig. 2.17 shows the phase diagram of the binary system glycerol-water, with the vapour-liquid equilibrium (VLE) and solid-liquid equilibrium (SLE). The VLE shows zeotropic behaviour with complete miscibility in both phases (V and L) and a large concentration difference between the dew line (separating V from V+L regime) and the bubble line (between L and V+L). The SLE exhibits eutectic behaviour with complete immiscibility in the solid phase. Each component forms a different crystal lattice. When one lattice grows, only the respective nutrient enters the solid phase and rejects the solute to the liquid. With increasing solute concentration in the liquid, the equilibrium temperature decreases. As this

works from both sides, the liquidus line reaches a minimum at approximately 72 mole% water and  $-48^{\circ}\text{C}$ . This is the eutectic point in which the liquid and both crystal phases are in equilibrium. Up to that eutectic water mole fraction, glycerol concentration would always exhibit  $k^* = 0$ , according to this phase diagram. An example where this is not the case is given in Fig. 2.18.a: at any



**Figure 2.17.** Phase diagram of the system glycerol-water. Symbols represent experimental data. Crystalline phases are denoted by the space group and nutrient, liquid by L, vapour by V. The broken lines of the VLE are calculated by a cubic plus association equation of state (CPA) [Oli09]. The SLE line is only added to guide the eye.

temperature, the liquidus line (hollow symbols) shows little concentration difference to the solidus line (solid symbols). Therefore, e.g.  $k^* = 0.86$  when liquid is a 50/50 mixture. The system forms a solid solution with total miscibility in the solid phase. This can be explained by the flexibility of the molecules (Fig. 2.15.c). This SLE can be treated analogous to a zoetrope VLE of a close-boiling mixture. Solid solutions and eutectic points can occur together in one phase diagram. Fig. 2.18.b gives an example.



**Figure 2.18.** Phase diagrams of binary n-alkane mixtures nonadecane-henicosane (a) and hexadecane-octadecane (b). Lines and data points are taken from [Mét99].

Fig. 2.19 gives an example of a phase diagram including cocrystals, hydrates in this case. The 2 crystalline phases I and II contain sucrose and water in a fixed molar ratio (1:2.5 in I and 1:3.5 in II). The transformation temperature from one hydrate to the other is fixed, forming a horizontal line in the diagram. The point where it meets the liquidus line is called a

peritectic point. The formation of a cocrystal puts a limit to the separation. However, the present example would allow equilibrium crystallization of pure sucrose from solutions with  $w_{\text{sucrose}} \geq 0.67$ . In this special case, the occurrence of the cocrystal could also be avoided, by using the metastable eutectic behaviour. The SLE may also be influenced by a miscibility gap in the liquid phase. Fig. 2.20.a presents the example of aqueous BuOH, which is also an example for an azeotrope. Fig. 2.20.b shows the LL-equilibrium of the ternary mixture glycerol-water-BuOH. In this case, the crystallization of glycerol can be carried out close to the miscibility gap, the significance of which will also be discussed below (Ch. 6.4). If more than 2 components are present in the system, the representation of the SLE becomes more complicated. In some cases, the matter can be simplified. An example that is of interest within the scope of the present study is the pseudobinary behaviour of a mixture containing a multinary mixture of long n-alkanes and one much shorter n-alkane.

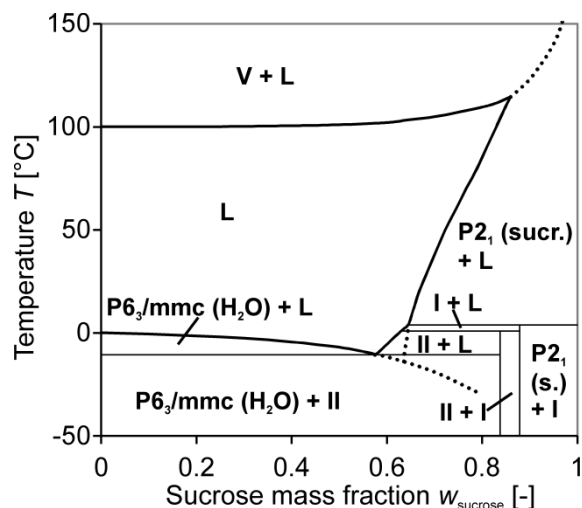


Figure 2.19. Phase diagram of the binary system water-sucrose. Crystal phases are represented by their space group and nutrient except for sucrose hemipentahydrate (I) and sucrose hemiheptahydrate (II). The dotted lines represent metastable parts of the curve. Based on [You49] and data compiled in [Sha95, Sta06].

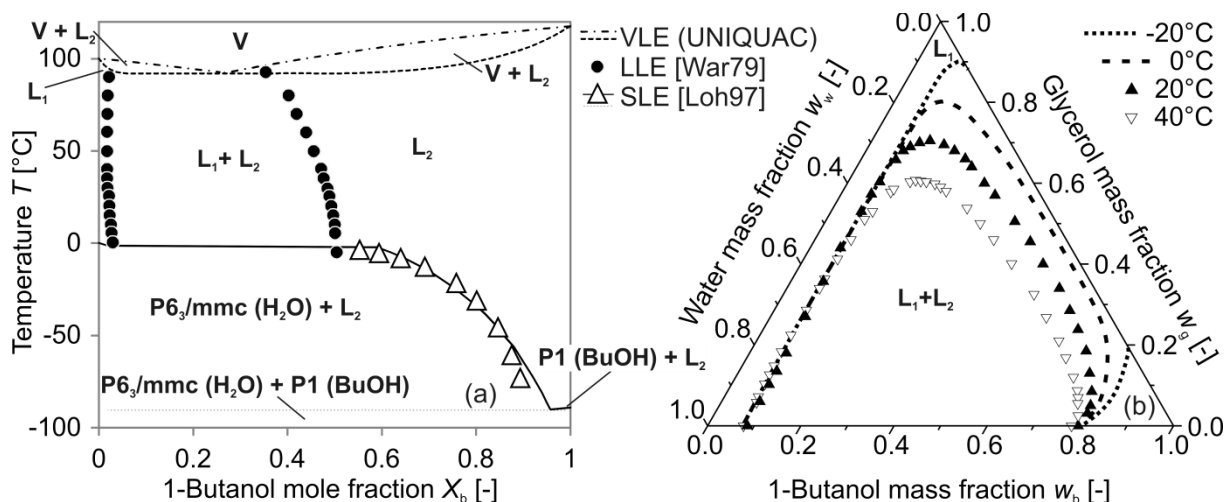
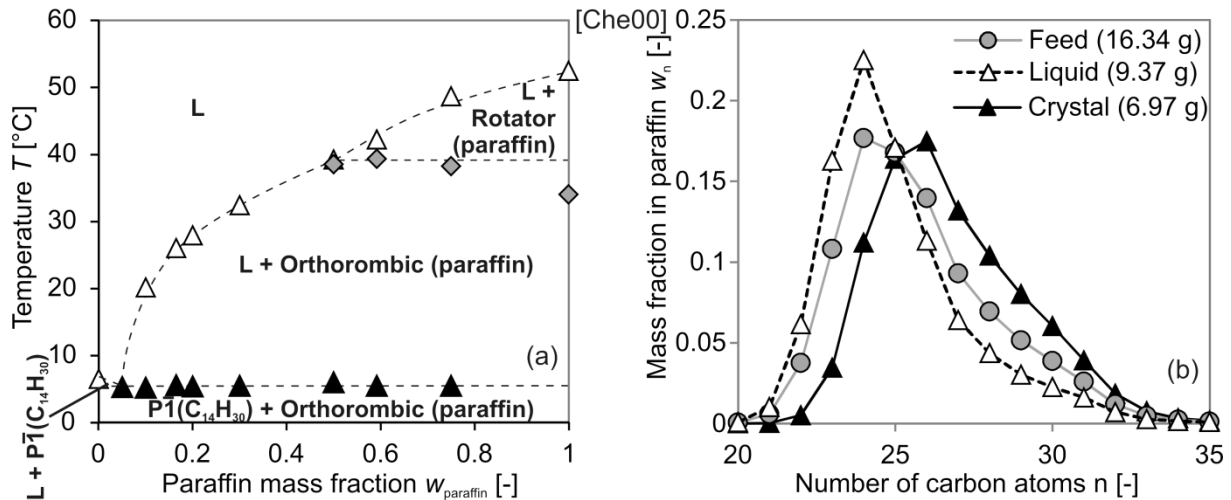


Figure 2.20. Phase diagram of the binary system water-BuOH, with experimental (symbols) and calculated data (lines) (a). The liquidus line was calculated by [Loh97] using UNIQUAC-Dortmund model. The VLE is a qualitative information for orientation, obtained by simple UNIQUAC. (b): Liquid phase diagram of the ternary system water-glycerol-BuOH with experimental data (symbols) from [Mat57] and linear extrapolation to lower temperatures (broken lines).

Fig. 2.21.a shows the phase diagram, in which the mixture of long alkanes (the paraffin wax) is regarded like one component. This is possible, because it forms a solid solution. A

fractionation of the paraffin wax does, nevertheless, occur, as can be seen in Fig. 2.21.b. This n-alkane system is also an example for the occurrence of order-disorder transformations in the solid phase. Fig. 2.21.a shows not only crystal and melt phase but also a rotator-phase, which is a solid that is less ordered than a crystal but not as amorphous as a melt [Wen10].



**Figure 2.21. Pseudobinary phase diagram of a system containing a multinary mixture of long n-alkanes (Paraffin) and one much shorter n-alkane (tetradecane, C<sub>14</sub>H<sub>30</sub>) (a). The composition of the feed paraffin, of the solid deposit at 15°C and of the paraffin remaining in the liquid phase at the same temperature is given in (b).**

The vast majority of known binary organic mixtures exhibits a eutectic point, and in most of them the miscibility in the solid phase is too small to be detected with common experimental accuracy, so that essentially  $k^* = 0$ . Some authors, e.g. [Lew15], distinguish between eutectic systems and solid solutions, based on whether they allow  $k^* = 0$  or not. Others, e.g. [Kön03], use the term eutectic system for any system exhibiting a eutectic point. The presented examples showed, that  $k^*$  is often very small but can also be unfavourably large. If  $k^* = 0$ , that does not mean that the separation will be successful, as is obvious from Eq. 2.11. The porosity,  $\Phi$ , and concentration polarization parameter,  $\kappa$ , have to be low, as well. Their dependence on each other and on the process parameters is a matter of ongoing research, including the present study. Therefore, it will be discussed in more detail in the following Chapter (Ch. 2.3) and in the discussion part of this study (Chs. 6.2-3).

## 2.3 Research techniques in melt layer crystallization

### 2.3.1 Crystallization equipment, experimental setups and measuring techniques

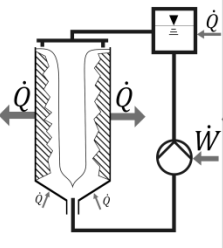
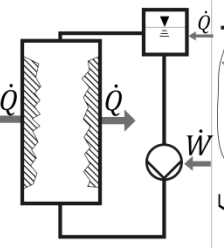
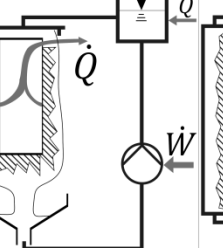
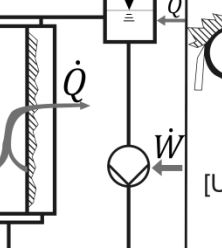
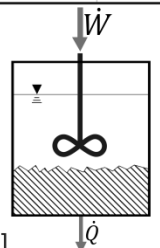

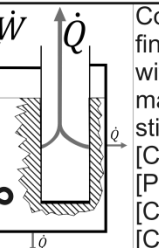
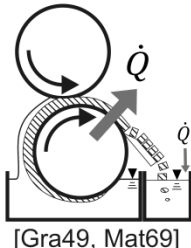
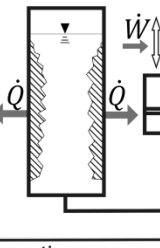
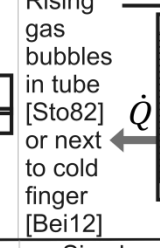
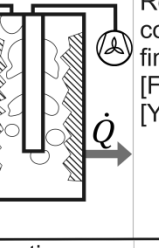
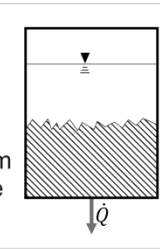
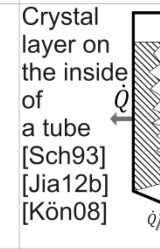
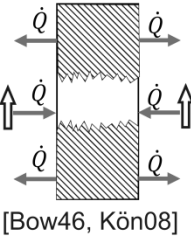
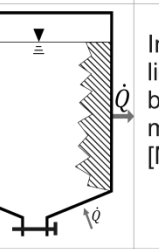
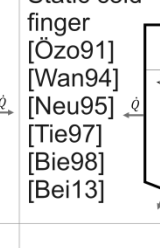
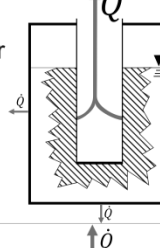
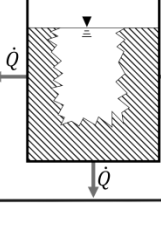
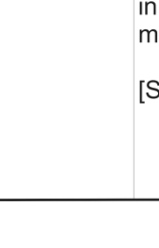
Many different types of equipment have been used in experiments on layer crystallization and many of them have been proposed for industrial application. Very detailed reviews with drawings of proposed equipment are available in German [Mat69, Rit85, Özo91]. English reviews are also available [Ark95, Ulr03b]. A more recent but less detailed review is given by

JIANG et al. [Jia14b]. However, recent years haven't produced many types of equipment that are substantially different from the earlier ones. Therefore, the available reviews are still valid, especially for the more elaborate setups. In order to not be repetitive, the present study will put an emphasis on the simpler experimental setups.

Tab. 2.3 compiles different types of setups with sketches and exemplary literature. 2 possible directions can be discerned in the strategy of experimentation on melt layer crystallization. The first is to use the industrial equipment itself, or a setup that has as much in common with it as possible. The second is to conduct experiments in a setup that is completely unrelated to the industrial equipment apart from the fact that they both allow the same phase transition. An example for the second strategy is KÖNIG & SCHREINER's [Kön01] proposal to assess the purification potential of layer crystallization by performing suspension melt crystallization and pastillation experiments. A similar strategy is the bottle test, in which the melt is put into a bottle which is then stored at sufficiently low temperature until partial crystallization has occurred. From the mass and composition of the residual melt and the product, which remains in the bottle during draining at low temperature, the order of magnitude of the growth rate and a worst case scenario for the separation can be gathered. The bottle possesses cooled surfaces for crystallization and is, thus, more similar to industrial equipment than the suspension crystallizers.

A very important type of laboratory setup is the cold finger setup. The cold finger is a tube, closed on one side, in which a second tube is immersed, such that a cooling liquid can flow through it. It is immersed into the melt, which is in a beaker, usually with thermostated jacket. During growth of the crystal layer on the cold finger, beaker and cold finger temperature can be controlled. The melt can be agitated by stirring [Kim02, Cha10a] or bubbling [Bei12], and cold fingers can even be used for falling film application [Özo91, Neu94]. Other setups including tubes with the crystal layer growing on the inner or outer wall and the cooling liquid flowing on the other side offer similar possibilities. An important possibility is that of on-line measurement of the growth rate. Proposed measurement techniques include a laser scanner, a thermometer grid, continuous weighing of feed and residuum in falling film operation [Sch93b] and recording with a camera [Bei13]. However, it is still common to determine the growth rate off line from the deposited mass or the layer thickness at the end of the experiment. The distribution coefficient is always determined off line in batch operation, even though a first approach towards an on-line determination has been made early on [Lei89].

Table 2.3 Crystallization equipment overview. The literature is only exemplary.

		Batchwise				Continuous
Melt is pumped around	Forced convection, dynamic	Crystallization on inside of tube		Crystallization on outside of tube		Belt crystallizer [Ulr90b, Ulr92]
		Falling film  [Sax68, Kön08] [Jia12a,b]	Tube flow  [Win76, Sch93]	Falling film  [Ulr90a, Özo91] [Neu95]	Tube flow  [Bie98]	
Melt stays in the crystallizer	Forced convection, (quasi-)dynamic	Stirring  [Sch93] [Jiang12]	Cold finger and shaft stirrer  [Ono93] [Kim02]	Cold finger with magnetic stirrer  [Chi93] [Par01] [Cha10a] [Cha10b]	Drum crystallizer  [Gra49, Mat69]	
		Other than stirring  [Keh89] [Keh90] [Kus90] [Jan90]	Rising gas bubbles in tube or next to cold finger  [Sto82] [Bei12]	Rotating cold finger  [Fuk13] [Yam16]		
	Natural convection, static	No sweating  [Lei89] [Lan80]		Simple sweating  [Sch93] [Jia12b] [Kön08]		Zone melting  [Bow46, Kön08]
		Intense sweating  [Mul01]		Static cold finger  [Özo91] [Wan94] [Neu95] [Tie97] [Bie98] [Bei13]		
G control and measurement  [Pet02]		Bottle test  [Ulr06] [Kön08]		Packing in the melt  [Ste06]		



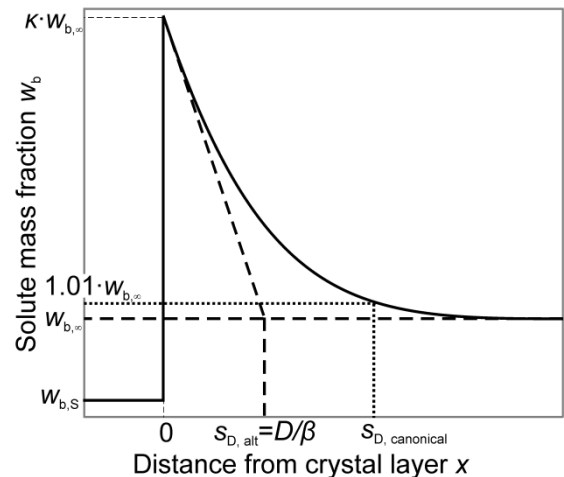
### 2.3.2 Scale up, correlation and prediction

Melt layer crystallization is ascribed the advantage of easy scale up. This is true for scale up from the pilot-plant scale to large scale if the pilot plant contains the same tubes or plates as the large scale plant, just in lower number. This is nowadays often the case, so scale up is only numbering up, which is rather trivial. For scale up from mL-scale to pilot plant scale, the most common method is purely empirical. A paper from KÖNIG et al. [Kön08], co-authored by STEPANSKI & KUSZLIK from Sulzer Chemtech, the largest supplier of melt layer crystallization equipment, illustrates the procedure. Starting from a zone melting experiment on mL-scale, the scale is gradually increased, employing several different types of setups. Whenever the separation on one scale seems to be successful, the experiments are carried on to the next larger scale, until finally the pilot plant is reached.

Attempts to reduce the number of required experiments by offering empirical correlations or predictive simulation, can often be expressed in terms of a dimensionless growth rate,  $\Gamma$ ,

$$\Gamma = \frac{G}{\lambda}, \quad \lambda \in \left\{ \beta, \quad \frac{D}{s_D}, \quad \beta \frac{\rho_L}{\rho_S}, \quad \frac{D \rho_L}{s_D \rho_S} \right\}, \quad (2.12)$$

where the growth rate reference,  $\lambda$ , is a measure of the speed with which rejected solute molecules can be transported away from the crystal front.  $\rho_S$  and  $\rho_L$  are the densities of crystal and melt, respectively,  $D$  is the diffusivity and  $\beta$  the mass transfer coefficient.  $s_D$  is the thickness of the diffusion boundary layer. Its canonical definition is the distance  $x$  at which the solute mass fraction  $w_b(x=s_D)$  differs from  $w_{b,\infty}$  by a certain factor, most often  $w_b(x=s_D)/w_{b,\infty} = 1.01$ . In the context of crystallization, some authors, e.g [Wil78], define  $s_D$  such that  $D \cdot (s_D)^{-1} = \beta$ . The difference is illustrated in Fig. 2.22. Even if  $D \cdot (s_D)^{-1}$  and  $\beta$  are not of the same value, they certainly scale with each other because they represent very similar physical concepts. Both give a measure of the ability of the system to transport impurities from the crystal front into the bulk of the melt. The factor  $\rho_L(\rho_S)^{-1}$  accounts for the fact that the contraction during crystallization leads to a velocity of the melt normal to and towards the crystal when  $\rho_L(\rho_S)^{-1} < 1$ . For water, in which  $\rho_L(\rho_S)^{-1} \approx 1.1$ , the expansion during freezing leads to a melt velocity away from the crystal layer. In glycerol it is  $\rho_L(\rho_S)^{-1} \approx 0.94$ , which is a very low value for an organic compound.



**Figure 2.22. Diffusion boundary layer and the relation between its thickness and the mass transfer coefficient  $\beta$ . For better visibility, the construction of  $s_{D, canonical}$  is done at  $1.05 w_{b,\infty}$  instead of the denoted  $1.01 w_{b,\infty}$ .**

Usually in crystallization of organics, the density ratio is close enough to one to be neglected. Therefore, the different definitions in Eq. 2.12 are not substantially different, in contrast to the

$k(G)$  or  $k(\Gamma)$ -correlations or predictions that have been proposed in the literature. These are compiled in Tab. 2.4. The distribution coefficient and concentration polarization ratio are not always defined in terms of mass fractions,  $w$ , but may also be defined in terms of mass concentrations,  $c$ , or mole fractions,  $X$ , which is indexed by  $c$  and  $X$ , respectively:

$$k_c = \frac{c_{\text{imp}}^{\text{Layer}}}{c_{\text{imp},\infty}}, \quad \kappa_c = \frac{c_{\text{imp},0}}{c_{\text{imp},\infty}}, \quad k_X = \frac{X_{\text{imp}}^{\text{Layer}}}{X_{\text{imp},\infty}}, \quad \kappa_X = \frac{X_{\text{imp},0}}{X_{\text{imp},\infty}}. \quad (2.13)$$

Frequently, melt layer crystallization is performed on mixtures of organics with very similar molar masses and densities and little excess volumes, so that the differences between these definitions are negligible. If that is the case, Eq. 2.16 and Eq. 2.21 are the same equation. They present the most important description of  $k(G)$  for the assumption that solute only enters the crystal layer in liquid inclusions and is not incorporated. WINTERMANTEL [Win86] derived Eq. 2.16 based on the boundary layer model [Bur53a,b] that is also the foundation of Eq. 2.15. From Eq. 2.16, it follows that when varying  $G$ ,  $\beta$  and  $c_\infty$  independently, all experimental points attained for one system can be fitted by one curve in a plot of  $k$  versus the parameter

$$\frac{c_{b,\infty}}{\rho_L - c_{b,\infty}} \left( e^{\frac{G\rho_C}{\beta\rho_L}} - 1 \right) = \zeta_{\text{ba},\infty} (e^\Gamma - 1), \quad (2.14)$$

if both  $\kappa$  and  $k$  depend only on this parameter. WINTERMANTEL [Win86] found this experimentally for the 2 systems water/NaCl and naphthalene/diphenyl, both in the same setup. BIERWIRTH [Bie98] later presented experimental results that suggested an influence of the setup geometry on the  $k(\zeta_{\text{ba},\infty} \cdot (e^\Gamma - 1))$ -relation. MYASNIKOV & UTESHINSKY [Mya05] attempted to add a calculation path of  $\kappa$  to arrive at a purely predictive formula Eq. 2.21. However, its applicability has not been widely acknowledged.

All in all, it is important to note that no predictive  $k(G)$ -simulation has yet become canonical or shown sufficiently universal accuracy to likely claim any such role. On the contrary, it is a widespread opinion, e.g. [Bei13, Ulr03b, Wan94b], that all purely theory-based  $k(G)$ -simulations are flawed and experimental help is always needed. Empirical or semiempirical correlations with universal applicability have also not been established yet, but experiments are required anew for each system. A prediction or correlation of  $k(G)$  that gives credit to the influence of the surface tension is also missing in the literature.

**Table 2.4. Types of empirical and semiempirical correlations and predictive theories for the dependence of the distribution coefficient  $k$  on the dimensionless growth rate  $\Gamma$ . For better comparability, nomenclature was harmonized and some equations were manipulated preserving mathematical equivalence.**

Principal equation	Applicable for	Experimental data set, on which the correlation was obtained or tested.
$k_c = \frac{k_c^*}{k_c^* + (1 - k_c^*)e^{-\Gamma}}$ (2.15) [Bur53a]	No liquid inclusions, $\Phi = 0$	Germanium with many different impurities [Bur53b]
$k_c = \frac{e^\Gamma - \kappa_c}{e^\Gamma - 1}$ (2.16) [Win86]	$k^* = 0$	Water/NaCl, naphthalene/diphenyl [Win86]
$k = 1 - b^\Gamma$ (2.17) [Özo92]	$k^* = 0$	$\epsilon$ -Caprolactam/cyclohexanon, p-dichlorbenzene/o-dichlorbenzene, n-dodecanole/n-decanole [Özo92], naphthalene/diphenyl [Win86].
$k = 1 - \frac{((e^{\Gamma_{k=0}}) - 1) \left(\frac{\Gamma}{\Gamma_{k=0}}\right)^{\frac{2}{3}}}{e^\Gamma - 1}$ (2.18) [Sch93b]	$k^* = 0$	Water/NaCl, water/sucrose, water/glycerol [Sch93b], naphthalene/diphenyl [Win86].
$k = b_1 + b_2 \ln(\zeta_{ba,\infty} (e^\Gamma - 1))$ (2.19) [Bie98]	$k^* = 0$	$\epsilon$ -Caprolactam/cyclohexanon, $\epsilon$ -caprolactam/water p-dichlorbenzene/o-dichlorbenzene, naphthalene/diphenyl [Bie98]
$k = b_1 G^{b_2} w_\infty^{b_3} t^{b_4}$ (2.20) [Gua01]	$k^* = 0$	$\epsilon$ -Caprolactam/water [Gua01]
$k_X = \frac{e^\Gamma - \kappa_X}{e^\Gamma - 1}$ (2.21) [Mya05]	$k^* = 0$	Naphthalene/benzoic acid [Lap77]
$k = 1 - \frac{(T_0 - T_\infty)}{\Gamma \left(\frac{dT^*}{dw}\right) w_\infty e^\Gamma}$ (2.22) [Jia12b]	Falling film	Phosphoric acid (H <sub>3</sub> PO <sub>4</sub> ) with water and different ionic impurities [Jia12b]

### 3 Motivation

The goal of the present study is to introduce and investigate new methods that extend the applicability of melt layer crystallization to the separation of highly viscous mixtures and allow better assessment of the process based on data from lab-scale experiments.

A large body of literature is available on solution crystallization in suspension and concerning the influence of solvents on the equilibrium separation (cf. Chs. 2.1.1 & 2.2.3-4). The use of solvents to reduce viscosity in melt crystallization has been mentioned [Has41, Roh12] but no comprehensive research is prior knowledge. Concepts to improve separation kinetics by forced convection are plenty (cf. Tab. 2.3), but all of them require addition of moving parts of machinery or gas streams in contact with the melt. A concept that uses the same simple equipment as static layer crystallization is missing.

The literature on assessing and extending economic feasibility of melt layer crystallization has produced some experimental [Kön01, 08] and some predictive strategies (cf. Tab. 2.4) but a method to scale up from lab scale is missing. Simulations that may be used for the purpose commonly depend on simplifications that are not valid when higher viscosity is encountered or a liquid additive is present. The quantitative comparability of process data obtained on a lab scale is, especially when viscosities are higher, very questionable as papers show unexplained discrepancies [Cha10a]. Therefore, the only established rule is that what works in the lab works even better on the large scale.

In order to make a major contribution to filling these vacancies in the state of the art, it is crucial that the present study shall combine experiments on the scarcely investigated concept of additives for faster separation with a critical discussion of established experimental methodology and a quantitative and comprehensive approach to the interpretation of the data. This combination allows not only the statement that the concept works for the investigated system, but it gives an understanding of the mechanism by which it works and provides methods for a future application to other systems.

For an understanding of the process, experiments are to be carried out on a glycerol-water mixture with BuOH and other organic solvents as additives. A number of different setups shall be used and methods shall be presented to make results from different setups comparable. Then, the measured effect of BuOH is to be compared with calculations based on different sets of assumptions to shed light onto the mechanism by which BuOH improves the separation process. From the knowledge of the mechanism, a protocol for choosing a suitable additive for other feeds shall be derived. In order to show the limits of the presented technique, its application to 2 actual industrial separation tasks, completely different from the binary aqueous glycerol mixture, shall be investigated.

## 4 Materials and Methods

### 4.1 Materials

#### 4.1.1 General

In the course of this study, a realistic assessment of industrial applicability should be given. Therefore, feeds and helping agents were not all of very high purity, but chemicals, and especially water, were used in qualities that are easily attainable.

Tab water used in the present study had a rather low content of dissolved solids, was not degassed and had no uncommon features. Specifications are given in Tab. 4.1.

**Table 4.1. Specifications of the tab water used in the present study as given by the supplier, Stadtwerke Halle GmbH. Dissolved substances of  $c < 10^{-4} \text{ kg m}^{-3}$  are not mentioned.**

Substance	$c [10^{-3} \text{ kg m}^{-3}]$			Substance	$c [10^{-3} \text{ kg m}^{-3}]$		
	min	mean	max		min	mean	max
$\text{Ca}^{2+}$	20	34	34	$\text{SO}_4^{2-}$	27	28	29
$\text{Mg}^{2+}$	3.3	3.3	3.3	$\text{Cl}^-$	17	17.5	18
$\text{Na}^+$	7.5	8.1	8.4	$\text{NO}_3^-$	4.6	4.9	5.2
$\text{K}^+$	0.74	0.75	0.76	TOC	1.7	1.75	1.8
				Si	2.9	2.9	2.9

Parameter	unit	min	mean	max
Conductivity	$10^{-4} \text{ S m}^{-1}$	197	199	201
pH	-	8.16	8.45	8.61
Acid capacity to pH 4.3	$\text{mol m}^{-3}$	0.8	0.8	0.8
Base capacity to pH 8.1	$\text{mol m}^{-3}$	0.00	0.01	0.02

#### 4.1.2 Paraffin

Middle machine oil (mmo)-type slack wax came from an Indonesian refinery and had an initial oil content of  $w_o \approx 20\%$ . It was a raffinate and not simply a distillate, i.e. aromatics had been removed by extraction. Its main components are n-alkanes. 2-propanon (methyl-ethyl-ketone, mek) from Roth was synthetic grade. All water used was tab water specified above (Tab. 4.1).

#### 4.1.3 Glycerol - water system (gw)

Chemicals used are gathered in Tab. 4.2. Feeds for the crystallization were often prepared from the residues of previous crystallization processes mixed with sufficient amounts of fresh glycerol and solvent to attain the desired composition.

**Table 4.2. Chemicals used in the system glycerol - water. Suppliers are Carl Roth GmbH + Co. KG, Germany and Merck KGaA, Germany.**

Material	Supplier	Grade	Material	Supplier	Grade
Glycerol	Roth	Rotipurán®, ≥ 99.5%	1-Propanol	Merck	For analysis
Methanol	Roth	Rotydry®, > 99.5%	1-Butanol	Roth	Rotisolv® HPLC
Ethanol	Roth	Rotipurán®	2-Butanon	Roth	For synthesis

#### 4.1.4 Raw glycerol system (rg)

Raw glycerol was provided from Hallesche Ölverarbeitungswerke GmbH, Germany. It was biodiesel glycerol after evaporation of methanol and parts of water. The dark-brown liquid had the specifications given in Tab. 4.3. Qualities of solvents were the same as given in Tab. 4.2.

**Table 4.3. Raw glycerol specifications as given by the supplier, Hallesche Ölverarbeitungswerke GmbH, Germany.**

Substance	Method	w	Parameter	Method	Value
Glycerol	Ph. Eur. 7.0	0.8213	Density at 20°C [kg m <sup>-3</sup> ]	En ISO 12185	1244.3
Water	En ISO 12937	0.1265	Refractive index	Ph. Eur. 2.2.6	1.4554
Chlorides (as NaCl)	Ph. Eur. 2.4.4	0.0373	pH	Ph. Eur. 2.2.3	7.07

## 4.2 Setups and procedures

### 4.2.1 General

This is not only a study on the physical mechanism of crystallization in high-viscous melts but it deals with the question of how to handle the high viscosity in both laboratory and plant. Therefore, instead of using one very sophisticated setup, a series of different simpler setups was used. Starting from very simple bottle tests and classical cold finger experiments, the study proceeds to slightly more complex setups which are better suited to the high-viscous melt, especially the one of glycerol. This strategy provides information about the practical implications when dealing with a high-viscous melt in the laboratory along with the understanding of the crystallization process in abstracto.

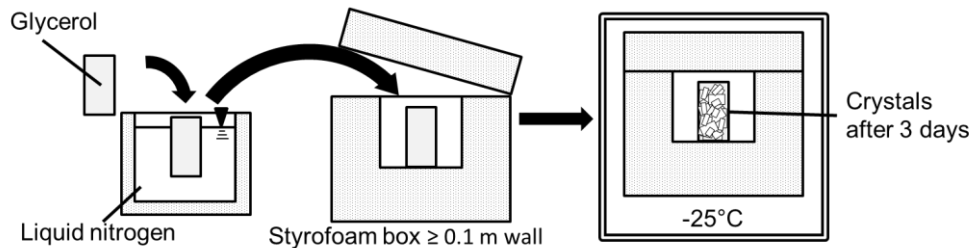
An overview over the used setups is given in Tab. 4.4. Detailed descriptions are provided in the subsequent chapters. All setups have similarities with setups that are already described in the literature. For these, cf. above (Ch. 2.3 & Tab. 2.4). All crystallization experiments were performed at ambient pressure.

**Table 4.4. Setup types used in the present study. Heat streams  $\dot{Q}$  and mechanical power  $\dot{W}$  are depicted with arrows. The thickness of the arrow as well as the size of the letter represents the approximate typical relative power levels of the heat and work streams. The setup geometries are not drawn to scale. Abbreviations: gw: glycerol-water, rg: raw glycerol.**

Setup	Bottle	Glass	Cold finger static	Classic cold finger	Cold finger translating	Tube, pack, inert liquid
Sketch						
For	gw, rg	gw, rg	gw	gw	gw	Paraffin
$V_{\text{melt}}$	0.01-2.5 L	0.03 L	1.2 L	0.4 L	0.1 L	0.1 L

### 4.2.2 Glycerol seed production

The production of first glycerol crystals is carried out similarly to the process described by GIBSON & GIAQUÉ [Gib23]. Different mixtures of glycerol were cooled with liquid nitrogen and slowly heated to  $-25^{\circ}\text{C}$  in a freezer. Additionally to the reduced environmental temperature, slow heating was ensured by keeping the samples in a Styrofoam box. The workflow is depicted in Fig. 4.1. The used glycerol mixtures contained water in mass fractions of  $0.2\% < w_w < 30\%$ . The process was also performed on a sample containing  $w_b = 50\%$  BuOH and  $w_w < 1\%$  water.



**Figure 4.1. Workflow for the production of glycerol seed crystals.**

### 4.2.3 Seed crystal growth

The influence of water and BuOH on the growth rate of glycerol was investigated by measuring the growth of seed crystals in different binary glycerol-water and glycerol-BuOH-mixtures. These mixtures were poured into tubes or flasks with seed crystals at their bottom, or into petri dishes with seed crystals in the centre. The flasks were closed by stoppers and the dishes by polyethylene sheets. Both were stored at  $-25^{\circ}\text{C}$  or  $6^{\circ}\text{C}$ . Little nucleation of glycerol is to be expected at these temperatures. Therefore, the crystal growth rate was determined by measuring the position of the crystal front in situ after different times after seeding. Fig. 4.2 shows an example. The crystals were not fixed to the centre of the dish but all experiments in which the seed crystal changed its position were not taken into account. In

case of a decrease in growth rate as result of the decreasing glycerol concentration towards the end of an experiment, only the constant growth rate at the beginning of the experiment was taken into account.

#### 4.2.4 Magnetic stirrer cold finger setup (MCF)

The simplest cold finger setup used for experiments on the glycerol-water system is depicted in Fig. 4.3. The nominal capacity of the double-walled beaker was 0.6 L, but the filling level was not held constant. Instead, a fast processing was facilitated by using the residual melt of one experiment in a series as feed for the next in the same series without taking it out of the beaker. The separation of the crystallization caused the desired variation of the melt composition. The mass fractions  $w_w$  and  $w_b$  of water and BuOH, respectively, were measured before each experiment and the influence of all minor impurities, i.e. all mixture components except glycerol, water and BuOH, was neglected. Therefore, the results are interpreted as if a new synthetic mixture of variable  $w_w$  and  $w_b$  had been fed into the beaker for each experiment.

Prior to the crystallization step, a thin but complete, smooth-surfaced polycrystalline seed layer was applied to the cold finger. To this end, the cold finger was centred in a 50 mL-centrifuge tube with seed crystals at its bottom and liquid glycerol ( $w_w = 0.2\%$ ) and stored at 6 °C until the glycerol was completely crystallized. The thickness, mass and purity of the seed layer were taken into account when calculating the growth rate and the purity

of the grown crystals. During the crystallization step the temperatures of the cold finger and the double-walled beaker,  $T_{CF}$  and  $T_B$ , respectively, were controlled by 2 thermostats. The beaker did not have a lid. It was closed towards the surrounding atmosphere by multiple layers of plastic sheeting. For the dynamic case, agitation of the melt was provided by a magnetic stirrer. The stirring rate was adjusted in 100 min<sup>-1</sup>-steps to the maximum possible as restricted by the viscosity of the melt.

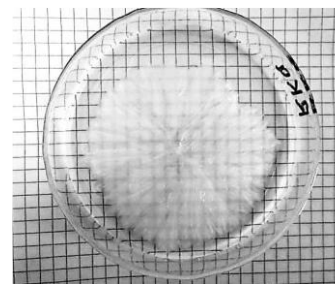


Figure 4.2. Example of determination of crystal growth rate in a petri dish. The position of the seed is obvious from the shape of the crystallite. The size is estimated by counting the squares and averaging over several directions.

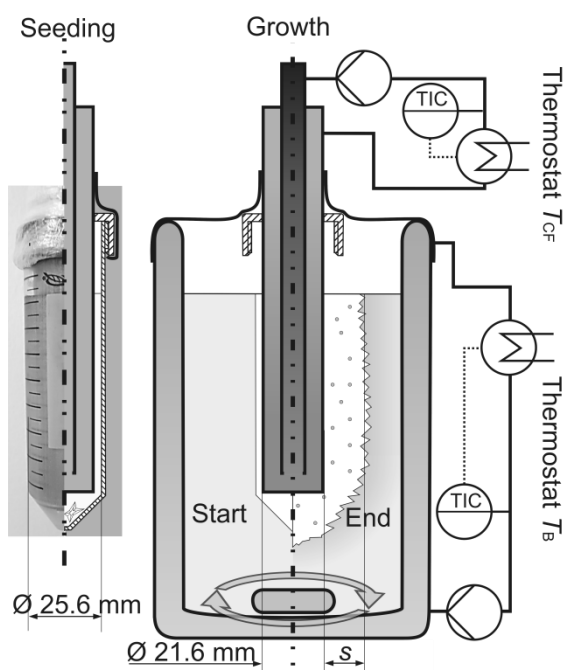


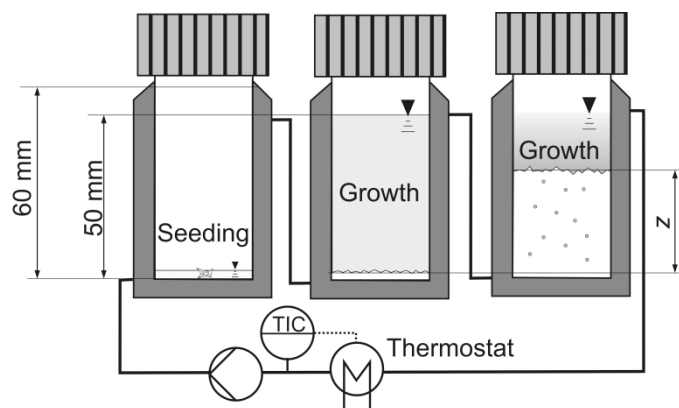
Figure 4.3. Sketch of the magnetic stirrer cold finger setup (MCF). Application of a complete seed layer onto the cold finger (Seeding) and crystal growth after immersion into the melt (Growth).



#### 4.2.5 Glass setup (GL)

In this study, 'glass setup' refers to 30 mL-double walled beakers in which the layer grows vertically upwards from a seed layer at the bottom covering the entire cross-sectional area. Fig. 4.4 gives a sketch. The bottom and complete jacket of 60 mm height was cooled to the stated crystallization temperature. The seed layer was built by covering the beaker's bottom with 1 mL liquid glycerol ( $w_w = 0.27\%$ ) and adding one small seed crystal. Hereafter, the seed glycerol was allowed to completely crystallize at the beaker temperature of the subsequent growth step. The growth step was started by pouring 25 mL feed into the beaker, on top of the seed layer and to a level of 50 mm. The thickness, i.e. height, of the grown crystal layer, not including the seed layer, was recorded over time by photographs and the growth rate evaluated as described below (Ch. 4.3.2). At the end of the growth step, the residual melt was removed by means of a syringe and the temperature increased to melt the crystal layer and remove it in the same manner. In the evaluation of the distribution coefficient a correction for the influence of the seed on the crystal composition is made, taking into account both the mass and composition of the seed layer.

A screw lid prevents the entrance of water from the surrounding atmosphere into the beaker. It is only opened for addition or removal of substances. 10 of these beakers are cooled in parallel circuit by one thermostat, allowing for rapid experimentation. This is a major advantage along with the possibility of a simple but detailed evaluation of the growth rate during the experiment. The major disadvantages are the missing possibility of post treatment and a relatively large risk of error in the separation of melt from crystal. Also, the glass setup differs from common industrial procedure in its geometry and temperature gradients. The resulting differences to cold finger setups in growth rate gradients have to be compensated by the data evaluation process described below (Ch. 4.3.2).



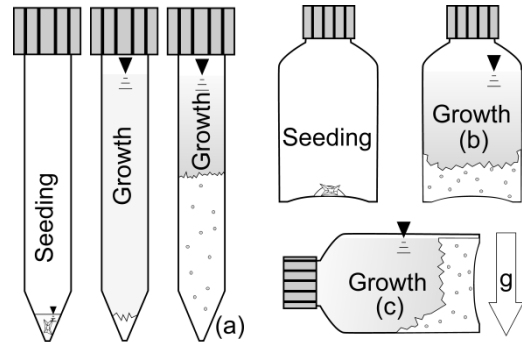
**Figure 4.4. Glass setup showing 3 glasses during different stages of one experiment. Actually, 10 glasses were operated in parallel.  $z$  is the thickness of the crystal layer.**

#### 4.2.6 Bottle tests

Vessels used for bottle tests were all of plastics, usually polypropylene, as glass bottles tend to burst when an inner glycerol crystal layer melts. The types of bottles for different

capacities were: 15 mL and 50 mL cone-tipped centrifuge tubes (Fig. 4.5.a), 0.25 L and 0.5 L laboratory sampling flasks and, of capacities 1 L and 2.5 L, the bottles in which Glycerol (Ph.Eur., Merck) is delivered (Fig. 4.5.b-c). Bottles were always seeded at the bottom,

centrifuge tubes either in the lid or in the tip. The seed crystal was attached to the surface by a small amount of liquid glycerol ( $x_w < 1\%$ ) which was allowed to crystallize before the melt was added. The bottles were stored in a freezer ( $-25^\circ\text{C}$ ) or fridge ( $6^\circ\text{C}$ ) for crystallization. Then the residual melt was poured out and the crystals were molten. For the glycerol-water system, vessels were always placed in a manner that the



**Figure 4.5. Sketch of the 3 different bottle test arrangements (a-c).**

seed was on the bottom such that the crystal layer would have to grow mainly vertically upwards (Fig. 4.5.a-b). For the raw glycerol system, bottles were lying on the side such that the crystal layer would have to grow mainly horizontally (Fig. 4.5.c).

#### 4.2.7 Experiments on layer stability

Primary experiments on the stability of glycerol crystal layers during sweating were carried out in a setup rather similar to the MCF setup described above (Ch. 4.2.4). The main modification is a grid in the seed layer that is fixed to the cold finger to prevent slipping off of the melt, similar in effect to Sulzer's patented construction [Ste06]. However, with the difference that it does not, like Sulzer's, reach from the cooled surface to the next surface but is only situated close to the cold finger in the area in which the crystal layer will grow. Fig. 4.6 shows a photograph of the cold finger and the grid. The seed layer was applied exactly as in the abovementioned classic cold finger process with the grid being introduced into the centrifuge tube and, thus, into the seed layer.



**Figure 4.6. Cold finger with grid and parts of burst crystal layer. Crystal layer was grown from a complete seed layer in a melt containing glycerol and  $w_w = 3\%$  water at  $T_B = 15^\circ\text{C}$  and  $T_{CF}$  decreasing exponentially from  $T_{CF}(t = 0) = 5^\circ\text{C}$  to  $T_{CF}(t = 60\text{ h}) = -10^\circ\text{C}$ . After draining of the melt, sweating was started at  $T_B = T_{CF} = 15^\circ\text{C}$  until layer burst.**

The main crystal layer was then grown in a melt containing glycerol and  $w_w = 3\%$  water at  $T_B = 15^\circ\text{C}$  and  $T_{CF}$  decreasing exponentially from  $T_{CF}(t = 0) = 5^\circ\text{C}$  to  $T_{CF}(t = 60\text{ h}) = -10^\circ\text{C}$ . The layers were then subjected either to a conventional sweating procedure or an alternative post treatment. In the first case the temperature of both the cold finger and beaker was held at  $T_B = T_{CF} = 15^\circ\text{C}$ , 4 K below the melting temperature of pure glycerol and 4 K above the melting temperature of the initial

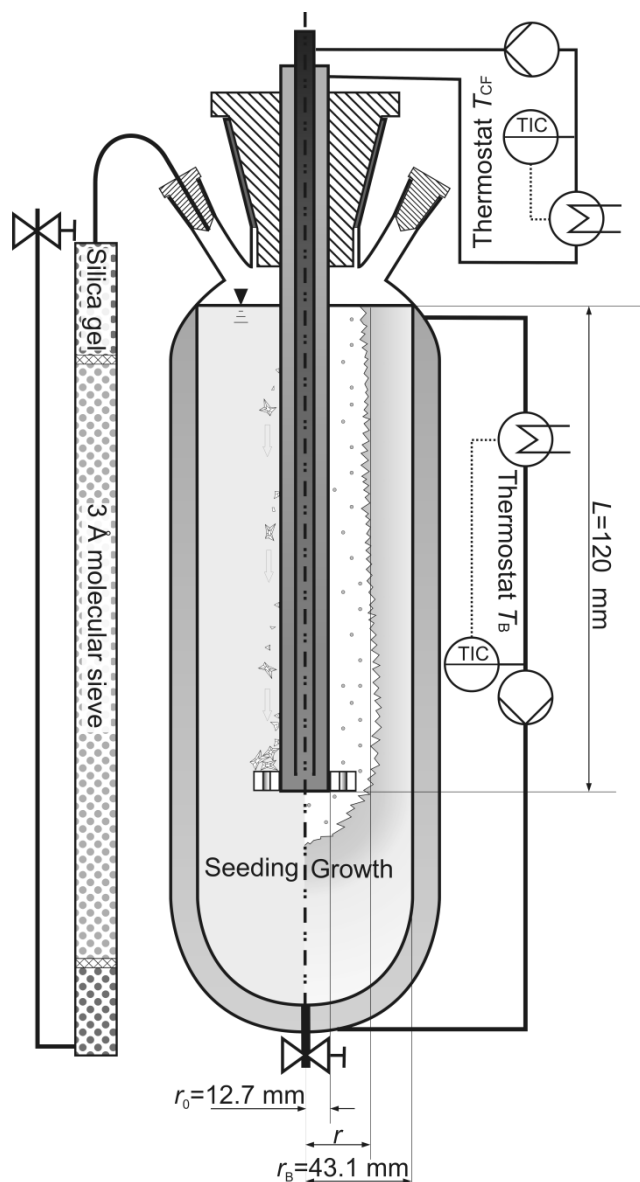
melt. In the latter case the temperature of the cold finger was  $T_{CF} = 10\text{ }^{\circ}\text{C}$  and that of the beaker  $T_B = 70\text{ }^{\circ}\text{C}$ . It was observed whether or not the crystal layer burst.

#### 4.2.8 Static cold finger setup (SCF)

Static layer crystallization experiments were carried out in a cold finger setup depicted in Fig. 4.7. In contrast to the MCF, this setup allowed post treatment and operation under dry atmosphere. The possibility of using a complete seed layer, direct measurement of the layer thickness, as well as stirring was foregone in this setup.

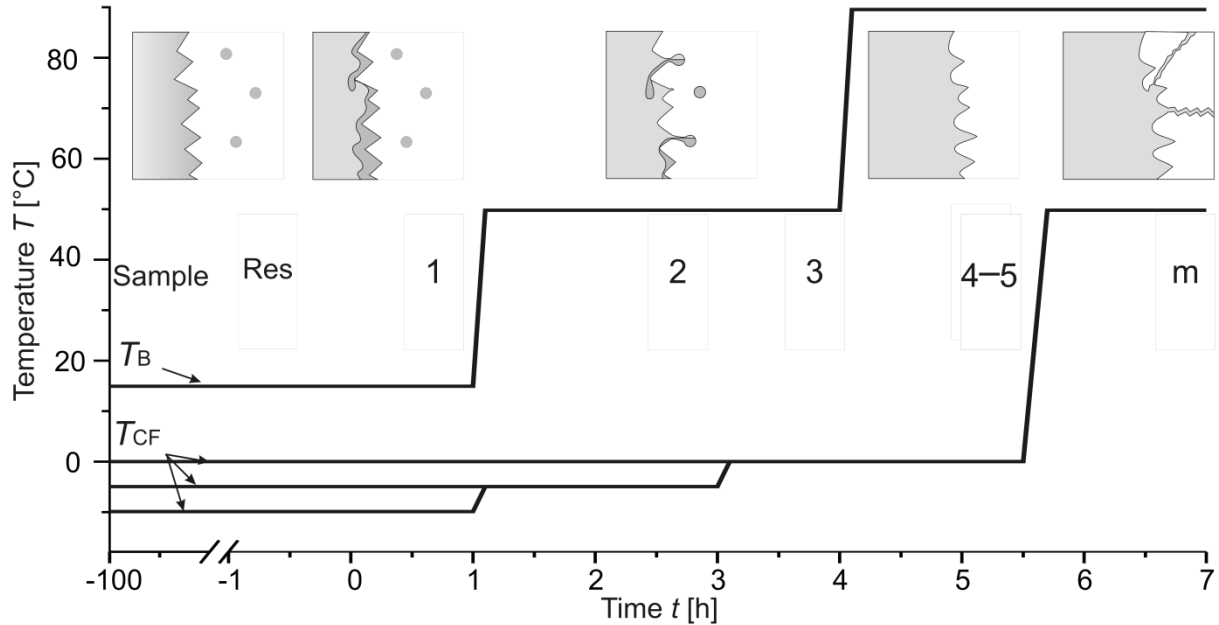
Melt and seed crystals entered the beaker through a conically tapered joint at the top. A stopcock at the bottom allowed draining of residual melt and molten product. An additional air valve was opened during filling and draining for the purpose of pressure compensation. To prevent water from coming into melt and crystals, the air that entered the beaker during draining passed through a drying column. This was 0.56 m in length, of which 0.34 m were packed with  $3\text{ \AA}$  molecular sieve in 1 mm beads and 0.14 m with silica gel. During the crystallization and sweating step the system was sealed airtight towards the atmosphere, but the gas above the liquid remained in contact with the drying column.

On the bottom of the cold finger, a plate was perpendicularly attached to allow seed crystals to rest and to prevent the crystal layer from slipping off the cold finger during the post treatment. By means of a special syringe with a glass needle of 3 mm inner diameter, the seed, together with a small amount of pure glycerol, was located close to the cold finger. The seed crystals would then slowly sink along the cold finger while causing secondary nucleation and crystal growth.



**Figure 4.7.** Cold finger setup for quantitative experiments on separation success. The left side shows the seed crystals sinking during the seeding process, leaving nuclei at the cold finger. The right side shows the uneven crystal layer with liquid inclusions towards the end of the growth step.

In a first set of experiments, the initial melt consisted of glycerol and  $w_w = 3\%$  water. It was used without additive at 3 different temperatures and was mixed with BuOH ( $w_b = 20\%$  in the final mixture) for one experiment. Fig. 4.8 depicts the temperature-protocol for the crystallization and post treatment and marks the chronological position of the samples, together with sketches of the expected form of the crystal layer during the different stages of the experiment.



**Figure 4.8.** Temperature and sampling protocol for static cold finger experiments on glycerol with  $w_w = 3\%$ . The predicted reaction of the crystal layer is also shown. The timeline is only an approximation because the actual duration of the steps depends on the crystal layer's behaviour, as does the number of samples. During growth ( $t < 0$  h) the 3 different  $T_{CF}$  used in different experiments are shown.  $T_{CF}(t > 3$  h) and  $T_B$  were the same for all experiments.

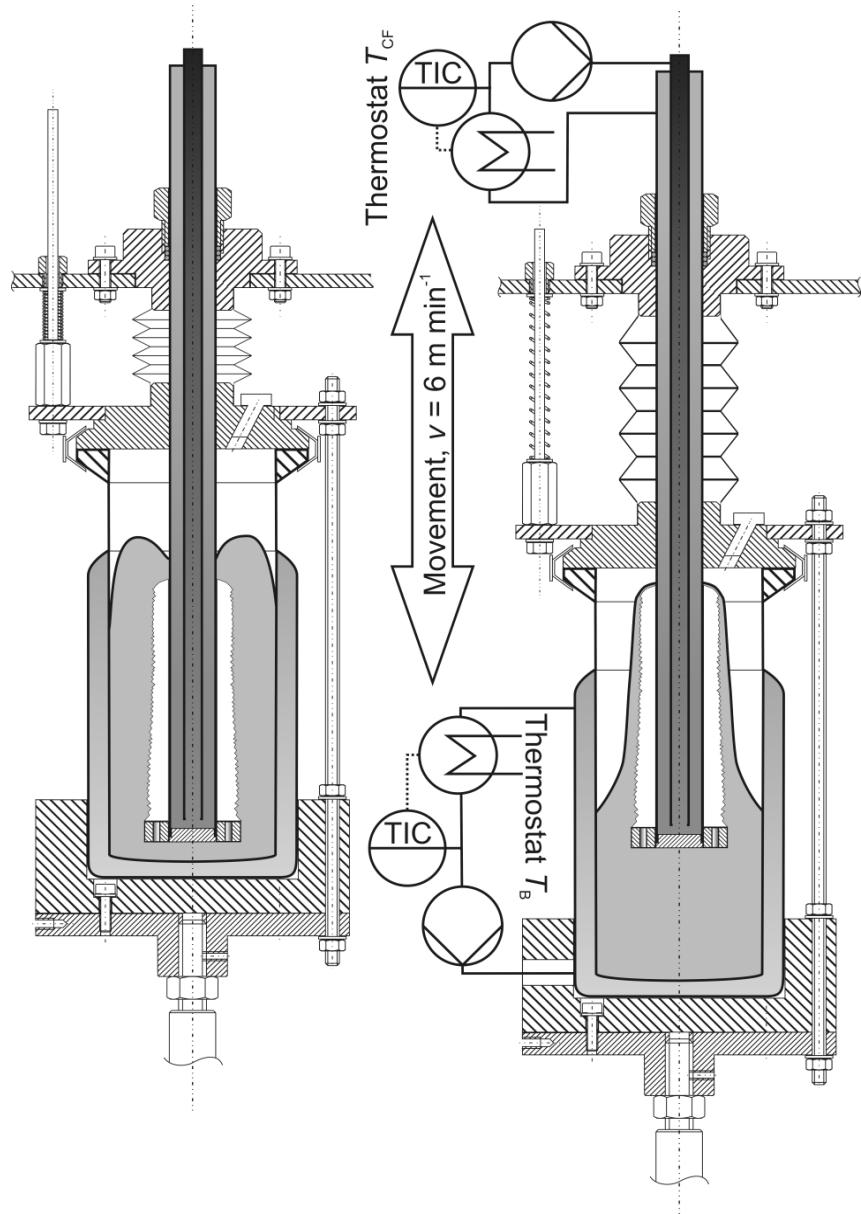
The protocol was the same for each experiment of the set with the exception of the cold finger temperature during the crystallization step. This temperature was for the 3 experiments without BuOH  $T_{CF} = -10^\circ\text{C}$ ,  $T_{CF} = -5^\circ\text{C}$  and  $T_{CF} = 0^\circ\text{C}$ , respectively, and  $T_{CF} = -10^\circ\text{C}$  for the experiment with use of BuOH. The crystal layer was grown for  $\Delta t = 110$  h at said cold finger temperatures and a beaker temperature of  $T_B = 15^\circ\text{C}$ . Thereafter the residual melt was drained. The melt adhering to the cold finger was then allowed to drip off at crystallization temperature. The dripping-off step was finished when the drops fell with a frequency of less than  $1 \text{ min}^{-1}$ . The dripping liquid is considered the first sample of the post treatment ( $m_1, x_{w,1}$ ). The temperature was then raised for the sweating step which was divided into 2 parts: First 2 h at cold finger temperature  $T_{CF} = -5^\circ\text{C}$  and then 1 h at  $T_{CF} = 0^\circ\text{C}$  with a beaker temperature  $T_B = 50^\circ\text{C}$  in both steps. The sweating liquids of these 2 steps were sampled separately and are considered samples 2 and 3 of the post treatment. The beaker temperature was then further raised to  $T_B = 60^\circ\text{C}$  to induce melting of the crystals. Samples were taken after 30 min and then after 1 h. If the crystal layers started to fall apart, one or both of these samples were omitted. This step can be considered either a sweating step with

a high product loss or a partial melting of the crystals, depending on whether gathered liquid is considered waste or product stream. The remaining crystal layer was molten at  $T_{CF} = 50\text{ °C}$  and  $T_B = 90\text{ °C}$  and was considered the last sample.

A second, larger set of experiments was executed on glycerol mixtures with  $w_w = 1\%$ . The temperature and sampling protocol was similar to the one depicted in Fig. 4.8 with the difference that number, durations and temperatures of the different steps were not held constant between experiments but were adjusted to the dripping behaviour of each melt and crystal layer. As in the MCF experiments, initial melts were composed using the residual melts of previous crystallization steps

#### 4.2.9 Translating beaker cold finger setup (TBCF)

This equipment was used to force stronger convection than possible by means of a magnetic stirrer. It consisted of a cold finger and double-walled beaker, in which the beaker moved up and down while the cold finger stayed fixed. Fig. 4.9 shows a drawing. When the beaker was at its higher position the cold finger was wetted with the melt while moving relative to it. Then, when the beaker moved to its lower position, the cold finger left the melt and the adhering melt could flow down. When the beaker was held in its upper position by the viscosity of the melt, it was forced down by springs attached to it and the frame. Filling, seeding, analytics and growth rate evaluation in this setup worked



**Figure 4.9. Setup with translational movement of the beaker and fixed cold finger for the purpose of forcing strong convection in the melt.**

to it and the frame. Filling, seeding, analytics and growth rate evaluation in this setup worked

exactly as they did in the SCF. Other setups for strong forced convection, i.e. different setups in which the melt was pumped over a cooled surface, were tried. These are not described in detail here because they proved not to allow the performance of complete experiments. The critical factors are briefly discussed below (Ch. 5.2.9)

#### 4.2.10 Experiments on raw glycerol

The scope of the experiments with raw glycerol was to explore the possibilities of substituting parts of the presently common separation process by melt layer crystallization. Therefore, the distillation steps of the Lurgi process described above (Ch. 2.1.3, Fig. 2.5) were imitated by a common laboratory distillation unit consisting of round-bottom flasks for feed and distillate, and a distillation bridge with Liebig-cooler. Temperature and pressure were measured in the bottom flask. The resulting head and bottom products of the different steps should be fairly similar to the corresponding intermediate products in the Lurgi process. They were subjected to bottle tests or crystallization in the glass setup described above (Ch. 4.2.5) in order to evaluate the possibility of their processing by layer crystallization. Furthermore, enrichment of the BuOH with glycerol by LL-extraction out of the NaCl-in-glycerol-suspension of the bottom of the last distillation step (bottom glycerol) was investigated. The LL-extraction was performed by mixing BuOH and bottom glycerol in a Schott flask, shaking and allowing settling for several days before the upper phase was sampled by a syringe. Its BuOH content was evaporated and the residue tested for its glycerol content. The resulting overall workflow is shown in Fig. 4.10.

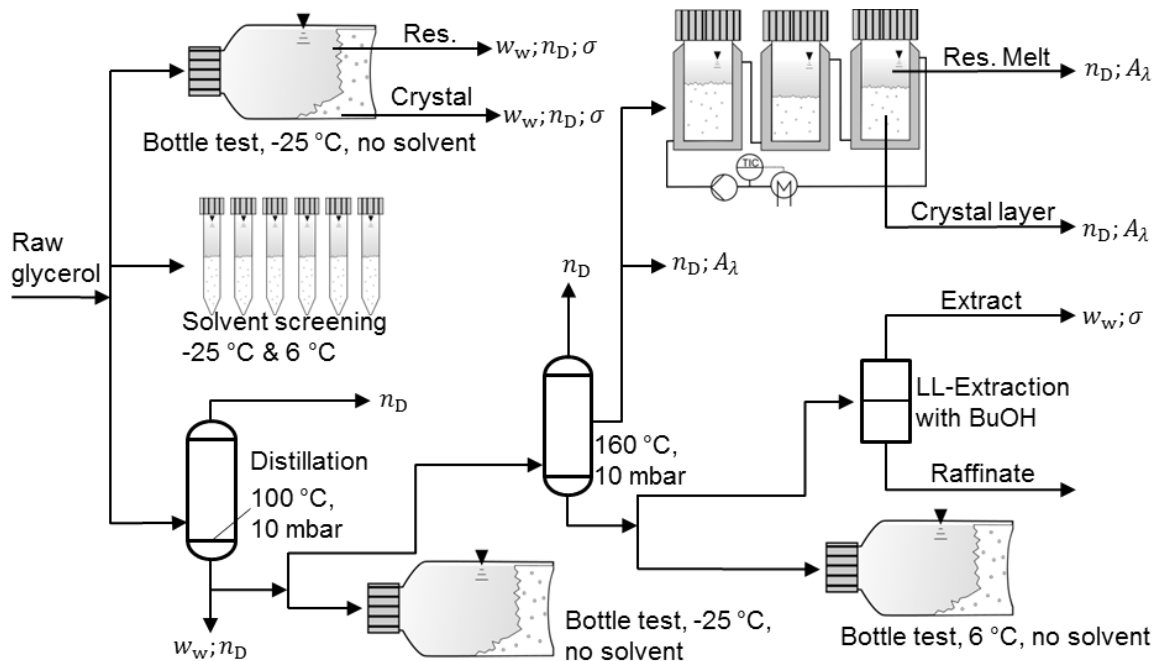


Figure 4.10. Workflow of the experiments with raw glycerol. Measurements are indicated by the symbols of the measured quantity: Water mass fraction  $w_w$  (Karl Fischer), refractive index  $n_D$ , electrical conductivity  $\sigma$ , and optical absorbance  $A_\lambda$ . If no measurement is indicated, only the visible phase separation behaviour was interpreted.

#### 4.2.11 Sweating of paraffin slack wax

Two different setups were used for the processing of slack wax. In both, the crystallization takes place in a double-walled glass tube with an outlet on the bottom. The lower part was filled with a random packing. Whenever a solvent was used, an intensive condenser of glass was attached to the top of the tube in such a manner that evaporated solvent was condensed and flowed back down into the tube.

In setup type I the glass tubes were actually dropping funnels and the random packings were saddle-type ceramic bodies.

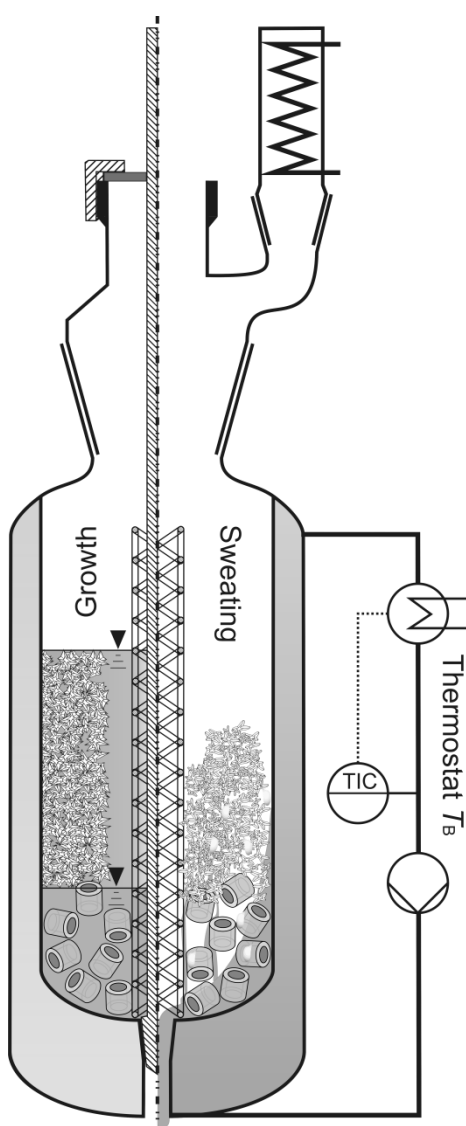


Figure 4.12. Sweating setup type II.



Figure 4.11. Sweating setup type I.

Fig. 4.11.a shows a photograph of such a tube with packings and attached condenser. 4 of these crystallizers were operated at the same time

and heated in series by the same thermostat. Their measured difference in temperature did not exceed 0.5 K. The length of the tubes differed, but the diameter and filling level was the same for all experiments.

Setup type II is shown in Fig. 4.12. It was larger in diameter and the packings were Raschig rings of glass. Instead of a stopcock, a stopper welded on a glass rod was immersed through the lid to block the outlet. When the lid and stopper were removed for draining, the removal of the rod left a channel in the centre, facilitating faster draining. To prevent packings from blocking re-immersion of the rod and stopper, a cylindrical steel grid was fixed and centred in the vessel by steel springs.

In both setups, the void of the packings was filled with water prior to crystallization. Then, the slack wax, molten in an oven, was poured into the crystallizer. In setup type I, experiments with and without solvent were conducted. The solvent was mixed into the wax prior to its entering the crystallizer. In setup type II, the solvent was mixed with the molten wax inside the crystallizer, the necessary agitation being

provided by cooking of the water. This process is discussed in further detail below (Chs. 5.1 & 6.5.1). After filling and mixing, the wax crystallized upon cooling of the beaker. Residual liquid was subsequently drained before the beaker was reheated. The resulting sweating liquid was gathered in different fractions, similar to the process described above for glycerol (cf. Fig. 4.8). Different temperature curves were compared. They are described together with the results below (Chs. 5.1 & 6.5.1).

### 4.3 Analytcs and data evaluation

#### 4.3.1 Analytcs

Water mass fraction  $w_w$  was measured by Karl Fischer titration using Mettler Toledo V30 and Mettler DL35 Volumetric Karl Fischer Titrators. BuOH mass fractions  $w_b$  of the ternary glycerol-water-BuOH mixtures were determined by evaporating BuOH in a flue at ambient temperature and collecting both the starting mass  $m_0$ , the residual mass  $m_1$  and the respective water mass fractions  $w_{w,0}$  and  $w_{w,1}$  of the sample (Fig. 4.13). The BuOH mass fraction  $w_{b,0}$  was calculated from the mass balance

$$w_{b,0} = \frac{m_1(1 - w_{w,1}) - m_0(1 - w_{w,0})}{m_0} \quad (4.1)$$

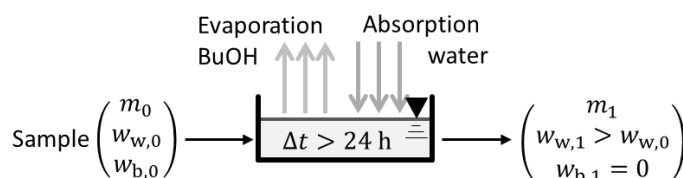
Viscosity  $\eta$  was measured using a Haake VT 550, a MV/DIN measuring geometry and a shear rate of  $20 \text{ s}^{-1}$ .

Electrical conductivity  $\sigma$  measurements were performed with a Knick Konduktometer 703, and a Knick 4-Pol-Meßzelle (4 pole

measuring cell) with a cell constant of  $112 \text{ m}^{-1}$ . Optical absorbance  $A_\lambda$  was measured by means of an analyticJena Specord 40 photometer. Dynamic scanning calorimetry (DSC) was performed on a Netzsch DSC 204 with a Netzsch TASC 414/4 controller using nitrogen as inert gas.

#### 4.3.2 Growth rate evaluation

Quantitative results on the performance of layer crystallization as separation technique require comparability of  $k(G)$ -dependencies acquired in different setups. In a data pair  $(k,G)$  with the overall distribution coefficient  $k$  and the average growth rate  $G$  for one experiment,  $k$  can often be trivially attained from the raw data while sensible averaging of  $G$  is a complicated matter but crucial to applicability of laboratory results to further processes.



**Figure 4.13. Gravimetric measurement of the BuOH mass fraction  $w_{b,0}$  by using Eq. 4.1 after weighing of masses  $m_0$  and  $m_1$  and Karl-Fischer titration for water mass fractions  $w_{w,0}$  and  $w_{w,1}$ .**



Usually in cold finger experiments, the growth rate is assumed to be constant over both time and space within one experiment. Additionally, the time needed for complete coverage of the cold finger surface is neglected. These are valid assumptions if a complete seed layer is provided at the start of each crystallization step and the undercooling near the crystal front is held constant by decreasing the cold-surface temperature. Both are realistic for many industrial processes. In this case, hereafter called case A, the layer thickness,  $s = \Delta r = r - r_0$ , after one growth step with duration  $t$ , cold finger radius  $r_0$  and growth rate  $G$  is

$$r - r_0 = G t \tag{4.A.1}$$

and the deposited mass  $m$  is, due to the cylindrical geometry, a 2<sup>nd</sup>-degree polynomial of that expression, so that the growth rate can be calculated from the polynomial root as

$$G = \frac{1}{t} \sqrt{\frac{m}{\pi h \rho_c} + r_0^2} - r_0. \tag{4.A.2}$$

Fig. 4.14 shows plots of the important functions for case A in comparison to the cases used in the present study, cases B and C, which are discussed below (this Ch.).

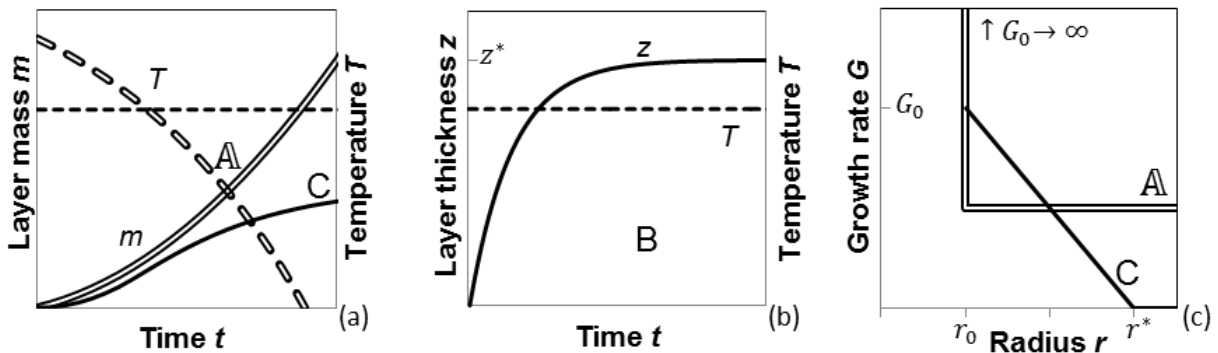


Figure 4.14. Assumptions for the calculation of the growth rate from the crystal mass  $m$  and crystallization time  $t$  in cold finger experiments (subfigure (a) and (c), cases A and C) and from the layer thickness  $z$  in the glass setup (subfigure (b) and case B). In (a) and (c), hollow lines show usual assumptions (case A) and solid lines show assumptions for the present cold-finger experiments (case C).

In neither the GL nor the SCF setups of this study, a constant growth rate is a valid assumption. In the SCF, immediate complete coverage of the cold surface is also not the case.

The calculation applied here is based on the following model: Every infinitesimal volume element of the crystal layer grows with a certain growth rate, depending on its local undercooling at that point in time at which it is a part of the crystal front, and incorporates a certain mass fraction of impurity, depending on said growth rate and other factors affecting

growth geometry and mass transport in the boundary layer. When the crystal layer is remolten and the liquid perfectly mixed, its impurity content is the average over all the volume elements and, therefore, correlates with the average growth rate of all the volume elements. Assuming a constant growth rate, as does Eq. 4.A.1, in calculating that average, as according to Eq. 4.A.2 would lead to an overrepresentation of the parts that grew slower, because they took relatively longer time to grow. Therefore, the relative growth rate as a function of space has to be calculated based on suitable assumptions first, before the absolute value of the average growth rate can be evaluated from the duration of the experiment and the deposited mass or grown layer thickness.

In the GL setup, the crystal layer only grows in one direction and the position of the crystal front can be visually observed over time. Given the linear liquidus line of glycerol-water mixtures in the relevant hypoeutectic concentration regime (water mass fraction  $w_w < 33\%$ ) [Lan25] and assuming a diffusion-controlled crystallization, a combination of McCabe's law and the mass balance using the measured distribution coefficient for the experiment gives a linear dependence

$$G(z) = \frac{dz(t)}{dt} = \frac{z^* - z(t)}{\tau}, \quad (4.B.1)$$

between growth rate,  $G$ , and the grown layer thickness,  $z(t)$ , with the height  $z^*$  at which saturation would be reached. The solution to this differential equation is, with  $z(t=0) = 0$ ,

$$z(t) = z^* \left(1 - e^{-\frac{t}{\tau}}\right), \quad (4.B.2)$$

which is fitted to the observed  $z(t)$ -data by variation of the time constant,  $\tau$ , and the saturation height,  $z^*$ . If the observed  $z(t)$ -points are too few to fit 2 parameters,  $z^*$  can also be calculated from the mass balance, leaving only one parameter to fit.

The average growth rate after duration  $t_1$  follows directly from Eq. 4.B.1 as

$$G = \frac{2z^* - z(t_1)}{2\tau}, \quad (4.B.3)$$

In the SCF, the growth rate has to be evaluated from the deposited mass  $m$  and duration  $t$  along with other known parameters but the thickness of the layer cannot be observed. It is only clear that its distribution around the cold finger at finite durations is not uniform and a cylindrical growth cannot be justified as approximation. Therefore, a set of more suitable

assumptions is used to model the layer geometry in relation to its total mass as a function of time. The assumptions made are still rather simple but are justified by the results.

Cylindrical coordinates with angular  $\varphi$ , radial  $r$  and vertical, i.e. axial,  $y$  are used.

All gradients in vertical  $y$ -direction are neglected and it is assumed that the seed line immediately covers the whole vertical span,  $L$ .

In radial direction, the layer grows from the cold finger towards the warmer beaker while the impurity concentration in the residual melt increases. These 2 effects lead to the existence of a saturation radius,  $r^*$ , that would be the radius of the layer after infinite duration. Assuming a linear profile of temperature in space ( $T(r) = T_0 + r(T_B - T_0)/(r_B - r_0)$ ) and a constant melt composition  $w_w = 0.5(w_w^{\text{Feed}} + w_w^{\text{Res}})$  the saturation radius can be approximated as

$$r^* = r_0 + \frac{T_g^* - \frac{dT^*}{dw_w} \frac{w_w^{\text{Feed}} - w_w^{\text{Res}}}{2} - T_0}{T_B - T_0} (r_B - r_0), \quad (4.C.1)$$

with the cold finger radius  $r_0$  inner beaker radius  $r_B$  cold finger and beaker temperatures  $T_0$  and  $T_B$ , respectively, the water mass fraction in the initial melt  $w_w^{\text{Feed}}$  and in the residual melt  $w_w^{\text{Res}}$  the melting temperature of pure glycerol  $T_g^* = 18.17 \text{ °C}$  [SDA90] and the slope of the liquidus line  $dT^*/dw_w = -192.24 \text{ K}$  for hypoeutectic mixtures, i.e.  $w_w < 0.33$  [Lan25]. The influence of BuOH on the melting temperature is neglected.

Between cold finger and saturation radius, a linear dependence of the growth rate on the radial position is assumed:

$$G(r) = G_0 \frac{r^* - r}{r^* - r_0}, \quad (4.C.2)$$

with  $G_0 := G(r = r_0)$ . The time  $t(\varphi, r)$  after which the crystal layer reaches a certain point  $(\varphi, r, y)$  is approximated by

$$t(\varphi, r) = \frac{r_0 \varphi}{G_0} + \int_{r_0}^r \frac{1}{G(r')} dr', \quad (4.C.3)$$

which is illustrated in Fig. 4.15.

The layer thickness  $r(t, \varphi) - r_0$  at time  $t$  and angle  $\varphi$  can be calculated by combining Eqs. 4.C.2-3 with the restriction that it cannot take negative values:

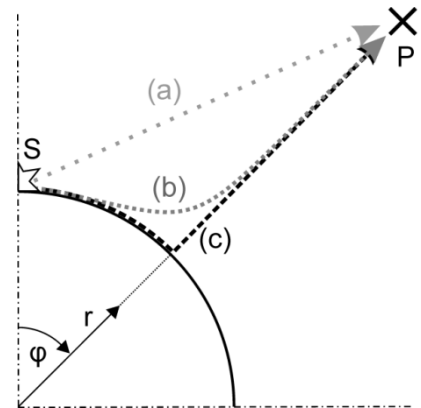


Figure 4.15. Coordinates  $\varphi$ ,  $r$  in horizontal cross section of cold finger with seed at point S and different paths for the crystal growth to reach point P: (a) shortest path, (b) fastest and, therefore, actual path, (c) approximation of fastest path made in this study.

$$r(\varphi, t) = \max\left(r_0, r^* - (r^* - r_0)e^{\frac{|\varphi|r_0 - G_0 t}{r^* - r_0}}\right). \quad (4.C.4)$$

The resulting layer geometry is plotted in Fig. 4.16 for variable growth time. The total deposited mass is given by

$$\begin{aligned} m(t) &= \int_{-\pi}^{\pi} \int_{r_0}^{r(\varphi, t)} \int_0^L r \rho_C dy dr d\varphi \\ &= \frac{L\rho_C}{2} \int_{-\pi}^{\pi} \left( \max\left(r_0, r^* - (r^* - r_0)e^{\frac{|\varphi|r_0 - G_0 t}{r^* - r_0}}\right) \right)^2 - r_0^2 d\varphi. \end{aligned} \quad (4.C.5)$$

It is assumed that the density of the crystal layer is the density of pure crystalline glycerol at 0 °C,  $\rho_C = 1341 \text{ kg m}^{-3}$  [Bla04]. Eq. 4.C.5 is an implicit expression for  $G_0 = f(m, t)$ , i.e. the absolute growth rate level as a function of total deposited mass and duration. It is solved by a generalized reduced gradient algorithm after discretisation of  $\varphi$ . The so gathered  $G_0$  is then used with Eq. 4.C.2. and the layer geometry  $r(\varphi)$  from Eq. 4.C.4 to calculate the average growth rate  $G$ :

$$G = \frac{G_0}{2} \left( 1 + \frac{1}{2\pi} \int_{-\pi}^{\pi} \frac{r^* - r(\varphi)}{r^* - r_0} d\varphi \right), \quad (4.C.6)$$

which is simply the arithmetic average of  $G(r)$  and  $G_0$  averaged over all  $r(\varphi)$ .

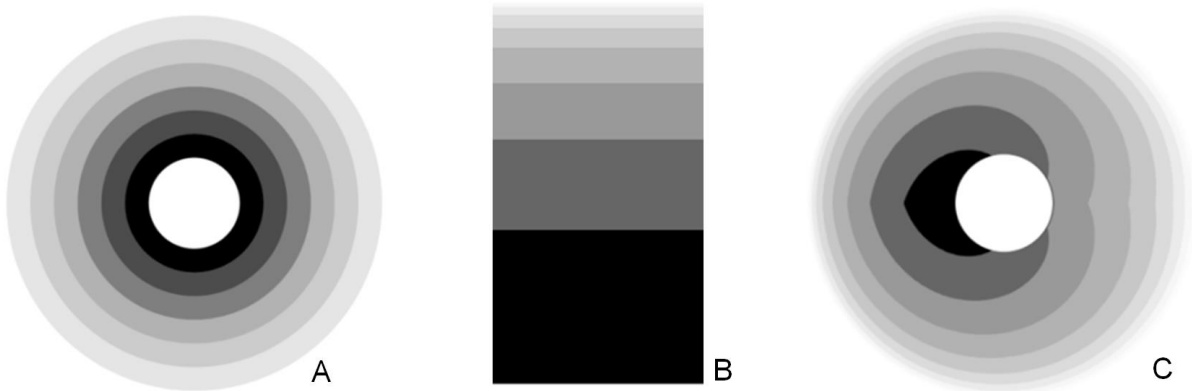


Figure 4.16. Assumed geometry of crystal layer for Cases A, B, and C after shorter time of growth (darker) and longer growth (lighter).

### 4.3.3 Processing of DSC curves for the analysis of paraffin

The separation task of layer crystallization and sweating on paraffin slack waxes is the removal of oil. For the separation to be successful, the gathered fractions should show large differences in their oil content. A quantitative evaluation of the separation success would,

therefore, require a determination of the oil content. Standard measurement procedures as described in DIN 51531 (English version ASTM D721) are very expensive and of rather low accuracy, making it common practice in both industry and research to first evaluate qualitatively whether or not a certain technique shows promising separation success and only move forward to the standard oil content measurement if that is the case. The primary results are usually obtained via the melting or crystallization behaviour of the fractions. A common method in the industry is the determination of the congealing point, e.g. described in ASTM D938. In laboratories, dynamic scanning calorimetry (DSC) has been used, with some efforts even being made to use DSC as direct measurement of the oil content [Gia73] or the chain length distribution [Cot10]. In the present study, DSC-curves are used for the first qualitative evaluation of the separation success. A direct determination of the oil content is not going to be necessary.

From each fraction, samples of 6 - 13 mg were taken and each of these samples was subjected to multiple DSC measurements. For long curves, the samples were cooled to -40 °C, then heated to 120 °C and then cooled to -40°C again. Heating and cooling rates of  $dT/dt = \pm 5$  K/min and  $dT/dt = \pm 1$  K/min were used. For short curves, the sample was heated from 40 °C to 80 °C and cooled back to 40 °C at  $dT/dt = \pm 5$  K/min. Only the long curves allowed determination of the peak area  $A$  but their measurement is very time-consuming. The short curves give the peak temperature  $T_{\max}$ .

To make curves comparable, the actual rate of temperature change  $dT/dt$  was recorded along with the DSC signal  $\dot{q}_{\text{DSC}}$ . Fig. 4.17 gives an example. The product of these 2

$$E_{\text{P+BL}} = \dot{q}_{\text{DSC}} \frac{dT}{dt} \quad (4.2)$$

should be equal to the heat capacity  $c_p$  at temperatures at which no phase change takes place. This part of the  $E_{\text{P+BL}}$  curve is linearly fitted and extrapolated into the phase change temperature interval to construct the linear baseline  $E_{\text{BL}}$ . Figs. 4.18-19 show the procedure. The corrected DSC curve  $E$  is obtained as

$$E = E_{\text{P+BL}} - E_{\text{BL}}. \quad (4.3)$$

The assumption of the baseline remaining linear over a temperature interval of more than 120 K is only sensible in the present case because the accuracy of the used DSC diminishes at temperatures below  $-20\text{ }^{\circ}\text{C}$ . A second node for the construction of a curved baseline can, therefore, not be found with sensible reliability. To compensate the inaccuracy of this baseline construction as well as of the measurement error, negative values of  $E$  below an intersection of  $E_{P+BL}$  and baseline  $E_{BL}$  are cut out when calculating the peak area  $A$ , as are values of  $E$  below a minimum at lower temperatures than the O-DO temperature (cf. Fig. 4.20). This procedure is discussed in further detail below (Ch. 5.1). As is known from the literature [Dir02], DSC-curves of paraffin slack waxes are a superposition of different peaks, including the solid-liquid (S-L) and an order-disorder (O-DO) phase change. The different peaks are separated numerically by the method illustrated in Fig. 4.20. Starting from the right hand side (higher temperatures), the onset, inflection and peak temperature are found by the common methods. The first inflection point to the left of the rightmost peak is found from the local  $\min(dE/dT)$  and this tangent is elongated to  $E = 0\text{ J kg}^{-1}\text{ K}^{-1}$  to give the virtual onset of the S-L-peak (Fig. 4.20.a). The values of that tangent

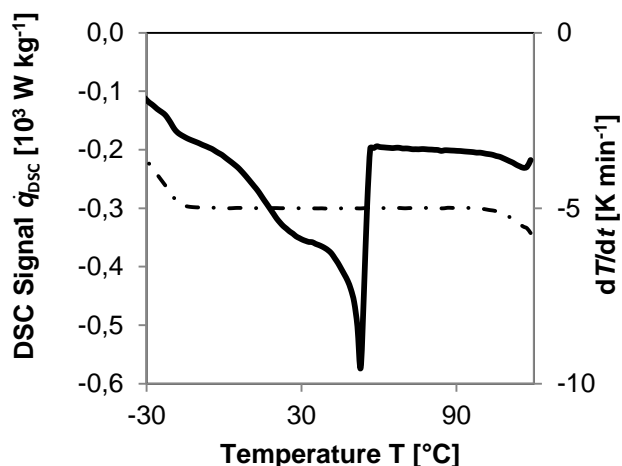


Figure 4.17. Raw data of a DSC long curve at a cooling rate of  $-5\text{ K/min}$ . The shown  $dT/dt$  (broken line) is the actual rate of temperature change.

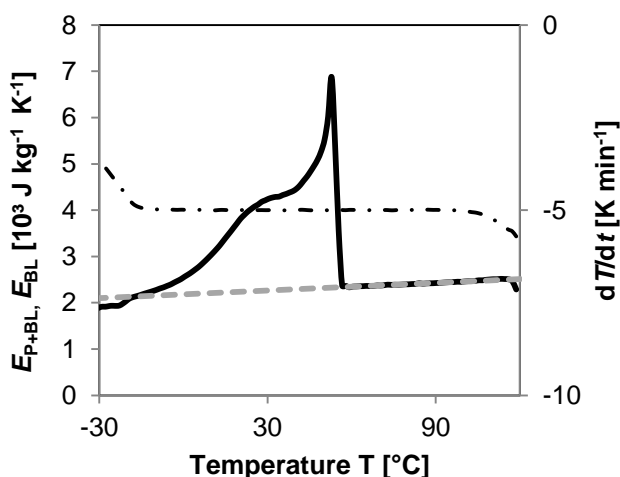


Figure 4.18. Example for the construction of the baseline by linear extrapolation from the temperature interval of completely molten sample.

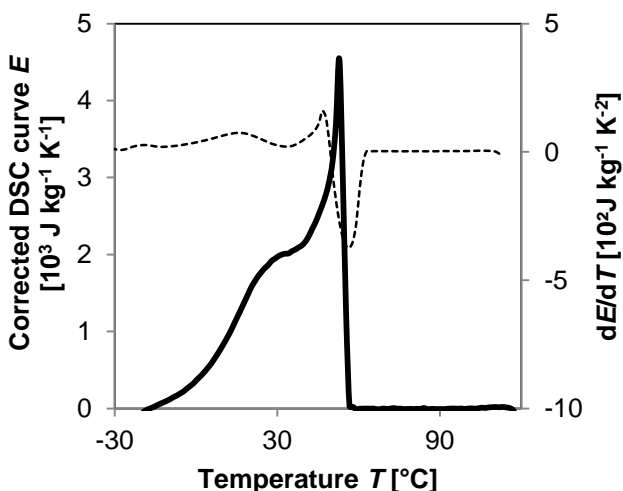


Figure 4.19. The resulting peak curve, after deduction of the baseline, and its derivative.

and the rest of the S-L-peak are subtracted from the original curve and the remaining curve is subjected to the same procedure (Fig. 4.20.b). After the second iteration, 3 curves are obtained: the S-L-peak, the O-DO-peak and a third peak at low temperatures, which is mainly an artefact of the measurement (Fig. 4.20.c).

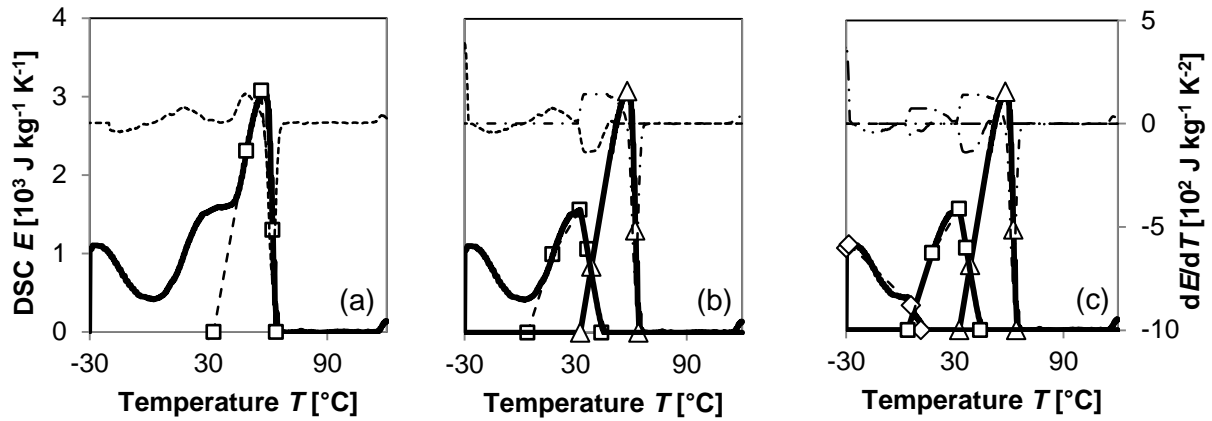


Figure 4.20. Numerical separation of the peaks in the DSC-curve  $E$  (solid lines) using the onset, inflection, and peak points (symbols), the tangents at inflection (dashed lines) and the derivative  $dE/dT$  (other broken lines).

## 5 Results

### 5.1 Paraffin

#### 5.1.1 Influence of the crystallization kinetics on the melting behaviour

The long curves ( $T_{\max} - T_{\min} \geq 120$  K) acquired upon heating of mmo showed a dependence on the thermal history of the sample. When heating and cooling the same sample multiple times with different cooling/heating rates  $dT/dE$ , the O-DO-peak and melting peak of heating following a fast cooling had a strong tendency to merge, giving a DSC curve like the one in Fig. 5.1.a. On the other hand, subsequent to slow cooling the DSC curve upon heating always displayed a local minimum between the O-DO and melting peaks. An example is given in Fig. 5.1.b. This observation was made on a total of 30 long measurements carried out on 12 samples from 6 slightly different fractions of the used mmo. The fractions were obtained in setup II. 5 measurements followed crystallization in the DSC at 1 K/min (2 cases) or were the first measurement on the sample (3 cases). All 5 showed the local minimum like in Fig. 5.1.b. 25 long heating curves were preceded by a fast cooling in the DSC at 5 K/min. In 23 cases (92%) the peaks merged and the minima in the remaining 2 cases were not as strong, the trenches not as broad as in the curves following slow cooling. One of these cases is shown in Fig. 5.1.c. The merging of the peaks occurred at both investigated heating rates. The thermal history prior to the last cooling did not show any clear influence on the curve, neither did the differences between the samples.

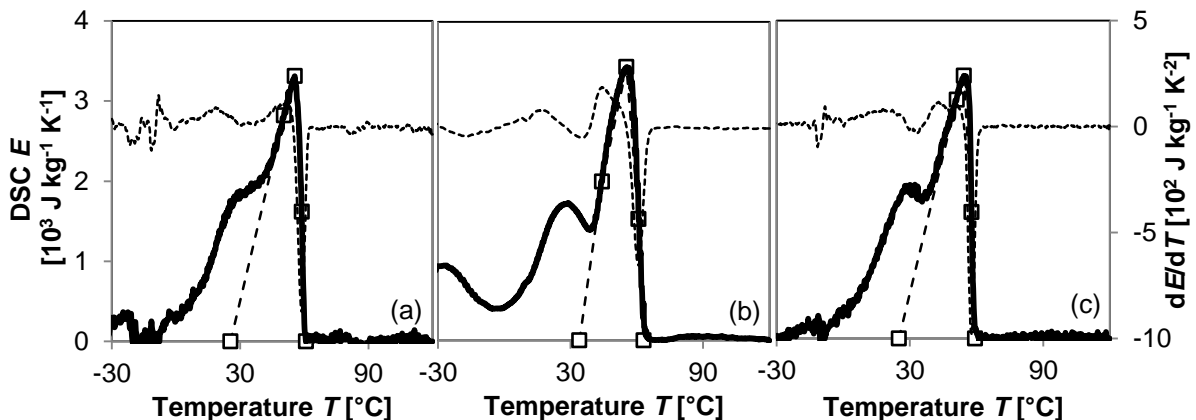


Figure 5.1. Examples of different shapes of DSC melting curves. (a) no separation of O-DO and S-L peaks, little signal at low temperatures, (b) separation of peaks and strong signal at low  $T$ , (c) weak separation of peaks and little signal at low  $T$ .

These results show that the cooling rate difference between 1 K/min and 5 K/min does influence the structure of the deposited solid matter and change its thermal behaviour. However, no sign of a change from a predominantly crystalline to a mostly amorphous phase or a change in the dominating polymorph is given: The position of the melting peak did not

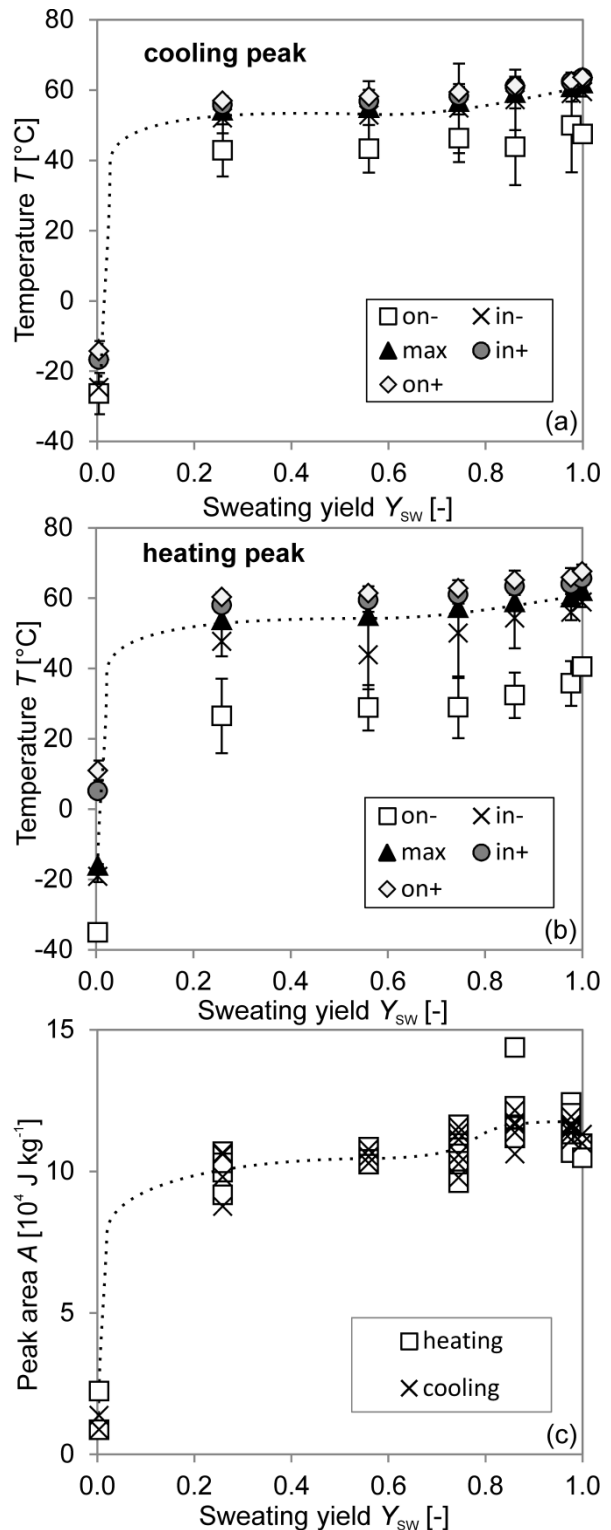


shift considerably with the merging of the peaks. The shape of the numerically isolated melting peak did also not change significantly.

### 5.1.2 Thermodynamic limits to the deoiling of mmo slack wax in layer crystallization

It is known that the oil content of a slack wax influences the position of the melting and crystallization peak as well as their peak areas. If the different sweating fractions of a slack wax show a significant difference neither in the position nor the area of the melting or crystallization peak, this is a very strong indicator that no significant deoiling has taken place during the sweating. The position of the peak can be quantified by its onset, inflection and peak temperatures. A quantity that describes the fraction size and its position in the process is the sweating yield  $Y_{sw}$  that is reached after the fraction is taken.

Fig. 5.2 gives all the position parameters and areas of the crystallization and melting peaks for all fractions gathered in one sweating process in setup II. The first fraction is the residual melt that was drained at 2 °C. After evaporation of the water and solvent it came with, its mass accounted for 0.3% of the total recovered mmo mass, hence its position at  $Y_{sw} = 0.003$  in the diagrams. This residual melt clearly had a high oil content, as can be seen from the low peak temperatures and peak areas. Its mass is, however, very little in comparison to the approximately  $w_o = 20\%$  oil content in the feed. The rest of the fractions show little differences in the peak temperatures and areas. A trend of increasing both with increasing sweating yield is to be



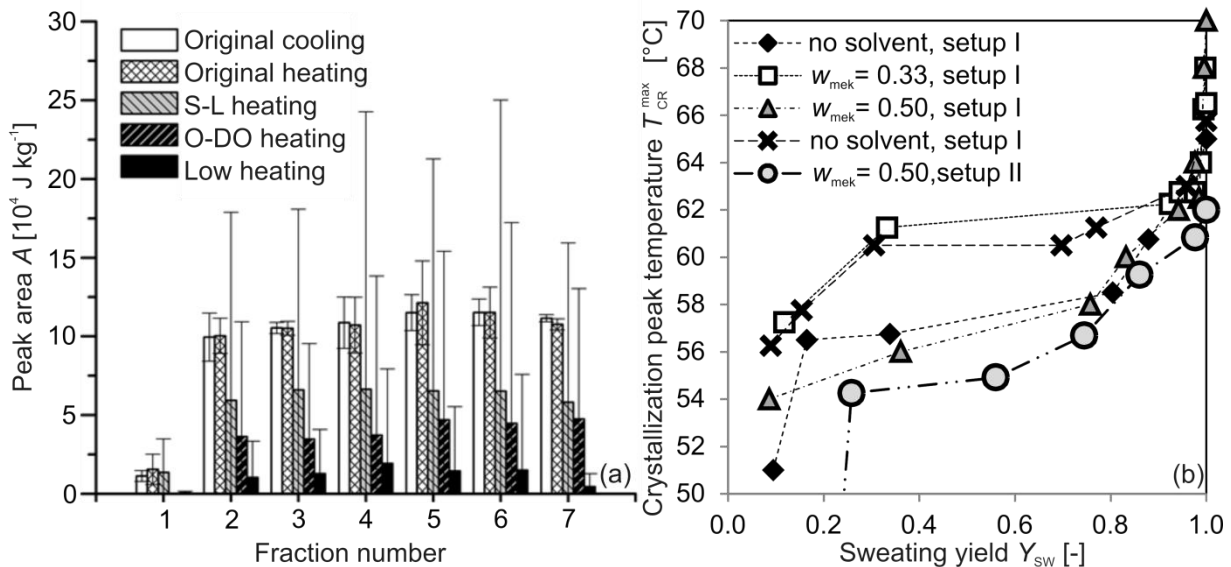
**Figure 5.2. Characteristic temperatures and areas of DSC curves of different fractions obtained in setup II. All data on the ordinates represent the measurement for the respective fraction (not an average of multiple fractions) but are drawn vs. the yield that is reached by combining the respective and all previous fractions. Abbreviations: 'on-': lower onset, 'in-': lower inflection, 'max': peak, 'in+': upper inflection, 'on+': upper onset.**

## Results

expected as the fractions at higher sweating yield are molten and gathered at higher temperature. However, the differences measured in this experiment range in the same order of magnitude as the scatter of the data.

Fig. 5.3.a shows the peak areas of the numerically separated DSC-curve parts along with the complete peak areas for the same experiment. As also evident from Fig. 5.2.c, the total peak areas are the same for crystallization and melting peaks, which is physically necessary and, thus, shows that the chosen method of compensating the errors in measurement and baseline construction for low temperatures were successful. The areas of the separated peaks show much more deviation and even less of a trend than the complete peaks. So there is no evidence of promising deoiling to be found here, either.

The comparison between the setups is done by means of the peak temperatures only, because they showed the least scatter in Fig. 5.2. It is plotted in Fig. 5.3.b in the same manner for 4 experiments in setup I along with the data from setup II.



**Figure 5.3. (a) Areas of the DSC peaks and their parts after numerical separation (cf. Ch. 4.3.3). Abbreviations: 'orig': original, complete DSC-curve; 'S-L' solid-liquid transformation peak, 'O-DO': order-disorder transformation peak, 'low' part of the curve left after deduction of S-L, and O-DO peaks. (b) Peak temperature of the DSC curve of cooling for the fractions obtained in different setups and with and without solvent. All data on the ordinates represent the measurement for the respective fraction (not an average of multiple fractions) but are drawn vs. the yield that is reached by combining the respective and all previous fractions.**

When zooming in on the temperature axis, all the curves show an inverse-error-function-like shape with low slope over a large, middle, part of the  $Y$ -interval, and higher slopes towards the ends. This means that the greater part of the mass is gathered in fractions with thermal behaviour similar amongst the fractions and similar to the feed. A linear or even error-function-like behaviour would be more promising. Furthermore, the differences in crystallization temperatures within each curve do not exceed the difference between curves resulting from experiments under the same conditions. In conclusion, the thermal behaviour

of the fractions shows no sign of successful deoiling during the investigated layer crystallization and deoiling process

### 5.1.3 Photometric evidence of separation of paraffin from non-paraffinic impurity

The major part of the used mmo slack wax consisted of n-alkanes, but other impurities are also present. While it was shown above (Ch. 5.1.2) that the separation of oil and wax, i.e. longer and shorter n-alkanes, respectively, failed in all investigated layer crystallization processes, a separation of the main component from some other impurities did still take place. This is evident from the change in opacity and colour of the fractions. Commercial paraffin waxes are white and opaque as solid and clear and colourless in the liquid state. The raw mmo slack wax of the present study is, like many slack waxes, a yellowish light brown solid that turned dark brown without gaining transparency upon melting. The liquid's absorbance of light in the complete visible wavelength range and near infrared until  $\lambda=1100$  nm is given in Fig. 5.4.a along with representative curves for fractions obtained in the separation experiments. These show a lower absorbance which is a clear sign that the concentration of some light-absorbing impurity has decreased during the separation. The degree to which this separation has happened can be expressed in the relative absorbance  $A_\lambda/A_\lambda^{\text{Feed}}$ , which is drawn vs. the wavelength in Fig. 5.4.b.

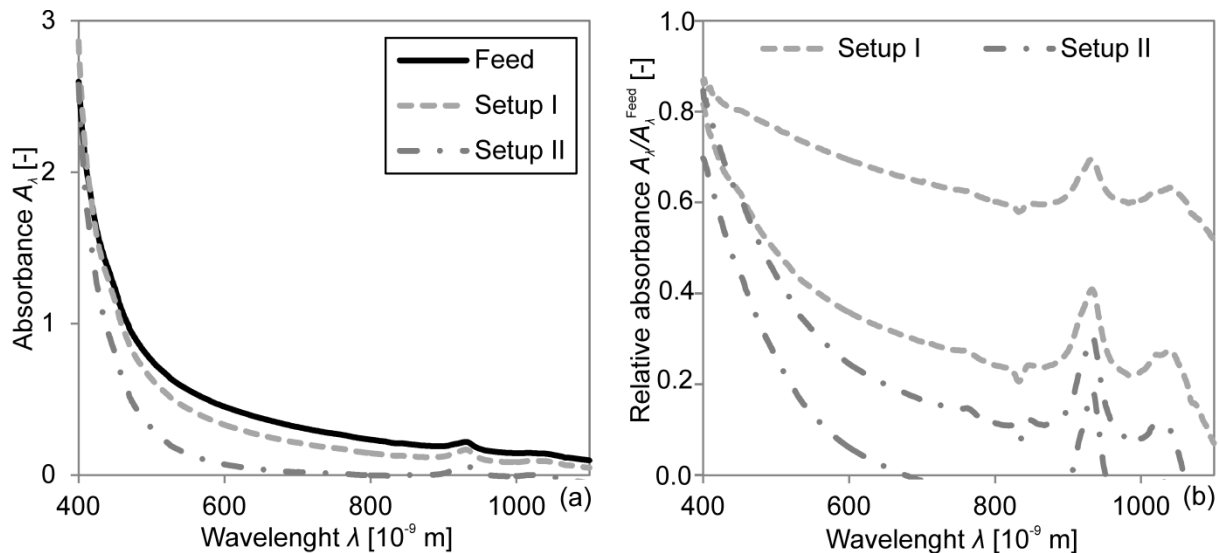


Figure 5.4. (a) Absorbance as a function of the wavelength for the feed and fractions attained in the different setups. The feed curve is an average of 4 samples. The curves for the fractions are no averages but show the absorbance of those actual fractions which were closest to the average of all fractions. (b) Absorbance of the fractions divided by the absorbance of the feed drawn vs the growth rate. For each setup the fraction with the lowest and the one with the highest absorption level are plotted.

## Results

The absorbance is different for different fractions obtained in the same setup. In Fig. 5.4.b the highest and lowest curve for each setup is given while in Fig. 5.4.a a curve in the middle of the array of curves is chosen. Fig. 5.5 shows the relative absorbance averaged over all wavelengths for each fraction. For non-solvent-aided experiments, a slight increase towards the fractions obtained at the end of sweating is apparent. This means that the fractions melting at higher temperatures carry more of the light-absorbing impurity. For solvent-aided experiments, such a trend is not given. Within setup I, the solvent-aiding did not decrease the absorbance in comparison to

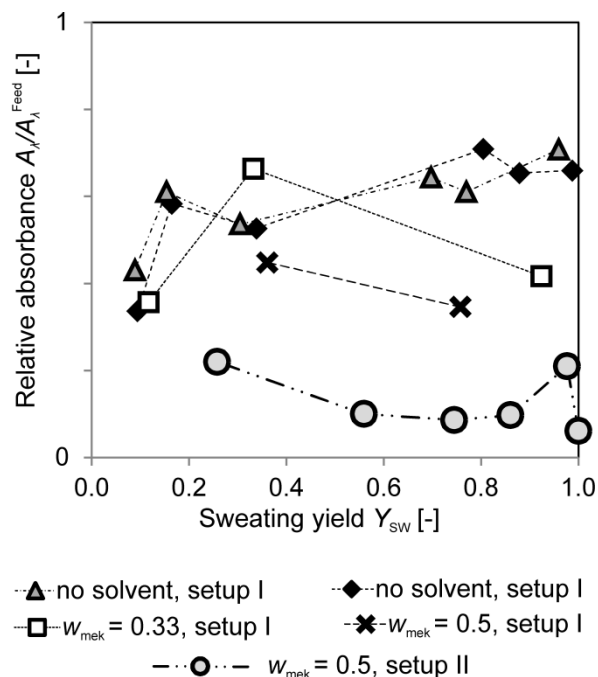


Figure 5.5. Relative absorbance, averaged over  $400 \text{ nm} < \lambda < 1100 \text{ nm}$  for each fraction, drawn versus the sweating yield obtained after that fraction.

crystallization and sweating without solvent. The procedure in setup II did, however, decrease the absorbance much stronger. While the exact nature of the impurity is not known, it is clear that it is separated better by the slower process in setup II, changing the colour from dark brown in the feed to yellow in the clear liquid of the product. The impurity partly came out in the oil fraction gathered at  $2 \text{ }^\circ\text{C}$ , which was brown but transparent and could not be measured by the photometer because its volume was too low. The other part of the impurity remained stuck to the Raschig rings in the setup. This makes clear that some kinetic hindrances to separation during crystallization and sweating are present in setup I but are largely done away with in setup II. The fact that the process in setup II was still not able to yield fractions of different thermal properties shows that it is the thermodynamic equilibrium of the multicomponent system mmo without or with little solvent which do not support the deoiling.

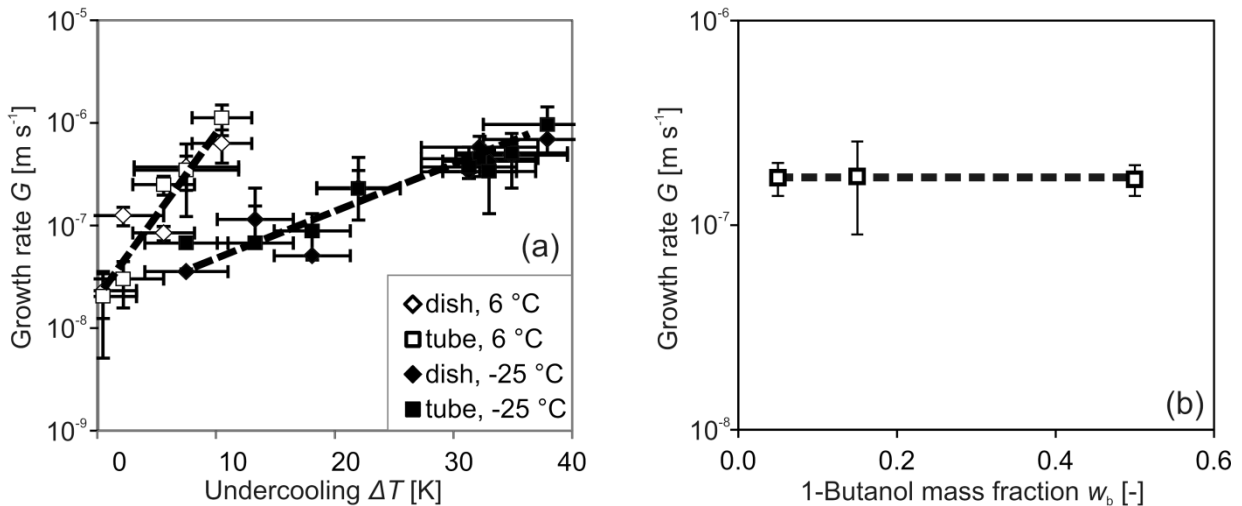
## 5.2 System glycerol-water

### 5.2.1 Glycerol seed production

The extremely slow heating from liquid air temperature yielded glycerol crystals in 2 of 2 samples of glycerol with  $w_w = 0.2\%$  water and in 1 of 2 samples of glycerol with  $w_w = 0.7\%$ . 3 samples with  $w_w \geq 10\%$  were still amorphous after the procedure. This suggests a strong nucleation-inhibiting effect of even small amounts of water. BuOH did not show this effect when a sample with  $w_b = 50\%$  revealed acicular crystals after the same process.

### 5.2.2 Seed crystal growth rate and viscosity

The growth rates of seed crystals in flasks and dishes gives a first insight into the growth behaviour of the system glycerol-water. Fig. 5.6.a shows an increasing growth rate with increasing undercooling for both temperatures investigated, as expected.  $-25\text{ }^{\circ}\text{C}$  is the freezing point of a mixture containing  $w_w = 22.5\%$  water and at  $6\text{ }^{\circ}\text{C}$ , the water mass fraction is  $w_w = 6\%$  when  $\Delta T = 0\text{ K}$ . The data points for  $-25\text{ }^{\circ}\text{C}$  do, therefore, represent mixtures with higher water contents while the curve for  $6\text{ }^{\circ}\text{C}$  represents lower water contents at equal undercooling.



**Figure 5.6. (a) Crystal growth rates of glycerol from aqueous mixtures at 2 different temperatures. At constant undercooling, the hollow symbols depict lower water contents (6 wt% at  $\Delta T = 0\text{ K}$ ) and the solid symbols represent higher water contents (22,5 wt% at  $\Delta T = 0\text{ K}$ ). The error bars represent maximum errors for 3 to 5 measurements per data point. The error in the undercooling is the sum of the maximum deviation in freezing temperature and actual temperature. (b) Crystal growth rates of binary glycerol mixtures containing different amounts of BuOH at 279 K. The trend lines are only a guide to the eye.**

It can be seen that a higher water content slows down the growth rate. That means that at higher water content a larger undercooling is necessary to achieve the same growth rate. This effect is increasing with increasing growth rate. In contrast to this effect of water, Fig. 5.6.b shows that the growth rates of glycerol crystals from binary mixtures with  $5\% < w_b < 50\%$  BuOH are equal at  $6\text{ }^{\circ}\text{C}$ . This means that the crystal growth rate of glycerol is not influenced by the BuOH content. If the addition of BuOH would change the freezing point of the mixture, this growth rate would stay the same for different  $\Delta T$ . Such behaviour, a plateau in the dependence of crystal growth rate on undercooling, occurs for many compounds [Mat69]. Pure glycerol, however, is an exception with its relatively narrow peak of the growth rate at an undercooling of  $\Delta T \approx 24\text{ K}$  [Lan25, Gün56]. The results suggest, therefore, that BuOH decreases the freezing point of glycerol only little or not at all. That is under the assumption, that influence on the  $G(\Delta T)$ -dependence is only of quantitative nature. While the BuOH contents of  $w_b < 50\%$  do not change the growth rate, they change the viscosity of the melt by orders of magnitude as can be seen in Fig. 5.7. Here, an important difference between BuOH and water can be found. Taking the freezing point depression into

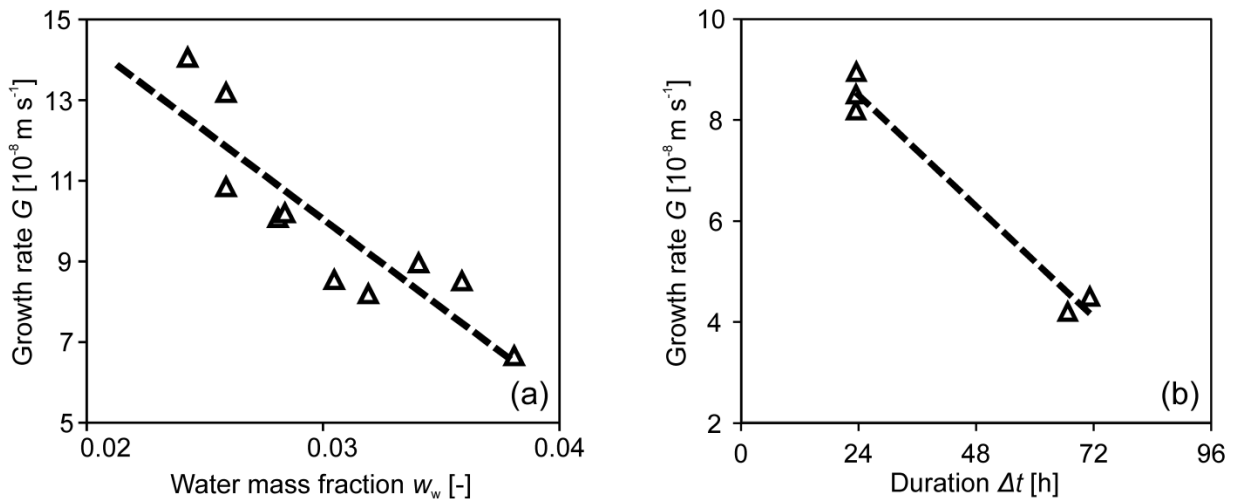
account, the addition of water cannot help lower the viscosity, while the BuOH can. That is a first important indication for it to be a suitable solvent.

### 5.2.3 Growth in the MCF setup without solvent-aiding

To evaluate the effect of an additional solvent on the layer crystallization, it has to be compared to other possibilities of changing the growth rate and distribution coefficient.

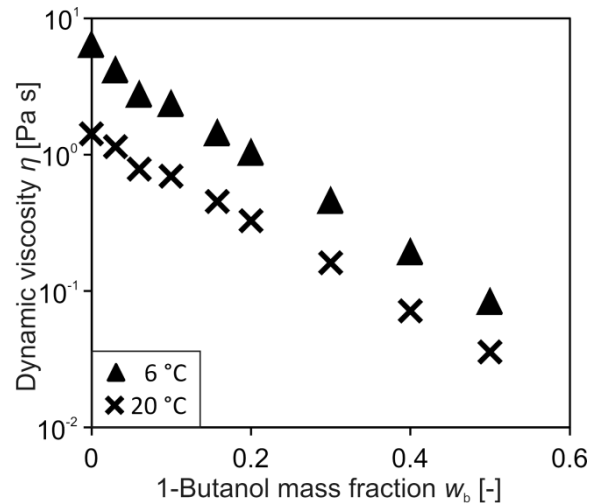
Therefore, the separation performance from the binary melt is to be investigated first. The complete comparison between crystallization with and without solvent will be reported for each setup separately in the results chapter (Ch. 5) with global conclusions to be drawn below in the discussion part (Ch. 6). The present and the following subsection (Chs. 5.2.3-4) concern results from the MCF only.

Fig. 5.8.a shows the dependence of layer growth rate on the water content if all other parameters (i.e. beaker and cold finger temperatures as well as stirring rate and duration of the experiment) are held constant. As expected, the growth rate decreases with increasing water content because the undercooling is decreased by the drop in the freezing points according to the eutectic phase diagram.



**Figure 5.8.** (a) Growth rates in cold finger experiments drawn vs. the initial water content of the melt. Cold finger temperature  $T_{CF} = -5\text{ }^{\circ}\text{C}$ , beaker temperature  $T_B = 15\text{ }^{\circ}\text{C}$ , duration  $\Delta t = 24\text{ h}$ , stirring rate  $n = 100\text{ min}^{-1}$ . (b) Growth rate in cold finger experiments drawn vs. the duration of the experiment.  $T_{CF} = -5\text{ }^{\circ}\text{C}$ ,  $T_B = 15\text{ }^{\circ}\text{C}$ , initial water content of the melt  $w_{w,0} = 0.031\text{-}0.035$ ,  $n = 100\text{ min}^{-1}$ .

Fig. 5.8.b shows a lower growth rate for longer experiments. Because the temperature of the cold finger was held constant over the course of the experiment, the insulation of the crystal

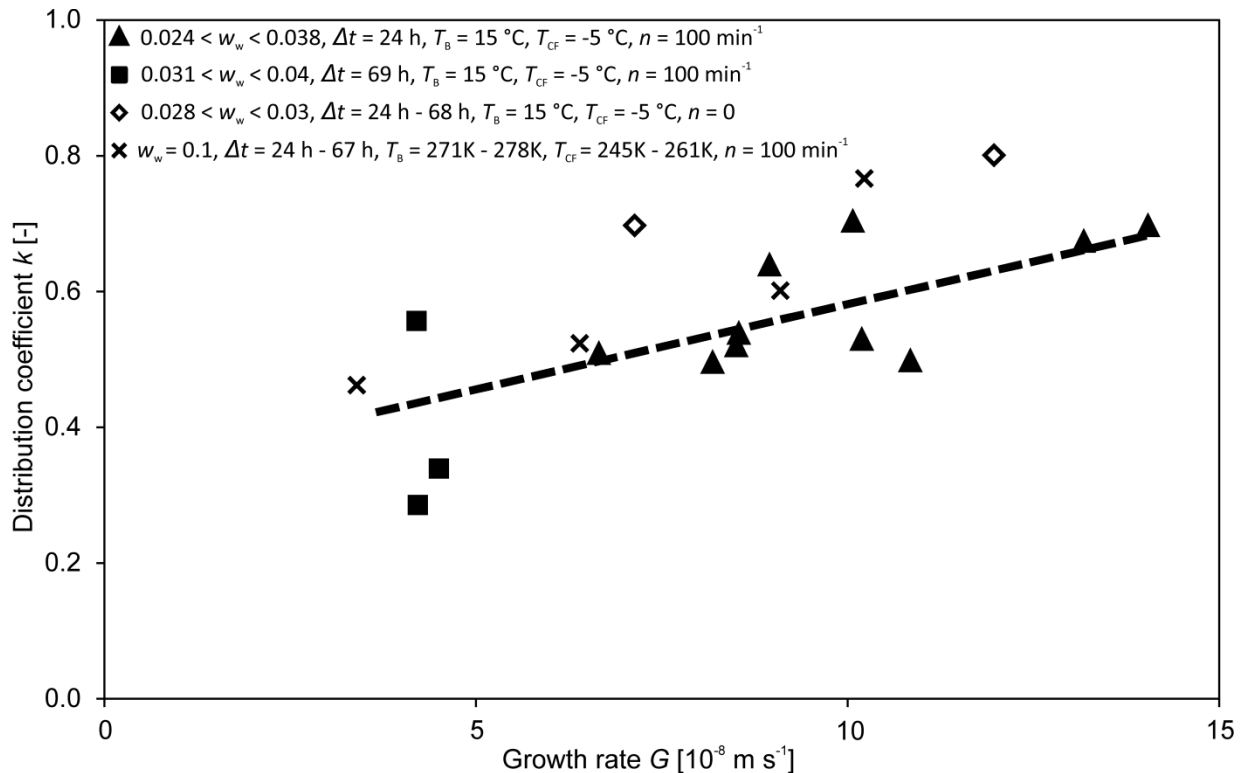


**Figure 5.7.** Viscosity of binary BuOH-glycerol mixtures drawn vs. the BuOH content. The values for pure glycerol are taken from the literature [Seg51].

## Results

layer leads to a rise of the temperature at the solid liquid interface, thus reducing the undercooling as the driving force for the crystal growth. In comparison to this effect, the rising water content of the melt as result of the separation is negligible.

Fig. 5.9 shows the distribution coefficient drawn vs. the growth rate. The data points form a cloud, as is typical for the results of laboratory-scale experiments, but the sufficiently high number of conducted experiments still allows the interpretation of some trends to identify important dependences.



**Figure 5.9.** Distribution coefficient drawn vs. the growth rate of different cold finger experiments conducted on a melt of water and glycerol. The line represents a linear fit for the first data row (represented by solid triangles).

Regarding the series of points in which all temperatures, stirring rate and duration of the experiment were held constant and only the water content was changed in order to allow a change in the growth rate, a trend of increasing distribution coefficient with increasing growth rate is evident. Extrapolation of this trend to the lower growth rates observed in the experiments of longer duration shows an accordance of the distribution coefficients within experimental accuracy. With respect to the integral separation, which is the scope of this study, the distribution coefficient can, therefore, be approximated as function of the growth only. Apart from changing the growth rate, the duration of the crystallization affected the distribution coefficient only negligibly. The same observation can be made for the water content. To compare the results of experiments with 2% < w<sub>w</sub> < 4% water with those of experiments with melts containing w<sub>w</sub> = 10% water, the temperatures had to be adjusted to increase the undercooling by a factor of 1.5 to 2.0 in comparison to said lower water contents

## Results

in order to get the same growth rates. As can be seen in Fig. 5.9 the distribution coefficients for both water contents are the same for the same growth rate.

Fig. 5.9 also shows 2 experiments of static crystallization performed in the MCF. Some systems show a much higher distribution coefficient if the agitation of the melt is missing [Neu96]. In the present case, the distribution coefficients are higher but the difference is rather small. The reason for the small gap between static and dynamic case is the high viscosity of the melt. It did not allow a high stirring rate with the usual magnetic stirring plate, used here. Furthermore, stirring of the melt at the bottom of the beaker did not lead to agitation of the complete melt but the upper part was still stagnant. It can also be assumed that the viscous boundary layer is very thick in this case. For these reasons the possibility to improve the separation performance by changing the agitation is very limited in the MCF as long as the high viscosity is maintained.

The purification of glycerol by layer crystallization from the binary mixture proves to be possible, but the separation performance is rather poor with distribution coefficients ranging from 0.3 to 0.8 for growth rates between  $4 \cdot 10^{-8}$  and  $1.4 \cdot 10^{-7}$  m/s. The dependence of the distribution coefficient on the growth rate is neither influenced by the duration nor by the water content, and only little by agitation. Higher product purity would always have to be bought at the price of a slower process.

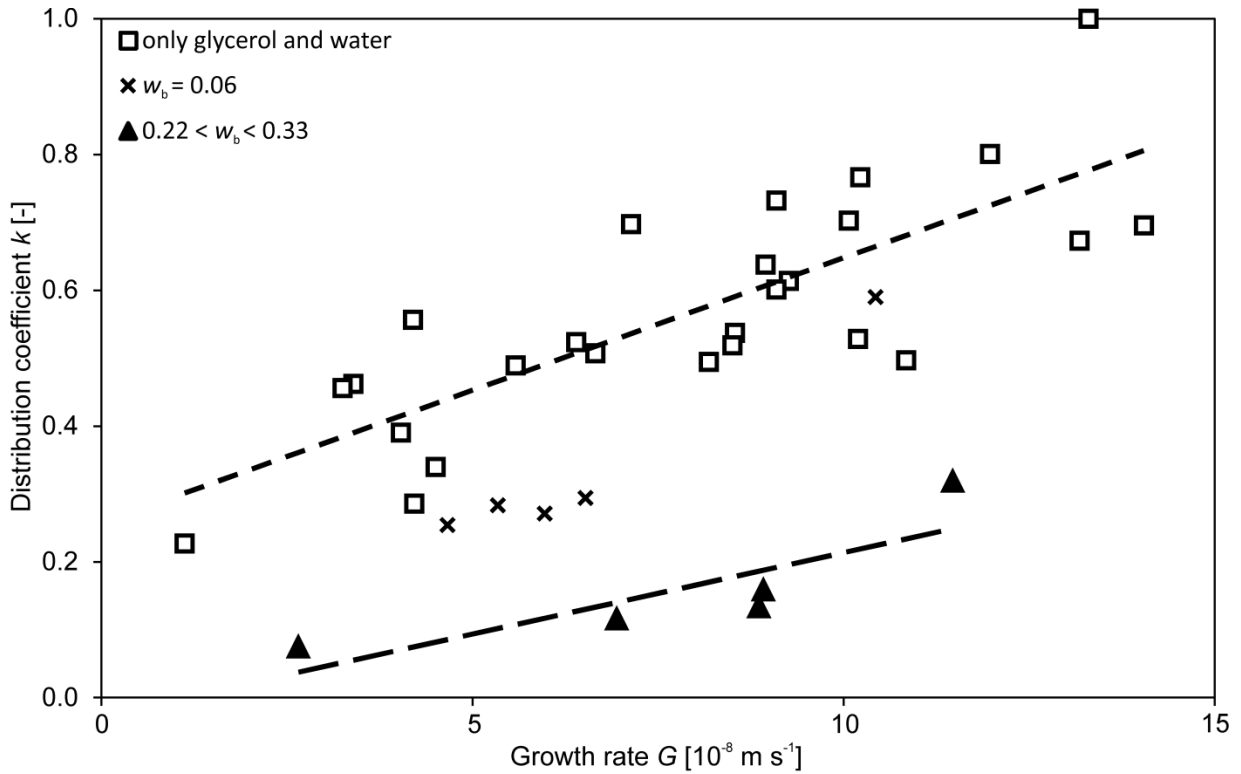
### 5.2.4 Influence of BuOH as assisting agent in the MCF process

Adding BuOH to the melt before performing the MCF experiment affects the separation performance as can be seen in Fig. 5.10. A BuOH content of  $w_b = 6\%$  only leads to slightly lower distribution coefficients at equal growth rates in comparison to the case of a binary melt. But the addition of higher amounts of solvent, i.e. BuOH contents of  $22\% < w_b < 33\%$ , leads to much better results. Distribution coefficients reduced by a factor of 2 to 4 without a loss in the growth rate. At growth rates around  $G = 5 \cdot 10^{-8}$  m/s, a reduction of the water content by approximately one order of magnitude took place. On the lower end of the crystal growth rate scale, the distribution coefficient dropped by a factor of 3, while the growth rate increased by a factor of 2.5.

The separation was even more successful when the water content in the melt was lower. This can be seen in Fig. 5.11. For water contents of  $1.5\% < w_w < 1.8\%$  and an addition of BuOH to  $17\% < w_b < 20\%$ , very low distribution coefficients of  $0.04 < k < 0.09$  were obtained at reasonable growth rates of  $5 \cdot 10^{-8} < G < 10^{-7}$  m/s.



## Results



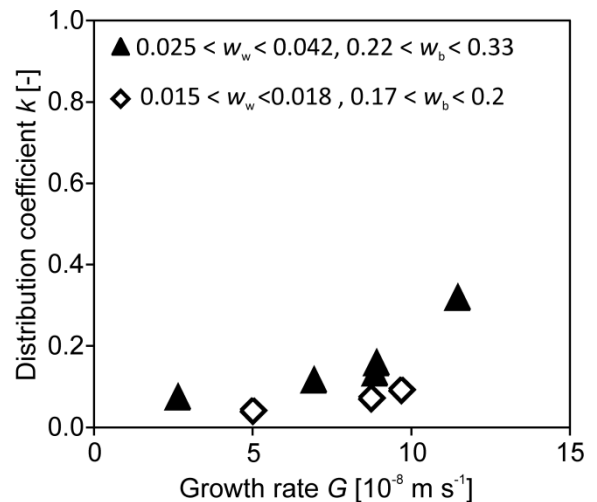
**Figure 5.10.** Distribution coefficient drawn vs. growth rate for cold finger experiments with a melt composed only of water and glycerol in comparison to experiments executed as solvent-aided layer crystallization with different BuOH contents. The lines are only meant as a guide to the eye.

Overall in the MCF, the added mass of BuOH ( $17\% < w_b < 33\%$ ) was lower than the  $w_b = 39\%$  that Hass & Patterson [Has41] used. A lower amount of solvent is advantageous due to lower energy cost for pumping, cooling and heating of the melt and smaller equipment.

### 5.2.5 Growth geometry in the SCF setup

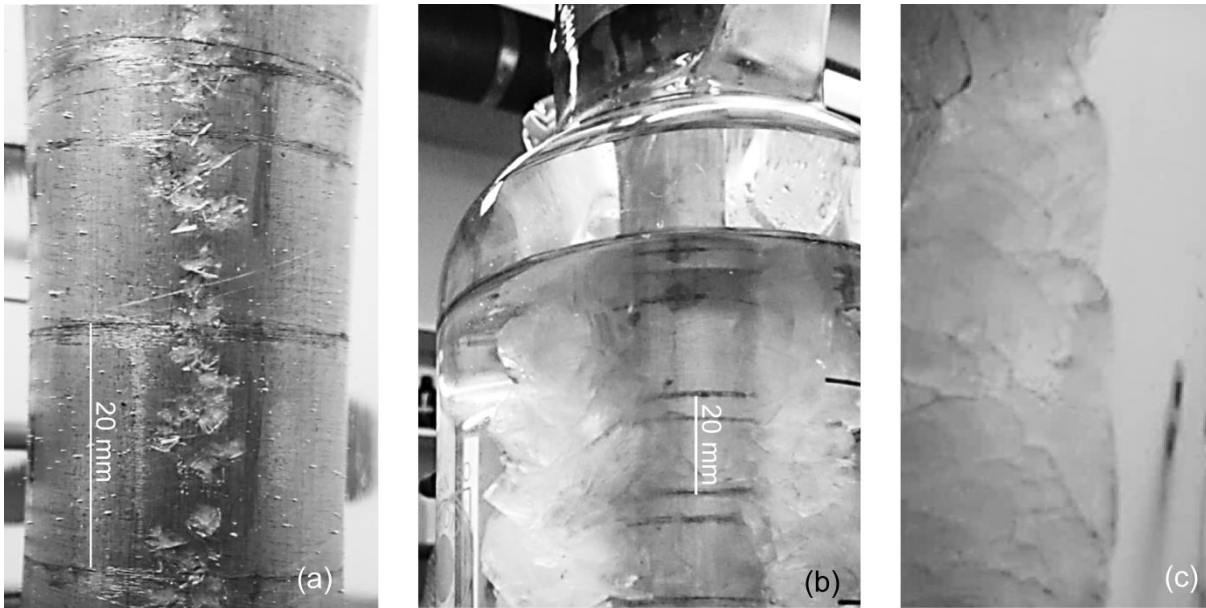
For the experiments in the SCF, the assumptions made for the evaluation of the growth rate, described above (Ch. 4.3.2) as case C, have to be checked by comparing the resulting supposed layer geometry (Fig. 4.16.C)

with the actual geometry. Fig. 5.12 shows representative photographs of the crystal layer. The seed line, shown in Fig. 5.12.a, covers the complete height of wetted cold finger, and allows a rough approximation as one continuous line. From Fig. 5.12.b, taken on the side opposite to the seed, it is obvious that the crystal layer has grown a significant distance in radial direction without covering the whole cold finger. This fits well with the assumed geometry shown in Fig. 4.16.C.



**Figure 5.11.** Distribution coefficient drawn vs. growth rate for solvent aided layer crystallizations at 2 different water contents.

## Results

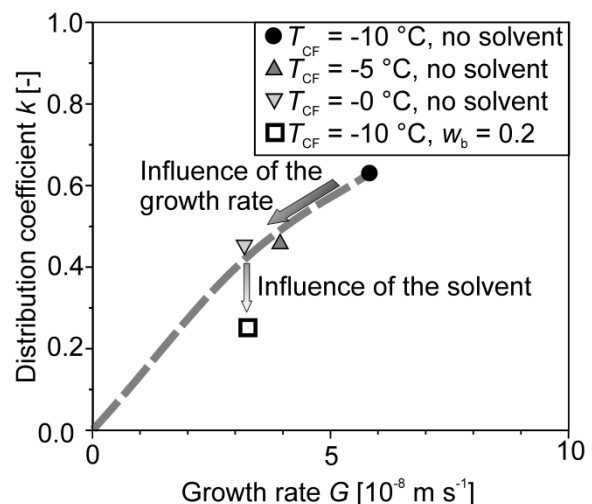


**Figure 5.12. Stages of SCF experiments: Seed line (a), growth with rhombic crystal grains and late covering of the cold finger side opposite to the seed (b), rounding of the crystal edges as the growth rate approaches zero towards the end of the experiment (c).**

The shape of the layer shows large facets and edges with angles close to  $90^\circ$ . The lattice orientation seems to have an influence on the layer thickness because grain boundaries are few and the effect of better heat transfer in the liquid than in the crystal is weak. In many other substances, the insulating effect of the crystal layer flattens the crystal front as it heats parts that have already grown further from the cooled surface, thus decelerating their growth. The temperature does take an influence towards the end of the experiment in causing rounding of the edges, as can be seen in Fig. 5.12.c. This is a strong indication for the approach of a saturation radius as is consistent with the assumptions made above (Ch. 4.3.2). All in all, the observed growth geometry shows sufficient agreement with the calculated one. This indicates that the used calculation can provide comparability between different setups. Further proof for this comparability will be given in the next section (Ch. 5.2.6).

### 5.2.6 Separation performance of growth step in SCF and GL setups

For a feed of  $w_g = 97\%$  glycerol and  $w_w = 3\%$  water, Fig. 5.13 shows the distribution coefficient of the growth step versus the growth rate for experiments with and without BuOH performed in



**Figure 5.13. Distribution coefficient of the growth step without post treatment drawn vs. the growth rate. The water content of the initial melt was  $w_{w,0} = 3\%$  and the duration of growth step was  $\Delta t = 110 \text{ h}$ . The line is only added to guide the eye.**

## Results

the SCF. Comparing the points depicting experiments without BuOH, one can see that a slower growth induced by a higher temperature leads to a better separation in the growth step. A comparison between the 2 points attained at the same temperature shows that BuOH slowed down the crystal growth. For the same growth rate the use of BuOH led to a lower distribution coefficient.

For a feed of  $w_g = 99\%$  glycerol and  $w_w = 1\%$  water, the separation of the growth step depends on the growth rate in the manner that can be seen in Fig. 5.14.

Fig. 5.14 combines results from the SCF and the GL. Results from the 2 different setups, taken at  $x_b=0.2$ , show very good agreement, which suggests that the assumptions made for data evaluation, case C, are valid. Assumptions according to case A would lead to an underestimation of  $G$  by a factor 8 to 11, clearly breaking comparability between the setups. In the SCF, like in the MCF, the positive effect of the BuOH is much higher at lower water contents of the melt.

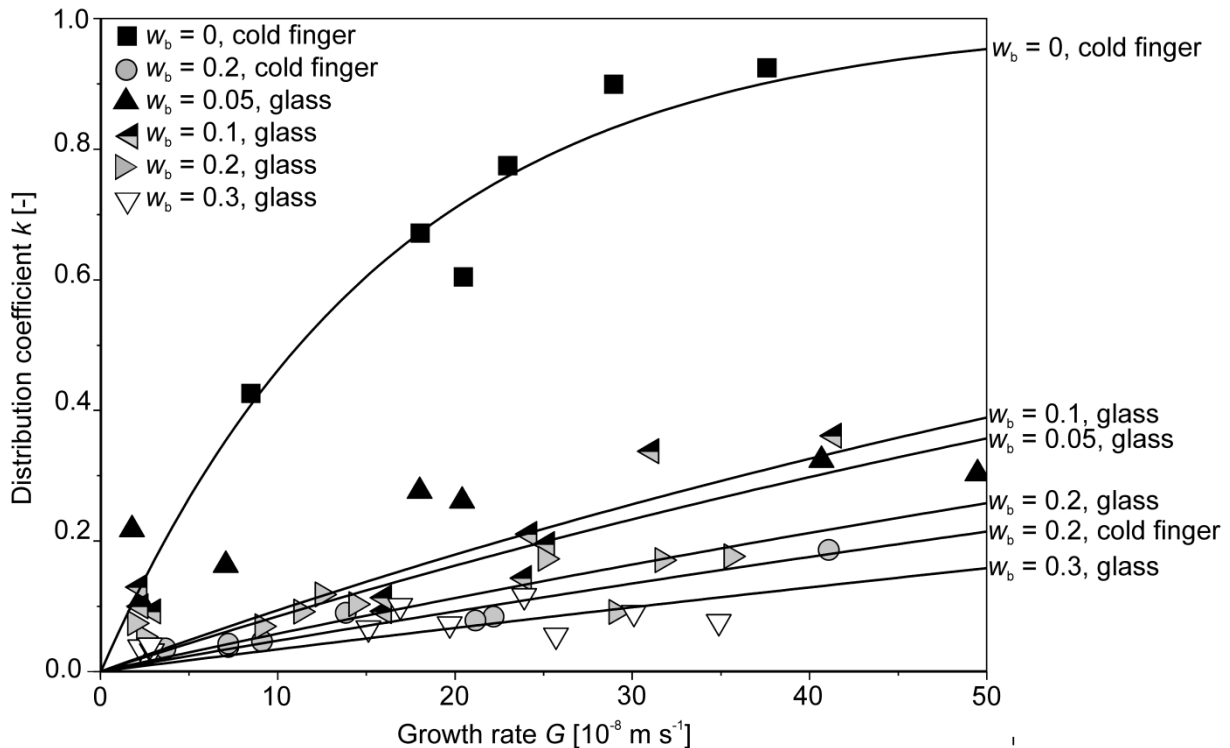


Figure 5.14. Distribution coefficient as a function of the growth rate for  $w_w = 1\%$ , variable  $w_b$ , and both the SCF and GL setup.

### 5.2.7 Layer stability

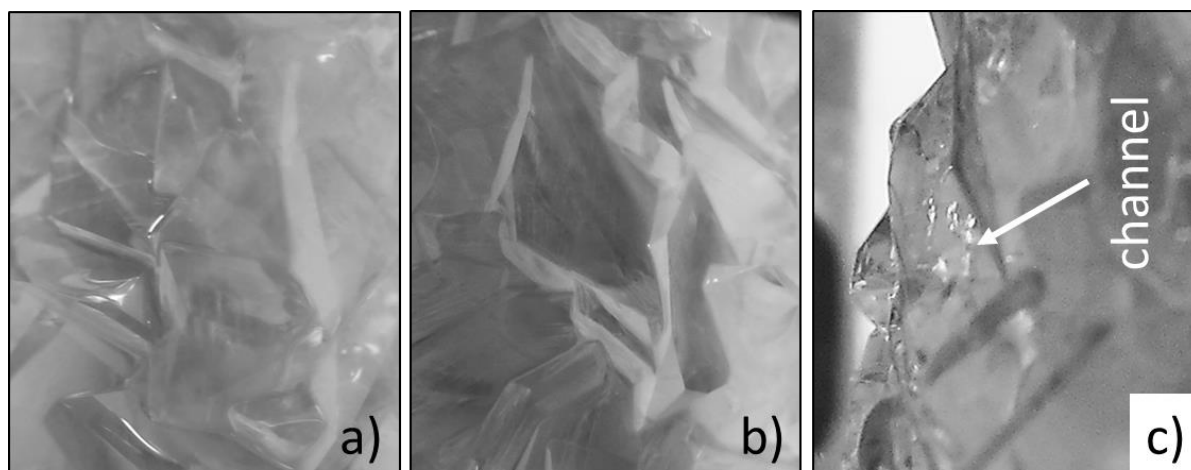
The experiments on layer stability showed that the crystal layer burst in all experiments with  $T_B = T_{CF}$ . This can be explained by the volume increase in melting, which is about 6 % for glycerol at the given temperature [Bla04]. The bursting makes a conventional sweating step in the cold finger setup impossible. Some industrial apparatus e.g. with crystallization on the inside of a pipe or between 2 plates with a random pack or a construction like Sulzer's [Ste06] stretching over the complete gap may allow sweating in this case. In these cases parts of the crystal layers would be held in the pack and thus prevented from blocking the

## Results

exit allowing draining of the sweating liquid. This technique is well-established for the industrial sweating from soft crystal layers. The presence of filling bodies or grids during the crystallization step may be problematic as they constitute a steric hindrance to the crystal growth that may lead to more crystallographic defects, especially more grain boundaries. For substances that show needle-shaped crystals or crystallize in many small grains anyway (e.g. paraffin waxes) this is not an issue. But in the case of glycerol it may disrupt the advantageous growth into large rhombic crystal grains. The experiments with  $T_{CF} = 10\text{ °C}$  and  $T_B = 70\text{ °C}$  showed no bursting of layers, thus pointing towards the possibility of a post-treatment that keeps the crystal layer intact and would, therefore, allow to avoid the steric hindrance during growth. Based on this, the procedure described above (Fig. 4.8) was established. It allows growth on a completely smooth surface with only a step below the crystal layer preventing it from slipping. This post-treatment combines aspects of sweating and melting. Its results are presented in right below (Ch. 5.2.8).

### 5.2.8 Post treatment

The change in shape of the crystal layer during post treatment followed the prediction given in Fig. 4.8. The adhering melt can be seen in Fig. 5.15.a. The effect of the dripping step is evident from the comparison of Fig. 5.15.a and Fig. 5.1.b, as Fig. 5.15.b shows the surfaces and edges of the crystal layer without the veil of a thick layer of adhering melt.

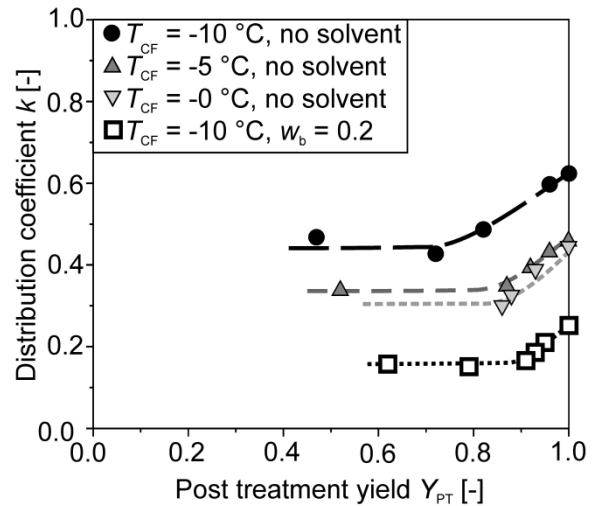


**Figure 5.15.** Crystal layer (a) after draining of the melt with adhering melt on the surface, (b) after dripping step with edges showing sharply, and (c) towards the end of the sweating step with channels inside the layer showing.

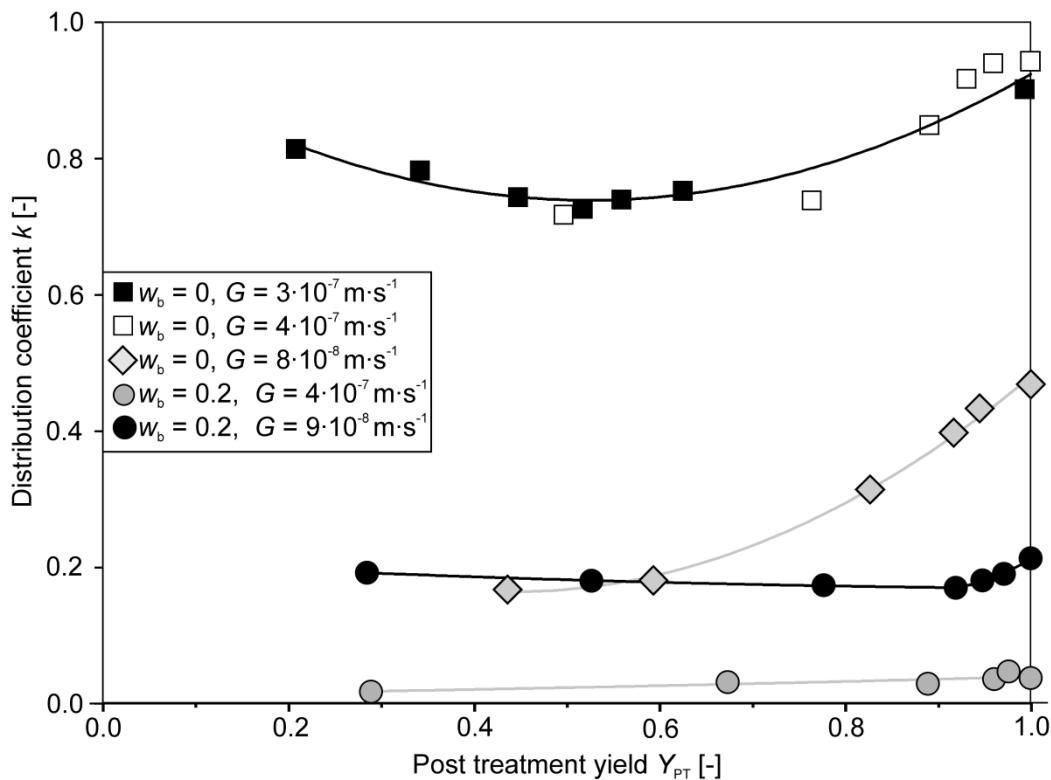
In Fig. 5.15.c the crystal layer does not appear completely compact but displays pores or channels. These channels form during the post treatment and allow the liquid inclusions to leave the crystal layer. This is an indicator that the post treatment has a sweating-like character and is not merely a partial melting from the surface inwards. A bursting of the crystal layer occurred also as predicted.

## Results

Fig. 5.16 shows the integral distribution coefficient versus the yield of the post treatment for the series with  $w_w = 3\%$ . Each point represents one fraction i.e. one sample. The chronological order of the samples can be read from right to left. Immediately after the draining of the melt,  $Y_{PT}$  equals unity and  $k$  is maximal. As the post treatment proceeds, both  $Y_{PT}$  and  $k$  decrease until  $k$  seems to reach equilibrium at approximately  $Y_{PT} = 0.8 \pm 0.1$ . At constant duration of the sweating steps the relative mass loss  $1 - Y_{PT}$  is much higher for the sweating steps of the experiments with higher distribution coefficient. A thicker crystal layer in these cases causes a higher temperature at the crystal front and therefore promotes a faster post treatment. For the crystal layers grown from melts with  $w_w = 1\%$ , the more flexible temperature protocol allowed longer prevention of the bursting. Thus, Fig. 5.17 reveals a different tendency in the post treatment results of slowly ( $G < 10^{-7}$  m/s) and fast ( $G > 2 \cdot 10^{-7}$  m/s) grown crystal layers.



**Figure 5.16.** Distribution coefficient vs. post-treatment yield. The water content was  $w_w = 3\%$  in all 4 experiments. The legend gives the conditions of the growth step. The temperature protocol of the sweating step is given in Fig. 4.8. The lines are only added as a guide to the eye.



**Figure 5.17.** Distribution coefficient vs. post-treatment yield. The water content was  $w_w = 1\%$ .

## Results

The former show  $k$  monotonously increasing with increasing  $Y_{PT}$  while for the latter, the curve passes through a minimum. This holds true for both solvent free and solvent-aided experiments. Yielded at low  $Y_{PT}$  are fractions grown closer to the cold finger, which can be assumed to have grown faster, cf. Eq. 4.C.2 and Fig. 4.14.c, and, therefore, less pure.

Explanations for the fractions gathered at high  $Y_{PT}$  could be that they contain impure liquid inclusions that migrated in the temperature gradient to the outside [Sch93a], or that the impurity incorporation during growth increased towards the outer parts of the layer due to increased impurity concentration in the vicinity of the layer caused by the rejection during growth of the purer layer parts. A strong migration effect could explain the difference between experiments with fast and slow growth.

### 5.2.9 Influence of other solvents, of surfactants and of strong agitation

Experiments on the influence of water and BuOH on the glycerol crystallization form the main body of work of the present study. However, the influence of other substances is investigated as well. Bottle tests on binary mixtures of glycerol and ethanol (EtOH, index: e) in mass fractions  $0 < w_e < 15\%$  revealed that the influence of EtOH on the growth rate of glycerol is similar to the influence of water. The result can be seen in Fig. 5.18. In bottle tests on ternary mixtures with a glycerol to water ratio of  $\zeta_{gw} = 99:1$  and methanol (MeOH), EtOH, 1-Propanol, (BuOH) or Butanon (mek) added to a mass fraction of 20% at 6 °C, MeOH inhibited the crystallization completely. EtOH and 1-Propanol inhibited growth within the first 24 hours but after this induction period, a growth in the same order of magnitude as in the reference without third component was found. The sample with mek separated into 2 phases. The lighter mek-phase did not show crystallization at 6 °C while the heavier glycerol-phase showed growth similar to the reference.

The influence of a surfactant is investigated on the example of sodium dodecyl sulphate (SDS) at a mass fraction of 100 ppm in the glass setup. Fig. 5.19 shows the result. At a glass temperature of  $T_{GL} = 5$  °C, the distribution coefficient concerning water was equal to unity if no BuOH was present. This was the same with and without SDS. The presence of BuOH reduced the distribution coefficient but this effect was weakened by the surfactant. As can be seen from Fig. 5.19.b, the slope of inverse distribution coefficient with increasing BuOH-content,  $dk^{-1}/dw_b$  reduces by half an order of magnitude in

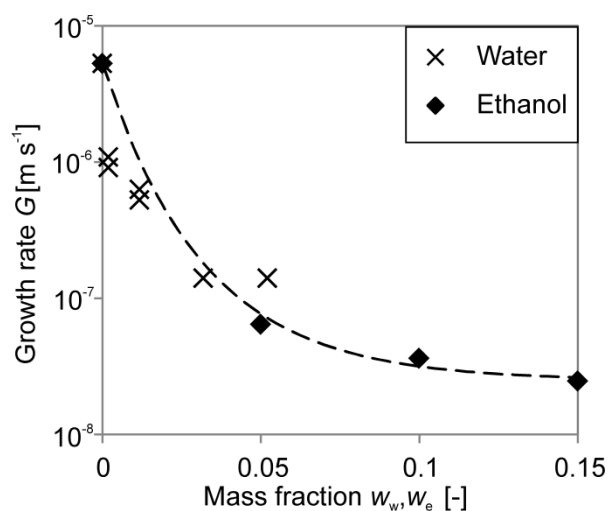
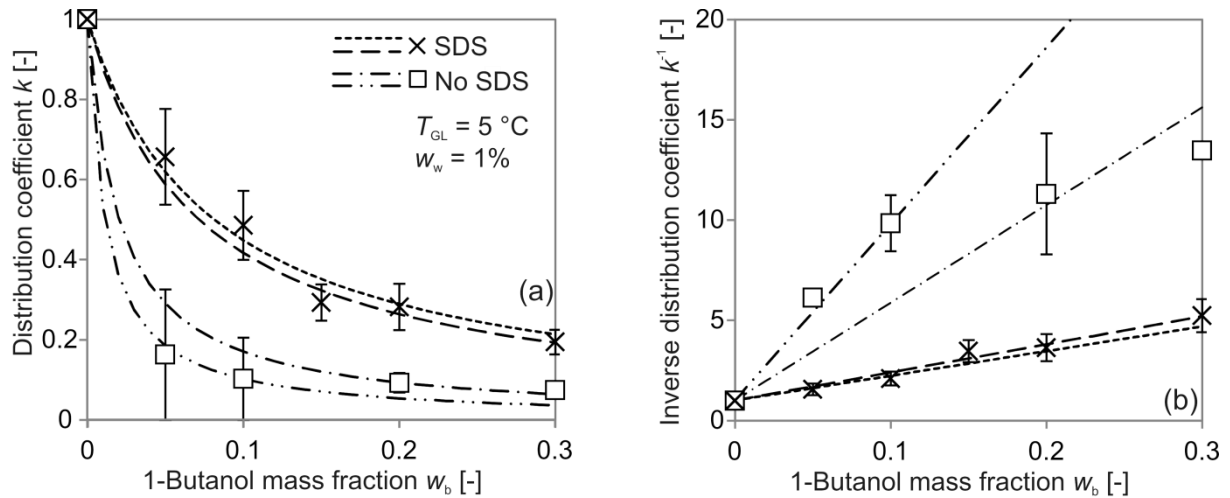


Figure 5.18. Growth rate of glycerol from binary mixtures with water or EtOH, measured in bottle tests in vertical tubes at 6 °C, drawn vs. the mass fraction of the second component.

## Results

the presence of SDS when compared to the case without the surfactant. The exact value of the growth rates in the experiment with SDS is not given, because the time intervals after which the layer thickness was measured were rather large. However, enough data points were obtained to state that the growth rate in the experiments with SDS was lower by a factor between 1.2 and 3 in comparison to the experiments without SDS. Therefore, it is clear that the influence of BuOH on  $k(G)$ , which is to allow lower distribution coefficients at higher growth rates is weakened by the SDS.

The experiment using strong agitation in the TBCF setup showed a distribution coefficient of  $k = 0.27$  at a growth rate of  $G = 1.55 \cdot 10^{-7}$  m/s on an initial melt containing glycerol and  $w_w = 3\%$  water.



**Figure 5.19.** Distribution coefficient (a) and its multiplicative inverse (b) with and without SDS in a glass setup with a glass temperature of 5°C and 1% water, drawn vs. the BuOH mass fraction in the initial melt. Each data set is shown with 2 fit curves, both of inversely linear type, but with the method of least squares being applied one time to  $k$  and the other time to  $k^{-1}$ .

### 5.3 Raw glycerol

#### 5.3.1 Sodium chloride determination via electrical conductivity

The raw glycerol is a multinary mixture. The third most important component after glycerol and water is sodium chloride (NaCl), which will simply be called salt within this section. In order to be able to measure the separation of salt and glycerol via the electrical conductivity, a reversible correlation for the influence of salt on the electrical conductivity of ternary glycerol-water-salt (gws) mixtures was measured first. The result is presented in Fig. 5.20.

The experimental data can be fitted by the linear relation

$$\frac{\sigma}{\text{S m}^{-1}} = (22.187w_w + 0.6774)w_{\text{NaCl}} \quad (5.1)$$

Eq. 5.1 can be used together with the water concentration according to Karl Fischer or the correlation for the refractive index given in the appendix to measure the salt and water concentrations in ternary mixtures. It can be applied to the raw glycerol under the assumption that the non-glycerol organic matter (MONG) takes little influence because its concentration is low and its behaviour similar to that of glycerol.

## Results

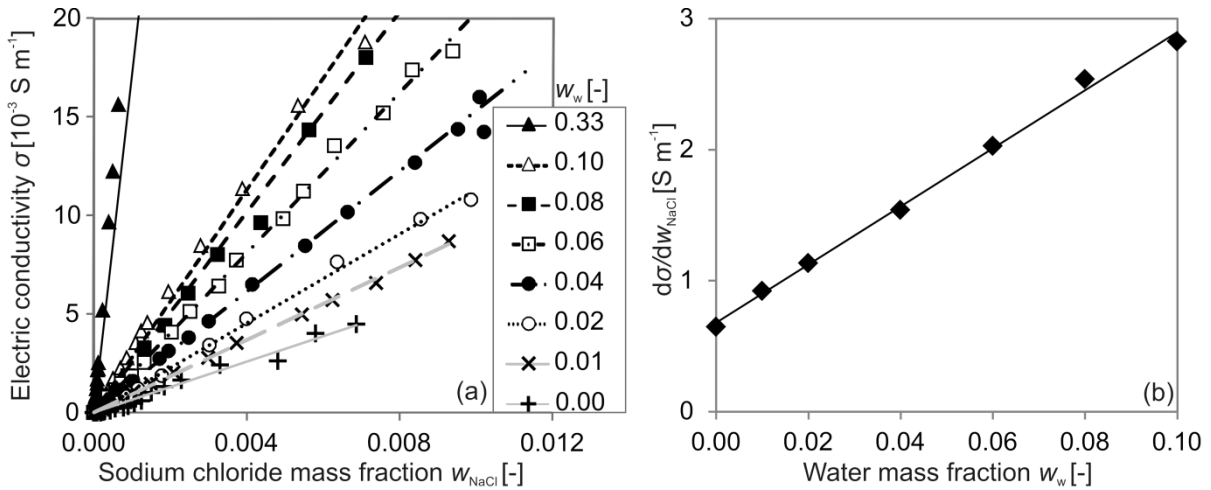


Figure 5.20. Electrical conductivity  $\sigma$  of ternary glycerol-water-NaCl mixtures as a function of sodium chloride mass fraction  $w_{\text{NaCl}}$  and water mass fraction  $w_w$  (a) and the slope of the linear dependence on the salt content drawn versus the water mass fraction (b).

### 5.3.2 Separation success of the crystallization

The bottle test on raw glycerol yielded the crystal layer shown in Fig. 5.21.b, the crystal growth rate at  $-25^\circ\text{C}$  was in the order of magnitude of  $10^{-8} \text{ m/s}$  and crystal layer and residual melt had approximately the same mass. The mass fractions of water and sodium chloride were determined from the refractive index and electric conductivity, using the correlations given in the appendix (Ch. A.1) The resulting distribution coefficients are given in Fig. 5.21.a, together with the results of synthetic binary glycerol-water mixtures with  $w_w = 10\%$ , obtained in the MCF (cf. Fig. 5.9).

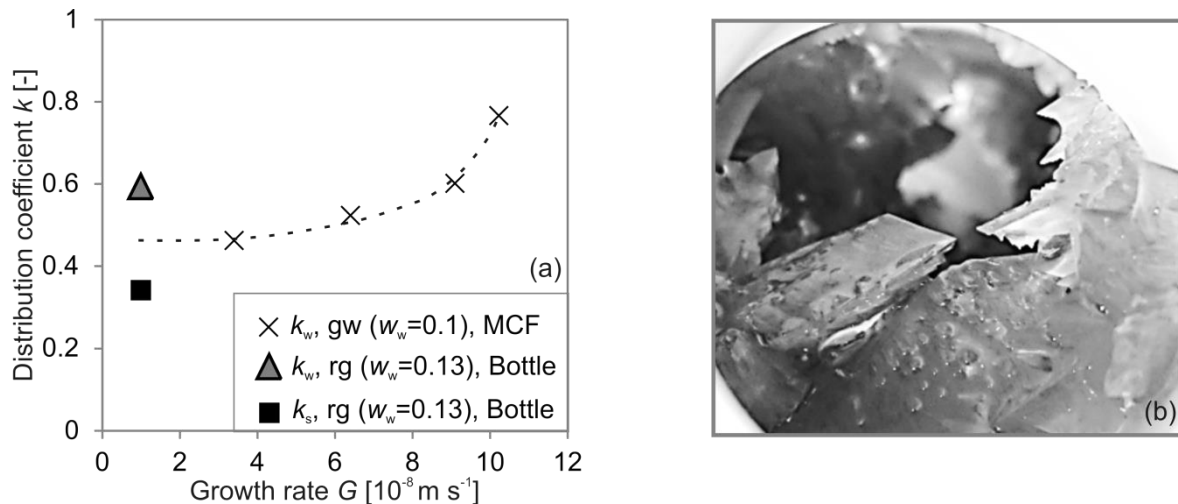


Figure 5.21. Results of a bottle test on raw glycerol. (a) Distribution coefficient concerning water  $k_w$  and salt  $k_s$  of the experiment on raw glycerol (rg) in comparison to  $k_w$  of experiments of binary glycerol-water mixtures (gw) of similar water mass fraction, all drawn vs. the growth rate. (b) Photograph of the crystal layer in the bottle after draining of the residual melt.

The distribution coefficient concerning salt  $k_s$  is lower than the one concerning water  $k_w$ , which means that the crystallization separated salt better than water. However, further investigation of this phenomenon is beyond the scope of the present study. The important



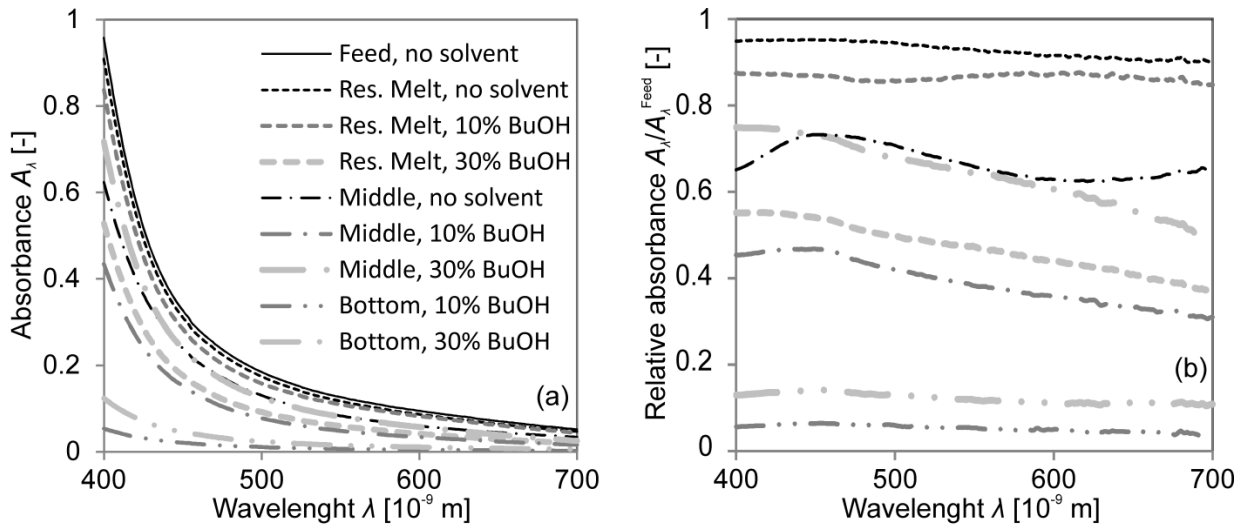
## Results

thing here is that both values are positioned in the middle third of the possible  $k$ -interval between zero and one, and their mean value continues the trend given by the values from the GW-system. Thus, the raw glycerol with  $w_w = 13\%$  water,  $w_s = 3\%$  salt and other impurities showed similar  $k(G)$ -behaviour to the binary system glycerol-10%-water. The  $G(T)$ -dependence is, however, different. The growth rate was smaller even at lower temperatures. The slow growth at low temperatures and mediocre distribution coefficients makes it seem unlikely that classic layer crystallization could compete with distillation for the feed of raw glycerol.

Furthermore, the solvent screening revealed a strong decrease in miscibility of glycerol feed and BuOH. While it was possible to use up to  $w_b = 40\%$  BuOH in glycerol-water mixtures of  $w_w < 5\%$  without the occurrence of liquid-liquid separation at the usual crystallization temperatures, the raw glycerol did not mix with  $w_b = 20\%$  BuOH, even at room temperature. At the abovementioned crystallization temperature of  $-25^\circ\text{C}$ , demixing occurred even at  $w_b < 3\%$ . The shorter n-alkanols showed better miscibility with the raw glycerol but they had a very similarly decreasing effect on the melting temperature and crystal growth rate as they had on the glycerol-water mixtures. Thus, directly applied to the raw glycerol, layer crystallization is no economically promising alternative to distillation. The bottle test on the heavy, glycerol and salt rich, residues of the first and second distillation step (cf. above Figure 3.10) showed even less promising results, at crystal growth rates  $G < 10^{-8}$ , they displayed dendritic growth to an extent which made draining of the residual melt impossible. The LL-extraction performed on the second heavy residue yielded an extract which, after evaporation of the solvent, had a refractive index ( $n_D = 1.44$ ) and viscosity similar to glycerol, but its lack in hygroscopy allowed the conclusion that it contained little glycerol.

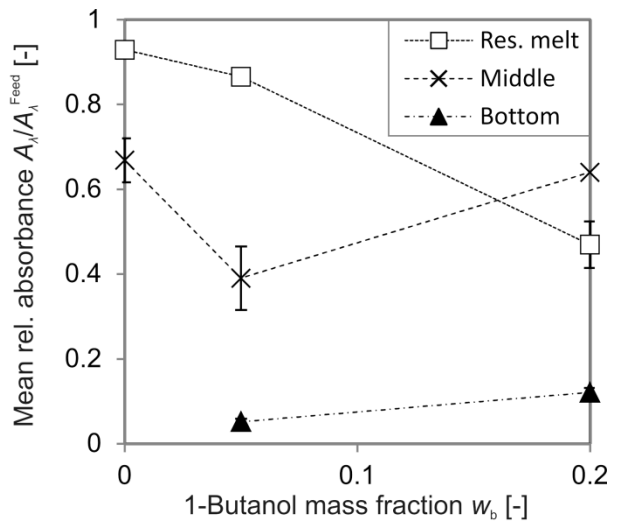
The crystallization in the GL setup, performed on the middle distillate of the second distillation, showed limited ability to remove the light-absorbing impurities Fig. 5.22.a shows the absorbance of visible light of the feed and the different fractions of experiments with and without BuOH. The feed was yellow and transparent. The relative absorbance  $A_\lambda/A_\lambda^{\text{Feed}}$ , shown in Fig. 5.22.b is always roughly independent of the wavelength. They are, therefore, averaged over all wavelengths in Fig. 5.23.

## Results



**Figure 5.22.** Absorbance of visible light as a function of the wavelength. (a) Absolute value of the absorbance. (b) Absorbance of the respective fraction divided by the absorbance of the feed to the crystallization, i.e. the middle distillate of the second distillation.

From this plot the influence of the BuOH on the performance of the separation can be read. The decrease in relative absorbance of the residual melt with increasing BuOH mass fraction is mainly due to the dilution by the colourless BuOH. The low fraction was weakly diluted by the seed layer, which was pure glycerol, but its lower absorbance may also result from separation of the impurity which accumulated in the residual melt close to the crystal front. This fact explains the irregular curve of the middle fractions absorbance: It is a mixture of crystal layer and residual melt or sweating liquid, with scatter in the mixing ratios as result of missing control in the sampling. Further interpretation of this result is, therefore, not sensible. It is also not necessary because the general result that the crystallization decreased the absorbance only moderately is sufficiently clear. No acquired fraction was completely colourless.



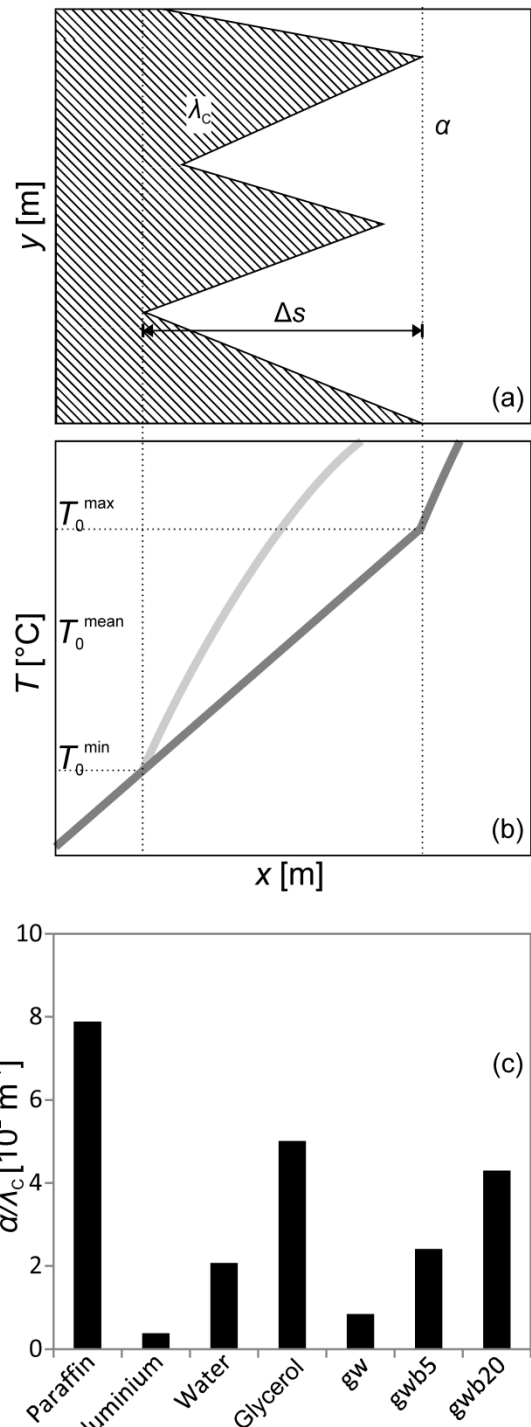
**Figure 5.23.** Relative absorbance of the different fractions, for each fraction averaged over all wavelengths of visible light.

## 6 Discussion

### 6.1 Macroscopic crystal layer roughness

The experiments of the present study produced 2 very different types of roughening of the crystal surface. The occurrence of micro-roughening that causes liquid inclusions is evident from the solute content of the crystal layers. The shape of this micro-roughness has not been captured in pictures. It may be dendritic, lamellar or something else. For information on the topic, the reader is referred to the literature cited in Ch. 2.2.2. The present study discusses the solute entrapment in an approach that needs no information on the geometry of the micro-roughness.

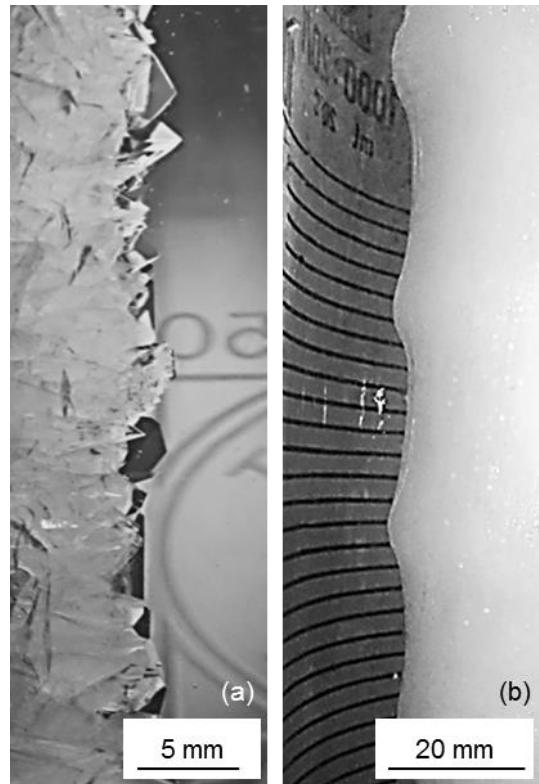
Apart from the micro-roughening, glycerol crystal layers exhibit a macroscopic roughness  $\Delta s$  (cf. Fig. 6.1.a) of a few mm. The process that occurs in glycerol could be described as faceting, in rough allusion to the geometrical term, because the layer develops many different faces that meet at straight edges. The faces themselves are macroscopically flat, so that the crystal layer appears like an agglomerate of multiple cuboidal crystal particles. As the crystal layer is not assembled by agglomeration, the faceting is probably a result of the formation of grain boundaries during growth. It may also be hypothesized that solute entrapment allows reorientation of the lattice because the lattice continuity is broken by the liquid inclusion. The region, in which the lattice orientation changes, regardless of whether it is a 2-dimensional or 3-dimensional defect, may be called a grain boundary in the broader sense. In both cases, these grain boundaries would be likely to contain more solute, either incorporated into the lattice or as liquid inclusions, than the lattice inside the grains. However, this does not mean



**Figure 6.1. Insulation during macro-roughening. Illustration (a,b) and ratio of heat transfer coefficient and crystal thermal conductivity, calculated for the SCF setup.**

that the solute uptake into the crystal layer only takes place at the concave edges, where a grain boundary meets the melt. The faces may be micro-rough, even if they appear smooth to the naked eye.

Two hypotheses shall be given on why the faceting of glycerol, with roughness and face area often exceeding 3 mm and 10 mm<sup>2</sup>, respectively, doesn't occur in many other materials. The first is that glycerol tends to build larger grains than other substances. This may be related to a very low nucleation and surface nucleation rate, which, in turn, can be explained by the very large metastable zone width (cf. Ch. 2.2.2). The second is that a glycerol crystal layer doesn't insulate the crystal front from the cooled surface as good as other layers would. In a temperature field between a cold finger and a warm beaker, the temperature at the crystal front increases with increasing layer thickness, at least in a quasi-stationary state if the effect of the heat of fusion is neglected. Fig. 6.1.a-b illustrates the matter. The thicker parts of the layer would recess while those which are thinner would grow further, flattening out the layer. A



**Figure 6.2. Two types of macro-roughening: faceting in glycerol, grown from a binary mixture with  $w_w = 1\%$  water (a) and marcelling in ice, grown from a binary mixture with  $w_{\text{sucr}} = 20\%$  sucrose, both in the SCF setup.**

quantity that describes the insulation effect and, thus, the resistance to macro-roughening is the ratio of heat transfer coefficient and thermal conductivity of the crystal,  $\alpha/\lambda_C$ . It is plotted in Fig. 6.1.c for a few pure components and 3 of the used glycerol mixtures. The value of paraffin is very high, which fits the fact that paraffin crystallizes in a macroscopically flat layer, even if the growth rate is high. The value of glycerol is relatively high, because of the high temperature level at which perfectly pure glycerol would crystallize. However, the mixtures containing water ( $\zeta_{wg} = 1\%$ ), show lower values. The value for water is also rather low and water does actually show another type of macro-roughening, which could be called marcelling, because the crystal layer becomes wavelike. While the reason for this behaviour is not known, its possibility can be explained by the relatively weak insulation effect. The marcelling of water has also been reported in other setups [Sch93b], and faceting is also visible on a photograph of a 2,2-dimethoxy-1,2-diphenylethanone crystal layer, grown from a binary mixture with  $w_b = 5\%$  1,2-diphenylethandiol [Par01]. However, such observations are rather rare and further research would be necessary to understand them.

## 6.2 Uniform representation and fitting of $k(G)$ relations from experiments on the system glycerol-water-BuOH

### 6.2.1 A suitable fitting function

The results from measuring distribution coefficient  $k$  as a function of growth rate  $G$  in 4 different setups: cold finger with magnetic stirrer (MCF), static cold finger (SCF), glass setup (GL) and cold finger with translating beaker (TBCF), with water contents  $1\% < w_w < 10\%$ , and BuOH contents  $0 < w_b < 33\%$  are all plotted together in Fig. 6.3.

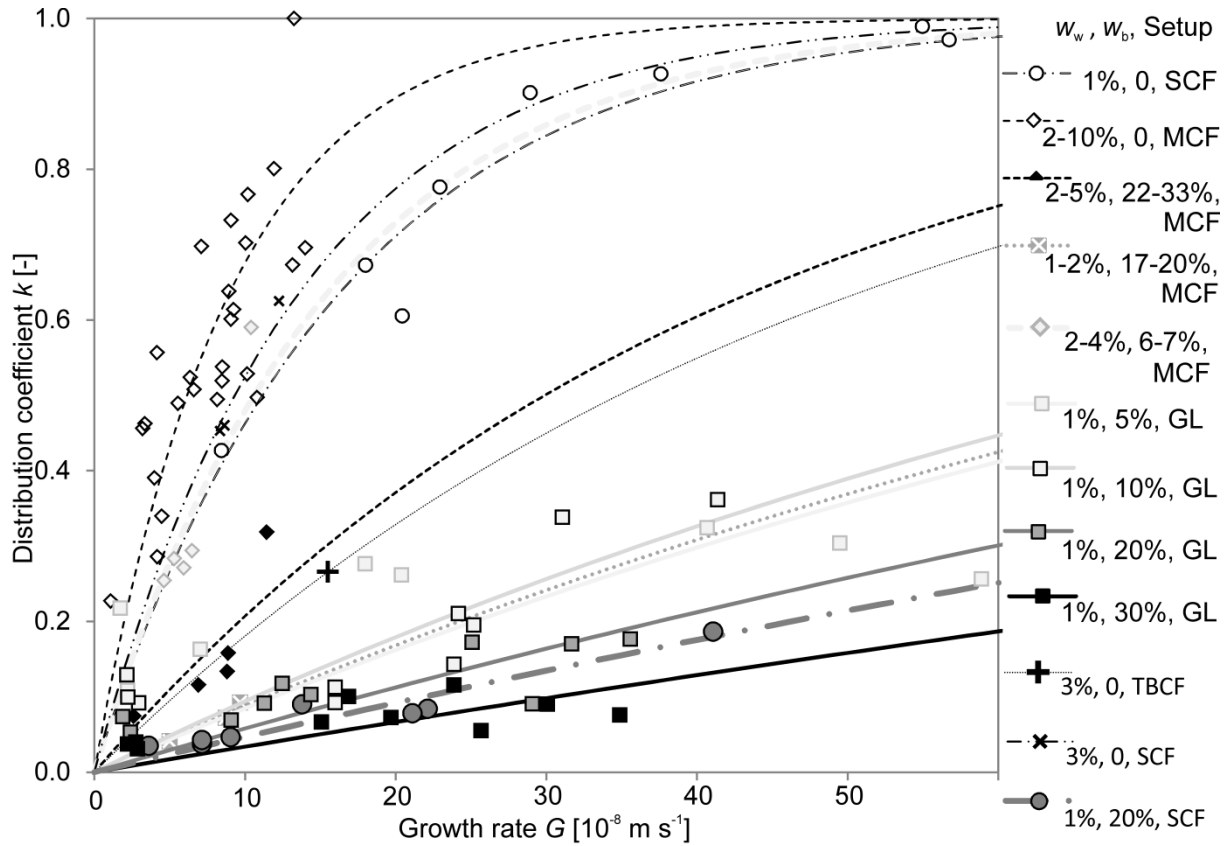


Figure 6.3. Overview over all  $k(G)$  measurements of this study. The legend gives the triple  $w_w, w_b, \text{Setup}$ . Setup abbreviations are: MCF: magnetic stirrer cold finger, SCF: static cold finger, GL: glass, TBCF: translating beaker cold finger.

Each series of data was fitted by

$$k = 1 - e^{-\left(\frac{dk}{dG}\right)_{G=0} G}, \quad (6.1.1)$$

with the initial slope  $(dk/dG)_{G=0}$  being the fit parameter. The curves are given in Fig. 6.3, as well. This common saturation curve is the simplest fit that satisfies the criteria that  $k$  monotonously increases with  $G$  but does never exceed unity. It also contains the assumption that  $k$  only reaches zero at  $G$  equal to null. This assumption is not based on theoretical reasoning but will be justified by the results.

As described above (Ch. 2.3.2), theoretical approaches to simulate  $k(G)$  often use the formula

## Discussion

$$k = \frac{e^{\Gamma} - \kappa}{e^{\Gamma} - 1} \quad (6.1.2)$$

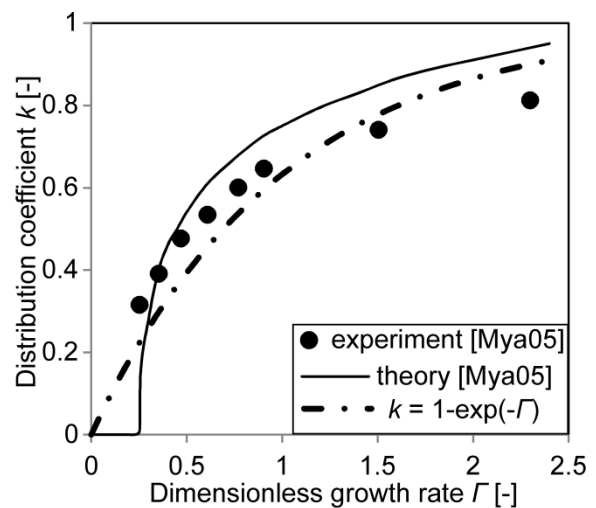
with a dimensionless growth rate  $\Gamma$  defined as

$$\Gamma = \frac{G}{\lambda}, \quad \lambda \in \left\{ \beta, \frac{D}{s_D}, \beta \frac{\rho_L}{\rho_S}, \frac{D \rho_L}{s_D \rho_S} \right\}, \quad (6.1.3)$$

where  $s_D$  is the thickness of the diffusion boundary layer,  $\rho_S$  and  $\rho_L$  are the densities of crystal and melt, respectively,  $D$  is the diffusivity and  $\beta$  the mass transfer coefficient. The concentration polarization ratio  $\kappa = w_{b,SL}/w_{b,L}$  is the ratio of impurity concentration at the interface and in the bulk of the melt. The growth rate reference  $\lambda$  is a quantity describing the quickness of mass transport close to the crystal layer. It can be interpreted as the tendency of the system to minimize concentration polarization. Therefore,  $\kappa$  is usually assumed to be a function of  $\Gamma$  and the concentration levels, and so MYASNIKOV & UTESHINSKY [Mya05] derived a predictive theory to calculate  $k(\Gamma)$ .

When comparing the theoretically deduced Eq. 6.1.2 with the simpler Eq. 6.1.1 assumed here, the only qualitative difference is that Eq. 6.1.2 predicts the existence of a non-zero dimensionless growth rate  $\Gamma_0 > 0$  below which  $k$  is zero. At  $\Gamma < \Gamma_0$  the layer would grow perfectly flat and pure.  $\Gamma_0$  is the critical growth rate at which roughening of the surface first occurs within the theory. There are experimental results on metals and also on organic compounds that very much show this behaviour, e.g. [Win86]. In the present study, however, the 2 reasons for dropping the matter are: First, the glycerol crystal layers never grew flat but showed roughening or faceting, even when growing very slowly and purely (cf. above, Ch. 6.1). Secondly, the experimental results do not suggest  $\Gamma_0 > 0$  because  $k > 0$  was measured even at very low growth rates. Given

the very limited accuracy of mathematical  $k(G)$ -simulations,  $\Gamma_0 = 0$  is a reasonable approximation. This is also illustrated by Fig. 6.4. The solid curve shows the theoretical  $k(\Gamma)$  for the system naphthalene-benzoic acid as calculated by MYASNIKOV & UTESHINSKY [Mya05] the points represent experimental results for the same system from [Lap77], cited in the same paper [Mya05]. The broken line is from Eq. 6.1.1. It is obvious that the broken line is as good a fit for the experimental data as the solid line. Therefore, the hitherto made comparisons to the theory shall suffice and the following shall be understood as merely an explanation of the experimentally shown phenomena and not as an attempt to establish a predictive theory.



**Figure 6.4.** Distribution coefficient  $k$  vs. dimensionless growth rate  $\Gamma$  for the system naphthalene benzoic acid. Theory (solid line) and experimental data (solid circles) are taken from [Mya05] and compared to the function that is used to fit data in the present study (broken line).

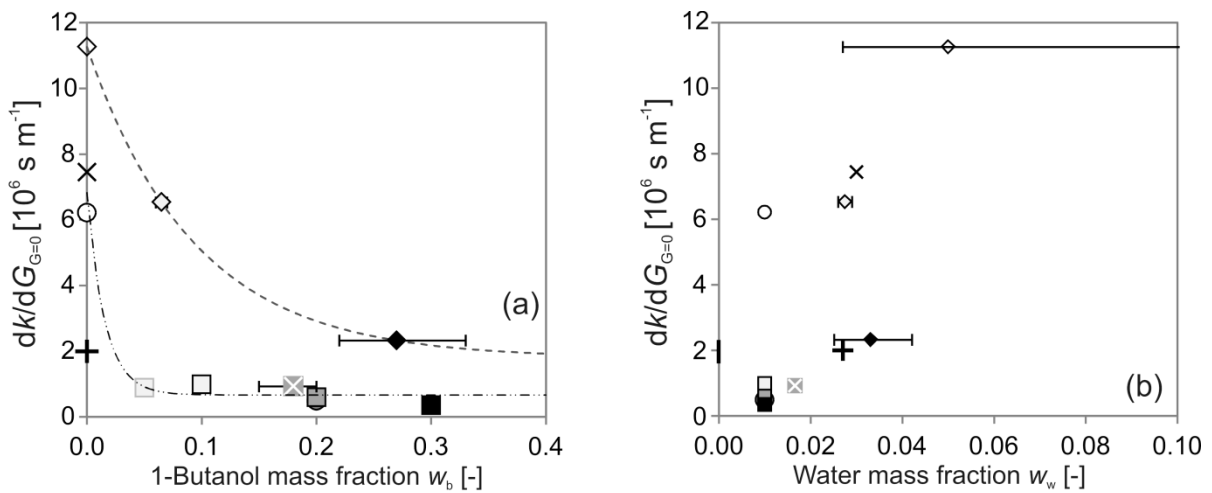
## Discussion

The broken line in Fig. 6.4 represents a function without any parameters. The fit parameter  $(dk/dG)_{G=0}$  in Eq. 6.1.1 vanishes in the dimensionless plot because

$$\Gamma = \left( \frac{dk}{dG} \right)_{G=0} G. \quad (6.1.4)$$

A lower value of  $(dk/dG)_{G=0}$  means that at any growth rate a lower distribution coefficient, i.e. better separation, is achieved if the representation by Eq. 6.1.1 is accurate. It is, therefore, a direct measure of the separation success.

This self-similarity allows the uniform representation of the results by plotting  $(dk/dG)_{G=0}$  vs. the varied parameters. This is done in Fig. 6.5 for the initial contents of water and BuOH in the melt.



**Figure 6.5.** Initial slope  $(dk/dG)_{G=0}$  of the fitting curves from Fig. 6.3, drawn versus the water and BuOH mass fraction of the initial melt. The symbols have the meaning given in the legend to Fig. 6.3. Each symbol represents one series of experiments. In case  $w_w$  or  $w_b$  were varied within one series, the point is positioned at the arithmetic mean of all values within the series and error bars ranging from the lowest to the highest value of the series are added. The lines represent exponential fits of points that lie approximately on the same curve, but are otherwise arbitrarily chosen.

The effect of the BuOH mass fraction is immediately evident from Fig. 6.5.a. Especially in the glass and static cold finger at  $w_w = 1\%$ , the system responds strongly even to low amounts of BuOH. The crystallization in the classic cold finger setup from a melt of  $w_w > 2\%$  shows a higher level of  $(dk/dG)_{G=0}$  and weaker dependence on  $w_b$ . The effect of  $w_b$  is, however, still clearly visible. The difference between the setups will be discussed below (Ch. 6.2.2). In Fig. 6.5.b the points separate into 2 groups: the upper group with binary melt and the much lower group which contains the solvent-aided examples and the experiment with strong agitation in the cold finger with translating beaker. The effects of strong agitation and of the presence of the helping liquid are similar because both affect the mass transport.

From Eq. 6.1.3-4 one sees that

$$\left(\frac{dk}{dG}\right)_{G=0} = \lambda^{-1} = \frac{1}{\beta} \frac{\rho_S}{\rho_L}. \quad (6.1.5)$$

So  $(dk/dG)_{G=0}$ , a direct measure for the separation success achieved in an experiment, should be inversely proportional to the mass transfer coefficient,  $\beta$ . It is well known that a strong agitation of a liquid increases the mass transfer coefficient and that this is the reason for the better separation success of falling film melt crystallization in comparison to static melt layer crystallization. The present finding that even small amounts of BuOH have a similar effect on the mass transfer coefficient will be explained in much detail below (Ch. 6.3).

### 6.2.2 Comparability between setups

In Fig. 6.5, a major difference between the MCF setup, presented by diamonds, and the other setups is visible. This is mainly caused by the difference in data evaluation and in setup geometry. The problem in scaling up melt crystallization from a laboratory scale to a pilot plant is discussed in detail above (Ch. 2.3.2). This section shall briefly present a concept of dealing with it.

An error in the calculation of the distribution coefficient arises from its calculation as the concentration ratio between the crystal layer and the entire drained melt. In an industrial crystallizer the ratio of melt volume to cooled surface is small and most of the melt, often 80%, is crystallized. All of the residual melt has a strongly increased impurity concentration and all of it influenced the purity of the crystal layer.

In cold finger setups with mainly stagnant melt and a low ration of melt volume to cooled surface, the drained melt is a mixture of melt that was close to the crystal surface during growth and melt that was further away. The melt that was close to the crystal layer strongly increased its impurity concentration and thus reduced the purity of the crystal layer. It can simulate the residual melt in an industrial crystallizer. The melt that was further away from the crystal layer changes its composition much less. It changes the average concentration of the drained melt to a value that is too low to simulate the industrial case. The canonical calculation is only valid in case of a melt well-enough mixed, by forced or natural convection, to make the volume of melt in the boundary layer in the laboratory setup less than the residual melt volume in the case of industrial geometry.

If the melt is stagnant and mass transport is slow, the melt in the beaker can be modelled as consisting of 2 parts, one part close to the beaker acting like the melt in an industrial crystallizer and the other part being dead volume. When assuming that the active part is a smaller fraction of the initial melt than the residual melt in the industrial case, e.g. 20%, the distribution coefficient  $k_{low}$  that would occur if the dead volume would not be drained is

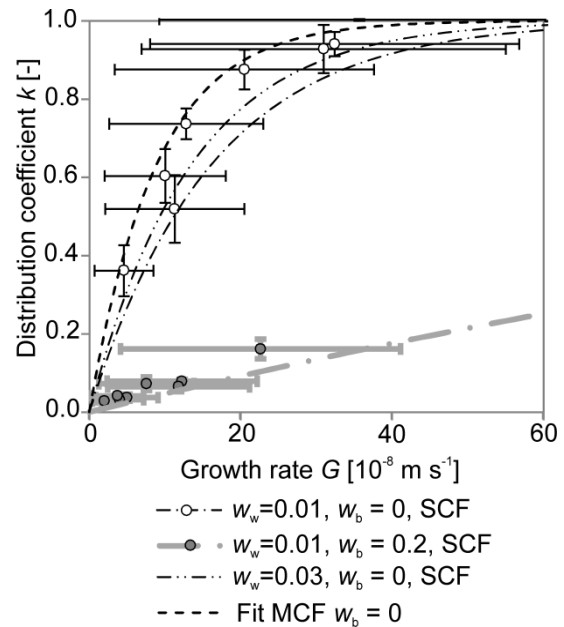
$$k_{low} = \frac{0.2 w_C m_0}{m_{Res} w_{Res} - w_0(0.8 m_0 - m_C)}. \quad (6.1.6)$$



As the index suggests, this is a lower estimate of the distribution coefficient. A real dead volume without any diffusive interaction with the active liquid in the same container is, of course, never to be found. Neither is a perfectly mixed melt, so the 2 different  $k$ -values resulting from the 2 different assumptions can be seen as limits with the most realistic value lying in between. In a melt of low viscosity, the upper, classic, value will be a good approximation while in a highly viscous melt, a more realistic assessment may tend to the lower value. If high accuracy is needed at an early stage, modelling the mass transport in the melt would allow narrowing down even further the realistic range of  $k$ . This is however, beyond the scope of this study.

The second source of error is the evaluation of the growth rate. Different methods to calculate the average growth rate of a lab experiment are discussed above (Ch. 4.3.2) in the material and methods part because they were applied to obtain values presented in the results section.

Fig. 6.6 presents data from the SCF setups after evaluation with the different methods. The upper end of the vertical error bar is the distribution coefficient like reported in the results section (Ch. 5.2.4), the lower end is the distribution coefficient calculated according to Eq. 6.1.6. The horizontal error bars range from the growth rate according to case A on the left to the growth rate according to case C on the right (cf. Ch. 4.3.2). It is obvious that the error in the growth rate calculation is much bigger than the error in the calculation of the distribution coefficient. This is especially interesting since the growth rate evaluation is often met with little interest. The upper limit of the error bars in  $G$ , i.e.  $G$  according to case C, is the more realistic



**Figure 6.6. Errors in distribution coefficient and growth rate, resulting from different methods of evaluation. In  $G$  the lower limit is according to Ch. 4.3.2, case A, and the upper limit according to case C of the same chapter. In  $k$  the upper limit is according to Eq. 2.2 and the lower from Eq. 6.1.6. The points are arbitrarily set at the average. The lines are the fit curves from Fig. 6.3.**

one. This can be seen from the comparison between SCF and GL setup. In the latter, the growth rate is directly optically measured over time. Only the upper value for the growth rate in the SCF allows comparability between the setups. Values reported in the literature are, however, often attained by a calculation closer to case A. This was also the case in the MCF experiments of the present study. The thickness at the end of the experiment was measured and divided by the duration. Such averaging under the assumption of constant growth rate, applied in a case where the growth rate is actually a function of the layer thickness, always

leads to an overrepresentation of the slowly-grown parts of the crystal layer because they took longer to grow. The resulting growth rate is too low. The values from the MCF are represented in Fig. 6.6 by the fit from Fig. 6.3. They do not stray as far from the values on the rightmost end of the error bars, as the leftmost ends do. This is due to the fact that in MCF a complete seed layer was provided. At a given growth rate and in a given time interval, the deposited mass is higher, if a larger area was seeded. Therefore, when assuming too large a seeded area, the growth rate calculated from deposited mass and duration becomes too low. The complete length of the error bar in  $G$ -direction is the sum of the 2 errors: assuming constant  $G$  and assuming immediate coverage of the surface by crystals. The difference between the upper broken line (MCF) and the rightmost ends of the black error bars (SCF,  $w_b = 0$ ), is due only to the first error, if no other difference affecting the performance was present. Judging from the position of these values, this could very well be the case. The difference between SCF-experiments with  $w_w = 1\%$  and  $w_w = 3\%$  is barely larger than the experimental inaccuracy. Therefore, an influence of the water content on the separation success cannot be seen from the results of the present study, neither in MCF nor in SCF.

These results show that sensible calculation of the average growth rate is absolutely crucial to comparability between setups and also for quantitative assessment of industrial applicability. The differences between MCF and SCF found in this study are likely to mostly be caused by the differences in growth rate evaluation with the results from the SCF being the more realistic ones.

### **6.3 Stronger natural convection as results of the additional liquid**

#### **6.3.1 Gradients of density, viscosity and diffusivity near the crystal front**

The previous subsection illustrated how the diffusive and convective mass transfer near the crystal front is crucial to the separation success and showed the experimental result that BuOH, added to the melt, vastly improves the process. The present subsection will argue that the differences in diffusivity, viscosity but also in density between the main component glycerol and the helping agent BuOH are important as BuOH strongly enhances natural convection. This subsection will only regard the liquid phase and will not make any statements about the crystal-liquid interaction, nor will its conclusions depend on any assumptions about such interaction. The phenomena at the S-L-interface will be discussed in Ch. 6.4. The only 3 facts used here are: First, concentration polarization, i.e. an increase of the non-crystallizing component's concentration somewhere near the crystal front, will take place to some extent. Secondly, the temperature at the crystal front cannot be lower than the temperature of the cooled surface, because the cooled surface is a heat sink while the crystal front is a heat source. Thirdly, the temperature near the crystal front cannot be higher than the melting temperature of pure glycerol. All 3 of these are necessarily the case

## Discussion

whenever crystallization at non-eutectic concentration is performed and succeeds in separating.

A very simple example calculation shall be used to clarify and illustrate the most important aspects: Consider a semi-infinite flat vertical crystal front growing horizontally in steady state into an infinite basin of binary melt. Viscosity  $\eta$  and diffusivity  $D$  may vary with the mass fraction of the second-component  $w_b$ . Apart from this, Boussinesq-approximation is applied.

The continuity equation is

$$\frac{\partial u}{\partial x} + \frac{\partial v}{\partial y} = 0, \quad (6.2.1)$$

momentum conservation in vertical  $y$ -direction yields

$$u \frac{\partial v}{\partial x} + v \frac{\partial v}{\partial y} = g \frac{\rho - \rho_\infty}{\rho_\infty} + \frac{\partial}{\partial x} \left( \frac{\eta}{\rho_\infty} \frac{\partial v}{\partial x} \right) + \frac{\partial}{\partial y} \left( \frac{\eta}{\rho_\infty} \frac{\partial v}{\partial y} \right) \quad (6.2.2)$$

and momentum conservation in horizontal  $x$ -direction yields

$$u \frac{\partial u}{\partial x} + v \frac{\partial u}{\partial y} = \frac{\partial}{\partial x} \left( \frac{\eta}{\rho_\infty} \frac{\partial u}{\partial x} \right) + \frac{\partial}{\partial y} \left( \frac{\eta}{\rho_\infty} \frac{\partial u}{\partial y} \right). \quad (6.2.3)$$

The energy conservation is described by

$$u \frac{\partial T}{\partial x} + v \frac{\partial T}{\partial y} = a \left( \frac{\partial^2 T}{\partial x^2} + \frac{\partial^2 T}{\partial y^2} \right). \quad (6.2.4)$$

From the mass conservation of the second component follows the diffusion equation

$$u \frac{\partial w_b}{\partial x} + v \frac{\partial w_b}{\partial y} = \frac{\partial}{\partial x} \left( D \frac{\partial w_b}{\partial x} \right) + \frac{\partial}{\partial y} \left( D \frac{\partial w_b}{\partial y} \right). \quad (6.2.5)$$

The density  $\rho$  varies not only with temperature but also with the second-component mass fraction  $w_b$ . In the context of solvent-aided layer crystallization, the density difference of the different components should be chosen large in comparison to the rather low influence of the temperature. Thus, the density in Eq. 6.2.2 shall be described as depending only on  $w_b$ :

$$\rho = \rho_\infty [1 - \chi w_b] \quad (6.2.6)$$

This allows decoupling of Eq. 6.2.4 from the other equations.

The horizontal velocity  $u$  at the crystal front is determined by the shift of the origin by growth rate  $G$  and by the contraction caused by the different densities of solid and liquid,  $\rho_s$  and  $\rho_l$ , respectively. In the present example of high-viscous melts, in the supposed geometry and at growth rates  $G \approx 10^{-7}$  m/s, the influence of this velocity on the overall stream conditions is unlikely to be big. Even for cylindrical geometries, neglecting of the growth rate in calculation of heat and mass transfer coefficients has been applied in simulation of the crystal layer growth, with good agreement between the simulated and experimental results [Bei13]. Furthermore, the classic theory on concentration near the crystal layer [Til53] predicts the concentration directly on the SL-interface to be independent of the growth rate in the steady state. Therefore, in this example the horizontal velocity at the interface shall be neglected:

## Discussion

$$u = G \frac{\rho_s}{\rho_l} \approx 0, \quad \text{at } x = 0. \quad (6.2.7)$$

This allows decoupling of Eq. 6.2.3, leaving a system of 3 partial differential equations Eqs. 6.2.1-2,5 with the boundary conditions

$$u = v = 0, \quad w_b = w_{b,0} \quad \text{at } x = 0, \quad (6.2.8)$$

$$v \rightarrow 0, \quad w_b = w_{b,\infty} \quad \text{as } x \rightarrow \infty. \quad (6.2.9)$$

The self-similarity of the system of Eqs. 6.2.1,2,5,8-9 allows its transformation into a system of ordinary differential equations by introducing

$$\omega = \frac{w_b - w_{b,\infty}}{w_{b,0} - w_{b,\infty}}, \quad \psi = 4 \nu_\infty \left[ \frac{Gr}{4} \right]^{\frac{1}{4}} f(\xi), \quad \xi = \left[ \frac{Gr}{4} \right]^{\frac{1}{4}} \frac{x}{y} \quad (6.2.10)$$

$$Gr = \frac{g\chi [w_{b,0} - w_{b,\infty}] y^3}{\nu_\infty^2}, \quad Sc_\infty = \frac{\nu_\infty}{D_\infty}, \quad \nu_\infty = \frac{\eta_\infty}{\rho_\infty} \quad (6.2.11)$$

where the index  $\infty$  signifies the properties at  $w_{b,\infty}$ .  $Gr$  is the Grashof number and  $Sc$  is the Schmidt number. The influence of  $w_b$  on viscosity and diffusivity is described by

$$\eta = \eta_\infty e^{-\varepsilon \omega} \quad (6.2.12)$$

$$D = D_\infty [1 + \delta \omega], \quad (6.2.13)$$

which are simplified forms of the empirical correlations given in the appendix (Ch. A.1).

Substitution of Eqs. 6.2.10-13 into Eqs. 6.2.1-2,5,8-9 gives

$$f''' + f'' [3 f e^{\varepsilon \omega} - \varepsilon \omega'] + e^{\varepsilon \omega} [\omega - 2 f'^2] = 0 \quad (6.2.14)$$

$$\omega'' + \left( \frac{3 Sc_\infty f}{1 + \delta \omega} \right) \omega' + \frac{\delta \omega'^2}{1 + \delta \omega} = 0 \quad (6.2.15)$$

with boundary conditions

$$f'(0) = 0, \quad f(0) = 0, \quad \omega(0) = 1, \quad (6.2.16)$$

$$f'(\xi) = 0, \quad \omega(\xi) = 0, \quad \text{as } \xi \rightarrow \infty. \quad (6.2.17)$$

The prime indicates differentiation with respect to  $\xi$ . The continuity Eq. 6.2.1 is solved by the stream function  $\psi$  with

$$\frac{\partial \psi}{\partial x} = v, \quad \frac{\partial \psi}{\partial y} = -u. \quad (6.2.18)$$

This problem is mathematically equivalent to a heat transfer problem presented by ELBASHBESHY & IBRAHIM [Elb93] and is treated similarly, here. However, some mistakes these authors made concerning the physical meaning are corrected.

The system of higher-order ordinary differential Eqs. 6.2.14-15 is transformed into a system of first-order ordinary differential equations by defining

## Discussion

$$\Psi_n \in \mathbb{R}^5, \quad n \in \mathbb{N}_0, \quad \Psi_n = \begin{pmatrix} \Psi_{1,n} \\ \Psi_{2,n} \\ \Psi_{3,n} \\ \Psi_{4,n} \\ \Psi_{5,n} \end{pmatrix} := \begin{pmatrix} f(n\Delta\xi) \\ f'(n\Delta\xi) \\ f''(n\Delta\xi) \\ \omega(n\Delta\xi) \\ \omega'(n\Delta\xi) \end{pmatrix} \quad (6.2.19)$$

for a fixed  $\Delta\xi > 0$ . Substituting Eqs. 6.2.19 into Eqs. 6.2.14-15 yields the system

$$\Psi'_n = F(\Psi_n) \quad (6.2.20)$$

with

$$F: \mathbb{R}^5 \rightarrow \mathbb{R}^5, \quad \begin{pmatrix} \Psi_{1,n} \\ \Psi_{2,n} \\ \Psi_{3,n} \\ \Psi_{4,n} \\ \Psi_{5,n} \end{pmatrix} \mapsto \begin{pmatrix} \Psi_{2,n} \\ \Psi_{3,n} \\ -\Psi_{3,n}[3\Psi_{1,n}e^{\varepsilon\Psi_{4,n}} - \varepsilon\Psi_{5,n}] - e^{\varepsilon\Psi_{4,n}}[\Psi_{4,n} - 2\Psi_{2,n}^2] \\ \Psi_{5,n} \\ -\left(\frac{3Sc_\infty\Psi_{1,n}}{1+\delta\Psi_{4,n}}\right)\Psi_{5,n} - \frac{\delta\Psi_{5,n}^2}{1+\delta\Psi_{4,n}} \end{pmatrix}. \quad (6.2.21)$$

Eq. 6.2.21 is solved by the 4<sup>th</sup>-order Runge-Kutta method: Define

$$\begin{aligned} b_{i,n} \in \mathbb{R}^5, \quad i \in \{1,2,3,4\}, \quad n \in \mathbb{N}_0, \quad b_{1,n} = F(\Psi_n), \quad b_{2,n} = F\left(\Psi_n + b_1 \frac{\Delta\xi}{2}\right), \\ b_{3,n} = F\left(\Psi_n + b_2 \frac{\Delta\xi}{2}\right), \quad b_{4,n} = F(\Psi_n + b_3 \Delta\xi) \end{aligned} \quad (6.2.22)$$

and evaluate  $\Psi_n$  by the recursive formula

$$\Psi_0 = \begin{pmatrix} 0 \\ 0 \\ \kappa_{f''} \\ 1 \\ \kappa_{\omega'} \end{pmatrix}, \quad \Psi_{n+1} = \Psi_n + \frac{(b_{1,n} + 2b_{2,n} + 2b_{3,n} + b_{4,n})}{6} \Delta\xi. \quad (6.2.23)$$

The starting values  $\kappa_{f''}$  and  $\kappa_{\omega'}$  have to be found from the boundary conditions, Eq. 6.2.17, by Nachtsheim-Swigert-like shooting technique, i.e. in an iterative process,  $\kappa_{f''}$  and  $\kappa_{\omega'}$  are chosen such that

$$\natural := \sqrt{f'(\xi_\infty)^2 + f''(\xi_\infty)^2 + \omega(\xi_\infty)^2} \quad (6.2.24)$$

yields a sufficiently low value for any sufficiently high value of  $\xi_\infty$ . In the present case,  $\xi_\infty$  was usually set to 10 with  $\Delta\xi = 0.01$  and  $\natural$  limited to  $10^{-4}$ . This example is easy enough to be implemented into an excel-worksheet.

The vertical velocity, parallel to the plate, as induced by natural convection is

$$v = \frac{2\nu\sqrt{Gr}}{y} f'. \quad (6.2.25)$$

## Discussion

Therefore  $f'$  is a dimensionless measure for the vertical velocity. Its profile,  $f'(\xi)$ , depends on  $Sc_\infty$ ,  $\varepsilon$  and  $\delta$  and influences the profiles of diffusivity and viscosity in the layer.

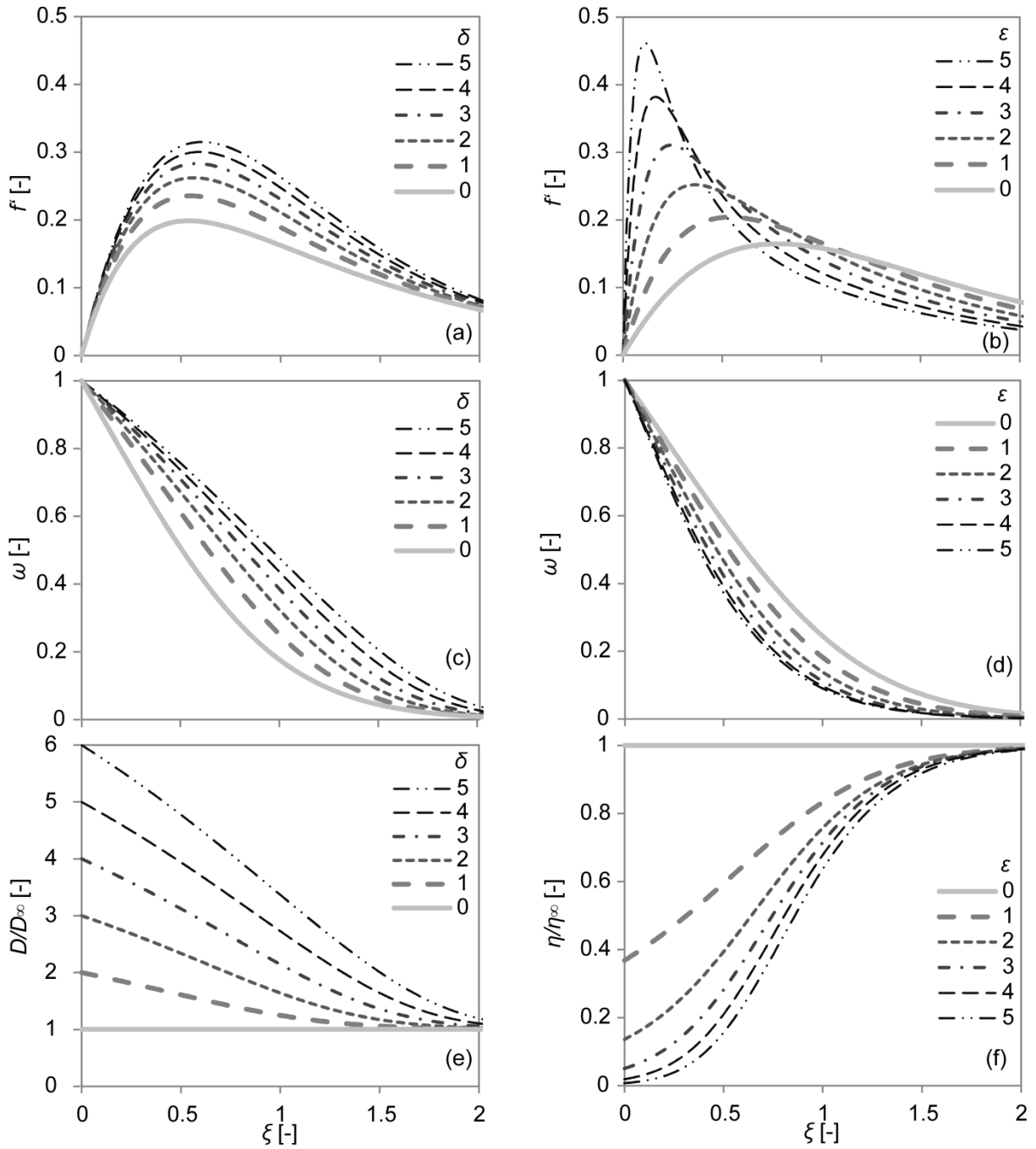
Values of  $\varepsilon$  and  $\delta$  depend on the system and also on the concentrations  $w_{b,0}$  and  $w_{b,\infty}$ . For the system glycerol-butanol and the theoretical case where an infinitely small fraction of BuOH in the free melt accumulates to a film of pure butanol right next to the crystal layer, i.e.  $\Delta w_b = w_{b,0} - w_{b,\infty} = 1$ , the values would be  $\varepsilon \approx \delta \approx 6$ . They are lower for lower values of  $\Delta w_b$ .

Different profiles arising from different values of  $\varepsilon$  and  $\delta$  at constant  $Sc_\infty = 4$  are shown in Fig. 6.7. An increasing value of  $\delta$ , which means that the diffusivity increases stronger with increasing  $\omega$ , leads to a slight decrease of the dimensionless velocity level and shifts the maximum of  $f'$  slightly further away from the crystal front (Fig. 6.7.a). Therefore, the slope of the solute mass fraction  $w_b$  directly at the crystal front increases with increasing  $\delta$ , i.e.  $-\omega'(0)$  decreases (Fig. 6.7.c). This means that the convective enhancement of the mass transport is weakened. However, the diffusive mass transport is favoured because the diffusivity increases near the crystal front (Fig. 6.7.e).

The overall influence can be assessed by substituting Eqs. 6.2.10,13 into the first Fickian law:

$$j = -D \left( \frac{\partial w_b}{\partial y} \right)_{y=0} \xrightarrow{(6.2.10,13)} \frac{j_\delta}{j_{\delta=0}} = \frac{(1 + \delta)\omega'(0)_\delta}{\omega'(0)_{\delta=0}}, \quad (6.2.26)$$

with the diffusive mass flux  $j$ . The value of  $-\omega'(0)$  has to be corrected by a factor  $(1 + \delta)$  to show the overall influence of  $\delta$  on the mass transport. The result is shown in Fig. 6.8. The weaker effect of natural convection is more than compensated by the increased diffusion coefficient at the crystal front. The overall mass transport rate increases.



**Figure 6.7.** Profiles of dimensionless vertical velocity  $f'$  (a,b), the reduced concentration parameter  $\omega$  (c, d), the relative diffusivity  $D/D_\infty$  (e) and relative viscosity  $\eta/\eta_\infty$  (f), for different values of the diffusivity variation parameter  $\delta$  (a, c, e) and the viscosity variation parameter  $\varepsilon$  (b, d, f), all drawn vs. the space coordinate, i.e. the dimensionless distance from the crystal front  $\xi$  at a constant Schmidt number in the bulk of the melt of  $Sc_\infty = 4$  and a constant value of the non-variated parameter of  $\varepsilon = 1$  (a,c,e) and  $\delta = 0.12$  (b,d,f).

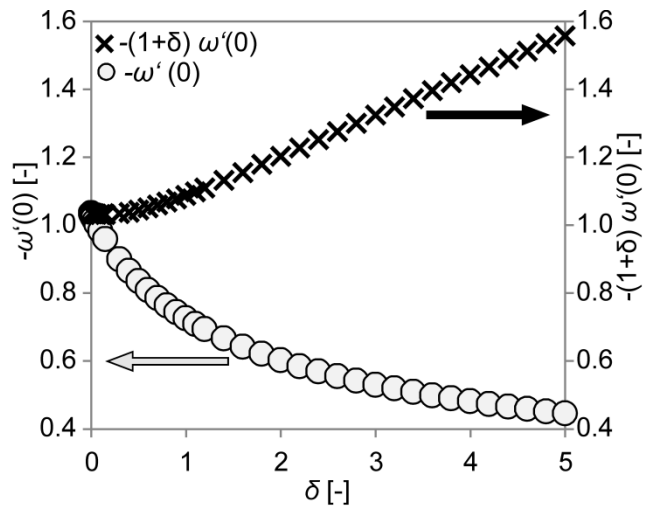
A higher value of  $\varepsilon$  shifts the maximum of  $f'$  closer to the crystal front and increases its value (Fig. 6.7.b).  $\omega$  decreases stronger near the crystal layer, which means that the convective enhancement of the mass transport increases (Fig. 6.7.d). This takes direct influence on the overall mass transport. A correction similar to the one made for the diffusivity is not necessary for the viscosity because diffusivity and viscosity are treated separately in this calculation and the viscosity does not directly appear in the Fickian law. Of course, the

## Discussion

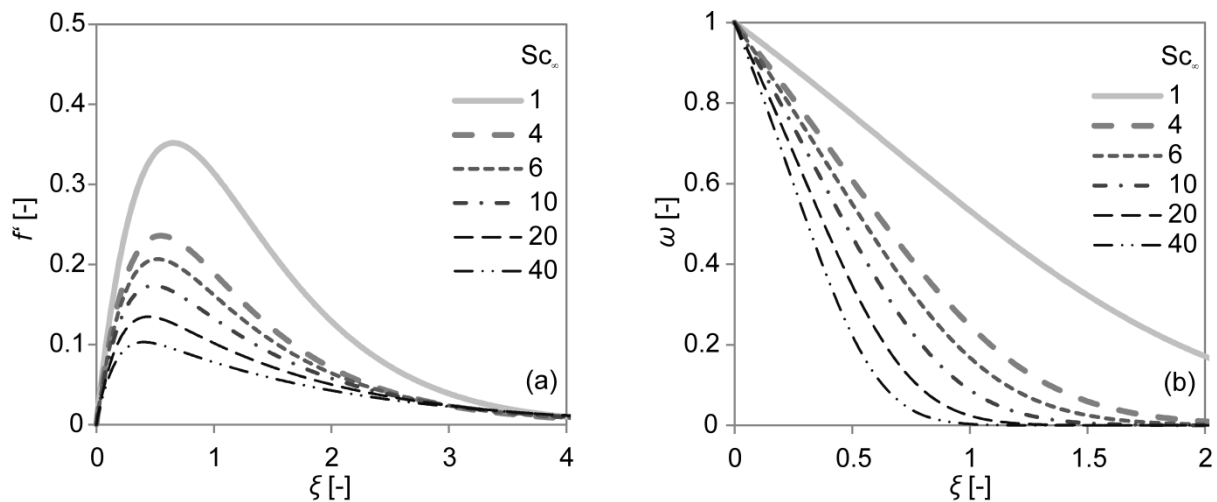
independent variation of diffusivity and viscosity is an experiment of thought as these 2 quantities strongly correlate in real organic systems.

The influence of  $Sc_\infty$  on the profiles of  $f'$  and  $\omega$  is shown in Fig. 6.9. A higher Schmidt number moves the maximum velocity closer to the crystal front but reduces the overall level of velocity. The decrease of  $\omega$  with  $\xi$  is shifted closer to the crystal front. The influence of convection on the mass transport increases with increasing  $Sc_\infty$ . This is to be expected because the Schmidt number is the ratio of convective to diffusive mass transport. The effect of  $Sc_\infty$  on the combined mass transfer is a topic below (Ch. 6.3.2).

The example calculation in this chapter illustrates how the dependence of viscosity and diffusivity on the second component mass fraction leads to a shift to favourable values of the quantities near the crystal front, i.e. right where they are needed. The dependence of the density on the composition leads to natural convection. The combination of these effects leads to an increase in the mass transfer coefficient, which is discussed in the following chapter.



**Figure 6.8.**  $-\omega'(0)$  as a parameter for the convection-induced mass transfer and  $-(1+\delta)\omega'(0)$  as a parameter for the overall mass transfer drawn as a function of the diffusivity variation parameter  $\delta$ .  $\varepsilon = 1$ ,  $Sc_\infty = 4$ .



**Figure 6.9.** Profiles of dimensionless vertical velocity  $f'$  (a) and reduced concentration parameter  $\omega$  (b) drawn vs. the dimensionless distance from the crystal front  $\xi$  for different values of the Schmidt-number in the bulk of the melt  $Sc_\infty$ .  $\varepsilon = 1$ ,  $\delta = 1$ .



### 6.3.2 The overall mass transfer coefficient $\beta$ at the crystal front

When considering a large vertical planar interface of height  $y$  or the portion below  $y$  of a semi-infinite vertical planar interface inserted into an infinite fluid environment, the Sherwood number  $Sh$  is defined as

$$Sh = \frac{\beta y}{D}. \quad (6.2.27)$$

This is the mass transport rate from the interface into the fluid divided by the mass transport rate through a perfectly stagnant layer of the same fluid with a layer thickness equal to  $y$  at the same driving concentration difference. Therefore, in the context of Eqs. 6.2.1,2,5,8-9 and Eqs. 6.2.14-17,  $Sh$  can also be written as

$$Sh = - \frac{y}{w_{b,0} - w_{b,\infty}} \left( \frac{\partial w_b}{\partial x} \right)_{x=0} = - \left( \frac{Gr}{4} \right)^{\frac{1}{4}} \omega'(0). \quad (6.2.28)$$

The Sherwood number is a measure for the influence of convection on the mass transport. In layer crystallization, a high Sherwood number is desirable for better transport of impurities out of the vicinity of the crystal front into the bulk of the melt.

A widely applied technique to attain  $Sh$  for the present case is an empirical correlation [Chu75]:

$$Sh = \left( 0.825 + 0.387 \left( Gr Sc_{0.5} \left( 1 + \left( \frac{0.492}{Sc_{0.5}} \right)^{\frac{9}{16}} \right)^{-\frac{16}{9}} \right)^{\frac{1}{6}} \right)^2. \quad (6.2.29)$$

The index 0.5 means that the liquid properties at  $w_{b,0.5} = 0.5 \cdot (w_{b,0} + w_{b,\infty})$  are taken. The correlation is valid for  $0.1 < Gr \cdot Sc < 10^{12}$ .

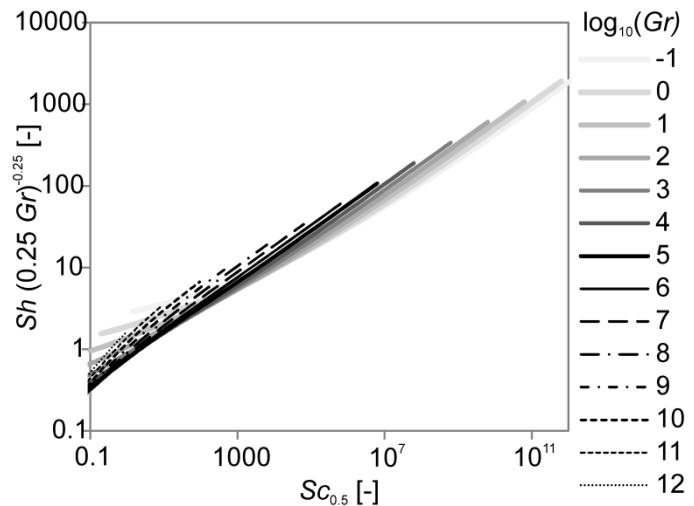


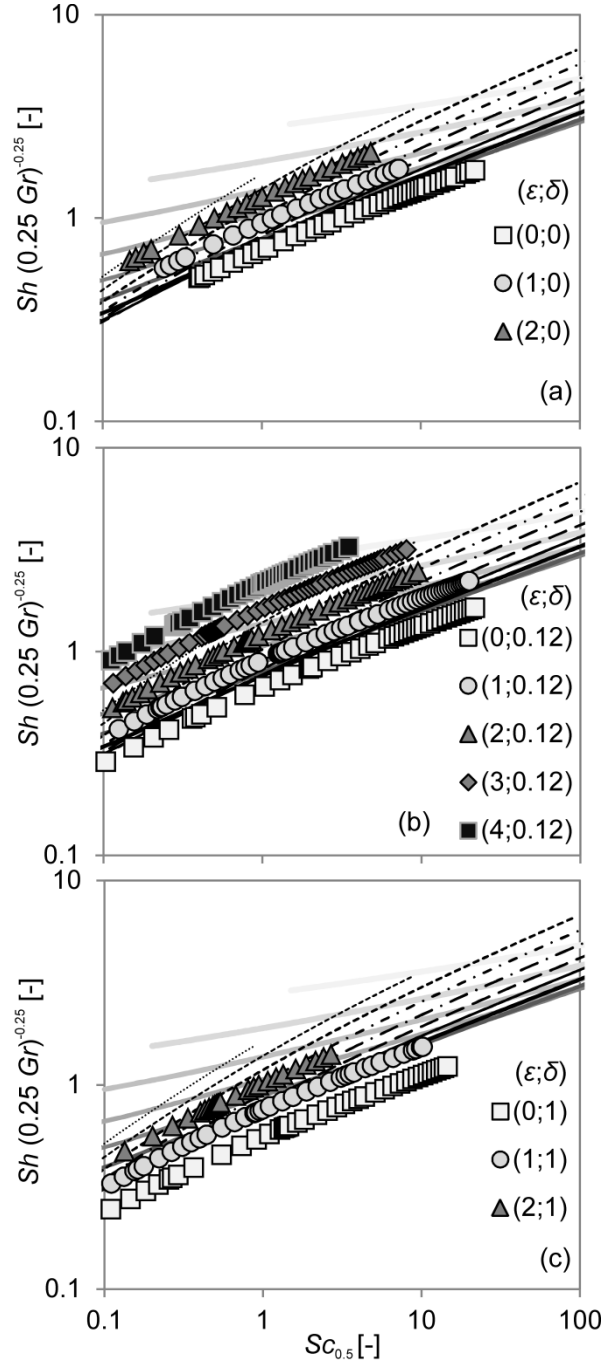
Figure 6.10.  $Sh \cdot [0.25 Gr]^{-0.25}$  calculated from Eq. 6.2.29 drawn vs. the Schmidt number at average temperature and concentration  $Sc_{0.5}$  for Garshof numbers  $Gr$  of 14 orders of magnitude ( $0.1 < Gr < 10^{12}$ ). The lines are only drawn in the  $Sc$ -interval in which  $0.1 < Gr \cdot Sc < 10^{12}$ .

Eqs. 6.2.1-28 and Eq. 6.2.29 describe the same physical phenomenon but they are not equivalent. On the one hand, in Eqs. 6.2.14-28,  $-\omega'(0) = Sh \cdot [0.25 Gr]^{-0.25}$  is a  $Gr$ -independent measure of the mass transport rate. In Eq. 6.2.29, on the other hand,  $Sh \cdot [0.25 Gr]^{-0.25}$  still weakly depends on  $Gr$ . For very high  $Gr$  it scales with  $Gr^{1/12}$ . Within the boundaries of applicability of the equation, this dependence is very limited, as can be seen in Fig. 6.10.

$Sh \cdot [0.25 Gr]^{-0.25}$  vs.  $Sc$  curves for 14 orders of magnitude of  $Gr$  are drawn with restriction to the  $Sc$  interval in which  $0.1 < Gr \cdot Sc < 10^{12}$  is satisfied. The width in  $Sh \cdot [0.25 Gr]^{-0.25}$  direction of the area of the coordinate plane that is covered by this set of curves is the maximal influence of  $Gr$ . In the physically interesting area of  $Sc < 10^8$ , this maximal influence amounts to approximately half an order of magnitude in  $Sh \cdot [0.25 Gr]^{-0.25}$  i.e. a change by a factor of circa  $10^{0.5}$ . On the other hand,  $\varepsilon$  and  $\delta$  are not explicitly mentioned in Eq. 6.2.29 even though the correlation is valid for substances that change their properties with temperature and composition. When comparing results from the calculation methods, Eqs. 6.2.1-28 and Eq. 6.2.29,  $\varepsilon$  and  $\delta$  become explicitly present in the conversion of  $Sc_\infty$  into  $Sc_{0.5}$ ,

$$Sc_{0.5} = \frac{2 e^{-\frac{\varepsilon}{2}} Sc_\infty}{\left(1 + \frac{\delta}{2}\right) \left(1 + \frac{\rho_0}{\rho_\infty}\right)} \quad (6.2.30)$$

The density ratio of BuOH to glycerol is  $\rho_0/\rho_g = 0.65$  within the relevant temperature range  $-15^\circ\text{C} < T < 15^\circ\text{C}$ , which is a very low value for 2 miscible organic liquids. The value  $\rho_0/\rho_\infty$  would in almost all cases be closer to unity. For the following examples,  $Sc_{0.5}$  was calculated with  $\rho_0/\rho_\infty^{\text{mean}} = 0.84$  and error bars representing the maximal influence of  $0.65 < \rho_0/\rho_\infty < 1$  being smaller than the used symbols.



**Figure 6.11.** Comparison between results from Eqs. 6.2.1-28,30 (symbols) and Eq. 6.2.29 (lines).  $-\omega'(0) = Sh \cdot [0.25 Gr]^{-0.25}$  as measure of the convective enhancement of the mass transport rate drawn vs. the Schmidt number  $Sc_{0.5}$ . The lines are the same as in Fig. 6.10. The symbols represent results for different values of  $\varepsilon$  and  $\delta$  as given in the legend.

## Discussion

Fig. 6.11 compares results from the different methods. The set of curves with  $\varepsilon$  ranging over the physically interesting range  $0.3 < \varepsilon < 4$  at a small value of  $\delta = 0.12$  covers the same area in the coordinate plane as the set of curves from Eq. 6.2.29 for all possible values of  $Gr$ . A higher value of  $\delta$  moves the results from Eqs. 6.2.1-28 towards lower values of  $Sh \cdot [0.25 Gr]^{0.25}$  but this does not necessarily produce a discrepancy in the final result of mass transfer rate because the correction described in Eq. 6.2.26 and Fig. 6.8 would be applied first. All in all, Fig. 6.11 shows that Eqs. 6.2.1-28 and Eq. 6.2.29 yield similar results without being equivalent. Quantitative discrepancies do exist. The main reason is that Eqs. 6.2.1-28 make simplifying assumptions that lead to quantitative errors while Eq. 6.2.29 is fitted to real data with high accuracy.

For high values of  $Sc_\infty$ ,  $\varepsilon$  and  $\delta$ , very small deviations in  $\kappa_{F'}$  and  $\kappa_{W'}$  lead to arithmetic overflow when applying Eq. 6.2.23. This makes the shooting very tedious or even impossible. Eq. 6.2.29, being an arithmetic expression, always produces a value as result. Eqs. 6.2.1-28 were used because they allow the illustration of different gradients forming near the crystal layer, as they are given above (Figs. 6.7,9). The integral and quantitative investigation of the solvents influence on the transport of impurity away from the crystal layer shall be performed by Eq. 6.2.29 only, due to its higher accuracy and stability.

When using Eq. 6.2.29, simplified functional dependencies of the melts properties on composition and temperature like Eqs. 6.2.6,12-13 are not necessary. Only melt properties for certain, discrete, values of  $w$  and  $T$  have to be fed into arithmetic equations like Eq. 6.2.29 and Eq. 6.2.27 while differential equations like Eqs. 6.2.1-5 require known functions. Therefore, the temperature-dependence as well as the influence of more than 2 components can be taken into account, too. Furthermore, the representation of actual physical data can be improved by allowing multiple-parameter correlations. In the present case, the properties of ternary gwb-melts were calculated with the correlations given in the appendix, accounting for the influence of temperature  $T$ , BuOH mass fraction  $w_b$ , and water mass fraction  $w_w$ .

The Grashof number  $Gr$  taking into account influences of temperature and second and third component is defined by

$$Gr = \frac{g y^3}{\nu_{0.5}^2} \left| \frac{\rho_0 - \rho_\infty}{\rho_\infty} \right|, \quad (6.2.31)$$

with gravitational acceleration  $g$  and vertical extension of the crystal front  $y$ . The index 0 signifies the value at the crystal front, i.e. at  $T_0$ ,  $w_{b,0}$ , and  $w_{w,0}$ . The index  $\infty$  means the values far away from the crystal front, e.g.  $\rho_\infty = \rho(T_\infty, w_{b,\infty}, w_{w,\infty})$ , and the index 0.5 is given to properties at the pairwise arithmetic mean of temperature and mass fractions at the crystal front and far away from it, e.g.  $T_{0.5} = 0.5 \cdot (T_0 + T_\infty)$ . Additionally to the actual, or total, Grashof

## Discussion

number  $Gr$  from Eq. 6.2.31, a thermal Grashof number  $Gr_{\text{therm}}$  that only takes the buoyancy force caused by expansion due to temperature change into account is defined as

$$Gr_{\text{therm}} = \frac{g y^3}{\nu_{0.5}^2} \left| \frac{\rho(T_0, w_{b,0.5}, w_{w,0.5}) - \rho(T_\infty, w_{b,0.5}, w_{w,0.5})}{\rho(T_\infty, w_{b,0.5}, w_{w,0.5})} \right|. \quad (6.2.32)$$

The composition at the crystal front is not known apart from the restrictions stated at the beginning of this subsection,

$$w_{b,\infty} \leq w_{b,0} \leq 1, \quad T_{\text{CF}}^{\text{min}} < T_0 \leq T_g^* = 18.17 \text{ }^\circ\text{C}, \quad (6.2.33)$$

with the lowest used cold finger temperature,  $T_{\text{CF}}^{\text{min}} = -20 \text{ }^\circ\text{C}$ . In order to meet the restriction to  $w_{b,0}$ , it is sensible to use another parameter than  $\kappa = w_{b,0}/w_{b,\infty}$  to describe the concentration polarization. Instead, assume for a binary gb-melt

$$w_{b,0} = (1 - e^{-\Omega w_{b,\infty}}), \quad (6.2.34)$$

with the new parameter  $\Omega$  describing the intensity of concentration polarization and

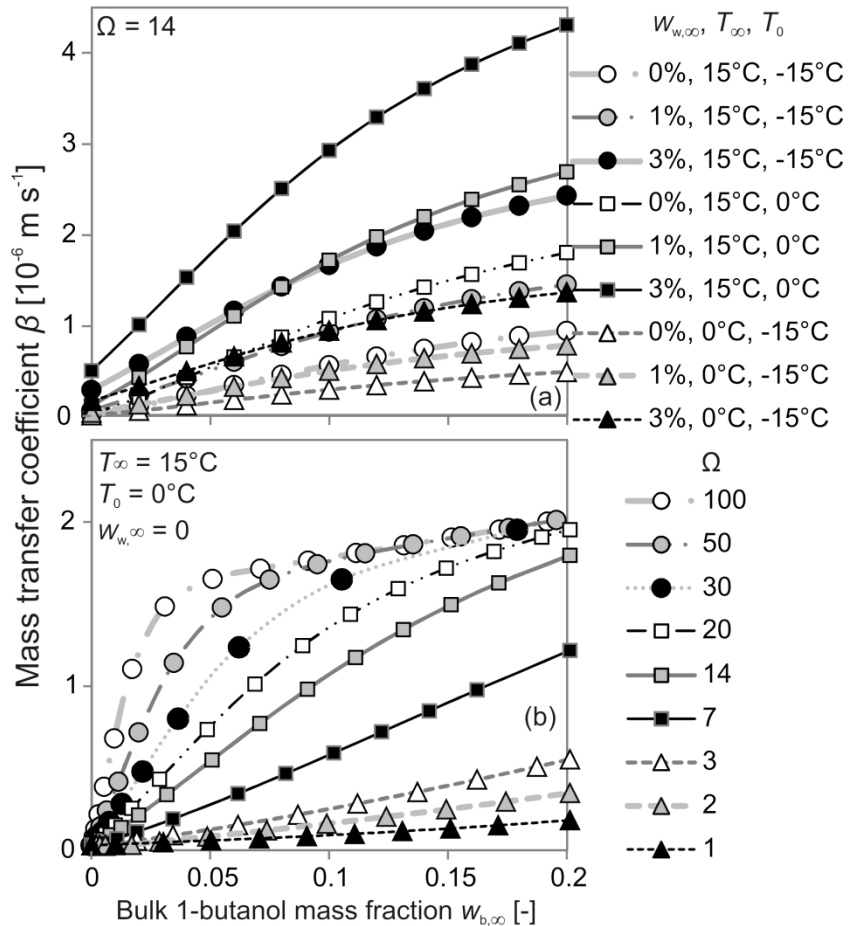
$$\lim_{w_{b,\infty} \rightarrow 0} \kappa = \Omega. \quad (6.2.35)$$

When considering only the liquid phase and no SL-interaction, water and BuOH can be treated similarly. So, for a ternary gw-melt,

$$w_{b,0} = \frac{w_{b,\infty}}{w_{b,\infty} + w_{w,\infty}} (1 - e^{-\Omega(w_{b,\infty} + w_{w,\infty})}), \quad (6.2.36)$$

$$w_{w,0} = \frac{w_{w,\infty}}{w_{b,\infty} + w_{w,\infty}} (1 - e^{-\Omega(w_{b,\infty} + w_{w,\infty})}). \quad (6.2.37)$$

Within the boundaries of Eq. 6.2.33,  $T_\infty$ ,  $T_0$  and  $\Omega$  can be varied freely. Fig. 6.12.a shows that for any combination an increasing  $w_{b,\infty}$  has a positive effect on the mass transfer coefficient  $\beta$ . The effect of temperature difference is less important than the effect of temperature level. A higher water content increases the overall level of  $\beta$  but very slightly decreases the effect of BuOH at high  $w_{b,\infty}$ . Note that this is only



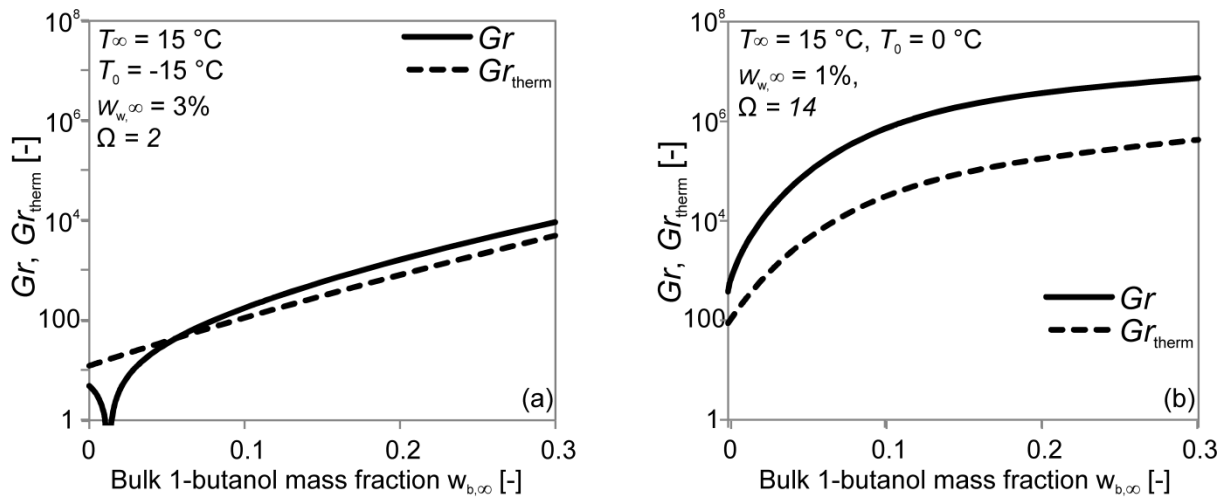
**Figure 6.12. Mass transfer coefficient as a function of the mass fraction of BuOH far away from the crystal front for different temperatures  $T_\infty$ ,  $T_0$  and different water mass fractions far away from the crystal front (a) and for different levels of concentration polarization (b).**

valid in this example, where temperature level and water content are varied independently. In a real crystallization, a higher water content would necessitate a lower temperature level.

The slope of the lower curves seems to be rather small, but in comparison to the absolute starting values, the increase in  $\beta$  with increasing  $w_{b,\infty}$  is never negligible. From Fig. 6.12.b. the influence of  $\Omega$  is visible. The initial slope  $(d\beta/dw_{b,\infty})_{w_{b,\infty}=0}$  increases with increasing  $\Omega$ , because  $w_{b,0}$  increases faster, leading to lower viscosity near the crystal front as well as a larger difference in density, causing stronger natural convection. At high values of  $\Omega$ , the curves reach a quasilinear part in which no influence of  $\Omega$  is apparent. In this regime,  $w_{b,0}$  reached its upper limit in unity, and further increase in  $w_{b,\infty}$  reduces the density gradient. However,  $\beta$  rises further, which is due to the overall decrease in viscosity and overall increase in diffusivity.

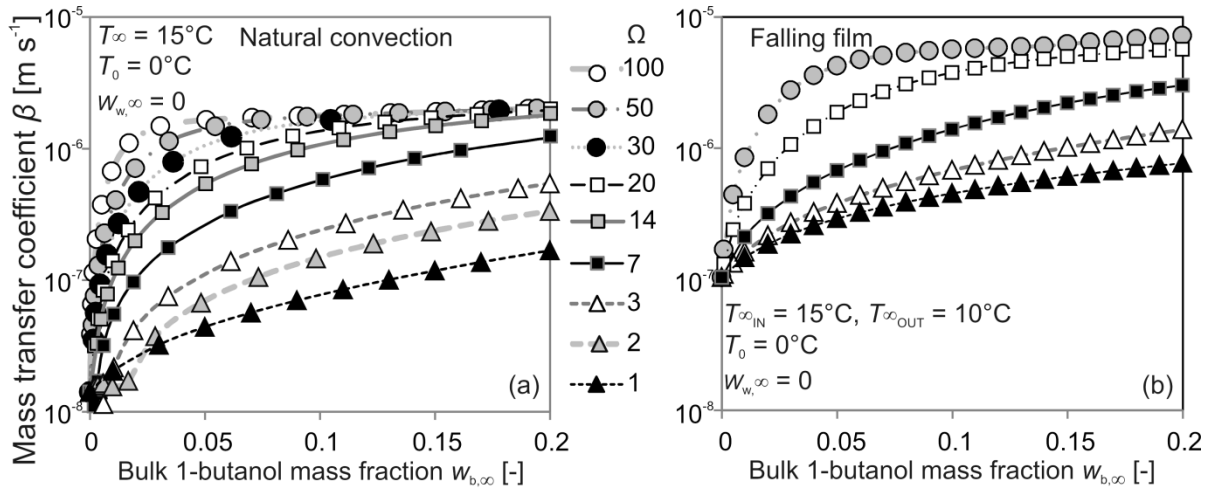
For further illustration of the role of viscosity and density difference, Fig. 6.13 gives a comparison of  $Gr$  and  $Gr_{\text{therm}}$ . The thermal expansion increases the density, because  $T_0 < T_\infty$  in this example, and would lead to a downwards velocity of the liquid near the crystal front. The compositional effect is pointed in the opposite direction.  $w_{b,0} > w_{b,\infty}$  decreases the density and causes upwards flow near the crystal front. In Fig. 6.13.a, a very high

$\Delta T = T_\infty - T_0 = 30 \text{ K}$  and little concentration polarization,  $\Omega = 2$ , were chosen to give an example of an extremely strong thermal effect in relation to a weak compositional effect. In this example, the thermal effect can fully compensate the compositional effect at  $w_{b,\infty} \approx 1.2\%$ . But at  $w_{b,\infty} > 5\%$ ,  $Gr$  surpasses  $Gr_{\text{therm}}$  and for  $w_{b,\infty} > 10\%$  remains approximately twice the value. Fig. 6.13.b. gives an example of mediocre  $\Delta T = 15 \text{ K}$  and stronger concentration polarization at  $\Omega = 14$ . In this case  $Gr$  is always much larger than  $Gr_{\text{therm}}$ . For  $w_{b,\infty} > 10\%$ , the ratio  $Gr/Gr_{\text{therm}}$  is approximately 20. Note that  $Gr$  is the final results, already including the partial compensation by the thermal effect. The increase in  $Gr_{\text{therm}}$  with increasing  $w_{b,\infty}$  is due to the viscosity reduction. While this effect is important, so is the effect of the unlike densities,  $\rho_b/\rho_g = 0.65$ , causing  $Gr/Gr_{\text{therm}} > 1$ .



**Figure 6.13.** Grashof number  $Gr$ , taking into account density change as result of changes in composition and temperature according to Eq. 6.2.31, and thermal Grashof number,  $Gr_{\text{therm}}$ , taking into account only density changes resulting from thermal expansion according to Eq. 6.2.32, drawn as a function of the mass fraction of BuOH in the melt far away from the crystal front. (a) is an extreme example of high temperature difference,  $\Delta T = T_\infty - T_0 = 30 \text{ K}$ , and little concentration polarization,  $\Omega = 2$ , thus an example of a small difference between  $Gr$  and  $Gr_{\text{therm}}$ . (b) is an example of medium temperature difference,  $\Delta T = T_\infty - T_0 = 15 \text{ K}$ , and stronger concentration polarization,  $\Omega = 14$ , thus an example of a larger difference between  $Gr$  and  $Gr_{\text{therm}}$ .

The experimental results of the present study suggested that a strong agitation of the melt has an effect on the separation success similar to the effect of using the aid of BuOH (cf. above, Ch. 6.1). The question of how the combination of strong agitation and solvent-aiding would affect the separation success has not been tackled experimentally within the present study. A first orientation can be found in Fig. 6.14. The falling film (b) increases the mass transfer coefficient without BuOH.  $\beta$  is further increased with increasing  $w_{b,\infty}$  and this effect as well as its dependence on  $\Omega$  is qualitatively similar to the case of natural convection (a) but the increase is smaller than in the case where only natural convection occurs.



**Figure 6.14.** Mass transfer coefficient of natural convection according to Eq. 5.2.29 (a) and of a falling film according to appendix A.3.

If a comparison between results from this example calculation and the experimental findings is desired, the cylindrical geometry of the cold finger as opposed to the planar geometry of the example calculation carried out so far, can be accounted for by using

$$Sh_{cylinder} = Sh_{plate} + 0.2175 \frac{y}{r_0 + \Delta r_{mean}} \quad (6.2.38)$$

where  $r_0 = 12.7$  mm is the radius of the cold finger,  $x = 120$  mm is the height and  $\Delta r_{mean} = 2.3$  mm is an assumed average thickness of the crystal layer.

Conversion of the experimental data fit parameter  $(dk/dG)_{G=0}$  into mass transfer coefficient,  $\beta$ , is done by Eq. 6.1.5. A result is presented in Fig. 6.15. The line shows  $\beta$  at  $T_0 = 2^\circ\text{C}$ ,  $T_\infty = 10^\circ\text{C}$  and  $\Omega = 14$ . The temperature  $T_\infty = 10^\circ\text{C}$  is approximately the average of the actually used beaker temperatures but the other values are chosen just to fit the curve. Even though the curve seems to fit the points within reasonable accuracy, no quantitative conclusions concerning the values of  $\Omega$  and  $T_0$  should be drawn. The assumption of  $\Omega = \text{const.}$  for all these experiments is not realistic.  $\Omega$  may not even be constant within one experiment. The same is true for the temperatures. The only conclusion that can be drawn from the Fig. 6.15 is that the effect of BuOH on the separation success can be explained by its effect on the mass transfer coefficient, if a sufficiently strong concentration polarization is supposed. The example calculation of this subsection overall shows that this effect on the mass transfer is not only caused by the increase in diffusivity but mainly by the enhancement of natural convection. This influence on natural convection, in turn, is not only caused by the reduction of overall viscosity level but also by the density gradient that forms during concentration polarization.

A value of  $\Omega = 14$  would mean that only very little liquid glycerol is present at the crystal front, e.g. at  $w_{b,\infty} = 20\%$ , the glycerol mass fraction would not be much more than  $w_{g,0} = 5\%$ . The mass ratio of water to glycerol would be  $\zeta_{wg} = 0.85$ , higher than in a eutectic binary mixture, where  $\zeta_{wg} = 0.5$ . On that side of the eutectic point, no glycerol could crystallize. A value of  $\Omega$  much lower than 14 would not be able to explain the effect found in the experiment. So either the concentration polarization is, more or less, as strong as supposed here and the BuOH does not

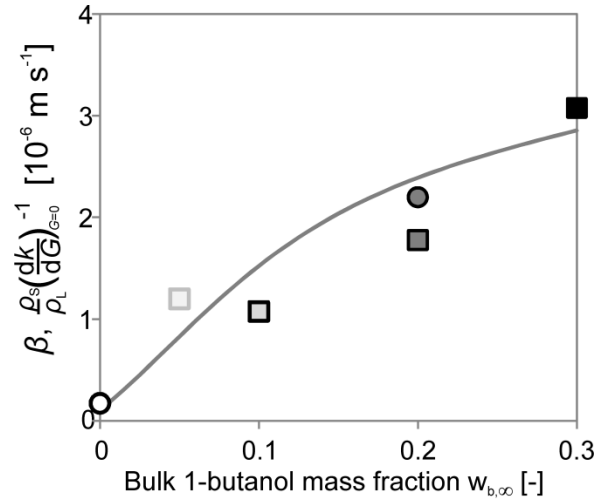


Figure 6.15. Mass transfer coefficient  $\beta$  according to Eqs. 6.2.29,36 for  $\Omega = 14$ ,  $T_0 = 2 \text{ }^\circ\text{C}$ ,  $T_\infty = 10 \text{ }^\circ\text{C}$ , (line) and pseudo mass transfer coefficient  $\rho_s(\rho_L(dk/dG)_{G=0})^{-1}$ , from experimental data (points). The symbols have the meaning given in the legend to Fig. 6.3.

interact with the crystal in any usual way, or the concentration polarization is actually much weaker than assumed here and a second effect of the BuOH combines with the effect in the liquid to make the experimentally shown difference. This, second, effect would most likely also occur at the crystal front. In both cases, the crystal front itself has to be discussed further. This will be done in the following (Ch.6.4).

## 6.4 Combined kinetic and thermodynamic effect of the additive

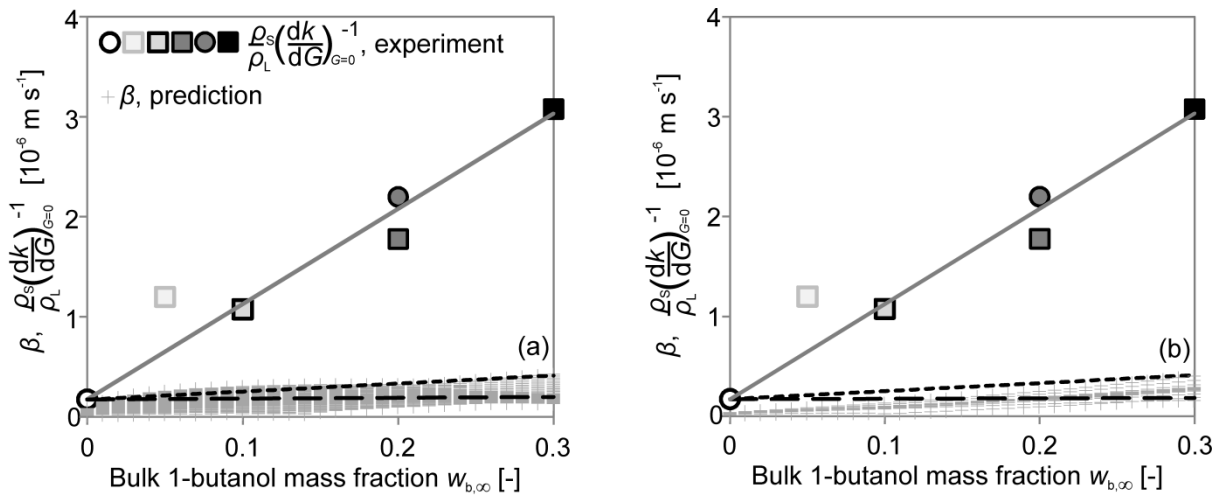
### 6.4.1 Quantitative comparison of different simplified simulation results to experimental values

Heretofore the discussion illustrated how BuOH would increase the mass transport coefficient  $\beta$  at the crystal front. The experimental results showed that BuOH allows the separation with the same distribution coefficient at faster growth rates. Both these findings fit with the cited theory, which always states that it is basically the ratio between growth rate and mass transfer coefficient that decides the distribution coefficient. However, no quantitative account of the relation between the theoretical and measured phenomena has been given hitherto. A quantitative comparison is, nevertheless, necessary to reveal whether or not the stated effects on mass transport have to be combined with other effects of BuOH to explain the extent of improvement it brings. This will be done in the present chapter by calculating all possible outcomes for  $\beta$  under different sets of assumptions for  $w_{w,\infty} = 1\%$ , always varying  $T_\infty$ ,  $w_{b,\infty}$  and  $\Omega$ , thus  $\kappa$ ,  $w_{w,0}$ , over the complete range that is physically sensible ( $0 \text{ }^\circ\text{C} \leq T_\infty \leq 20 \text{ }^\circ\text{C}$  in 1 K-steps,  $0 \leq w_{b,\infty} \leq 0.3$  in 0.01-steps,  $1 \leq \Omega \leq 19$  in 0.5-steps). In all of these calculations, the temperature at the crystal front is assumed to be the equilibrium temperature of the melt at that place. The cloud of possible  $\beta$  is plotted together



## Discussion

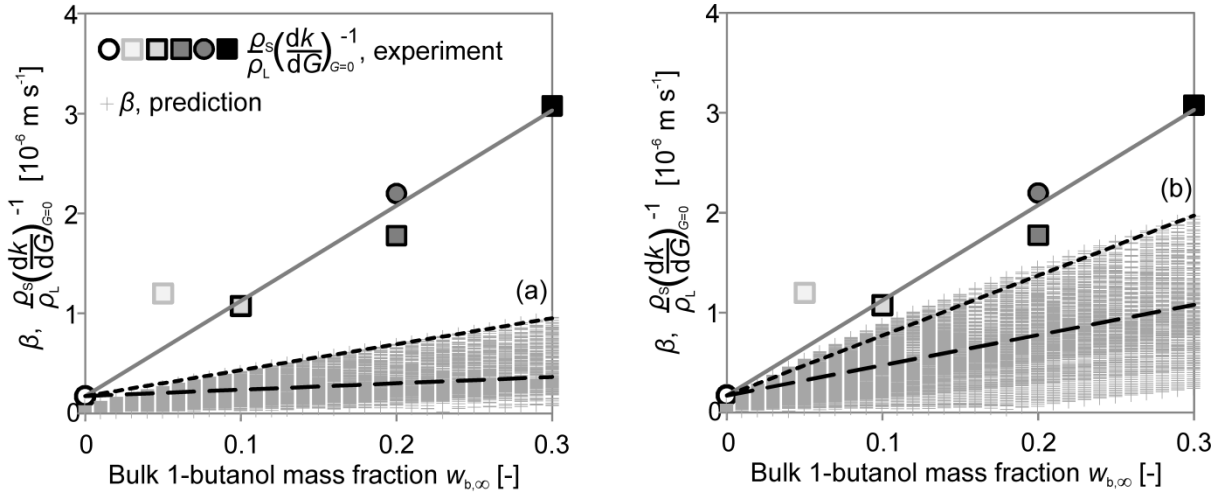
with experimentally found  $\rho_S/\rho_L \cdot (dk/dG)_{G=0}^{-1}$  vs.  $w_{b,\infty}$ . As follows from the discussion above (Ch. 6.2.1),  $\beta$  and  $\rho_S/\rho_L \cdot (dk/dG)_{G=0}^{-1}$  should show the same dependence on  $w_{b,\infty}$  if the BuOH only works through its influence on the mass transport and this influence is calculated correctly. If, therefore, the measured points of  $\rho_S/\rho_L \cdot (dk/dG)_{G=0}^{-1}$  are outside of the cloud of possible  $\beta$ , this shows the presence of another effect of BuOH besides those that are accounted for in the respective set of assumptions. Examples of large discrepancy are shown in Fig. 6.16. Fig. 6.16.a uses the assumption that BuOH takes an influence on  $T^*$ , though much less than water:  $dT^*/dw_b = -43 \text{ K} < dT^*/dw_w = -192 \text{ K}$ . Fig. 6.16.b assumes  $dT^*/dw_b = 0 \text{ K}$  but neglects concentration polarization of BuOH:  $w_{b,0} = w_{b,\infty}$ . In both cases, the calculated effect is much lower than the measured, which makes clear that a solvent's isothermal viscosity reduction is rather useless, as is the drop in the overall level of the viscosity. The viscosity reduction has to be paired with little influence on the crystallization temperature and the additive has to accumulate close to the crystal front.



**Figure 6.16.** Separation speed parameter  $\rho_S/\rho_L \cdot (dk/dG)_{G=0}^{-1}$  from experiments in GL (squares) and SCF (circles) setups drawn vs. the mass fraction of BuOH in the bulk of the melt  $w_{b,\infty}$  together with the mass transfer coefficient  $\beta$  (crosses) calculated under the false assumptions that BuOH would linearly change the liquids temperature at  $dT^*/dw_b = -43 \text{ K}$  (a) or that it didn't accumulate near the crystal front (b).

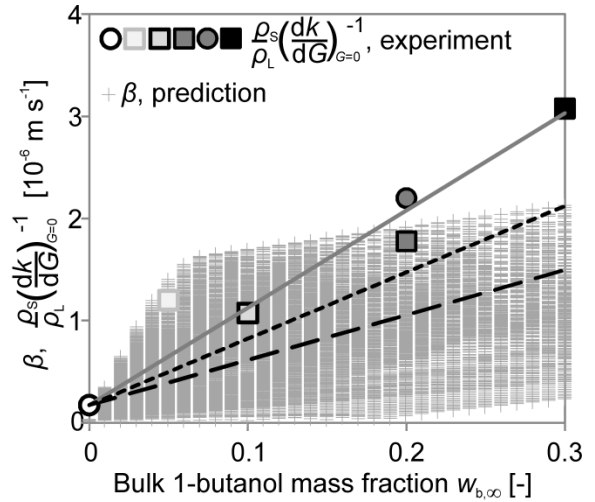
Fig. 6.17 plots results from calculations assuming  $dT^*/dw_b = 0 \text{ K}$  and concentration polarization of BuOH. Fig. 6.17.a uses  $Gr_{\text{therm}}$ , neglecting the BuOH's influence on the density and Fig. 6.17.b takes it into account. The difference between the 2 results shows that the density difference between BuOH and glycerol is important. The fact that both clouds still don't overlap with the experimental data shows that the BuOH does not work through its influence on  $\beta$  alone. Apart from affecting diffusion and convection, it also has to have an interfacial effect.

## Discussion



**Figure 6.17.** Separation speed parameter  $\rho_S/\rho_L \cdot (dk/dG)_{G=0}^{-1}$  from experiments in GL (squares) and SCF (circles) setups drawn vs. the mass fraction of BuOH in the bulk of the melt  $w_{b,\infty}$  together with the mass transfer coefficient  $\beta$  (crosses). The influence of BuOH on the density is neglected in (a) and taken into account in (b).

The polarity of BuOH is lower than that of glycerol. Because the glycerol crystal lattice doesn't contain BuOH, it is safe to say that the surface tension  $\gamma$  between a glycerol crystal and a liquid gwB-mixture will increase with increasing  $w_b$  in the liquid. The roughening of the crystal layer, including the faceting discussed above (Ch. 6.1), has to cause some fluctuations in  $w_b$  and  $w_w$ . Assuming that parts with higher  $w_b$  are less likely to be included into the melt, this would lead to  $K_b < K_w$ . Such an assumption can be justified theoretically, e.g. by MULLINS & SEKERKA's [Mul63] argument (cf. Figs. 2.12,13), and it fits the experimental finding that  $k_b < k_w$ . This would also mean that



**Figure 6.18.** Separation speed parameter  $\rho_S/\rho_L \cdot (dk/dG)_{G=0}^{-1}$  from experiments in GL (squares) and SCF (circles) setups drawn vs. the mass fraction of BuOH in the bulk of the melt  $w_{b,\infty}$  together with the mass transfer coefficient  $\beta$  (crosses) calculated under the assumption that  $\kappa_w = 2$ .

BuOH accumulates faster at the crystal front than water does,  $\kappa_b > \kappa_w$ , which was used for the calculation presented in Fig. 6.18, where  $\kappa_w = 2$  was assumed and  $\kappa_b$  was calculated as before. In this scenario, measured and calculated data overlap, but only for lower  $w_{b,\infty}$  and even there, the vast majority of possible  $\beta$  is below the measured  $\rho_S/\rho_L \cdot (dk/dG)_{G=0}^{-1}$ .

For a concise overview, a parameter  $\Xi$ , which puts the effect of BuOH on the time-efficiency of separation as found in more than 50 experiments into one number, shall be defined as

$$\Xi = \frac{\partial}{\partial w_{b,\infty}} \left( \frac{\rho_S}{\rho_L} \left( \left( \frac{\partial k}{\partial G} \right)_{G=0} \right)^{-1} \right). \quad (6.4.1)$$

It is taken from the linear fits that are shown in Figs 6.16-18. For each scenario,  $\Xi$  can be compared to the slopes of a linear regression of the  $\beta$  cloud and of a line through the highest point of the cloud. The axis intersection of these lines is fixed to the experimental one. The former slope can be called the mean and the latter the upper value of the  $\Xi$ -prediction. Fig. 6.19 compiles the results.

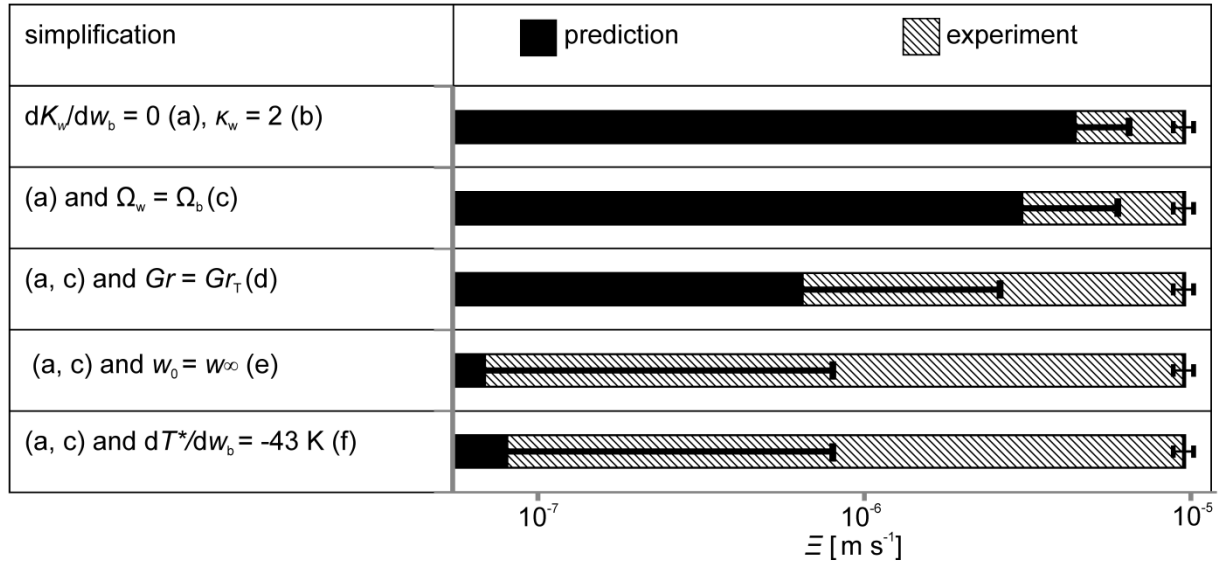


Figure 6.19. The parameter  $\Xi$ , expressing the influence of BuOH on the separation speed, as measured and as calculated under different sets of assumptions.

The effect that fills the gap between the predicted and experimental value is most probably the reduction of microroughening by the higher surface tension when BuOH is present. This effect can only occur if the growth proceeds far from equilibrium, because in equilibrium the BuOH would leave the interface which would be enriched by the component leading to the least surface tension. But if the process is slow enough to approach equilibrium, the separation would be very good, with or without the help of BuOH. So that again the effect of the additive is the stronger, the more it is needed. This conclusion, drawn from a hydrodynamic argument, that the surface tension has to play a role in the effect of BuOH fits the experimental finding that BuOH takes much less influence in the presence of a surfactant (cf. above, Ch. 5.2.9).

### 6.4.2 Classification of additives according to their effect on the separation

Three criteria can be used to classify the additives concerning their most likely influence on the quickness of separation: polarity, viscosity and density.

It is well known that there are cases in which solutes of very low concentration in the melt can take a large influence on the growth process. The premise for this effect is a strong affinity of the solute to the crystal surface, allowing surface enrichment, so that its concentration on the surface is not very low at all. This is only possible, if the solute reduces the interfacial tension. Such solutes would not be suitable additives to speed up the

## Discussion

separation process in melt layer crystallization, first, because they slow down the growth and, secondly, because the reduced surface tension favours liquid inclusions. An example encountered in the present study, is the surfactant SDS which had a negative influence on the separation, even at a concentration of only 100 ppm in the melt. A suitable additive would increase the surface tension if present in the liquid right next to the interface. To do so, it must differ from the nutrient in polarity. A polarity lower than that of the nutrient is more favourable than a higher one, because the former increases mobility of the solute in the interface. Lacking mobility would slow down the growth process and increase the risk of micro-roughening. If the solute increases the surface tension, it would leave the interface as equilibrium is approached. It can, therefore, only execute its influence on the interface because its rejection during growth makes the moving interface act like a source of solute and the process doesn't reach equilibrium. This nullifies the possibility of such an additive having a strong effect if its concentration in the melt is very low. Therefore, the polarity must still be close enough to that of the nutrient for miscibility to be given. In the case of glycerol, solutes of no or very low polarity, like N<sub>2</sub>, O<sub>2</sub>, Ar or butanon (mek), couldn't be expected to take any significant influence when brought in contact with the melt, because their solubility was too low. This was explicitly tested and verified for mek.

The reduction of viscosity is the most important task of the solute. It is important to evaluate the viscosity reduction at the liquidus line rather than isothermally. The difference between the 2 may again be related to the polarity, i.e. the affinity to the nutrient in the liquid. A solute with great affinity to the liquid nutrient but which does not form a cocrystal or solid solution with it, will generally cause a stronger freezing point depression than a solute with lower affinity. If the freezing point depression is low, an isothermal viscosity reduction may translate into a viscosity reduction along the liquidus line. This is why the experiments of the present study have shown, that BuOH is suitable for viscosity reduction in glycerol, but MeOH or EtOH are not. An increase in diffusivity usually comes along with the drop in viscosity.

The third quantity that should be considered, beside polarity and viscosity, is the density. A solute concentration gradient will form in front of the growing crystal layer and that will cause natural convection if the density difference between solute and nutrient is suitable. If the density of the melt decreases with increasing solute content, this might counteract the effect of the temperature and natural convection may even be hindered. However, if the density difference is large, the solutes influence will far outweigh that of temperature and the overall result will be stronger natural convection. This has been demonstrated in the present study for glycerol and BuOH. In polar nutrients, many ionic compounds would be able to do so, but these would generally be unfavourable with respect to the polarity and viscosity criteria. A substance that could be even more suitable for glycerol than BuOH, considering only the 3 given physical criteria, is iodomethane (Mel, CH<sub>3</sub>I). It resembles BuOH in viscosity (0.48

mPa s [Sou38]) and hydrophilie (miscibility with water  $c^* = 14 \text{ kg m}^3$  at  $20 \text{ }^\circ\text{C}$ ), but possesses a density of  $2280 \text{ kg/m}^3$ . However, the more difficult handling and much higher price of Mel make BuOH seem to be the better alternative from an economic point of view.

## **6.5 New approaches to use and manipulation of layer growth kinetics in industrial separation technology**

### **6.5.1 Agitation by additives**

The enhanced natural convection that is described above (Ch. 6.3-4) is an example of bringing movement into the melt without introducing a moving part of machinery or bubbling a gas into the melt. An additive is mixed with the feed prior to filling both into the crystallizer and then, when crystallization starts, the presence of the additive causes agitation of the melt. Of course, the agitation caused by BuOH in glycerol is not very strong in comparison to the agitation caused by shaft stirrers or falling films. A more radical example is presented on the example of paraffin. As described above (Ch. 4.2.11), 2 liquids were introduced into the crystallizer, together with the paraffin: water and mek. Water has a higher and mek has a lower density than paraffin and both have boiling points that are not much higher than the melting point of the paraffin. When the crystallizer is heated above  $100^\circ\text{C}$ , the water begins to boil such that the rising steam bubbles stir the paraffin. The steam doesn't leave the crystallizer, but drips back into the melt from the condenser. The water drops sink through the paraffin melt. The interesting thing is that the movement in the melt doesn't come to an end, when the temperature sinks below the boiling point of water and not even when it sinks below the boiling point of mek. The crystallization takes place in a melt that is stirred by lighter droplets rising and heavier droplets sinking.

Of course, this mode of operation may not necessarily be advantageous from an energetic point of view. The strength of melt crystallization that no component has to be evaporated and condensed vanishes when the boiling is used for agitation. However, the introduction of condensers into a crystallizer is already patented [Roh12]. The agitation by boiling has some similarity to agitation by bubbling an inert gas through the melt. The introduction of another phase will always cause a mass transport over the interface. If the inert gas is not recycled, then the crystallization is combined with a stripping process in the same apparatus. If it is recycled, the melt components that entered the gas may have to be condensed at the top of the crystallizer, in order to prevent their condensation in the fan. However, most melts have a very low vapour pressure close to their melting temperature, so the stripping effect is very low. Therefore, the introduction of gas bubbles through a nozzle will almost always be energetically advantageous to the creation of gas bubbles by boiling. The main advantage of the boiling process is that the crystallizer may be completely sealed during crystallization.

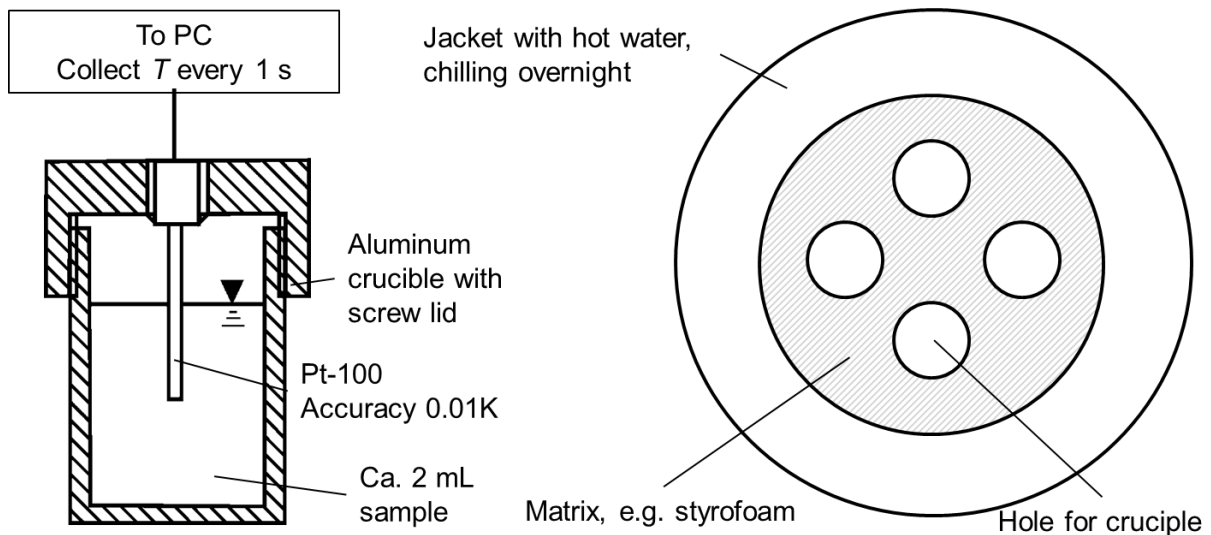
The agitation by rising and sinking droplets without boiling may be more interesting, but more research is necessary to understand the possibilities of this concept.

### 6.5.2 Choice of the cooling profile for paraffin deoiling

The established strategy for slack wax deoiling is a quick cooling of the liquid melt until it seems to be completely crystallized, followed by a long sweating step. Creating a compact crystal layer of deoiled hard wax by controlling the growth is not considered a realistic goal. At one and the same temperature, different solid phases, each containing different chemical compounds may grow or nucleate or both. This is similar for lighter and heavier slack waxes. The melt layer crystallization of lighter slack wax succeeds in deoiling despite this growth step, because the sweating step is effective. Since the separation is only in the sweating step, the growth step is sped up as far as possible to save time. For heavier slack waxes, this approach fails, due to thermodynamic and kinetic reasons. An important kinetic reason has been shown in the DSC-curves presented above (Ch. 5.1.1). An increased cooling rate during crystallization (5 K/min instead of 1 K/min) changed the solid structure in such a way that the DSC curve of the subsequent melting didn't show the separation of melting and O-DO peak anymore. Usually, the difference between a compact and a porous crystal layer cannot be seen in a DSC curve. Only when the SL-interfacial area is largely increased, the structural melting point depression as described by the Gibbs-Thomson-law [Tho71, Gib28, Jac90] may be visible. The results on paraffin do not suggest this, because the melting peak doesn't change when the cooling rate changes. It is the O-DO-peak that shifts and changes its shape, i.e. the transformation from the ordered crystal to the less ordered rotator phase appears at higher temperatures or not at all. Every attempt to explain such behaviour would be purely conjectural at the present moment, but it can be stated that the results suggest a large influence of the cooling rate on the inner structure of the solid rather than merely on the outer structure of the liquid inclusions. The common concept of sweating can barely be applied. It supposes a 2-phase system of one pure crystalline solid and one impure residual melt surrounded by it. The paraffin system is likely to contain at least 4 phases at the beginning of the sweating step: one residual melt, one glass, one very ordered crystalline phase and a rotator phase of intermediate order, and even the most ordered of these allows a large number of different components to be incorporated into it. Therefore, the relation between growth and sweating step has to be reconsidered, and it seems sensible to reach for a slower and more controlled growth. However, the large temperature interval that is usually gone through during the growth step cannot be completely traversed in a slow cooling rate, because this would increase the residence time far beyond economical reason. The temperature interval of slow cooling has to be confined to a few K and primary optical observations of the present study suggest that this is possible, because the major part of the mass solidifies within a very narrow  $T$ -interval. This is counterintuitive in sight of the DSC-

curves, which display a broad melting peak, and more research is needed to understand the phenomenon. However, this task is left to future researchers and the only thing left to do within the present study is to introduce a procedure that allows to find the relative temperature interval at conditions closer to those in the crystallizer than in the DSC.

The apparatus is sketched in Fig. 6.20. The sample is poured into a crucible with a digital thermometer fixed in the lid. Multiple crucibles are placed in an environment that slowly cools. It is important that the sample temperature is not controlled, like in a DSC, but it is recorded overnight. Only  $T(t)$  is collected and from it  $dT/dt$  is approximated as a moving slope with the method of least squares. The  $dT/dt$ -data may show a lot of scatter, which can be filtered by a moving average that includes everything but the highest peak. Such a criterion can easily be implemented into almost any code. The resulting plot is shown in Fig. 6.21.a. The melting peak is clearly visible at 62 °C. Zooming in on this  $T$ -interval in the  $T(t)$  plot reveals the curves given in Fig. 6.21.b. The different samples may reach the crystallization point after different times, but it is exactly the same temperature in all of them.



**Figure 6.20. Equipment for the measurement of the temperature interval in which a slow cooling rate is necessary for the crystallization of heavy paraffin slack waxes.**

This measurement technique is similar in principle to the standard method of freezing point determination where the mixture is stirred with a thermometer while cooling and the freezing is noticed directly by the operator. However, this method uses much less sample and it operates at much lower cooling rates without making it tedious for an operator, because the result can be taken after the end of the experiment. This result also reveals more realistically, how the slack wax will react to a very low cooling rate: the solidification will take place almost isothermally at a layer growth rate of about  $5 \cdot 10^{-5}$  m/s, which is still a fast growth. So the implication for this mixture would be to cool as fast as economically sensible to slightly above 62 °C and then very slowly to slightly below that value before starting the sweating process. The results from the present study show, that the combination of agitation by additives and

slow cooling is successful in that solutes which cannot be incorporated into the lattice can be separated. However, this does not mean that the deoiling is successful, because it can also be hindered by an unfavourable thermodynamic equilibrium. It might be possible to change this equilibrium by a different additive. The literature cited above (Ch. 2.2.4) may be used as a starting point for the search of a suitable substance. This would go beyond the scope of the present study, which focused on the kinetic rather than the thermodynamic side of the problem.

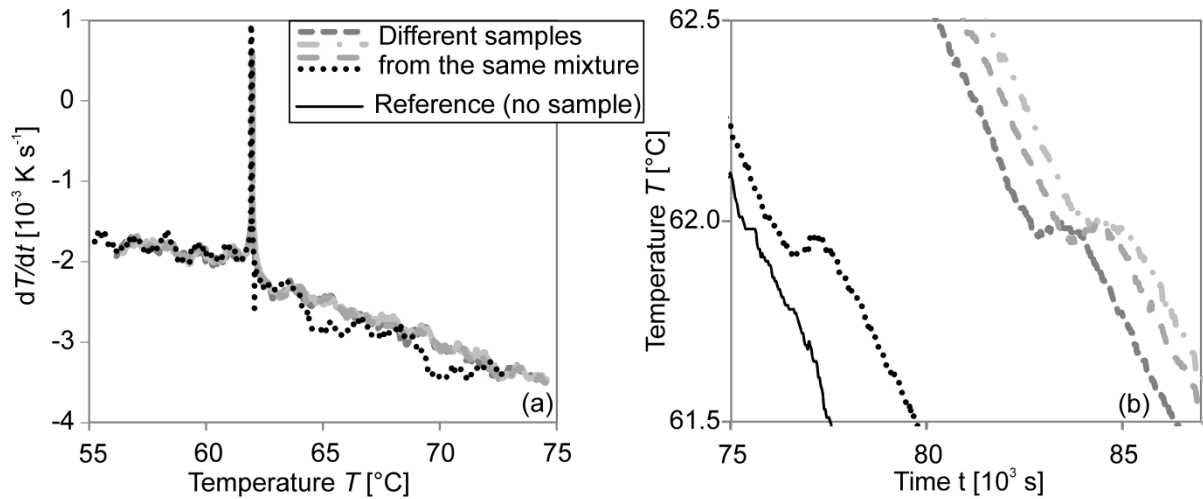


Figure 6.21. Curves obtained from the experiment described in Fig. 6.20. Cooling rate vs. temperature (a) and temperature vs. time (b), zoomed in on the  $T$ -interval of the peak in (a).

## 6.6 Conclusion

The most important findings of the present study can be concluded as follows:

- Glycerol crystal layers show a macro-roughening that can be called faceting. It is caused by the anisotropic growth rate with respect to lattice orientation and the formation of boundary layers during growth. It is favoured by a rather small insulation effect of the crystal layer.
- Additional to the macro-roughening, the glycerol crystal layer exhibits micro-roughening causing the formation of liquid inclusions and, thus, diminishing the separation success.
- The micro-roughening is favoured by the presence of a surfactant, i.e. by a lower surface tension.
- The presence of BuOH strongly diminishes the inclusion of water into the crystal layer.
- The BuOH acts in 4 different ways: it increases diffusivity, reduces viscosity, causes a density gradient that enhances natural convection, and increases the surface tension.



## Discussion

- The effect of BuOH that is experimentally found is a combination of all 4 of these, as a comparison between the measured effect and the effect as calculated based on the mass transfer coefficient shows.
- BuOH is, therefore, an additive that allows a faster separation of glycerol and water in melt layer crystallization, meaning a lower distribution coefficient at a given growth rate or a higher possible growth rate without an increase in the distribution coefficient.
- Three criteria are important for the choice of such an additive:
  - Its polarity should be lower than and as different as possible from that of the nutrient without sacrificing miscibility in the liquid at the crystallization temperature.
  - Its density should be as different as possible from that of the nutrient and most favourably it should be higher rather than lower, again without causing de-mixing in the liquid phase.
  - Its viscosity should be as low as possible and its presence in the liquid phase should reduce the viscosity of the mixture at its liquidus line.
- An additive that meets these criteria will exhibit the strongest positive effect when needed the most, i.e. at high growth rates and low mass transfer coefficients, because this is when concentration polarization is strongest.
- If the growth rate is not measured on line, but calculated based on the deposited mass, a sensible set of assumptions for this calculation is crucial to achieving results that are comparable to those from other setups.
- The salt-content of raw glycerol increases the polarity and, thus, causes a miscibility gap between raw glycerol and BuOH.
- In deoiling of paraffin slack wax, water and mek were used to agitate the melt by rising and sinking of droplets.
- The possibility of a successful sweating step in paraffin slack wax deoiling is dependent on the cooling rate during the crystallization step.
- A simple device is presented that allows the detection of the relevant temperature interval, in which cooling should be slow.
- By combining slow cooling with agitation by water and mek, the kinetic hindrance to the separation in crystallization has largely been overcome.
- The deoiling of mmo-type paraffin slack wax is limited not only by kinetic hindrance but also by an unfavourable SL-equilibrium.

## 7 Summary

The use of additives to improve the kinetics of layer crystallization without introduction of moving parts of machinery was investigated in detail for the first time. An understanding of the process was obtained on the example of a synthetic binary glycerol-water mixture. Its application to 2 real industrial separation tasks, raw glycerol and paraffin, was also investigated to gain further insight. Apart from this main task, encountered problems of experimental procedure and peculiarities of the 3 investigated systems were discussed and solutions to problems proposed.

A lot of experiments, performed in 3 different setups on the system glycerol-water, have shown that even small amounts of BuOH can take a huge influence on the speed of separation. The use of  $w_b = 5\%$  BuOH in a static crystallizer allowed increase of the growth rate by a factor 10 without loss in the separation success. This factor increases approximately linearly with increasing BuOH mass fraction  $w_b < 30\%$ . Calculations of the mass transfer in the melt reveal that the measured extend of effect cannot be explained simply by its influence on the overall viscosity level. It has to be taken into account that the BuOH accumulates close to the crystal front, that the composition-induced density gradient is stronger than the temperature-induced one and, therefore, causes even stronger natural convection and that the lower polarity of BuOH increases the surface tension between the liquid glycerol-water-BuOH mixture and the glycerol crystal. From this discussion, a protocol for choosing a suitable additive was derived. The most important points are that, first, the reduction in viscosity has to be considered together with the influence on the melting temperature and, secondly, a large difference in density is desirable. Thirdly, the difference in polarity between nutrient and additive has to be as large as possible without losing liquid miscibility. If the additive is chosen well, its effect will increase when needed the most. For glycerol, BuOH is good, but not the ideal additive. However, its influence can be as large as the influence of an agitation stronger than that in a falling film.

Limitations to the applicability of such additives showed in the experiments on raw glycerol.

It was further found that comparability between different common lab-scale setups depends heavily on sensible evaluation of the growth rate and much more so than acknowledged in the literature. A few simple strategies of calculation are proposed that allow better comparability and a more quantitative scale-up directly from lab scale.

For the investigated paraffin system, a process was introduced that removed the kinetic hindrances to the separation by slow cooling through the relevant temperature interval and use of 2 liquid additives that cause increased natural convection. A very simple measurement technique that allows finding the relevant  $T$ -interval was also put forward. However, the influence on kinetics did not resolve the problem of separation in paraffin, because the SL-equilibrium did not support separation.

## 8 Zusammenfassung

Der Einsatz von Hilfsstoffen für eine Verbesserung der Kinetik in der Schichtkristallisation ohne das Einbringen beweglicher Maschinenteile wurde erstmals detailliert untersucht. Ein Verständnis des Prozesses wurde am Beispiel einer synthetischen Mischung aus Glycerol und Wasser erlangt. Ferner wurde seine Anwendung auf zwei reale industrielle Trennaufgaben, Rohglyzerol und Paraffin, untersucht. Neben diesem Hauptanliegen diskutiert die Studie Probleme der experimentellen Methodik und Eigenheiten der untersuchten Stoffsysteme, und bietet Lösungen an.

Zahlreiche Experimente, durchgeführt in drei verschiedenen Aufbauten, zeigten, dass selbst kleine Mengen an BuOH einen großen Einfluss auf die Geschwindigkeit der Trennung von Glycerol und Wasser nehmen können. Bereits  $w_b = 5\%$  BuOH in einem statischen Kristaller erlaubten eine Erhöhung der Wachstumsrate um einen Faktor 10 ohne Reinheitsverlust. Dieser Faktor wuchs in etwa linear mit dem BuOH-Massenbruch  $w_b < 30\%$ . Berechnungen des Stoffübergangskoeffizienten zeigten, dass dieser Effekt nicht allein durch den Einfluss auf das Viskositätsniveau erklärt werden kann. Die Anreicherung des BuOHs nahe der Kristallfront, der so entstehende Dichtegradient und die daraus resultierende verstärkte freie Konvektion, ebenso wie die Erhöhung der Grenzflächenspannung zwischen Glycerolkristall und BuOH-haltiger Schmelze müssen berücksichtigt werden. Auf dieser Erkenntnis basiert ein hier erstelltes Protokoll für die Auswahl eines geeigneten Hilfsstoffes. Die drei wichtigsten Punkte sind: 1. Die Einflüsse auf Viskosität und auf Schmelzpunkt müssen gemeinsam berücksichtigt werden. 2. Ein großer Dichteunterschied ist wünschenswert. 3. Die Polarität von Produkt und Hilfsstoff sollte sich so stark unterscheiden, wie es möglich ist, ohne die Mischbarkeit im Flüssigen einzubüßen. Wenn der Hilfsstoff sinnvoll gewählt wurde, ist seine Wirkung umso größer, je mehr er gebraucht wird. Für Glycerol ist BuOH ein guter, aber nicht der ideale Hilfsstoff. Trotzdem steht seine Wirkung nicht hinter der einer erzwungenen Konvektion, wie sie nicht einmal in einem Rieselfilm realisiert wird, zurück. Grenzen der Anwendbarkeit dieser Hilfsstoffe wurden bei den Experimenten an Rohglyzerin offenbar.

Ferner wurde gezeigt, dass die Vergleichbarkeit von Ergebnissen aus verschiedenen üblichen Laboranlagen empfindlicher von der Auswertung der Wachstumsrate abhängt, als bisher angenommen. Einfache Berechnungsstrategien für bessere Vergleichbarkeit und Maßstabsübertragung wurden vorgeschlagen.

Für das Paraffin wurde ein Prozess vorgestellt, der die kinetische Hinderung der Trennung durch zwei Hilfsstoffe und langsames Kühlen in einem  $T$ -Intervall, für dessen Bestimmung ebenfalls eine Methode vorgestellt wurde, überwindet. Der gewünschte Trennerfolg blieb jedoch aufgrund eines ungünstigen thermodynamischen Gleichgewichts aus.

## Literature

- [Abb07] ABBOTT, A. P.; CULLIS, P. M.; GIBSON, M. J.; HARRIS, R. C. & RAVEN, E. (2007), *Extraction of glycerol from biodiesel into a eutectic based ionic liquid*, Green Chemistry **9**(8), 868-872.
- [Abd00] ABDALLAH, D. J. & WEISS, R. G. (2000), *n-Alkanes Gel n-Alkanes (and Many Other Organic Liquids)*, Langmuir **16**(2), 352-355.
- [Afo07] AFOAKWA, E. O.; PATERSON, A. & FOWLER, M. (2007), *Factors influencing rheological and textural qualities in chocolate – a review*, Trends in Food Science & Technology **18**(6), 290-298.
- [Aik06] AIKEN, J. E. (2006), *Purification of glycerin*, United States Patent US7126032, Sunoco Inc. (R&M), Philadelphia, PA, USA.
- [Ale06] ALEXANDROV, D. V. & MALYGIN, A. P. (2006), *Self-similar solidification of an alloy from a cooled boundary*, International Journal of Heat and Mass Transfer **49**(3–4), 763-769.
- [Ark95] ARKENBOUT, G. F. (1995), Melt Crystallization Technology, Lancaster, PA, USA, **Technomic**.
- [Ase06] ASEEV, D. L. & ALEXANDROV, D. V. (2006), *Directional solidification of binary melts with a non-equilibrium mushy layer*, International Journal of Heat and Mass Transfer **49**(25–26), 4903-4909.
- [Ash56] ASHER, D. R. & SIMPSON, D. W. (1956), *Glycerol Purification by Ion Exclusion*, The Journal of Physical Chemistry **60**(5), 518-521.
- [Ask10] ASKELAND, D. R.; FULAY, P. P. & WRIGHT, W. J. (2010), The Science and Engineering of Materials, Andover, UK, **Wadsworth**.
- [Ayo12] AYOUB, M. & ABDULLAH, A. Z. (2012), *Critical review on the current scenario and significance of crude glycerol resulting from biodiesel industry towards more sustainable renewable energy industry*, Renewable and Sustainable Energy Reviews **16**(5), 2671-2686.
- [Bar63] BARTON, E. (1963), *Purification process*, British Patent GB4767863A, Imperial Chemical Industries, London, UK.
- [Bat91] BATSBERG PEDERSEN, W.; BALTZER HANSEN, A.; LARSEN, E.; NIELSEN, A. B. & ROENNINGSSEN, H. P. (1991), *Wax precipitation from North Sea crude oils. 2. Solid-phase content as function of temperature determined by pulsed NMR*, Energy & Fuels **5**(6), 908-913.
- [Bec35] BECKER, R. & DÖRING, W. (1935), *Kinetische Behandlung der Keimbildung in übersättigten Dämpfen*, Annalen der Physik **416**(8), 719-752.
- [Bei12] BEIERLING, T. & RUETHER, F. (2012), *Separation of the isomeric long-chain aldehydes dodecanal/2-methylundecanal via layer melt crystallization*, Chemical Engineering Science **77**, 71-77.
- [Bei13] BEIERLING, T., GORNY, R. & SADOWSKI, G. (2013), *Modeling Growth Rates in Static Layer Melt Crystallization*, Crystal Growth & Design **13**(12), 5229-5240.

## Literature

- [Bie98] BIERWIRTH, J. (1998), Zur Trennung von Schichtkristallisationsprozessen, Dissertation, **Martin-Luther-Universität Halle-Wittenberg**, Germany; Aachen, Germany, **Shaker**.
- [Bla04] BLAZHNOV, I. V.; MALOMUZH, N. P. & LISHCHUK, S. V. (2004), *Temperature dependence of density, thermal expansion coefficient and shear viscosity of supercooled glycerol as a reflection of its structure*, The Journal of Chemical Physics **121**(13), 6435-6441.
- [BoS11] United States Bureau of Standards (1911), *The determination of the optical properties of materials*, Washington, DC, USA, Letter Circular **28**.
- [Bou05] BOUKADI, A.; PHILP, R. P. & THANH, N. X. (2005), *Characterization of paraffinic deposits in crude oil storage tanks using high temperature gas chromatography*, Applied Geochemistry **20**(10), 1974-1983.
- [Bow46] BOWMAN, J. R. (1946), *Method and apparatus for separating mixtures*, United States Patent **US2427042**, Gulf Research Development Co., Harmorville, PA, USA.
- [Bra38] BRANT, G. W. (1938), *Purification of glycerol*, United States Patent **US2120227**, E. I. du Pont de Nemours Co., Wilmington, DE, USA.
- [Bur53a] BURTON, J. A.; PRIM, R. C. & SLICHTER, W. P. (1953), *The Distribution of Solute in Crystals Grown from the Melt. Part I. Theoretical*, The Journal of Chemical Physics **21**(11), 1987-1991.
- [Bur53b] BURTON, J. A.; KOLB, E. D.; SLICHTER, W. P. & STRUTHERS, J. D. (1953), *Distribution of Solute in Crystals Grown from the Melt. Part II. Experimental*, The Journal of Chemical Physics **21**(11), 1991-1996.
- [Car09a] CARMONA, M.; VALVERDE, J. L.; PÉREZ, A.; WARCHOL, J. & RODRIGUEZ, J. F. (2009), *Purification of glycerol/water solutions from biodiesel synthesis by ion exchange: sodium removal Part I*, Journal of Chemical Technology and Biotechnology **84**(5), 738-744.
- [Car09b] CARMONA, M.; LECH, A.; DE LUCAS, A.; PEREZ, A. & RODRIGUEZ, J. F. (2009), *Purification of glycerol/water solutions from biodiesel synthesis by ion exchange: sodium and chloride removal. Part II*, Journal of Chemical Technology and Biotechnology **84**(8), 1130-1135.
- [Cha10a] CHALEEPA, K.; SZEPE, A. & ULRICH, J. (2010), *Dry fractionation of coconut oil by melt crystallization*, Chemical Engineering Research and Design **88**(9), 1217-1222.
- [Cha10b] CHALEEPA, K. (2010), A New Concept in Layer-Based Fractional Crystallization Processes for Fats, Dissertation, **Martin-Luther-Universität Halle-Wittenberg**, [online] <http://141.48.65.178/hs/content/titleinfo/788208>
- [Che00a] CHEVALLIER, V.; BOUROUKBA, M.; PETITJEAN, D.; DIRAND, M.; PAULY, J.; DARIDON, J. L. & RUFFIER-MERAY, V. (2000), *Crystallization of a multiparaffinic wax in normal tetradecane*, Fuel **79**(14), 1743-1750.

## Literature

- [Che00b] CHEVALLIER, V.; BRIARD, A. J.; PETITJEAN, D.; HUBERT, N.; BOUROUKBA, M. & DIRAND, M. (2000), *Influence of the Distribution General Shape of n-Alkane Molar Concentrations on the Structural State of Multi-Alkane Mixtures*, Molecular Crystals and Liquid Crystals Science and Technology. Section A. Molecular Crystals and Liquid Crystals **350**(1), 273-291.
- [Che04] CHENLO, F.; MOREIRA, R.; PEREIRA, G. & BELLO, B. (2004), *Kinematic viscosity and water activity of aqueous solutions of glycerol and sodium chloride*, European Food Research and Technology **219**(4), 403-408.
- [Che07] CHEN, W.; ZHAO, Z.; ZHANG, X. & WANG, L. (2007), *Thermodynamic phase equilibria of wax precipitation in crude oil*, Fluid Phase Equilibria **255**(1), 31-36.
- [Che08] CHENG, N.-S. (2008), *Formula for the Viscosity of a Glycerol–Water Mixture*, Industrial & Engineering Chemistry Research **47**(9), 3285-3288.
- [Che70] CHEN, D. H. T. & THOMPSON, A. R. (1970), *Isobaric vapor-liquid equilibriums for the systems glycerol-water and glycerol-water saturated with sodium chloride*, Journal of Chemical & Engineering Data **15**(4), 471-474.
- [Chi05] CHIU, C.-W.; DASARI, M. A.; SUTTERLIN, W. R. & SUPPES, G. J. (2005), *Removal of Residual Catalyst from Simulated Biodiesel's Crude Glycerol for Glycerol Hydrogenolysis to Propylene Glycol*, Industrial & Engineering Chemistry Research **45**(2), 791-795.
- [Chi93] CHIANESE, A.; DI CAVE, S. & SANTILLI, N. (1993), *An investigation on the removal of liquid inclusions from an organic crystal layer*, 12th symposium on industrial crystallization. Z. H. ROJKOWSKI (ed.), Warsaw, Poland, **1**, 1.037-1.042.
- [Chu75] CHURCHILL, S. W. & CHU, H. H. S. (1975), *Correlating equations for laminar and turbulent free convection from a vertical plate*, International Journal of Heat and Mass Transfer **18**(11), 1323-1329.
- [Cle13] VAN CLEEF, E. H. C. B.; UWITUZE, S.; ALVARADO, C. A. et al. (2013), *Crude glycerin improves feed efficiency in finishing heifers*, Cattlemen's Day, Kansas State University, Manhattan, KS, USA, 59-62.
- [Cir14] CIRIMINNA, R.; PINA, C. D.; ROSSI, M. & PAGLIARO, M. (2014), *Understanding the glycerol market*, European Journal of Lipid Science and Technology **116**(10), 1432-1439.
- [OED16] CORLETT, K.; KIRKHAM, S.; PADLEY, D.; SOFIELD, C.; STEWART, P.; ARSTALL, R.; MARSHALL, J.; SHIRT, D.; TRUMBLE, B.; BANKS, D.; MURRAY, M. & WARD, A. (2016). *fractional*, Oxford English Dictionary, M. PROFFITT, J. PEARSALL, P. DURKIN et al. (Eds.) Oxford, UK, **Oxford University Press** [online] <http://www.oed.com/view/Entry/74098?redirectedFrom=fractional#eid> [Access Jan. 2017]
- [Cot08] COTO, B.; MARTOS, C.; PEÑA, J. L.; ESPADA, J. J. & ROBUSTILLO, M. D. (2008), *A new method for the determination of wax precipitation from non-diluted crude oils by fractional precipitation*, Fuel **87**(10–11), 2090-2094.

## Literature

- [Cot10] COTO, B.; MARTOS, C.; ESPADA, J. J.; ROBUSTILLO, M. D. & PEÑA, J. L. (2010), *Analysis of paraffin precipitation from petroleum mixtures by means of DSC: Iterative procedure considering solid–liquid equilibrium equations*, Fuel **89**(5), 1087-1094.
- [Cou05] COUTINHO, J. A. P.; GONÇALVES, C.; MARRUCHO, I. M.; PAULY, J. & DARIDON, J.-L. (2005), *Paraffin crystallization in synthetic mixtures: Predictive local composition models revisited*, Fluid Phase Equilibria **233**(1), 28-33.
- [Cou06] COUTINHO, J. A. P.; MIRANTE, F. & PAULY, J. (2006), *A new predictive UNIQUAC for modeling of wax formation in hydrocarbon fluids*, Fluid Phase Equilibria **247**(1–2), 8-17.
- [Cou95] COUTINHO, J. A. P.; ANDERSEN, S. I. & STENBY, E. H. (1995), *Evaluation of activity coefficient models in prediction of alkane solid-liquid equilibria*, Fluid Phase Equilibria **103**(1), 23-39.
- [Cou97] COUTINHO, J. A. P. & RUFFIER-MÉRAY, V. (1997), *Experimental Measurements and Thermodynamic Modeling of Paraffinic Wax Formation in Undercooled Solutions*, Industrial & Engineering Chemistry Research **36**(11), 4977-4983.
- [Del93] DELANNOY, C.; ULRICH, J. & FAUCONET, M. (1993), *Laboratory tests on an organic acid as a basis for a scale up calculation*, Symposium on Industrial Crystallization. Z. H. ROJKOWSKI (ed.), Warsaw, Poland. **1**, 49-54.
- [Dem11] DEMICHELIS, R.; RAITERI, P.; GALE, J. D.; QUIGLEY, D. & GEBAUER, D. (2011), *Stable prenucleation mineral clusters are liquid-like ionic polymers*, Nature Communications **2**, 590.
- [D'er04] D'ERRICO, G.; ORTONA, O.; CAPUANO, F. & VITAGLIANO, V. (2004), *Diffusion Coefficients for the Binary System Glycerol + Water at 25 °C. A Velocity Correlation Study*, Journal of Chemical & Engineering Data **49**(6), 1665-1670.
- [Dev10] DEVILLE, S. (2010), *Freeze-Casting of Porous Biomaterials: Structure, Properties and Opportunities*, Materials **3**(3), 1913-1927.
- [Día12] DÍAZ BORBÓN, V. & ULRICH, J. (2012), *Solvent freeze out crystallization of lysozyme from a lysozyme-ovalbumin mixture*, Crystal Research and Technology **47**(5), 541-547.
- [Dir02] DIRAND, M.; BOUROUKBA, M.; CHEVALLIER, V.; PETITJEAN, D.; BEHAR, E. & RUFFIER-MERAY, V. (2002), *Normal Alkanes, Multialkane Synthetic Model Mixtures, and Real Petroleum Waxes: Crystallographic Structures, Thermodynamic Properties, and Crystallization*, Journal of Chemical & Engineering Data **47**(2), 115-143.
- [Dir98] DIRAND, M.; CHEVALLIER, V.; PROVOST, E.; BOUROUKBA, M. & PETITJEAN, D. (1998), *Multicomponent paraffin waxes and petroleum solid deposits: structural and thermodynamic state*, Fuel **77**(12), 1253-1260.
- [Dub07] DUBÉ, M. A.; TREMBLAY, A. Y. & LIU, J. (2007), *Biodiesel production using a membrane reactor*, Bioresource Technology **98**(3), 639-647.

## Literature

- [Eis12] EISENBART, F. J. (2012). Einsatz von Magnetfeldern für die Minimierung von Scaling bei der Membranfiltration: Untersuchung im kontinuierlichen Betrieb. Diploma-thesis, Engler-Bunte-Institut, Lehrstuhl für Wasserchemie und Wassertechnologie. **Karlsruher Institut für Technologie**, Germany.
- [Eis14a] EISENBART, F. J. & ULRICH, J. (2014), *Verfahren zur Reinigung von Glycerin mittels einer lösemittelgestützten Schichtkristallisation*, German Patent DE102014001533A1, Martin-Luther-Universität Halle-Wittenberg, Germany.
- [Eis14b] EISENBART, F. J. & ULRICH, J. (2014), *Solvent-aided layer crystallization – Case study glycerol-water*, 19<sup>th</sup> International Symposium on Industrial Crystallization, B. BISCANS (ed.), Toulouse, France, **EFCE**, 181-182.
- [Eis15a] EISENBART, F. J. & ULRICH, J. (2015), *Solvent-aided layer crystallization – case study glycerol-water*, Chemical Engineering Science, **133**, 24-29.
- [Eis15b] EISENBART, F. J. & ULRICH, J. (2015), *A New Concept of Melt Layer Crystallization for High Viscous Feed Streams*, ACHEMA World Forum and 31<sup>st</sup> Leading Show for the Process Industries, T. SCHEURING (ed.), Frankfurt am Main, Germany.
- [Eis15c] EISENBART, F. J. & ULRICH, J. (2015), *Solvent-Aided Layer Crystallization of Glycerol – The Sweating Step and the Influence of Agitation*, BIWIC2015, 22<sup>nd</sup> International Workshop on Industrial Crystallization, K.-J. KIM & K. LEE (eds.), Daejeon, Republic Korea, 164-172.
- [Eis16a] EISENBART, F. J. & ULRICH, J. (2016), *Solvent-Aided Layer Crystallization of Glycerol – Post-Treatment and the Influence of Agitation*, Chemical Engineering & Technology, **39**(7), 1251-1256.
- [Eis16b] EISENBART, F. J.; ANGERMEIER, N. & ULRICH, J. (2016), *Production of highly dry glycerol by solvent-aided melt layer crystallization*, Journal of Crystal Growth, in press, [pre-version] <http://dx.doi.org/10.1016/j.icrysgro.2016.09.001>
- [Eis16c] EISENBART, F. J.; ANGERMEIER, N. & ULRICH, J. (2016), *Production of highly dry glycerol by solvent-aided melt layer crystallization*, Asian Crystallization Technology Symposium, Asian Crystallization Technology Society (ed.), Tianjin, China, 98-100.
- [Eis16d] EISENBART, F. J. & ULRICH, J. (2016), *Dynamic layer crystallization of high-viscous melts – Case study glycerol-water*, BIWIC2016, 23<sup>rd</sup> International Workshop on Industrial Crystallization, Magdeburg, Deutschland; H. LORENZ & H. BUCHHOLZ (eds.), Göttingen, Germany, **Cuvillier**, S. 207-212.
- [Elb93] ELBASHBESHY, E. M. A. & IBRAHIM, F. N. (1993), *Steady free convection flow with variable viscosity and thermal diffusivity along a vertical plate*, Journal of Physics D: Applied Physics **26**(12), 2137.
- [Erd75] ERDMANN, H. H. (1975), Modellvorstellungen zur quasi-kontinuierlichen Gegenstromkristallisation aus der Schmelze am Beispiel des Systems Naphthalin-beta-Methylnaphthalin. Dissertation, **Universität Dortmund**, Germany.
- [Esp13] ESPADA, J. J.; FERNÁNDEZ, S.; VELASCO, L. & COTO, B. (2013), *Evaluation of different methodologies to determine the n-paraffin distribution of petroleum fractions*, Fuel **109**, 470-475.



## Literature

- [Fel06] FELTHAM, D. L.; UNTERSTEINER, N.; WETTLAUER, J. S. & WORSTER, M. G. (2006), *Sea ice is a mushy layer*, Geophysical Research Letters **33**(14), L14501.
- [Fel36] FELDMAN, H. B. & DAHLSTROM, W. G. (1936), *FREEZING POINTS OF THE TERNARY SYSTEM GLYCEROL-METHANOL-WATER*, Industrial & Engineering Chemistry **28**(11), 1316-1317.
- [Fel99] FELTHAM, D. L. & WORSTER, M. G. (1999), *Flow-induced morphological instability of a mushy layer*, Journal of Fluid Mechanics **391**, 337-357.
- [Fje09] FJERBAEK, L.; CHRISTENSEN, K. V. & NORDDAHL, B. (2009), *A review of the current state of biodiesel production using enzymatic transesterification*, Biotechnology and Bioengineering **102**(5), 1298-1315.
- [Fla71] FLAHERTY, B. (1971), *Characterisation of waxes by differential scanning calorimetry*, Journal of Applied Chemistry and Biotechnology **21**(5), 144-148.
- [Fuk13] FUKUI, K.; MAEDA, K. & KURAMOCHI, H. (2013), *Melt crystallization for refinement of triolein and palmitic acid mixture as a model waste oil for biodiesel fuel production*, Journal of Crystal Growth **373**, 102-105.
- [GEA12a] GEA Messo PT, *Mass Crystallization from solutions*. [Pamphlet, Pdf online] [http://www.gea.com/en/binaries/2012-05\\_Solution%20Crystallization\\_sm2\\_tcm11-21921.pdf](http://www.gea.com/en/binaries/2012-05_Solution%20Crystallization_sm2_tcm11-21921.pdf) [accessed Dec. 2016]
- [GEA12b] GEA Messo PT, *Suspension Melt Crystallization. The Efficient Purification Alternative*. [Pamphlet, Pdf online] [http://www.gea.com/en/binaries/2012-05\\_Melt\\_Crystallization\\_sm\\_tcm11-21876.pdf](http://www.gea.com/en/binaries/2012-05_Melt_Crystallization_sm_tcm11-21876.pdf) [accessed Dec. 2016]
- [Geb08] GEBAUER, D.; VÖLKELE, A. & CÖLFEN, H. (2008), *Stable Prenucleation Calcium Carbonate Clusters*, Science **322**(5909), 1819-1822.
- [Geb10] GEBAUER, D.; GUNAWIDJAJA, P. N.; KO, J. Y. P.; BACSIK, Z.; AZIZ, B.; LIU, L.; HU, Y.; BERGSTRÖM, L.; TAI, C.-W.; SHAM, T.-K.; EDÉN, M. & HEDIN, N. (2010), *Proto-Calcite and Proto-Vaterite in Amorphous Calcium Carbonates*, Angewandte Chemie International Edition **49**(47), 8889-8891.
- [Geb11] GEBAUER, D. & CÖLFEN, H. (2011), *Prenucleation clusters and non-classical nucleation*, Nano Today **6**(6), 564-584.
- [Ger05] GERPEN, J. V. (2005), *Biodiesel processing and production*, Fuel Processing Technology **86**(10), 1097-1107.
- [Ger91] GERSON, A. R.; ROBERTS, K. J. & SHERWOOD, J. N. (1991), *An instrument for the examination of nucleation from solution and its application to the study of precipitation from diesel fuels and solutions of n-alkanes*, Powder Technology **65**(1), 243-249.
- [Gha12] GHANAEI, E.; ESMAEILZADEH, F. & FATHIKALAJAHI, J. (2012), *Wax formation from paraffinic mixtures: A simplified thermodynamic model based on sensitivity analysis together with a new modified predictive UNIQUAC*, Fuel **99**, 235-244.

## Literature

- [Gia73] GIAVARINI, C. & POCHETTI, F. (1973), *Characterization of petroleum products by DSC analysis*, Journal of thermal analysis **5**(1), 83-94.
- [Gib23] GIBSON, G. & GIAUQUE, W. (1923), *The third law of thermodynamics. Evidence from the specific heats of glycerol that the entropy of a glass exceeds that of a crystal at the absolute zero*, Journal of the American Chemical Society **45**(1), 93-104.
- [Gib28] GIBBS, J. W. (1928), The collected works of J. Willard Gibbs. New York, NY, USA, **Longmans, Green and Co.**
- [Gra49] GRAHAM, B. L. (1949), *Crystallization process and apparatus*. United States Patent, **US2651922**, ConocoPhillips Co., Houston, TX, USA.
- [Gre99] GREVEN, K.; LUDWIG, A. & SAHM, P. R. (1999), *Time dependent interface stability during rapid solidification*, Journal of Applied Physics **86**(7), 3682-3687.
- [Gua01] GUARDANI, R.; NEIRO, S. M. S.; BÜLAU, H. & ULRICH, J. (2001), *Experimental comparison and simulation of static and dynamic solid layer melt crystallization*, Chemical Engineering Science **56**(7), 2371-2379.
- [Gué88] GUÉRIN, R. Z.; BILLIA, B.; HALDENWANG, P. & ROUX, B. (1988), *Solutal convection during directional solidification of a binary alloy: Influence of side walls*, Physics of Fluids **31**(8), 2086-2092.
- [Gün56] GÜNTHER, P.; ZEIL, W.; VERSUCHEN, N.; GÖRING, W. & BORNHARDT, J. F. (1956), *Die Kristallisationsgeschwindigkeit von Glycerin und von Benzophenon im Ultraschallfeld*, Zeitschrift für anorganische und allgemeine Chemie **285**(3-6), 191-204.
- [Háj10] HÁJEK, M. & SKOPAL, F. (2010), *Treatment of glycerol phase formed by biodiesel production*, Bioresource Technology **101**(9), 3242-3245.
- [Ham95] HAMM, W. (1995), *Trends in edible oil fractionation*, Trends in Food Science & Technology **6**(4), 121-126.
- [Han88] HANSEN, J. H.; FREDENSLUND, A.; PEDERSEN, K. S. & RØNNINGSEN, H. P. (1988), *A thermodynamic model for predicting wax formation in crude oils*, AIChE Journal **34**(12), 1937-1942.
- [Has41] HASS, H. & PATTERSON, J. (1941), *Purification of Glycerol by Crystallization*, Industrial & Engineering Chemistry **33**(5), 615-616.
- [Hau87] HAULAIT-PIRSON, M. C.; HUYS, G. & VANSTRAELEN, E. (1987), *New predictive equation for the solubility of solid n-alkanes in organic solvents*, Industrial & Engineering Chemistry Research **26**(3), 447-452.
- [Haz03] HAZIMAH, A.; OOI, T. & SALMIAH, A. (2003), *Recovery of glycerol and diglycerol from glycerol pitch*, Journal of oil palm research **15**, 1-5.
- [Her16] HERFURTH, J.; MAHNKEN, K.; FABIAN, J. & ULRICH, J. (2016), *Crystalline Layer Formation of Highly Viscous Supersaturated Liquids*, Chemical Engineering & Technology **39**(7), 1219-1223.

## Literature

- [Hoa76] HOARE, M. & MCINNES, J. (1976), *Statistical mechanics and morphology of very small atomic clusters*, Faraday Discussions of the Chemical Society **61**, 12-24.
- [Hus14] HUSBAND, T. (2014), *The sweet science of candymaking*, ChemMatters(Oct/Nov), 5-8.
- [Jac04] JACKSON, K. A. (2004), *Constitutional supercooling surface roughening*, Journal of Crystal Growth **264**(4), 519-529.
- [Jac08] JACKSON, K. A. & SCHRÖTER, W. (eds.), (2008), Handbook of Semiconductor Technology, Weinheim, Germany, **Wiley-VCH**.
- [Jac90] JACKSON, C. L. & MCKENNA, G. B. (1990), *The melting behavior of organic materials confined in porous solids*, The Journal of Chemical Physics **93**(12), 9002-9011.
- [Jan87] JANČIĆ, S. J. (1987), *Fractional Crystallization*, Industrial Crystallization **87**. J. NÝVLT & S. ŽÁČEK (eds.), Bechyně, ČSSR, 57-70.
- [Jan90] JANČIĆ, S. J. & EHRSAM, C. (1990), *Kristallisationsvorrichtung und deren Verwendung*, European Patent, **EP0218545**, Gebr. Sulzer AG, Winterthur, Switzerland.
- [Jia11] JIANG, X.; ZHAO, Y.; HOU, B.; ZHANG, M. & BAO, Y. (2011), *Density, Viscosity, and Thermal Conductivity of Electronic Grade Phosphoric Acid*, Journal of Chemical & Engineering Data **56**(2): 205-211.
- [Jia12a] JIANG, X.; WANG, J. & HOU, B. (2012), *Coarse crystal layer growth and liquid entrapment study with gradient freeze technology*, Crystal Research and Technology **47**(6), 649-657.
- [Jia12b] JIANG, X.; HOU, B.; HE, G. & WANG, J. (2012), *Falling film melt crystallization (I): Model development, experimental validation of crystal layer growth and impurity distribution process*, Chemical Engineering Science **84**, 120-133.
- [Jia13] JIANG, X.; HOU, B.; HE, G. & WANG, J. (2013), *Falling film melt crystallization (II): Model to simulate the dynamic sweating using fractal porous media theory*, Chemical Engineering Science **91**, 111-121.
- [Jia14a] JIANG, X.; XIAO, W. & HE, G. (2014), *Falling film melt crystallization (III): Model development, separation effect compared to static melt crystallization and process optimization*, Chemical Engineering Science **117**, 198-209.
- [Jia14b] JIANG, X.; LI, M.; HE, G. & WANG, J. (2014), *Research Progress and Model Development of Crystal Layer Growth and Impurity Distribution in Layer Melt Crystallization: A Review*, Industrial & Engineering Chemistry Research **53**(34), 13211-13227.
- [Jon02] JONES, A. G. (2002), Crystallization process systems, Oxford, UK, **Butterworth-Heinemann**.
- [Jud95] JUDGE, R. A.; JOHNS, M. R. & WHITE, E. T. (1995), *Protein purification by bulk crystallization: The recovery of ovalbumin*, Biotechnology and Bioengineering **48**(4), 316-323.

## Literature

- [Kar06] KARPINSKI, P. H. (2006), *Polymorphism of Active Pharmaceutical Ingredients*, Chemical Engineering & Technology **29**(2), 233-237.
- [Kas95] KASHCHIEV, D. (1995), *Nucleation, Science and Technology of Crystal Growth*, J. P. VAN DER EERDEN & O. S. L. BRUINSMA (eds.), Dordrecht, Netherlands, **Kluwer Academic Publishers**, 53-66.
- [Kas03] KASHCHIEV, D. & VAN ROSMALEN, G. M. (2003), *Review: Nucleation in solutions revisited*, Crystal Research and Technology **38**(7-8), 555-574.
- [Keh89] KEHM, D.; WEICHT, B. & GEORGE, J. (1989), *Verfahren zur Stofftrennung durch Kühlkristallisation*, European Patent, **EP0354433**, Bayer AG, Leverkusen, Germany.
- [Keh90] KEHM, D. (1990), *Schichtkristallisation aus oszillierender Rohrströmung*, Dissertation, **Universität Dortmund**, Germany.
- [Kim02] KIM, K.-J. & ULRICH, J. (2002), *A quantitative estimation of purity and yield of crystalline layers concerning sweating operations*, Journal of Crystal Growth **234**(2-3), 551-560.
- [Kle06a] KLEIBER, M. & JOH, R. (2006), *Berechnungsmethoden für Stoffeigenschaften*, VDI-Wärmeatlas, Verein Deutscher Ingenieure (ed.), 10th ed., Berlin, Germany, **Springer**, Da1-Da30.
- [Kle06b] KLEIBER, M. & JOH, R. (2006), *Stoffwerte von sonstigen chemisch einheitlichen Flüssigkeiten und Gasen*, VDI-Wärmeatlas, Verein Deutscher Ingenieure (ed.), Berlin, Germany, **Springer**, Dca1-Dca46.
- [Kön01] KÖNIG, A. & SCHREINER, A. (2001), *Purification potential of melt crystallisation*, Powder Technology **121**(1), 88-92.
- [Kön03] KÖNIG, A. (2003), *Phase Diagrams, Melt Crystallization*. J. ULRICH & H. GLADE (eds.), Aachen, Germany, **Shaker**, 7-40.
- [Kön08] KÖNIG, A.; STEPANSKI, M.; KUSZLIK, A.; KEIL, P. & WELLER, C. (2008), *Ultra-purification of ionic liquids by melt crystallization*, Chemical Engineering Research and Design **86**(7), 775-780.
- [Kon10] KONGJAO, S.; DAMRONGLERD, S. & HUNSOM, M. (2010), *Purification of crude glycerol derived from waste used-oil methyl ester plant*, Korean Journal of Chemical Engineering **27**(3), 944-949.
- [Kra71] KRAUT, K. (1871), British Patent 873, C.D. Abel. [cited in [Has41]]
- [Kre91] KRESIN, M. & KÖRBER, C. (1991), *Influence of additives on crystallization kinetics: Comparison between theory and measurements in aqueous solutions*, The Journal of Chemical Physics **95**(7), 5249-5255.
- [Kus10] KUSZLIK, A. K.; MEYER, G.; HEEZEN, P. A. M. & STEPANSKI, M. (2010), *Solvent-free slack wax de-oiling—Physical limits*, Chemical Engineering Research and Design **88**(9), 1279-1283.
- [Kus90] KUSZLIK, A. K. (1990), *Einfluss der Pulsation auf die Stofftrennung in Apparaten zur Statischen Gerichteten Kristallisation*, Dissertation, **Universität Bremen**, Germany.

## Literature

- [Lan08] LANCRENON, X. & FEDDERS, J. (2008), *An innovation in glycerin purification*, Biodiesel Magazine. [online]  
<http://www.biodieselmagazine.com/articles/2388/an-innovation-in-glycerin-purification>
- [Lan25] LANE, L. B. (1925), *Freezing Points of Glycerol and Its Aqueous Solutions*, Industrial & Engineering Chemistry **17**(9), 924-924.
- [Lan80] LANGER, J. (1980), *Instabilities and pattern formation in crystal growth*, Reviews of Modern Physics **52**(1), 1-29.
- [Lap77] LAPIN, N. V. (1977). Study of the phenomena of interphase heat and mass transfer during crystallization of organic melts on a cooled surface. Dissertation, **Kurnakov Institute**, Russian Academy of Sciences, Moscow, USSR. [in Russian]
- [Lei89] LEITCH, A. M. (1989), *Evolution of a binary system crystallizing in a confined region*, International Journal of Heat and Mass Transfer **32**(11), 2087-2098.
- [Leu10] LEUNG, D. Y. C.; WU, X. & LEUNG, M. K. H. (2010), *A review on biodiesel production using catalyzed transesterification*, Applied Energy **87**(4), 1083-1095.
- [Lew15] LEWIS, A.; SECKLER, M.; KRAMER, H. & VAN ROSMALEN, G. (2015), Industrial Crystallization: Fundamentals and Applications, Cambridge, UK, **Cambridge University Press**.
- [Li76] LI, C. C. (1976), *Thermal conductivity of liquid mixtures*, AIChE Journal **22**(5), 927-930.
- [Loh97] LOHMANN, J.; JOH, R. & GMEHLING, J. (1997), *Solid-Liquid Equilibria of Viscous Binary Mixtures with Alcohols*, Journal of Chemical & Engineering Data **42**(6), 1170-1175.
- [Lor07] LORENZ, H.; CAPLA, F.; POLENSKE, D.; ELSNER, M. P. & SEIDEL-MORGENSTERN, A. (2007), *Crystallization based separation on enantiomers*, Journal of the University of Chemical Technology and Metallurgy **42**(1), 5-16.
- [Lot05] LOTERO, E.; LIU, Y.; LOPEZ, D. E.; SUWANNAKARN, K.; BRUCE, D. A. & GOODWIN, J. G. (2005), *Synthesis of Biodiesel via Acid Catalysis*, Industrial & Engineering Chemistry Research **44**(14), 5353-5363.
- [Ma99] MA, F. & HANNA, M. A. (1999), *Biodiesel production: a review*, Bioresource Technology **70**(1), 1-15.
- [Mat57] MATSUMOTO, K. & SONE, S. (1957), *Mutual Solubility of Glycerol-Water-Butanol System*, Yakugaku Zasshi [Journal of the Pharmaceutical Society of Japan] **77**(10), 1151-1152. [in Japanese]
- [Mat69] MATZ, G. (1969), Kristallisation: Grundlagen und Technik, Berlin, Germany, **Springer**.
- [Mee02] MEENAN, P. A.; ANDERSON, S. R. & KLUG, D. L. (2002), *The Influence of Impurities and Solvents on Crystallization*, Handbook of Industrial Crystallization, A. MYERSON (ed.), Boston, MA, USA, **Butterworth-Heinemann**, 67-97.

## Literature

- [Meh06] MEHER, L. C.; VIDYA SAGAR, D. & NAIK, S. N. (2006), *Technical aspects of biodiesel production by transesterification—a review*, Renewable and Sustainable Energy Reviews **10**(3), 248-268.
- [Met99] METIVAUD, V.; RAJABALEE, F.; OONK, H. A. J.; MONDIEIG, D. & HAGET, Y. (1999), *Complete determination of the solid (RI)-liquid equilibria of four consecutive n-alkane ternary systems in the range C<sub>14</sub>H<sub>30</sub>-C<sub>21</sub>H<sub>44</sub> using only binary data*, Canadian Journal of Chemistry **77**(3), 332-339.
- [Mey09] MEYER, G. (2009), *Thermal Properties of Micro-crystalline Waxes in Dependence on the Degree of Deoiling*, SOFW Journal **135**(8), 43-50.
- [Moh04] MOHAMED, N. H. & ZAKY, M. T. (2004), *Separation of Microcrystalline Waxes from Local Crude Petrolatums using Solvent–Antisolvent Mixtures*, Petroleum Science and Technology **22**(11-12), 1553-1569.
- [Moh08] MOHAMED, N. H.; ZAKY, M. T.; FARAG, A. S. & FAHMY, A. F. M. (2008), *Separation of Paraffin Wax Using Solvent Fractionation*, Petroleum Science and Technology **26**(5), 562-574.
- [Mor13] MORADI, G.; MOHADESI, M. & MORADI, M. R. (2013), *Prediction of wax disappearance temperature using artificial neural networks*, Journal of Petroleum Science and Engineering **108**, 74-81.
- [Mul01] MULLIN, J. W. (2001), Crystallization, Oxford, UK, **Butterworth-Heinemann**.
- [Mul64] MULLINS, W. W. & SEKERKA, R. F. (1964), *Stability of a Planar Interface During Solidification of a Dilute Binary Alloy*, Journal of Applied Physics **35**(2), 444-451.
- [Mus11] MUSSATTO, S. I.; MACHADO, E. M. S.; MARTINS, S. & TEIXEIRA, J. A. (2011), *Production, Composition, and Application of Coffee and Its Industrial Residues*, Food and Bioprocess Technology **4**(5), 661-672.
- [Mus98] MUSSER, B. J. & KILPATRICK, P. K. (1998), *Molecular Characterization of Wax Isolated from a Variety of Crude Oils*, Energy & Fuels **12**(4), 715-725.
- [Mya05] MYASNIKOV, S. K. & UTESHINSKY, A. D. (2005), *Melt entrapment during growth of crystal layer with nonplanar interface and diffusive transport of captured impurities out of layer pores*, Journal of Crystal Growth **275**(1–2), e39-e45.
- [Mya88] MYASNIKOV, S.; MURAV'EV, Y. N. & MALYUSOV, V. (1988), *Fractional Melting of Thin Crystal Layers*, Teoreticheskie Osnovy Khimicheskoi Tekhnologii [Theoretical Foundations of Chemical Engineering] **22**(1), 29.
- [Neu96] NEUMANN, M. (1996), Vergleich statischer und dynamischer Schichtkristallisation und das Reinigungspotential der Diffusionswäsche, Dissertation, **Universität Bremen**, Germany; Clausthal-Zellerfeld, Germany, **Papierflieger**.
- [Nýv82] NÝVLT, J. (1982), Industrial Crystallization, Weinheim, Germany, **Verlag Chemie**.

## Literature

- [Oli09] OLIVEIRA, M. B.; TELES, A. R. R.; QUEIMADA, A. J. & COUTINHO, J. A. P. (2009), *Phase equilibria of glycerol containing systems and their description with the Cubic-Plus-Association (CPA) Equation of State*, Fluid Phase Equilibria **280**(1–2), 22-29.
- [Ols30] OLSEN, J. C.; BRUNJES, A. S. & OLSEN, J. W. (1930), *Freezing and Flow Points for Glycerol, Prestone, Denatured Alcohol, and Methanol*, Industrial & Engineering Chemistry **22**(12), 1315-1317.
- [Ono93] ONOE, K.; MURAKOSHI, K.; TOYOKURA, K. & WÜRMSEHER, H. (1993), *Effect of Crystallization Rate on Physical Properties of Solidified Paraffin*, 12th Symposium on Industrial Crystallization; Z. H. ROJKOWSKI (ed.), Warsaw, Poland. **1**, 1.043-1.048.
- [Ost97] OSTWALD, W. (1897), *Studien über die Bildung und Umwandlung fester Körper*, Zeitschrift für physikalische Chemie **22**, 289-330.
- [Özo91] ÖZOGUZ, M. Y. (1991), Zur Schichtkristallisation als Schmelzkristallisationsverfahren, Dissertation, **Universität Bremen**, Germany.
- [Pag07] PAGLIARO, M.; CIRIMINNA, R.; KIMURA, H.; ROSSI, M. & DELLA PINA, C. (2007), *From Glycerol to Value-Added Products*, Angewandte Chemie International Edition **46**(24), 4434-4440.
- [Par01] PARISI, M. & CHIANESE, A. (2001), *The crystal layer growth from a well-mixed melt*, Chemical Engineering Science **56**(14), 4245-4256.
- [Pau01] PAULY, J.; DARIDON, J.-L. & COUTINHO, J. A. P. (2001), *Measurement and prediction of temperature and pressure effect on wax content in a partially frozen paraffinic system*, Fluid Phase Equilibria **187–188**, 71-82.
- [Pau04] PAULY, J.; DARIDON, J.-L. & COUTINHO, J. A. P. (2004), *Solid deposition as a function of temperature in the nC10 + (nC24–nC25–nC26) system*, Fluid Phase Equilibria **224**(2), 237-244.
- [Pet02] PETERS-ERJAWETZ, S. (2002), Schichtkristallisation von Lebensmitteln an den Beispielen Milch und Zucker, Dissertation, **Universität Bremen**, Germany (2001); Aachen, Germany, **Shaker**.
- [Pos93] POSCHMANN, M.; NEUMANN, M. & ULRICH, J. (1993), *The Washing Procedure in Solid Layer Melt Crystallization*, Delft + Bremen International Workshop for Industrial Crystallization, J. ULRICH & O. S. L. BRUINSMA (eds.) Delft, Netherlands & Bremen, Germany; Aachen, Germany, **J.Mainz**, 114-121.
- [Pot10] POTTHAST, R.; CHUNG, C. P. & MATHUR, I. (2010), *Purification of Glycerin Obtained as a Bioproduct from the Transesterification of Triglycerides in the Synthesis of Biofuel*, United States Patent **US7718833**, Johann Haltermann Ltd., Houston, TX, USA.
- [Rah10] RAHMAT, N.; ABDULLAH, A. Z. & MOHAMED, A. R. (2010), *Recent progress on innovative and potential technologies for glycerol transformation into fuel additives: A critical review*, Renewable and Sustainable Energy Reviews **14**(3), 987-1000.

## Literature

- [Rai10] RAITERI, P. & GALE, J. D. (2010), *Water Is the Key to Nonclassical Nucleation of Amorphous Calcium Carbonate*, Journal of the American Chemical Society **132**(49), 17623-17634.
- [Ras67] RASTORGUEV, Y. L. & GANIEV, Y. A. (1967), *Thermal conductivity of non-electrolyte solutions*, Russian Journal of Physical Chemistry **41**(6), 717.
- [Rav12] RAVENTÓS, M.; HERNÁNDEZ, E. & AULEDA, J. M. (2012), *Freeze Concentration Applications in Fruit Processing*, Advances in Fruit Processing Technologies, S. RODRIGUES & F. A. N. FERNANDES (Eds.) Boca Raton, FL, USA, **CRC**, 263-286.
- [Rig12] RIGNEY, W. J. (1912), *Process and apparatus for the manufacture of rock-candy*, United States Patent **US1031199**.
- [Rit85] RITTNER, S. & STEINER, R. (1985), *Die Schmelzkristallisation von organischen Stoffen und ihre großtechnische Anwendung*, Chemie Ingenieur Technik **57**(2), 91-102.
- [Roh12] ROHR, R.; NIKZAD, A. & KUSZLIK, A. (2012), *Method and device for purifying high melting organic raw products or compound mixtures by means of fractional layer crystallisation*, European Patent **EP1907088B1**, Sulzer Chemtech AG, Winterthur, Switzerland & Resitec Participaceos Ltda., Campinas, SP, Brazil.
- [Ros08] ROSSI, M.; DELLA PINA, C.; PAGLIARO, M.; CIRIMINNA, R. & FORNI, P. (2008), *Greening the Construction Industry: Enhancing the Performance of Cements by Adding Bioglycerol*, ChemSusChem **1**(10), 809-812.
- [Ros54] ROSS, H. K. (1954), *Cryoscopic Studies - Concentrated Solutions of Hydroxy Compounds*, Industrial & Engineering Chemistry **46**(3), 601-610.
- [Rut53] RUTTER, J. W. & CHALMERS, B. (1953), *A prismatic substructure formed during solidification of metals*, Canadian Journal of Physics **31**(1), 15-39.
- [Ryu12] RYU, B. H. & ULRICH, J. (2012), *Controlled Nucleation and Growth of Protein Crystals by Solvent Freeze-Out*, Crystal Growth & Design **12**(12), 6126-6133.
- [San77] SANDBERG, O.; ANDERSSON, P. & BACKSTROM, G. (1977), *Heat capacity and thermal conductivity from pulsed wire probe measurements under pressure*, Journal of Physics E: Scientific Instruments **10**(5), 474-477.
- [Sax68] SAXER, K. (1968), *Fractional crystallization process*, United States Patent, **US3621664**, Buchs Metallwerk AG, St. Gallen, Switzerland.
- [Sch01] SCHLAPBACH, L. & ZUTTEL, A. (2001), *Hydrogen-storage materials for mobile applications*, Nature **414**(6861), 353-358.
- [Sch55] SCHAERER, A. A.; BUSO, C. J.; SMITH, A. E. & SKINNER, L. B. (1955), *Properties of Pure Normal Alkanes in the C17 to C36 Range*, Journal of the American Chemical Society **77**(7), 2017-2019.
- [Sch56] SCHAERER, A. A.; BAYLÉ, G. G. & MAZEE, W. M. (1956), *Thermodynamics of n-alkanes*, Recueil des Travaux Chimiques des Pays-Bas **75**(5), 529-542.



## Literature

- [Sch93a] SCHOLZ, R.; WANGNICK, K. & ULRICH, J. (1993), *On the distribution and movement of impurities in crystalline layers in melt crystallization processes*, Journal of Physics D: Applied Physics **26**(8B), B156.
- [Sch93b] SCHOLZ, R. (1993), Die Schichtkristallisation als thermisches Trennverfahren, Dissertation, **Universität Bremen**, Germany; VDI-Fortschrittsberichte, Reihe 3 **347**, Düsseldorf, Germany, **VDI-Verlag**.
- [Sch94] SCHNABEL, G. & PALEN, J. W. (1994), *Wärmeübertragung an senkrechten berieselten Flächen*, VDI-Wärmeatlas, Verein Deutscher Ingenieure (ed.), 7th ed., Düsseldorf, Germany, **VDI-Verlag**, Md1-Md8.
- [SDA90] The Soap and Detergent Association (ed.) (1990), Glycerine: an overview, New York, NY, USA. [online] [www.aciscience.org/docs/glycerine\\_-\\_an\\_overview.pdf](http://www.aciscience.org/docs/glycerine_-_an_overview.pdf)
- [Seg51] SEGUR, J. B. & OBERSTAR, H. E. (1951), *Viscosity of Glycerol and Its Aqueous Solutions*, Industrial & Engineering Chemistry **43**(9), 2117-2120.
- [Sei15] SEIDEL, J. & ULRICH, J. (2015), *Generation of Crystalline Microcontainers of Salicylic Acid*, Chemical Engineering & Technology **38**(6), 984-990.
- [Sha94] SHANKAR, P. N. & KUMAR, M. (1994), Experimental Determination of the Kinematic Viscosity of Glycerol-Water Mixtures, Proceedings of the Royal Society of London A: Mathematical, Physical and Engineering Sciences **444**(1922), 573-581.
- [Sha95] SHALAEV, E. Y. & FRANKS, F. (1995), *Equilibrium phase diagram of the water-sucrose-NaCl system*, Thermochimica acta **255**, 49-61.
- [Sou38] SOUDERS, M. (1938), *Viscosity and Chemical Constitution*, Journal of the American Chemical Society **60**(1), 154-158.
- [Spa43] SPANGLER, J. & DAVIES, E. (1943), *Freezing Points, Densities, and Refractive Indexes of System Glycerol-Ethylene Glycol-Water*, Industrial & Engineering Chemistry Analytical Edition **15**(2), 96-99.
- [Sri11] SRIMANI, P. K. & MURTHY, M. V. (2011), *New Oscillatory Instability in a Mushy Layer in a Modulated Environment during the Solidification of Binary Alloys*, AIP Conference Proceedings **1414**(1), 195-200.
- [Sri93] SRIVASTAVA, S. P.; HANDOO, J.; AGRAWAL, K. M. & JOSHI, G. C. (1993), *Phase-transition studies in n-alkanes and petroleum-related waxes—A review*, Journal of Physics and Chemistry of Solids **54**(6), 639-670.
- [Sri97] SRIVASTAVA, S. P.; SAXENA, A. K.; TANDON, R. S. & SHEKHER, V. (1997), *Measurement and prediction of solubility of petroleum waxes in organic solvents*, Fuel **76**(7), 625-630.
- [Sul16a] Sulzer Chemtech, *Suspension Crystallization Technology*, [Pamphlet, Pdf online] [http://www.sulzer.com/de/-/media/Documents/ProductsAndServices/Process\\_Technology/Reaction\\_Technology/Brochures/Suspension\\_Crystallization\\_Technology.pdf](http://www.sulzer.com/de/-/media/Documents/ProductsAndServices/Process_Technology/Reaction_Technology/Brochures/Suspension_Crystallization_Technology.pdf) [accessed Dec. 2016].

## Literature

- [Sul16b] Sulzer Chemtech, *Falling Film Crystallization*, 2016, [online] <https://www.sulzer.com/nl/Products-and-Services/Separation-Technology/Crystallization/Falling-Film-Crystallization>, [accessed Dec. 2016].
- [Sta06] STARZAK, M. & MATHLOUTHI, M. (2006), *Temperature dependence of water activity in aqueous solutions of sucrose*, *Food Chemistry* **96**(3), 346-370.
- [Ste03] STEPANSKI, M. & SCHÄFER, E. (2003), *Separate Organics by Melt Crystallization: A Guide to When and How to Use this Technique*, *Melt Crystallization*, J. ULRICH & H. GLADE. (eds.), Aachen, Germany, **Shaker**, 167-212.
- [Ste06] STEPANSKI, M. & JANS, B. (2006), *Verfahren zur fractionierten Kristalliation von Substanzen, zur Durchführung des Verfahrens geeigneter Kristallisor, sowie Verwendung des Kristallisators*, *European Patent EP0891798*, Sulzer Chemtech AG, Winterthur, Switzerland.
- [Sto82] STOLZENBERG, K.; KOCH, K. H. & MARRETT, R. (1982), *Verfahren und Vorrichtung zur Stofftrennung eines flüssigen Gemisches durch fraktionierte Kristallisation*, *European Patent EP0085791*, Rütgerswerke AG, Castrop-Rauxel, Germany.
- [Str51] STROMQUIST, D. M. & REENTS, A. C. (1951), *C.P. Glycerol by Ion Exchange*, *Industrial & Engineering Chemistry* **43**(5), 1065-1070.
- [Tam22] TAMMANN, G. (1922), *Aggregatzustände*, Leipzig, Germany, **Barth**.
- [Tan16] TANG, H. (2016), *Purification of phosphoric acid by melt crystallization*, Dissertation, **Martin-Luther-Universität Halle-Wittenberg**, Germany. [online] <http://141.48.65.178/hs/content/titleinfo/2414172>
- [Ter96] TERNSTRÖM, G.; SJÖSTRAND, A.; ALY, G. & JERNQVIST, Å. (1996), *Mutual Diffusion Coefficients of Water + Ethylene Glycol and Water + Glycerol Mixtures*, *Journal of Chemical & Engineering Data* **41**(4), 876-879.
- [Tho71] THOMSON, W. (1871), *On the equilibrium of vapour at a curved surface of liquid*, *Philosophical Magazine Series 4* **42**(282), 448-452.
- [Tie97] TIEDKE, M. (1997), *Die Fraktionierung von Milchfett - ein neues Einsatzgebiet für die Schichtkristallisation*, Dissertation, **Universität Bremen**, Germany; Aachen, Germany, **Shaker**.
- [Til06] TILLEY, R. (2006), *Crystals and Crystal Structures*, Chichester, UK, **Wiley**.
- [Til53] TILLER, W. A.; JACKSON, K. A.; RUTTER, J. W. & CHALMERS, B. (1953), *The redistribution of solute atoms during the solidification of metals*, *Acta Metallurgica* **1**(4), 428-437.
- [Til91a] TILLER, W. A. (1991), *The Science of Crystallization: Microscopic Interfacial Phenomena*, Cambridge, UK, **Cambridge University Press**.
- [Til91b] TILLER, W. A. (1991), *The Science of Crystallization: Macroscopic Phenomena and Defect Formation*, Cambridge, UK, **Cambridge University Press**.
- [Tin34] TING, H. H. & MCCABE, W. L. (1934), *Supersaturation and Crystal Formation in Seeded Solutions*, *Industrial & Engineering Chemistry* **26**(11), 1201-1207.

## Literature

- [Tom73] TOMLINSON, D. (1973), *Temperature dependent self-diffusion coefficient measurements of glycerol by the pulsed NMR technique*, Molecular Physics **25**(3), 735-738.
- [Ubb65] UBBELOHDE, A. R. (1965), Melting and Crystal Structures, Oxford, UK, **Oxford University Press**.
- [Ulr03a] ULRICH, J. (2003), *Introduction*, Melt Crystallization, J. ULRICH & H. GLADE (eds.), Aachen, **Shaker**, 1-6.
- [Ulr03b] ULRICH, J. (2003), *Solid Layer Crystallization*, Melt crystallization, ULRICH & H. GLADE (eds.), Aachen, **Shaker**, 71-92.
- [Ulr06] ULRICH, J. & NORDHOFF, S. (2006), *Schmelzkristallisation, Fluidverfahrenstechnik*, R. GOEDECKE (ed.), Weinheim, Germany, **WILEY-VCH**, 1131-1196.
- [Ulr90a] ULRICH, J. & ÖZOĞUZ, Y. (1990), *Progressive freezing and sweating in a test unit*, Journal of Crystal Growth **99**(1-4, Part 2), 1134-1137.
- [Ulr90b] ULRICH, J.; STEPANSKI, M. & ÖZOGUZ, M. Y. (1990), *Vorrichtung zur Stofftrennung aus einem flüssigen Gemisch durch Kristallisation*, European Patent EP0488953, Sulzer Chemtech AG, Winterthur, Switzerland & Sandvik Process Systems GmbH, Sandviken, Sweden.
- [Ulr90c] ULRICH, J.; JANČIĆ, S. J. & KUSZLIK, A. (1990), *The effect of dissipative mixing on separation efficiency of progressive freezing of organic melts*, Symposium of Industrial Crystallization, A. MERSMANN (ed.), Garmisch-Partenkirchen, Germany, 815-820.
- [Ulr92] ULRICH, J.; HÜNKEN, I.; FISCHER, O. & KÖNIG, A. (1992), *Eine Apparatur zur kontinuierlichen Stofftrennung mittels gerichteter Kristallisation*, Chemie Ingenieur Technik **64**(9), 842-844.
- [Vai00] VAINSHTEIN, B. K.; FRIDKIN, V. M. & INDENBOM, V. L. (2000), Structure of Crystals, Berlin, Germany, **Springer**.
- [Ver91] VERMA, A. R. & SRIVASTAVA, O. N. (1991), Crystallography Applied to Solid State Physics, New Delhi, India, **New Age**.
- [Wac96] WACHTMAN, J. B.; CANNON, W. R. & MATTHEWSON, M. J. (1996), Mechanical Properties of Ceramics, Chichester, UK, **Wiley**.
- [Wag06] WAGNER, W. (2006), *Stoffwerte von Wasser*, VDI-Wärmeatlas, Verein Deutscher Ingenieure (ed.), 10th ed., Berlin, Germany, **Springer**, Db1-Db15.
- [Wan94a] WANGNICK, K. & ULRICH, J. (1994), *A model for the calculation of the purification efficiency of a solid layer melt crystallization process*, Crystal Research and Technology **29**(3), 349-356.
- [Wan94b] WANGNICK, K. (1994), Das Waschen als Nachbehandlungsprozeß der Schichtkristallisation, Dissertation, **Universität Bremen**, Germany; Düsseldorf, Germany, **VDI-Verlag**.

## Literature

- [Wen10] WENTZEL, N. & MILNER, S. T. (2010), *Crystal and rotator phases of n-alkanes: A molecular dynamics study*, The Journal of Chemical Physics **132**(4), 044901.
- [Wen15] WENDT, K.; PETERSEN, S. & ULRICH, J. (2015), *Influence of seeding on concentration distribution within pastilles drop formed out of binary melts*, Chemical Engineering Science **133**, 70-74.
- [WHO96] World Health Organisation (1996), *Total dissolved solids in Drinking-water. Guidelines for drinking-water quality 2 Health criteria and other supporting information*, Geneva, Switzerland.
- [Wie14] WIESEN, S.; TIPPKÖTTER, N.; MUFFLER, K.; SUCK, K.; SOHLING, U.; RUF, N. & ULBER, R. (2014), *Adsorptive Vorbehandlung von Rohglycerin für die 1,3-Propandiol Fermentation mit Clostridium diolis. Adsorptive Pretreatment of Crude Glycerol Prior to Fermentation to 1,3-Propanediol by Clostridium Diolis*, Chemie Ingenieur Technik **86**(1-2), 129-135.
- [Wil78] WILSON, L. O. (1978), *On interpreting a quantity in the burton, prim and slichter equation as a diffusion boundary layer thickness*, Journal of Crystal Growth **44**(2), 247-250.
- [Win76] WINTERMANTEL, K.; STOCKBURGER, D. & FUCHS, H. (1976), *Methods for material separation of a liquid mixture by fractional crystallization*, German Patent DE2606364, BASF SE, Ludwigshafen am Rhein, Germany.
- [Win86] WINTERMANTEL, K. (1986), *Die effektive Trennwirkung beim Ausfrieren von Kristallschichten aus Schmelzen und Lösungen – eine einheitliche Darstellung*, Chemie Ingenieur Technik **58**(6), 498-499.
- [Wol11] WOLF, S. E.; MULLER, L.; BARREA, R.; KAMPF, C. J.; LEITERER, J.; PANNE, U.; HOFFMANN, T.; EMMERLING, F. & TREMEL, W. (2011), *Carbonate-coordinated metal complexes precede the formation of liquid amorphous mineral emulsions of divalent metal carbonates*, Nanoscale **3**(3), 1158-1165.
- [Yam16] YAMAMOTO, T.; FUJIKAWA, T.; OKAMOTO, N.; MAEDA, K.; FUKUI, K. & KURAMOCHI, H. (2016), *Melt crystallization of binary mixture of fatty acids as model biofuel*, Asian Crystallization Technology Symposium, Asian Crystallization Technology Society (ed.), Tianjin, China, 5-6.
- [Yan16] YANG, J.; WANG, W.; SHI, B.; MA, Q.; SONG, P. & GONG, J. (2016), *Prediction of wax precipitation with new modified regular solution model*, Fluid Phase Equilibria **423**, 128-137.
- [Yor06] YORI, J. C.; D'IPPOLITO, S. A.; PIECK, C. L. & VERA, C. R. (2006), *Deglycerolization of Biodiesel Streams by Adsorption Over Silica Beds*, Energy & Fuels **21**(1), 347-353.
- [You49] YOUNG, F. E. & JONES, F. T. (1949), *Sucrose Hydrates. The Sucrose–Water Phase Diagram*, The Journal of Physical and Colloid Chemistry **53**(9), 1334-1350.
- [Yu14] YU, X.; WANG, J. & ULRICH, J. (2014), *Purification of Lysozyme from Protein Mixtures by Solvent-Freeze-Out Technology*, Chemical Engineering & Technology **37**(8), 1353-1357.

## Literature

- [Zag51] ZAGER, S. E. & DOODY, T. C. (1951), *Glycerol Removal from Aqueous Solutions by Anion Exchange*, Industrial & Engineering Chemistry **43**(5), 1070-1073.
- [Zak10] ZAKY, M. T. & MOHAMED, N. H. (2010), *Comparative study on separation and characterization of high melting point macro- and micro-crystalline waxes*, Journal of the Taiwan Institute of Chemical Engineers **41**(3), 360-366.

## List of Symbols

Symbols are listed alphabetically. For each letter, the lower case is mentioned before the capital. Physical quantities, constants and mathematical operators are listed together. A unit is only given for physical quantities, not for operators.

### Latin letters

Symbol	Meaning	Unit
$a$	Thermal diffusivity	$\text{m}^2 \text{s}^{-1}$
$A_\lambda$	Optical absorbance	-
$b$	Runge-Kutta functions in Eq. 6.2.22 and arbitrary fitting constants in Eqs. 2.17,19,20	
$c$	Mass concentration	$\text{kg m}^{-3}$
$c_p$	Isobaric heat capacity	$\text{J kg}^{-1} \text{K}^{-1}$
$d$	total differential operator	
$\partial$	partial differential operator	
$D$	Mass diffusivity	$\text{m}^2 \text{s}^{-1}$
$e$	Euler's constant, 2.7828182845905	-
$E$	Specific energy according to DSC-signal	$\text{J kg}^{-1} \text{K}^{-1}$
$f$	Displacement function in stream calculation, Eqs. 6.2.10,14-17	-
$F$	Help function in differential equation system, Eq. 6.2.20	
$g$	Gravitational acceleration	$\text{m s}^{-2}$
$G$	Crystal growth rate	$\text{m s}^{-1}$
$G_{(100)}$	Crystal growth rate of a (100)-face	$\text{m s}^{-1}$
$G_{(110)}$	Crystal growth rate of a (110)-face	$\text{m s}^{-1}$
$G_{(111)}$	Crystal growth rate of a (111)-face	$\text{m s}^{-1}$
$Gr$	Grashof number	-
$H$	Enthalpy	J
$i$	Index number	-
$j$	Diffusive mass flux	$\text{kg m}^{-2} \text{s}^{-1}$
$k$	Effective distribution coefficient, based on residual melt and on mass fractions	-
$k^l$	Desired effective distribution coefficient	
$K$	Differential distribution coefficient, based on liquid at interface	-
$l$	Length	m

## List of Symbols

$L$	Wetted length of the cold finger	m
$m$	Mass	kg
$M$	Molar mass	kg mol <sup>-1</sup>
$n$	number of nuclei	-
$\dot{n}$	nucleation rate	s <sup>-1</sup>
$n_D$	Refractive index	-
$n_{St}$	Stirring speed, rounds per minute	min <sup>-1</sup> = 1/60 s <sup>-1</sup>
$Nu$	Nusselt number	-
$p$	Pressure	Pa
$Q$	Heat	J
$r$	Radius, radial coordinate	m
$r_0$	Radius of the cold finger	m
$Re$	Reynolds number	-
$s$	Layer thickness	m
$s_D$	Diffusion boundary layer thickness	m
$Sc$	Schmidt number	-
$Sh$	Sherwood number	-
$t$	Time	s, h = 3600 s
$t_{PT}$	Time needed for post treatment or draining	s
$T$	Temperature	K, °C = K - 273.15
$u$	Velocity in x-direction	m s <sup>-1</sup>
$U$	Inner Energy	J
$v$	Velocity in y-direction	m s <sup>-1</sup>
$V$	Volume	m <sup>3</sup>
$w$	Mass fraction	-
$w_{imp}$	Impurity mass fraction	-
$W$	Work	J
$x$	Coordinate in space, horizontal distance from a horizontally growing layer	m
$X$	Mole fraction	-
$y$	Coordinate in space, vertical extension of a horizontally growing layer	m
$Y$	Yield	-
$z$	Coordinate in space, thickness of vertically growing layer	m

## List of Symbols

### Greek letters

Symbol	Meaning	Unit
$\alpha$	Heat transfer coefficient	$\text{W m}^{-2} \text{K}^{-1}$
$\beta$	Mass transfer coefficient	$\text{m s}^{-1}$
$\gamma$	Surface tension	-
$\Gamma$	Dimensionless growth rate	-
$\delta$	Compositional diffusivity variation parameter	-
$\Delta$	Difference operator	
$\Delta T$	Undercooling (also called 'supercooling')	K
$\varepsilon$	Compositional viscosity variation parameter	-
$\zeta$	Mass ratio	-
$\eta$	Dynamic viscosity	-
$\kappa$	Ratio of mass fractions at crystal front and in bulk	-
$\lambda$	Thermal conductivity, in Ch. 6 and Appendix	$\text{W m}^{-1} \text{K}^{-1}$
$\lambda$	Wavelength, in Ch. 4-5	m
$\mu$	Chemical potential	$\text{J mol}^{-1}$
$\nu$	Kinematic viscosity	$\text{m}^2 \text{s}^{-1}$
$\xi$	Reduced space coordinate in self-similar system	-
$\Xi$	Parameter of the influence of the additive	$\text{m s}^{-1}$
$\pi$	Archimedes' constant, 3.14159265358979	-
$\Pi$	Product operator	
$\rho$	Density	$\text{kg m}^{-3}$
$\sigma$	Electrical conductivity	$\text{S m}^{-1}$
$\Sigma$	Sum operator	
$\tau$	Time constant	-
$\tau_r$	Residence time	s
$\varphi$	Angle, angular coordinate	-
$\Phi$	Porosity, liquid inclusion volume fraction	-
$\chi$	Compositional expansion coefficient	-
$\psi$	Stream function	$\text{m}^2 \text{s}^{-1}$
$\Psi$	Help function for Eqs. 6.2.19-23	-
$\omega$	Reduced mass fraction	-
$\Omega$	Concentration polarization parameter	-



## List of Symbols

### Hebrew letters

Symbol	Meaning	Unit
$\kappa$	Start value obtained by shooting in Eq. 6.2.23	-
$\gamma$	Cost function of shooting in Eq. 6.2.24	-
$\lambda$	Growth rate reference	$\text{m s}^{-1}$

### Subscripts

Symbol	Meaning
PT	Post Treatment
S	In the solid phase
0	At the crystal front, i.e. at the SL-interface
$\infty$	In the bulk of the melt, far away from the SL-interface
C	In the crystalline phase
c	With respect to mass concentrations, rather than mass fractions
L	In the liquid phase
g	Glycerol
w	Water
b	BuOH when referring to real mixture, arbitrary solute in example calculations of Eqs. 2.13-15 & 6.2.1-28 .
B	At the beaker
CF	At the cold finger
X	With respect to mole fractions, rather than mass fractions

### Superscripts

Symbol	Meaning
!	Desired value
tot	Total
*	At the liquidus line, at equilibrium, at the critical size

### Abbreviations

Abbreviation	Meaning
A	Case A, set of assumptions in Eqs. 4.A.1-2
API	Active pharmaceutical ingredient
ASTM	ASTM International (American Society for Testing and Materials)
B	Case B, set of assumptions in Eqs. 4.B.1-3
BuOH	1-butanol

## List of Symbols

C	Case C, set of assumptions in Eqs. 4.C.1-6
Ch.	Chapter
Chs.	Chapters
CPA	Cubic plus association equation of state
dao	De-asphalted oil
DIN	Deutsches Institut für Normung
EMIM-Cl	1-ethyl-3-methyl-imidazolium chloride
EtOH	Ethanol
FAME	Fatty acid methyl ester
Fig.	Figure
Figs.	Figures
Fmmm	Crystalline phase with space group $F 2/m 2/m 2/m$ (orthorhombic)
g	Glycerol
gw	Binary glycerol-water mixture
gwb	Ternary glycerol-water-BuOH mixture
in-	Lower inflection point of DSC curve
in+	Upper inflection point of DSC curve
Imo	Light machine oil
L	Liquid phase
LL	Liquid-liquid
max	Maximum function, peak of a curve
mek	methyl-ethyl-ketone (2-butanon)
Mel	Methylene iodine
MeOH	Methanol
min	Minimum function
mmo	Middle machine oil
MONG	Matter organic non-glycerol
O-DO	Order-Disorder
on-	Lower onset of DSC curve
on+	Upper onset of DSC curve
P1	Crystalline phase with space group $P 1$ (triclinic)
$P\bar{1}$	Crystalline phase with space group $P \bar{1}$ (triclinic)
$P2_1$	Crystalline phase with space group $P 1 2_1 1$ (monoclinic)
$P2_1 2_1 2_1$	Crystalline phase with space group $P 2_1 2_1 2_1$ (orthorhombic)
$P6_3/mmc$	Crystalline phase with space group $P 6_3/m 2/m 2/c$ (hexagonal)
Ph.Eur.	Pharmacopoea Europaea

## List of Figures

rg	Raw glycerol, glycerol pitch
sin	Sinus function
S	Solid phase
SL	Solid-liquid, when referring to interface or equilibrium
S-L	Solid-liquid, when referring to phase transition
spo	Spindle oil
Tab.	Table
TOC	Total organic carbon
UNIQUAC	Universal quasi-chemical model
V	Vapour phase
VLE	Vapour-liquid-equilibrium
w	Water
WHO	World Health Organization

## List of Figures

<b>No.</b>	<b>Page</b>	<b>Caption (shortened)</b>
2.1	6	Typical process of layer crystallization in the industry with sweating step. The temperature of the cooling medium is drawn vs. the process time, together with the melting temperature of the pure product and sketches of the crystal layer and melt.
2.2	7	Sketch of an industrial static layer crystallizer, showing four cooling plates instead of the large number that is used in a real apparatus.
2.3	8	Examples of industrial equipment for dynamic layer crystallization.
2.4	9	Most important industrially established applications of melt layer crystallization [Ste03]. The dynamic viscosity at melting temperature, obtained from extrapolating an exponential fit of data from various sources to the melting temperature, is drawn vs. The melting temperature of the pure product.
2.5	10	Simplified flow chart of an established process for the purification of glycerol, comprising 3 distillation units and one adsorption over active carbon.

## List of Figures

- 2.6 12 Classification of nucleation with sketch of mechanisms.
- 2.7 13 Qualitative plot of chemical potential vs. reaction coordinate for the nucleation of  $\text{CaCO}_3$  from aqueous solution, according to classical nucleation theory (a), experimental values (b) [Geb08], and dynamic simulation results assuming dry (c) or wet (d) clusters [Rai10]. Reproduced from [Eis12].
- 2.8 13 Nucleation rate vs. undercooling for glycerol, according to experimental data from Tamman [Tam22, Mat69]. Lines are drawn as guide to the eye.
- 2.9 14 Hypothetical  $n(T, w)$ -diagram, combining phase diagram and nucleation behaviour independent of the cooling profile.
- 2.10 15 Illustration of important phenomena on the growing crystal surface on a microscopic scale.
- 2.11 16 Constitutional undercooling (a) and one possible mechanism of fast dendritic growth caused by it (b), as opposed to no constitutional undercooling (c) and a growth mechanism that flattens out the crystal layer (d).
- 2.12 17 Example for the influence of the surface tension on the tendency of a periodical perturbation to change the amplitude of its Fourier parts.
- 2.13 18 Perturbation in the crystal layer growing or retreating, depending on the surface tension. The plot is constructed from the data shown in Fig. 2.12.
- 2.14 19 Point defects and the lattice distortion caused by it: substitutional molecule of larger (a) or smaller size (b), interstitial molecule (c) and molecule of same size but different structure (d).
- 2.15 19 Mixed crystals: cocrystal (a), small interstitial molecules (b) and flexible molecules (c).
- 2.16 20 Edge dislocation (a) and its influence on solute uptake: small substitutional molecules in compressed volume above the edge (b), large substitutional molecules in stretched volume below the edge (c) and interstitial molecules in stretched volume below the edge (d).

## List of Figures

- 2.17 22 Phase diagram of the system glycerol-water.
- 2.18 22 Phase diagrams of binary n-alkane mixtures nonadecane-henicosane (a) and hexadecane-octadecane (b).
- 2.19 23 Phase diagram of the binary system water-sucrose.
- 2.20 23 Phase diagram of the binary system water-BuOH, with experimental (symbols) and calculated data (lines) (a).  
(b): Liquid phase diagram of the ternary system water-glycerol-BuOH with experimental data (symbols) from [Mat57] and linear extrapolation to lower temperatures (broken lines).
- 2.21 24 Pseudobinary phase diagram of a system containing a multinary mixture of long n-alkanes (Paraffin) and one much shorter n-alkane (tetradecane,  $C_{14}H_{30}$ ) (a). The composition of the feed paraffin, of the solid deposit at  $15^{\circ}C$  and of the paraffin remaining in the liquid phase at the same temperature is given in (b).
- 2.22 27 Diffusion boundary layer and the relation between its thickness and the mass transfer coefficient  $\beta$ . For better visibility, the construction of  $s_{D, \text{canonical}}$  is done at  $1.05 w_{b, \infty}$  instead of the denoted  $1.01 w_{b, \infty}$ .
- 4.1 33 Workflow for the production of glycerol seed crystals.
- 4.2 34 Example of determination of crystal growth rate in a petri dish. The position of the seed is obvious from the shape of the crystallite. The size is estimated by counting the squares and averaging over several directions.
- 4.3 34 Sketch of the magnetic stirrer cold finger setup (MCF). Application of a complete seed layer onto the cold finger (Seeding) and crystal growth after immersion into the melt (Growth).
- 4.4 35 Glass setup showing 3 glasses during different stages of one experiment. Actually, 10 glasses were operated in parallel. Z of the thickness of the crystal layer.

## List of Figures

- 4.5 36 Sketch of the 3 different bottle test arrangements (a-c).
- 4.6 36 Cold finger with grid and parts of burst crystal layer.
- 4.7 37 Cold finger setup for quantitative experiments on separation success. The left side shows the seed crystals sinking during the seeding process, leaving nuclei at the cold finger. The right side shows the uneven crystal layer with liquid inclusions towards the end of the growth step.
- 4.8 38 Temperature and sampling protocol for static cold finger experiments on glycerol with  $w_w = 3\%$ . The predicted reaction of the crystal layer is also shown.
- 4.9 39 Setup with translational movement of the beaker and fixed cold finger for the purpose of forcing strong convection in the melt.
- 4.10 40 Workflow of the experiments with raw glycerol. Measurements are indicated by the symbols of the measured quantity.
- 4.11 41 Sweating setup type I.
- 4.12 41 Sweating setup type II.
- 4.13 42 Gravimetric measurement of the BuOH mass fraction  $w_{b,0}$  by using Eq. 4.1 after weighing of masses  $m_0$  and  $m_1$  and Karl-Fischer titration for water mass fractions  $w_{w,0}$  and  $w_{w,1}$ .
- 4.14 43 Assumptions for the calculation of the growth rate from the crystal mass  $m$  and crystallization time  $t$  in cold finger experiments (subfigure (a) and (c), cases A and C) and from the layer thickness  $z$  in the glass setup (subfigure (b) and case B).
- 4.15 45 Coordinates  $\varphi$ ,  $r$  in horizontal cross section of cold finger with seed at point S and different paths for the crystal growth to reach point P: (a) shortest path, (b) fastest and, therefore, actual path, (c) approximation of fastest path made in this study.

## List of Figures

- 4.16 46 Assumed geometry of crystal layer for Cases A, B, and C after shorter time of growth (darker) and longer growth (lighter).
- 4.17 48 Raw data of a DSC long curve at a cooling rate of - 5K/min. The shown  $dT/dt$  (broken line) is the actual rate of temperature change.
- 4.18 48 Example for the construction of the baseline by linear extrapolation from the temperature interval of completely molten sample.
- 4.19 48 The resulting peak curve, after deduction of the baseline, and its derivative.
- 4.20 49 Numerical separation of the peaks in the DSC-curve  $E$  (solid lines) using the onset, inflection, and peak points (symbols), the tangents at inflection (dashed lines) and the derivative  $dE/dT$  (other broken lines).
- 5.1 50 Examples of different shapes of DSC melting curves. (a) no separation of O-DO and S-L peaks, little signal at low temperatures, (b) separation of peaks and strong signal at low  $T$ , (c) weak separation of peaks and little signal at low  $T$ .
- 5.2 51 Characteristic temperatures and areas of DSC curves of different fractions obtained in setup II.
- 5.3 52 (a) Areas of the DSC peaks and their parts after numerical separation (cf. Ch. 4.3.3).  
(b) Peak temperature of the DSC curve of cooling for the fractions obtained in different setups and with and without solvent.
- 5.4 53 (a) Absorbance as a function of the wavelength for the feed and fractions attained in the different setups.  
(b) Absorbance of the fractions divided by the absorbance of the feed drawn vs the growth rate.
- 5.5 54 Relative absorbance, averaged over  $400 \text{ nm} < \lambda < 1100 \text{ nm}$  for each fraction, drawn versus the sweating yield obtained after that fraction.

## List of Figures

- 5.6 55 (a) Crystal growth rates of glycerol from aqueous mixtures at 2 different temperatures. At constant undercooling, the hollow symbols depict lower water contents (6 wt% at  $\Delta T = 0$  K) and the solid symbols represent higher water contents (22,5 wt% at  $\Delta T = 0$  K).
- 5.7 56 Viscosity of binary BuOH-glycerol mixtures drawn vs. the BuOH content. The values for pure glycerol are taken from the literature [Seg51].
- 5.8 56 (a) Growth rates in cold finger experiments drawn vs. the initial water content of the melt. Cold finger temperature  $T_{CF} = -5$  °C, beaker temperature  $T_B = 15$  °C, duration  $\Delta t = 24$  h, stirring rate  $n = 100$  min<sup>-1</sup>. (b) Growth rate in cold finger experiments drawn vs. the duration of the experiment.  $T_{CF} = -5$  °C,  $T_B = 15$  °C, initial water content of the melt  $w_{w,0} = 0.031$ - $0.035$ ,  $n = 100$  min<sup>-1</sup>.
- 5.9 57 Distribution coefficient drawn vs. the growth rate of different cold finger experiments conducted on a melt of water and glycerol. The line represents a linear fit for the first data row (represented by solid triangles).
- 5.10 59 Distribution coefficient drawn vs. Growth rate for cold finger experiments with a melt composed only of water and glycerol in comparison to experiments executed as solvent-aided layer crystallization with different BuOH contents.
- 5.11 59 Distribution coefficient drawn vs. growth rate for solvent aided layer crystallizations at 2 different water contents.
- 5.12 60 Stages of SCF experiments: Seed line (a), growth with rhombic crystal grains and late covering of the cold finger side opposite to the seed (b), rounding of the crystal edges as the growth rate approaches zero towards the end of the experiment (c).
- 5.13 60 Distribution coefficient of the growth step without post treatment drawn vs. the growth rate. The water content of the initial melt was  $w_{w,0} = 3\%$  and the duration of growth step was  $\Delta t = 110$  h.
- 5.14 61 Distribution coefficient as a function of the growth rate for  $w_w = 1\%$ , variable  $w_b$ , and both the SCF and GL setup.



## List of Figures

- 5.15 62 Crystal layer (a) after draining of the melt with adhering melt on the surface, (b) after dripping step with edges showing sharply, and (c) towards the end of the sweating step with channels inside the layer showing.
- 5.16 63 Distribution coefficient vs. post-treatment yield. The water content was  $w_w = 3\%$  in all 4 experiments. The legend gives the conditions of the growth step. The temperature protocol of the sweating step is given in Fig. 4.8. The lines are only added as a guide to the eye.
- 5.17 63 Distribution coefficient vs. post-treatment yield. The water content was  $w_w = 1\%$ .
- 5.18 64 Growth rate of glycerol from binary mixtures with water or EtOH, measured in bottle tests in vertical tubes at 6 °C, drawn vs. The mass fraction of the second component.
- 5.19 65 Distribution coefficient (a) and its multiplicative inverse (b) with and without SDS in a glass setup with a glass temperature of 5°C and 1% water, drawn vs. the BuOH mass fraction in the initial melt.
- 5.20 66 Electrical conductivity  $\sigma$  of ternary glycerol-water-NaCl mixtures as a function of sodium chloride mass fraction  $w_{\text{NaCl}}$  and water mass fraction  $w_w$  (a) and the slope of the linear dependence on the salt content drawn versus the water mass fraction (b).
- 5.21 66 Results of a bottle test on raw glycerol. (a) Distribution coefficient concerning water  $k_w$  and salt  $k_s$  of the experiment on raw glycerol (rg) in comparison to  $k_w$  of experiments of binary glycerol-water mixtures (gw) of similar water mass fraction, all drawn vs. The growth rate. (b) Photograph of the crystal layer in the bottle after draining of the residual melt.
- 5.22 68 Absorbance of visible light as a function of the wavelength. (a) Absolute value of the absorbance. (b) Absorbance of the respective fraction divided by the absorbance of the feed to the crystallization, i.e. the middle distillate of the second distillation.

## List of Figures

- 5.23 68 Relative absorbance for the different fractions, for each fraction averaged over all wavelengths of visible light.
- 6.1 69 Insulation during macro-roughening. Illustration (a,b) and ratio of heat transfer coefficient and crystal thermal conductivity, calculated for the SCF setup.
- 6.2 70 Two types of macro-roughening: faceting in glycerol, grown from a binary mixture with  $w_w = 1\%$  water (a) and marcelling in ice, grown from a binary mixture with  $w_{\text{sucr}} = 20\%$  sucrose, both in the SCF setup.
- 6.3 71 Overview over all  $k(G)$  measurements of this study. The legend gives the triple  $w_w, w_b, \text{Setup}$ . Setup abbreviations are: MCF: magnetic stirrer cold finger, SCF: static cold finger, GL: glass, TBCF: translating beaker cold finger.
- 6.4 72 Distribution coefficient  $k$  vs. dimensionless growth rate  $\Gamma$  for the system naphthalene benzoic acid. Theory (solid line) and experimental data (solid circles) are taken from [Mya05] and compared to the function that is used to fit data in the present study (broken line).
- 6.5 73 Initial slope  $(dk/dG)_{G=0}$  of the fitting curves from Fig. 6.3, drawn versus the water and BuOH mass fraction of the initial melt. The symbols have the meaning given in the legend to Fig. 6.3.
- 6.6 75 Errors in distribution coefficient and growth rate, resulting from different methods of evaluation. In  $G$  the lower limit is according to Ch. 4.3.2, case A, and the upper limit according to case C of the same chapter. In  $k$  the upper limit is according to Eq. 2.2 and the lower from Eq. 6.1.6.
- 6.7 81 Profiles of dimensionless vertical velocity  $f'$  (a,b), the reduced concentration parameter  $\omega$  (c, d), the relative diffusivity  $D/D_\infty \in$  and relative viscosity  $\eta/\eta_\infty$  (f), for different values of the diffusivity variation parameter  $\delta$  (a, c, e) and the viscosity variation parameter  $\varepsilon$  (b, d, f), all drawn vs. The space coordinate, i.e. the dimensionless distance from the crystal front  $\xi$ .

## List of Figures

- 6.8 82  $-\omega'(0)$  as a parameter of the convection-induced mass transfer and  $-(1+\delta)\omega'(0)$  as a parameter of the overall mass transfer drawn as a function of the diffusivity variation parameter  $\delta$ .  $E = 1$ ,  $Sc_{\infty} = 4$ .
- 6.9 82 Profiles of dimensionless vertical velocity  $f'$  (a) and reduced concentration parameter  $\omega$  (b) drawn vs. the dimensionless distance from the crystal front  $\xi$  for different values of the Schmidt-number in the bulk of the melt  $Sc_{\infty}$ .  $\varepsilon = 1$ ,  $\delta = 1$ .
- 6.10 83  $Sh \cdot [0.25 Gr]^{-0.25}$  calculated from Eq. 6.2.29 drawn vs. the Schmidt number at average temperature and concentration  $Sc_{0.5}$  for Grashof numbers  $Gr$  of 14 orders of magnitude ( $0.1 < Gr < 10^{12}$ ).
- 6.11 84 Comparison between results from Eqs. 6.2.1-28,30 (symbols) and Eq. 6.2.29 (lines).  $-\omega'(0) = Sh \cdot [0.25 Gr]^{-0.25}$  as measure of the convective enhancement of the mass transport rate drawn vs. the Schmidt number  $Sc_{0.5}$ . The lines are the same as in Fig. 6.10. The symbols represent results for different values of  $\varepsilon$  and  $\delta$  as given in the legend.
- 6.12 87 Mass transfer coefficient as a function of the mass fraction of BuOH far away from the crystal front for different temperatures  $T_{\infty}$ ,  $T_0$  and different water mass fractions far away from the crystal front (a) and for different levels of concentration polarization (b).
- 6.13 88 Grashof number  $Gr$ , taking into account density change as result of changes in composition and temperature according to Eq. 6.2.31, and thermal Grashof number,  $Gr_{\text{therm}}$ , taking into account only density changes resulting from thermal expansion according to Eq. 6.2.32, drawn as a function of the mass fraction of BuOH in the melt far away from the crystal front.
- 6.14 89 Mass transfer coefficient of natural convection according to Eq. 5.2.29 (a) and of a falling film according to appendix A.3.
- 6.15 90 Mass transfer coefficient  $\beta$  according to Eqs. 6.2.29,36 for  $\Omega = 14$ ,  $T_0 = 2$  °C,  $T_{\infty} = 10$  °C, (line) and pseudo mass transfer coefficient  $,\rho_S(\rho_L(dk/dG)_{G=0})^{-1}$ , from experimental data (points).

## List of Figures

- 6.16 91 Separation speed parameter  $\rho_S/\rho_L \cdot (dk/dG)_{G=0}^{-1}$  from experiments in GL (squares) and SCF (circles) setups drawn vs. the mass fraction of BuOH in the bulk of the melt  $w_{b,\infty}$  together with the mass transfer coefficient  $\beta$  (crosses) calculated under the false assumptions that BuOH would linearly change the liquids temperature at  $dT^*/dw_b = -43$  K (a) or that it didn't accumulate near the crystal front (b).
- 6.17 92 Separation speed parameter  $\rho_S/\rho_L \cdot (dk/dG)_{G=0}^{-1}$  from experiments in GL (squares) and SCF (circles) setups drawn vs. The mass fraction of BuOH in the bulk of the melt  $w_{b,\infty}$  together with the mass transfer coefficient  $\beta$  (crosses). The influence of BuOH on the density is neglected in (a) and taken into account in (b).
- 6.18 92 Separation speed parameter  $\rho_S/\rho_L \cdot (dk/dG)_{G=0}^{-1}$  from experiments in GL (squares) and SCF (circles) setups drawn vs. The mass fraction of BuOH in the bulk of the melt  $w_{b,\infty}$  together with the mass transfer coefficient  $\beta$  (crosses) calculated under the assumption that  $\kappa_w = 2$ .
- 6.19 93 The parameter  $\Xi$ , expressing the influence of BuOH on the separation speed, as measured and as calculated under different sets of assumptions.
- 6.20 97 Equipment for the measurement of the temperature interval in which a slow cooling rate is necessary for the crystallization of heavy paraffin slack waxes.
- 6.21 98 Curves obtained from the experiment described in Fig. 6.20. Cooling rate vs. temperature (a) and temperature vs. time (b), zoomed in on the  $T$ -interval of the peak in (a).
- A.1 136 Viscosity of glycerol mixtures as a function of the BuOH content. The water mass fraction  $w_w$  is below  $10^{-3}$ .
- A.2 138 Thermal conductivity of glycerol mixtures with BuOH or water as a function of the mole fraction of the second component. Data from [Ras67].
- A.3 139 Mutual diffusion coefficient of aqueous glycerol mixtures at 25°C, data from [Ter96, D'Er04].

## List of Tables

No.	Page	Caption (shortened)
2.1	3	Classification of industrial application tasks of crystallization with examples. Abbreviation API is active pharmaceutical ingredient.
2.2	4	Common classification of separative crystallization processes and the typical equipment of the different classes.
2.3	26	Crystallization equipment overview. The literature is only exemplary.
2.4	29	Types of empirical and semiempirical correlations and predictive theories for the dependence of the distribution coefficient $k$ on the dimensionless growth rate $\Gamma$ .
4.1	31	Specifications of the tap water used in the present study as given by the supplier, Stadtwerke Halle GmbH.
4.2	32	Chemicals used in the system glycerol - water.
4.3	32	Raw glycerol specifications as given by the supplier, Hallesche Ölverarbeitungswerke GmbH, Germany.
4.4	33	Setup types used in the present study.

## Appendix

### A.1 Correlations for the properties of ternary glycerol-water-BuOH mixtures.

The thermal and mechanical properties of ternary mixtures of glycerol, water and BuOH are calculated from data provided in the literature in combination with some own experimental data.

#### A.1.1 Viscosity

Experimental data of the viscosity of binary aqueous glycerol mixtures from the literature [Seg51, Sha94, Che04] are correlated by CHENG [Che08]. After all substitutions, the CHENG correlation predicts the dynamic viscosity of the binary aqueous glycerol mixture  $\eta_{gw}$  as

## Appendix

$$\frac{\eta_{gw}}{\text{Pa s}} = 0.00179 e^{\left(\frac{(-1230 - \frac{T}{^\circ\text{C}}) \frac{T}{^\circ\text{C}}}{36100 + 360 \frac{T}{^\circ\text{C}}}\right)} \cdot \left( \frac{12100 e^{\left(\frac{(-1233 + \frac{T}{^\circ\text{C}}) \frac{T}{^\circ\text{C}}}{9900 + 70 \frac{T}{^\circ\text{C}}}\right)}}{1.79 e^{\left(\frac{(-1230 - \frac{T}{^\circ\text{C}}) \frac{T}{^\circ\text{C}}}{36100 + 360 \frac{T}{^\circ\text{C}}}\right)}} \right)^{w_w} \frac{(0.705 - 0.0017 \frac{T}{^\circ\text{C}})^{2.5} (4.9 + 0.036 \frac{T}{^\circ\text{C}}) w_w}{\frac{w_w}{(1 - w_w)} + (4.9 + 0.036 \frac{T}{^\circ\text{C}}) (0.705 - 0.0017 \frac{T}{^\circ\text{C}})^{1.5}} \quad (\text{A.1.1})$$

where  $w_w$  is the water mass fraction and  $T/^\circ\text{C}$  is the Celsius temperature divided by  $1^\circ\text{C}$ . This equation is taken from data for  $0^\circ\text{C} < T < 100^\circ\text{C}$ , but is here also used for extrapolation to  $T > -10^\circ\text{C}$ .

The influence of BuOH on the viscosity is taken from own experimental data shown in Fig. A.1.

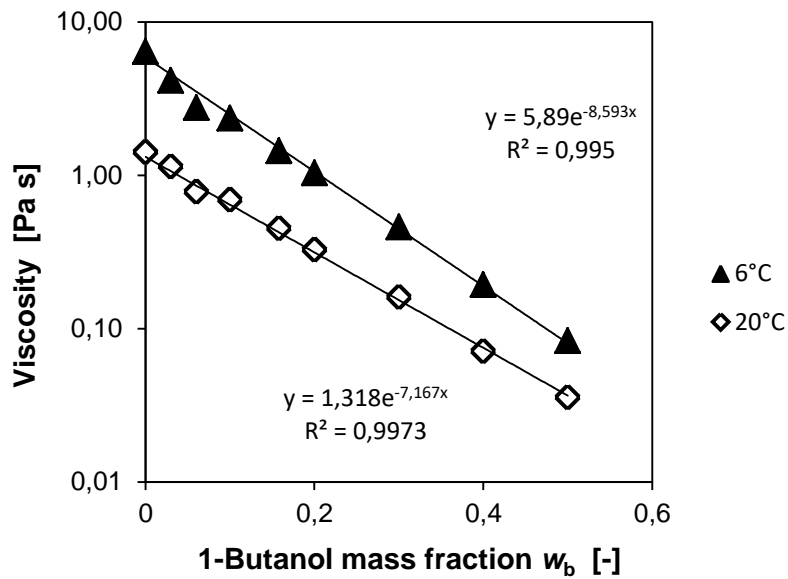


Figure A.1. Viscosity of glycerol mixtures as a function of the BuOH content. The water mass fraction  $w_w$  is below  $10^{-3}$ .

The data are fitted by the function

$$\eta_{gwb} = \eta_{gw} e^{\left(-6.556 - 0.102 \frac{T}{^\circ\text{C}}\right) w_b}. \quad (\text{A.1.2})$$

### A.1.2 Density

A second-degree polynomial fit for the density of water for  $-15^\circ\text{C} < T < 15^\circ\text{C}$  reported in [Wag06] is used:

## Appendix

$$\frac{\rho_w}{\text{kg m}^{-3}} = 269.73 + 5.262 \frac{T}{\text{K}} - 0.0095 \left(\frac{T}{\text{K}}\right)^2. \quad (\text{A.1.3})$$

The densities of glycerol and BuOH are calculated according to [Kle06a, b].

$$\frac{\rho_g}{\text{kg m}^{-3}} = \frac{0.4567818}{0.01799 \left(1 + \left(1 - \frac{T}{874.776 \text{K}}\right)^{0.07136}\right)} \quad (\text{A.1.4})$$

$$\frac{\rho_b}{\text{kg m}^{-3}} = \frac{2.9864379}{0.05482 \left(1 + \left(1 - \frac{T}{579.589 \text{K}}\right)^{0.10323}\right)} \quad (\text{A.1.5})$$

Neglecting excess volumes, the density of the mixture is

$$\rho_{gwb} = \left( \frac{w_w}{\rho_w} + \frac{w_b}{\rho_b} + \frac{(1 - w_w - w_b)}{\rho_g} \right)^{-1}. \quad (\text{A.1.6})$$

### A.1.3 Thermal conductivity

The thermal conductivities of the pure substances are calculated according to [Kle06a, b]:

$$\begin{aligned} \frac{\lambda_g}{\text{Wm}^{-1}\text{K}^{-1}} &= 0.2562 + 1.19 \cdot 10^{-4} \frac{T}{\text{K}} + 2.3 \cdot 10^{-8} \left(\frac{T}{\text{K}}\right)^2 - 1.05 \cdot 10^{-10} \left(\frac{T}{\text{K}}\right)^3 \\ &+ 1.02 \cdot 10^{-13} \left(\frac{T}{\text{K}}\right)^4, \end{aligned} \quad (\text{A.1.7})$$

$$\begin{aligned} \frac{\lambda_w}{\text{Wm}^{-1}\text{K}^{-1}} &= -0.3623 + 0.0050659 \frac{T}{\text{K}} - 5.805 \cdot 10^{-6} \left(\frac{T}{\text{K}}\right)^2 - 1.527 \cdot 10^{-9} \left(\frac{T}{\text{K}}\right)^3 \\ &+ 1.847 \cdot 10^{-12} \left(\frac{T}{\text{K}}\right)^4 \end{aligned} \quad (\text{A.1.8})$$

$$\begin{aligned} \frac{\lambda_b}{\text{Wm}^{-1}\text{K}^{-1}} &= 0.2139 - 2.011 \cdot 10^{-4} \frac{T}{\text{K}} - 4.4 \cdot 10^{-8} \left(\frac{T}{\text{K}}\right)^2 + 1.78 \cdot 10^{-10} \left(\frac{T}{\text{K}}\right)^3 \\ &- 2.15 \cdot 10^{-13} \left(\frac{T}{\text{K}}\right)^4. \end{aligned} \quad (\text{A.1.9})$$

The widely used mixing rule of Li [Li76] proved unnecessarily complicated for the purpose of the present study. From Fig. A.2, it is obvious that the conductivity changes in good approximation linearly with the mole fraction of BuOH.

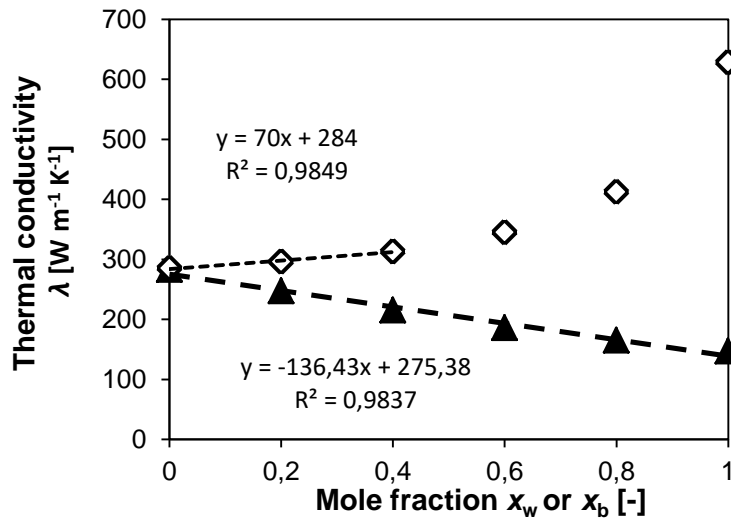


Figure A.2. Thermal conductivity of glycerol mixtures with BuOH or water as a function of the mole fraction of the second component. Data from [Ras67].

The water mole fraction does not in any experiment or any likely industrial application of the presented technique exceed 0.4. For the most important cases, it stays below 0.05. Therefore, a linear fit for  $0 \leq x_w \leq 0.4$  is chosen. Extrapolated to  $x_w = 1$ , it yields 56.4% of the actual value for pure water. Neglecting the possible temperature dependence of this relation, the resulting simplified mixing rule is

$$\lambda_{gwb} = 0.564 x_w \lambda_w + x_b \lambda_b + (1 - x_w - x_b) \lambda_g. \quad (\text{A.1.10})$$

#### A.1.4 Heat capacity

The heat capacity of the pure substances is calculated according to [Kle06a, b] as

$$\frac{c_{p,g}}{\text{J kg}^{-1}\text{K}^{-1}} = 852 + 5.219 \frac{T}{\text{K}} \quad (\text{A.1.11})$$

$$\frac{c_{p,w}}{\text{J kg}^{-1}\text{K}^{-1}} = 3092 + 12.328 \frac{T}{\text{K}} - 0.044504 \left(\frac{T}{\text{K}}\right)^2 + 5.226 \cdot 10^{-5} \left(\frac{T}{\text{K}}\right)^3, \quad (\text{A.1.12})$$

$$\frac{c_{p,b}}{\text{J kg}^{-1}\text{K}^{-1}} = 2573.3 - 9.785 \frac{T}{\text{K}} + 0.030783 \left(\frac{T}{\text{K}}\right)^2 + 2.8 \cdot 10^{-7} \left(\frac{T}{\text{K}}\right)^3, \quad (\text{A.1.13})$$

and the mixture's heat capacity is calculated as

$$c_{p,gwb} = w_w c_{p,w} + w_b c_{p,b} + (1 - w_w - w_b) c_{p,g}. \quad (\text{A.1.13})$$



### A.1.5 Diffusivity

Experimental literature data [Ter96, D'Er04] for the influence of the water mass fraction on the mutual diffusivity  $D_{gw}$  are shown in Fig. A.3 and are used by the linear fit given in the figure. As a rough approximation, it is assumed that the influence of BuOH is the same as the influence of water. TOMLINSON [Tom73] found that the product of self diffusivity and viscosity,  $D \cdot \eta$ , of pure glycerol is almost constant for  $20^\circ\text{C} < T < 160^\circ\text{C}$ . Assuming that this fact is valid for the mutual diffusivities in the relevant glycerol mixtures and for lower temperatures, the diffusivity is calculated as

$$\frac{D_{gwb}}{\text{m}^2\text{s}^{-1}} = (1.4 \cdot 10^{-11} + 9.518 \cdot 10^{-10} (w_w + w_b)) \frac{\eta_{gwb}(T = 25^\circ\text{C})}{\eta_{gwb}}. \quad (\text{A.1.14})$$

The viscosities of the ternary mixtures at  $25^\circ\text{C}$ ,  $\eta_{gwb}(T=25^\circ\text{C})$ , and at the actual temperature,  $\eta_{gwb}$ , are calculated by Eqs. A.1.1-2.

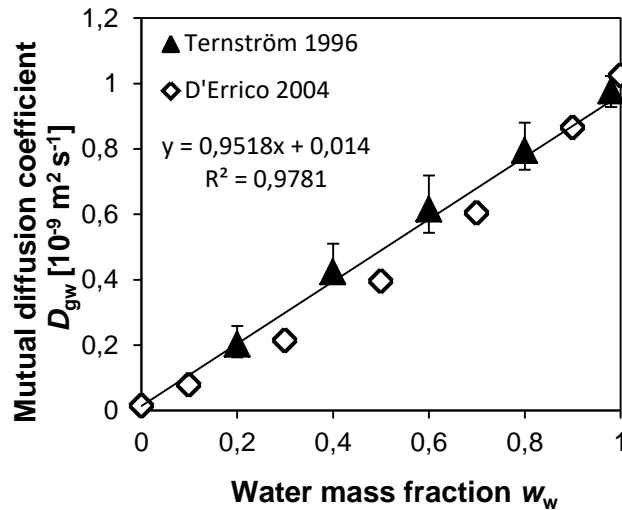


Figure A.3. Mutual diffusion coefficient of aqueous glycerol mixtures at  $25^\circ\text{C}$ , data from [Ter96, D'Er04].

### A.1.6 Solid-liquid equilibrium temperature

The melting point of pure glycerol  $T_g^* = 18.17^\circ\text{C}$  is taken from [SDA90]. The liquidus line for aqueous glycerol mixtures was measured by LANE [Lan25]. For  $0 < w_w < 0.3$ , the straight line

$$\frac{T_{gw}^*}{^\circ\text{C}} = 18.17 - 192.24 w_w \quad (\text{A.1.15})$$

gives a very good fit. The Influence of BuOH on the equilibrium temperature is neglected. Therefore, independent of the BuOH content, an equilibrium mass ratio of water to glycerol  $\zeta_{wg}$  is given for each Temperature:

$$\zeta_{wg}^* = \frac{\frac{T}{\text{K}} - 291.32}{99.08 - \frac{T}{\text{K}}}. \quad (\text{A.1.16})$$

## A.2 Properties of the crystal layer

### A.2.1 Porosity

Porosity of the crystal layer arises from the inclusion of the liquid next to the crystal front. If no BuOH is present, the pores are filled with a binary aqueous glycerol mixture of equilibrium composition  $w_w^*$ , the water in which accounts for all the water in the layer. Therefore,

$$\Phi = \frac{1}{\frac{w_w^* \rho_L^*}{w_w \rho_{g,C}} - \frac{\rho_L^*}{\rho_{g,C}} + 1}, \quad (\text{A.2.1})$$

where  $w_w^*$  is obtained by substituting the average crystal layer temperature  $\bar{T}$  into Eq. A.1.16 and solving for  $w_w$ .  $\rho_L^*$  is the liquid density at  $\bar{T}$  and  $w_w^*$  from Eqs. A.1.3-6.

If BuOH is present, the assumption is made, that the mass ratio of water to butanol  $\zeta_{wb}$  in the pores is the same as in the residual melt.

### A.2.2 Density

The density of crystalline glycerol is given by BLAZHNOV et al. [Bla65], based on UBBELOHDE [Ubb65], as

$$\frac{\rho_{g,C}}{\text{kg m}^{-3}} = 1393.705 - 0.19255 \frac{T}{\text{K}}. \quad (\text{A.2.2})$$

For the density of the crystal layer, it is assumed that the crystalline part is pure glycerol, i. e. no other substance is built into the lattice. The porosity  $\Phi$  of the layer is, however, taken into account:

$$\rho = (1 - \Phi) \rho_{g,C} + \Phi \rho_L. \quad (\text{A.2.3})$$

### A.2.3 Thermal conductivity

SANDBERG et al. [San77] measured the thermal conductivity of pure crystalline glycerol and found it to be proportional to  $T^{0.7}$  for  $130 \text{ K} < T \leq 273 \text{ K}$ . Over the temperature interval relevant to the present study, a linear fit of the measured data at  $258 \text{ K} \leq T \leq 273 \text{ K}$  is sufficient. Its formula is

$$\frac{\lambda_{g,C}}{\text{Wm}^{-1}\text{K}^{-1}} = 0.96448294 + 0.001312336 \frac{T}{\text{K}}. \quad (\text{A.2.4})$$

For the thermal conductivity of the crystal layer, the liquid inclusions are neglected.

### A.2.4 Heat capacity

The volume-specific heat capacity  $\rho c_p$  of pure crystalline glycerol was measured by SANDBERG et al. [San77]. The data points for  $258 \text{ K} \leq T \leq 273 \text{ K}$  can be approximated by

$$\frac{(\rho c_p)_{g,C}}{\text{J m}^{-3}\text{K}^{-1}} = 8.21604 \cdot 10^5 + 4.608865711 \cdot 10^3 \frac{T}{\text{K}}. \quad (\text{A.2.5})$$

## Appendix

Eq. A.2.5 is combined with Eq. A.2.2 to give

$$\frac{c_{p,g,C}}{\text{J kg}^{-1} \text{K}^{-1}} = \frac{8.21604 \cdot 10^5 + 4.608865711 \cdot 10^3 \frac{T}{\text{K}}}{1393.705 - 0.19255 \frac{T}{\text{K}}}. \quad (\text{A.2.6})$$

### A.3 Mass transfer coefficient in a falling film

The calculation of mass transfer coefficients was performed using the analogy between heat and mass transfer and the equations compiled by SCHNABEL & PALEN [Sch94]:

$$Sh = \frac{\beta}{D} \left( \frac{v^2}{g} \right)^{\frac{1}{3}}, \quad (\text{A.3.1})$$

$$Re = \frac{\dot{m}}{2 \pi r \eta}, \quad (\text{A.3.2})$$

$$Sc = \frac{\nu}{D}, \quad (\text{A.3.3})$$

$$\beta = D \left( \frac{v^2}{g} \right)^{-\frac{1}{3}} \max(Sh_i), \quad i \in \{1; 2; 3; 4\}, \quad Sh_1 = 1.3 Re^{-\frac{1}{3}},$$

$$Sh_2 = 0.912 \left( Re^{\frac{1}{3}} Sc \left( \frac{v^2}{g} \right)^{\frac{1}{3}} L^{-1} \right)^{\frac{1}{3}}, \quad Sh_3 = 0.0425 Re^{0.2} Sc^{0.344}, \quad (\text{A.3.4})$$

$$Sh_3 = 0.0136 Re^{0.4} Sc^{0.344}.$$

### A.4 Refractive index of ternary mixtures of glycerol, water and sodium chloride

The refractive index  $n_D$  of binary aqueous glycerol mixtures was reported by HOYT [Hoy34] to fit the following formula:

$$n_{D,gw} = \begin{cases} 1.3303 + 0.1124 w_g + 0.0605 w_g^2 - 0.0555 w_g^3, & w_g < 0.445 \\ 1.32359 + 0.149 w_g, & 0.445 < w_g < 0.795 \\ 0.90799 + 1.54 w_g - 1.55 w_g^2 + 0.576 w_g^3, & 0.795 < w_g \end{cases} \quad (\text{A.4.1})$$

The refractive index and salt mass fraction of aqueous glycerol mixtures saturated with sodium chloride were reported by CHEN [Che70]. The data can be fitted within experimental accuracy to the following 2 formulae:

$$n_{D,gwNaCl}^* - n_{D,gw} = 0.0018 + 0.0366 w'_w + 0.009 w'_w{}^2, \quad (\text{A.4.2})$$

## Appendix

$$w_{\text{NaCl}}^* = 0.00639 + 0.1582 w_w' - 0.0125 w_w'^2, \quad (\text{A.4.3})$$

where  $n_{\text{D,gwNaCl}}^*$  and  $w_{\text{NaCl}}^*$  are the refractive index and sodium chloride mass fraction of a ternary mixture saturated with sodium chloride,  $n_{\text{D,gw}}$  is the refractive index of the salt free binary mixture and  $w_w'$  is the water mass fraction in said salt-free basis.

By interpolating linearly between the point without salt and the point at saturation, the refractive index of the ternary mixture can be calculated as

$$n_{\text{D,gwNaCl}} = n_{\text{D,gw}} + \frac{n_{\text{D,gwNaCl}}^* - n_{\text{D,gw}}}{w_{\text{NaCl}}^*} w_{\text{NaCl}}. \quad (\text{A.4.4})$$

## **Authorship Statement**

I, Felix Johannes Seidel, né Eisenbart, hereby declare that I have written this thesis myself and unaided and have used no sources, devices or support other than those indicated. I have marked all parts that I took, literally or analogously, from my sources appropriately.

Berlin, 20 July 2017

A handwritten signature in black ink, appearing to read 'F. J. Seidel', written in a cursive style.

F. J. Seidel

## Curriculum Vitae

### Personal data

Name Felix Johannes Seidel, né Eisenbart

Date of birth 18.04.1989

Place of birth Clausthal-Zellerfeld

### Education and professional experience

- Since 11. 2013 Research fellow at  
Martin-Luther-Universität Halle-Wittenberg  
Centre for engineering science  
Thermal process engineering
- 4.-10. 2013 Junior engineer at  
Knauf Gips KG, Iphofen  
Department for energy management and process innovation
- 2008-2012 Studies in process engineering at  
Karlsruhe Institute of Technology (KIT)  
Diploma (Dipl.-Ing.) in Dec. 2012  
Thesis: Scaling mitigation in membrane filtration
- Internships at MASA, machine construction, Andernach,  
Dyckerhoff AG, cement production, Lengerich,  
Stadtwerke Andernach, fresh water supply
- 1999 - 2008 Bertha-von-Suttner-Gymnasium Andernach
- 1995 - 1999 Primary School Krufft

## List of Publications and Conference Contributions

### Papers in scientific journals

- 2016 F.J. EISENBART, N. ANGERMEIER, J. ULRICH, *Production of highly dry glycerol by solvent-aided melt layer crystallization*, Journal of Crystal Growth, in press, preliminary version:  
<http://dx.doi.org/10.1016/j.jcrysgro.2016.09.001>
- 2016 F.J. EISENBART, J. ULRICH, *Solvent-Aided Layer Crystallization of Glycerol – Post-Treatment and the Influence of Agitation*, Chemical Engineering & Technology, **39**, 1251-1256.
- 2015 F.J. EISENBART, J. ULRICH, *Solvent-aided layer crystallization – case study glycerol-water*, Chemical Engineering Science, **133**, 24-29.
- 2012 L.L. HECHT, C. WAGNER, Ö. ÖZCAN, F.J. EISENBART, K. KÖHLER, K. LANDFESTER, H.P. SCHUCHMANN, *Influence of the Surfactant Concentration on Miniemulsion Polymerization for the Preparation of Hybrid Nanoparticles*, Macromolecular Chemistry and Physics, **213**, 2165-2173.

### Contributions to conferences

- 2016 F.J. EISENBART, J. ULRICH, *Dynamic layer crystallization of high-viscous melts – Case study glycerol-water*, BIWIC2016, 23<sup>rd</sup> International Workshop on Industrial Crystallization, 6-8 Sept., Magdeburg, Germany, 207-212, poster presentation.
- 2016 F.J. EISENBART, N. ANGERMEIER, J. ULRICH, *Production of Highly Dry Glycerol by Solvent-Aided Melt Layer Crystallization*, Asian Crystallization Technology Symposium, 25-27 May, Tianjin, China, 98-100, oral presentation.
- 2015 F.J. EISENBART, J. ULRICH, *Solvent-Aided Layer Crystallization of Glycerol – The Sweating Step and the Influence of Agitation*, BIWIC2015, 22<sup>nd</sup> International Workshop on Industrial Crystallization, 9-11 Sept., Daejeon, Republic Korea, S.164-172, poster presentation.

## List of Publications and Conference Contributions

- 2015 F.J. EISENBART, J. ULRICH, *A New Concept of Melt Layer Crystallization for High Viscous Feed Streams*, ACHEMA World Forum and 31<sup>st</sup> Leading Show for the Process Industries, 15-19 June, Frankfurt am Main, Germany, oral presentation.
- 2015 F.J. EISENBART, J. ULRICH, *Trennung hochviskoser Schmelzen durch lösemittelunterstützte Schichtkristallisation*, Jahrestreffen der Fachgruppe Kristallisation der DECHEMA, 19-20 March, Magdeburg, Germany, oral presentation.
- 2014 F.J. EISENBART, J. ULRICH, *Solvent-aided layer crystallization – Case study glycerol-water*, 19th International Symposium on Industrial Crystallization, 16-19 Sept., Toulouse, France, 181-182, oral presentation.

### Patents

- 2015 F.J. EISENBART, J. ULRICH, *Verfahren zur Reinigung von Glycerin mittels einer lösemittelgestützten Schichtkristallisation*, German Patent application DE 10 2014 001 533 A1, Martin-Luther-University Halle-Wittenberg, Germany, publication 13 August 2015.